Co- and postseismic deformation patterns and Coulomb stress changes on thrust and normal faults: Insights from finite-element models including pore fluid pressure changes and postseismic viscoelastic relaxation

Von der Naturwissenschaftlichen Fakultät der

Gottfried Wilhelm Leibniz Universität Hannover

zur Erlangung des Grades

Doktorin der Naturwissenschaften (Dr. rer. nat.)

genehmigte Dissertation

von

Jill Benyna Peikert, M.Sc.

2023

Referentin: Prof. Dr. rer. nat. Andrea Hampel

Korreferent: Prof. Dr. sci. nat. Ulrich Heimhofer

Tag der Promotion: 11.10.2023

Table of contents

Abstract

Earthquakes on intra-continental faults do not only cause immediate displacements and damage on the surface, but also induce sudden changes in pore fluid pressure as well as postseismic viscoelastic flow in the lower crust and lithospheric mantle. Such transient processes affect the velocity and stress field of the crust in the surrounding of the source fault for decades and cause significant Coulomb stress changes, which may trigger or delay next earthquakes on adjacent faults (receiver faults). The calculation of these stress changes has become an important tool for seismic hazard evaluation, but the combined influence of coseismic slip, interseismic stress accumulation and transient postseismic processes including poroelastic effects and viscoelastic relaxation on the velocity and stress field in the crust has not been systematically studied so far. 2D and 3D finite-element models with a generalized model setup are used to investigate the relative importance of the different earthquake-induced processes during the co- and postseismic phase of an intra-continental dip-slip earthquake. The models include gravity, isostatic effects, a regional stress field, elastic and viscoelastic layers and pore fluid pressure. In different experiments, important model parameters, including permeability, viscosity, friction coefficient, the size of the coseismic slip and the extension/shortening rate are varied to evaluate their influence on the model results. In the 2D models, a variation of the permeability of the crust and the viscosity of the lower crust and lithospheric mantle shows, that postseismic velocity fields contain signals from overlapping poroelastic and viscoelastic effects. Both processes may influence the velocity field already in the early postseismic phase, up to several decades, depending on the combination of upper-crustal permeability and lower-crustal viscosity. In the 3D models, the permeability of the crust and the viscosity of the lower crust and lithospheric mantle, as well as the friction coefficient, coseismic slip and deformation rate are varied, to evaluate their effect on the Coulomb stress changes on the receiver faults in the model fault array. While the latter three parameters have only an effect on the stress change magnitude, poroelastic effects and viscoelastic relaxation have a strong impact on the magnitudes and patterns of Coulomb stress changes. Poroelastic effects alter the coseismic Coulomb stress changes immediately in the first month after the earthquake, causing stress changes one order of magnitude stronger than those caused by viscoelastic relaxation. If the permeability and viscosity are low enough, the signals from both processes overlap already in the early postseismic phase for decades after the earthquake.

Keywords: finite-element models, earthquake interaction, Coulomb stress changes, poroelastic effects, viscoelastic relaxation

Kurzzusammenfassung

Erdbeben auf intra-kontinentalen Störungen verursachen nicht nur unmittelbare Verschiebungen und Schäden an der Oberfläche, sondern auch plötzliche Veränderungen des Porenfluiddrucks sowie postseismische viskoelastische Relaxation in der unteren Kruste und im lithosphärischen Mantel. Solche transienten Prozesse beeinflussen das Geschwindigkeits- und Spannungsfeld der Kruste in der Umgebung der Ausgangsstörung über Jahrzehnte und führen zu signifikanten Coulomb-Spannungsänderungen, die nächste Erdbeben an benachbarten Störungen (Empfängerstörungen) auslösen oder verzögern können. Die Berechnung dieser Spannungsänderungen ist zu einem wichtigen Werkzeug für die Bewertung seismischer Gefahren geworden, aber der kombinierte Einfluss von koseismischen Versatz, interseismischer Spannungsaufbau und transienten postseismischen Prozessen, einschließlich poroelastischer Effekte und viskoelastischer Relaxation, auf das Geschwindigkeits- und Spannungsfeld in der Kruste wurde bisher nicht systematisch untersucht. In 2D- und 3D-Finite-Elemente-Modellen mit einem generalisierten Modellaufbau wird die relative Bedeutung der verschiedenen erdbebeninduzierten Prozesse während der ko- und postseismischen Phase eines intra-kontinentalen Erdbebens untersucht. Die Modelle beinhalten Schwerkraft-, isostatische Effekte, ein regionales Spannungsfeld, elastische und viskoelastische Schichten sowie Porenfluiddruck. In verschiedenen Experimenten werden wichtige Modellparameter wie Permeabilität, Viskosität, Reibungskoeffizient, Größe des koseismischen Versatzes und Dehnungs-/Verkürzungsrate variiert, um ihren Einfluss auf die Modellergebnisse zu bewerten. In den 2D-Modellen zeigt eine Variation der Permeabilität der Kruste und der Viskosität der unteren Kruste und des lithosphärischen Mantels, dass die postseismischen Geschwindigkeitsfelder Signale aus sich überlappenden poroelastischen und viskoelastischen Effekten enthalten. Beide Prozesse können das Geschwindigkeitsfeld bereits in der frühen postseismischen Phase über mehrere Jahrzehnte hinweg beeinflussen, abhängig von der Kombination aus Permeabilität der oberen Kruste und Viskosität der unteren Kruste. In den 3D-Modellen werden die Permeabilität der Kruste und die Viskosität der unteren Kruste und des lithosphärischen Mantels sowie der Reibungskoeffizient, der koseismische Versatz und die Deformationsrate variiert, um ihre Auswirkungen auf die Größe und Verteilung der Coulomb-Spannungsänderungen auf den Empfängerstörungen zu bewerten. Während sich die drei letztgenannten Parameter nur auf die Größe der Spannungsänderungen auswirken, haben poroelastische Effekte und viskoelastische Relaxation einen starken Einfluss auf die Größe und Muster der Coulomb-Spannungsänderungen. Poroelastische Effekte verändern die koseismischen Coulomb-Spannungsänderungen sofort im ersten Monat nach dem Erdbeben und verursachen Spannungsänderungen, die eine Größenordnung stärker sind als durch die viskoelastische Relaxation. Wenn die Permeabilität und Viskosität ausreichend niedrig sind, überlappen sich die Signale beider Prozesse bereits in der frühen postseismischen Phase über Jahrzehnte nach dem Erdbeben.

Stichwörter: Finite-Elemente-Modelle, Erdbebeninteraktion, Coulomb – Spannungsänderungen, poroelastische Effekte, viskoelastische Relaxation

1. Introduction

1.1 Motivation

On February 6th, 2023, Turkey and Syria were surprised by a strong earthquake with a magnitude of M_w 7.8 in the early morning. During the 80 sec earthquake, many buildings collapsed, almost 60,000 people died, many lost their homes. A large area was devastated. Also, the tsunamis triggered by the earthquake caused significant damage in the coastal areas. Every year there are thousands of earthquakes around the world, most are weak, but some cause significant damage and claim many lives. Therefore, the investigation of earthquakes and their associated processes is very important.

1.1.1 Geological background

Earthquakes are caused by sudden movements in the Earth's crust along tectonically active faults, releasing elastic strain energy in form of seismic waves, which results from the accumulation of elastic strain energy over a long time on time scales of usually $10^2 - 10^4$ years. The movements and the seismic waves lead to significant damages and so far, it is impossible to predict when and where the next earthquake will occur. Hence, earthquakes pose a significant seismic hazard to populated areas. Most of the strong earthquakes occur along plate-boundaries, such as the 2011 $M_w = 9.1$ Tohoku Earthquake or the 2023 $M_w = 7.8$ Turkey-Syria earthquake. Intra-continental earthquakes have received less attention, but also intra-continental faults have the potential to cause major earthquakes, for example, the 1999 $M_w = 7.7$ Chi-Chi earthquake (Figure 1.1) or the 2009 $M_w = 6.3$ L'Aquila earthquake.
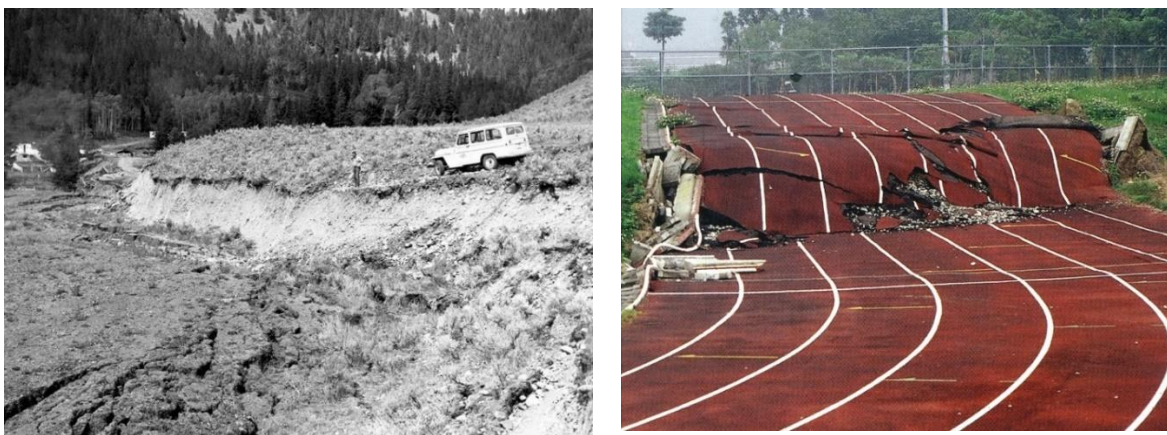
Figure 1.1: Examples of intra-plate earthquakes, which led to significant damages: a normal fault scarp caused by the 1959 Hebgen Lake Earthquake (left side; USGS homepage https://www.usgs.gov/media/images/hebgen-lake-fault-scarp-1959) and a thrust fault scarp caused by the 1999 Chi-Chi earthquake (right side; Yeats, 2012).

1.1.1.1 Fault types

Faults are fracture zones within the Earth's crust from a few millimeters to thousands of kilometers in length, between which two fault blocks (hanging wall and footwall) move relative to each other. The movement of the fault blocks, which do not slip past each other due to friction, builds up elastic stress, that is released during an earthquake, resulting in a rupture and a sudden slip of up to several meters between the fault blocks. For earthquakes with a magnitude of ~6 or larger, the displacement caused by the earthquake can be observed at the surface as a fault scarp (Figure 1.1) (e.g., Burbank and Anderson, 2001). The vertical and horizontal surface displacements can be determined by geodetic measurements (GPS, InSAR) and can be used, for example, to derive the deformation rate and the slip distribution or calculate stress changes (e.g., Cheloni et al., 2010; Chen et al., 2006; Serpelloni et al., 2012; Yu et al., 2001).
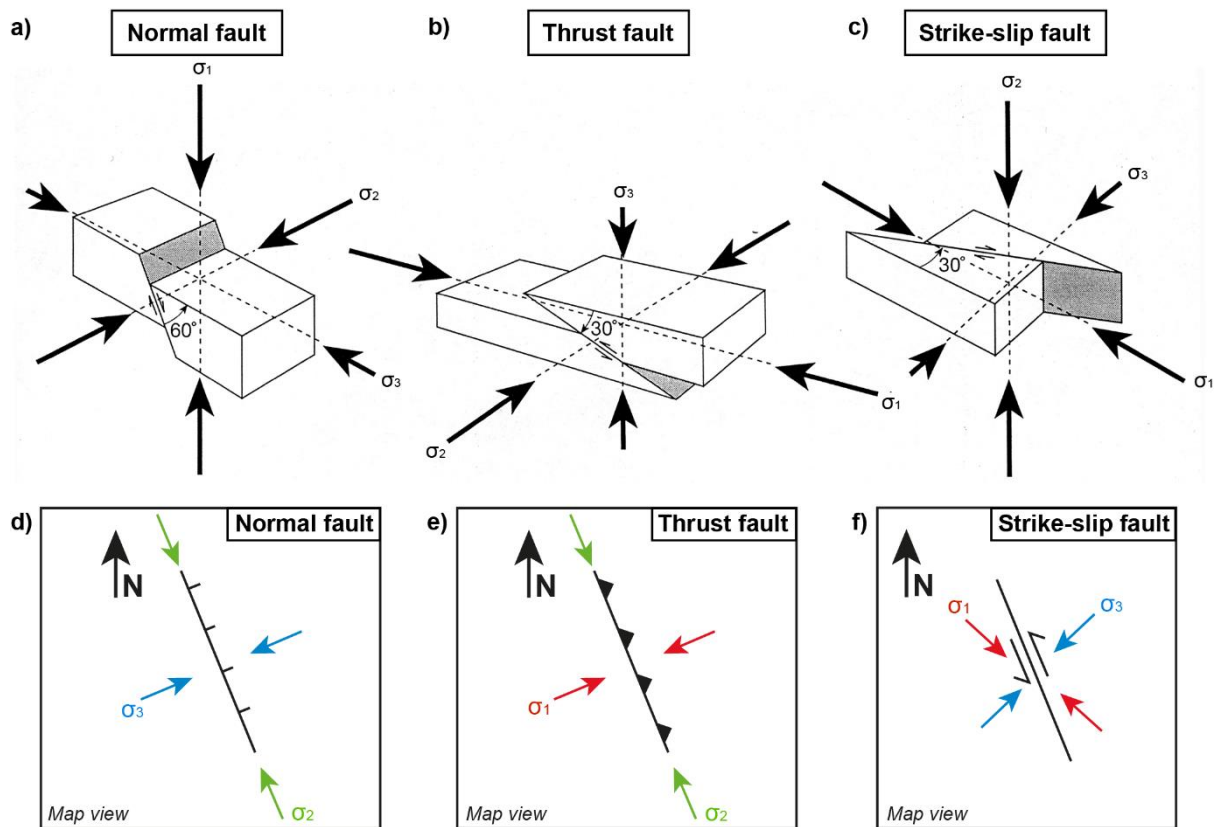
Figure 1.2: a)-c) Three fault types with principal normal stress directions. d)-f) Map view of the three fault types with principal stress directions (a-c: modified from Eisbacher, 1991; d-f: figure provided by A. Hampel).

Three types of faults with different fault dips and slip directions can be classified, determined by the orientation of the three principal stress directions σ_1, σ_2, σ_3 (Anderson, 1951). The principal stresses are directed perpendicular to each other, σ_1 and σ_3 are the maximum and

minimum principal stresses, respectively. No shear stress occurs at the principal stress planes. Anderson's Fault Theory is based on the assumption that the Earth's surface must be a principal plane of stress with zero shear stress. Two of the principal stresses are directed parallel to the surface, one is oriented perpendicular to the surface. The three types of faults are shown in Figure 1.2. For normal faults, the maximum principal stress σ_1 is vertical while σ_2 and σ_3 are horizontal. The hanging wall moves downwards relative to the footwall, which leads to a coseismic vertical displacement pattern of hanging wall subsidence and footwall uplift. The typical fault dip of the normal fault is 60°. For thrust faults, the maximum principal stress σ_1 and σ_2 are oriented horizontally, σ_1 perpendicular to the fault plane, and σ_3 is vertical. The hanging wall moves upwards relative to the footwall, which leads to shortening. At the surface, hanging wall uplift and footwall subsidence can be observed. The typical dip of a thrust fault is 30°. Both normal and thrust faults are known as dip-slip faults. In case of the third fault type, strike-slip faults, σ_1 and σ_3 are horizontal, σ_2 is vertical and the two fault blocks slide past each other in horizontal direction. In each fault type, $\sigma2$ is always parallel to the fault plane and σ_1 always forms an angle of 30° to the fault plane (Anderson, 1951).

1.1.1.2 The earthquake cycle

The sequence, in which the elastic strain is built up on the faults over a long time period by the regional deformation rate and suddenly released in form of an earthquake, defines the earthquake cycle, based on the elastic rebound theory (Reid, 1910; Scholz, 2019). The earthquake cycle is a continuous process and is subdivided into three repetitive stages, with varied lengths of each stage depending on the location and the characteristics of the faults involved (Figure 1.3a). In the interseismic phase, the fault-bounding blocks slowly move at a certain rate past each other but do not slip due to friction, the fault is locked. This results in an accumulation of elastic strain energy. Once the strain energy reaches a critical level and the critical shear stress on the fault is exceeded, the fault fails and an earthquake is triggered, during which the elastic strain energy accumulated in the interseismic phase is suddenly released and the fault experiences a stress drop and a sudden coseismic slip. This process represents the coseismic phase. The shear failure on the fault planes can be described by the Mohr-Coulomb-Criterion (Scholz, 2019):

$$\tau_{max} = c + \mu\ \sigma_n$$

where τ_{max} is the critical shear stress, c is the cohesion, μ the friction coefficient and σ_n is the normal stress. The postseismic phase immediately follows after the coseismic phase and can

last for weeks up to years, depending on the size and characteristics of the earthquake. The fault and its surrounding are still affected by the consequences of the earthquake. Deformation, changes in stress and seismic activity continue due to different processes caused by the earthquake, such as afterslip and viscoelastic or poroelastic relaxation (Scholz, 2019).
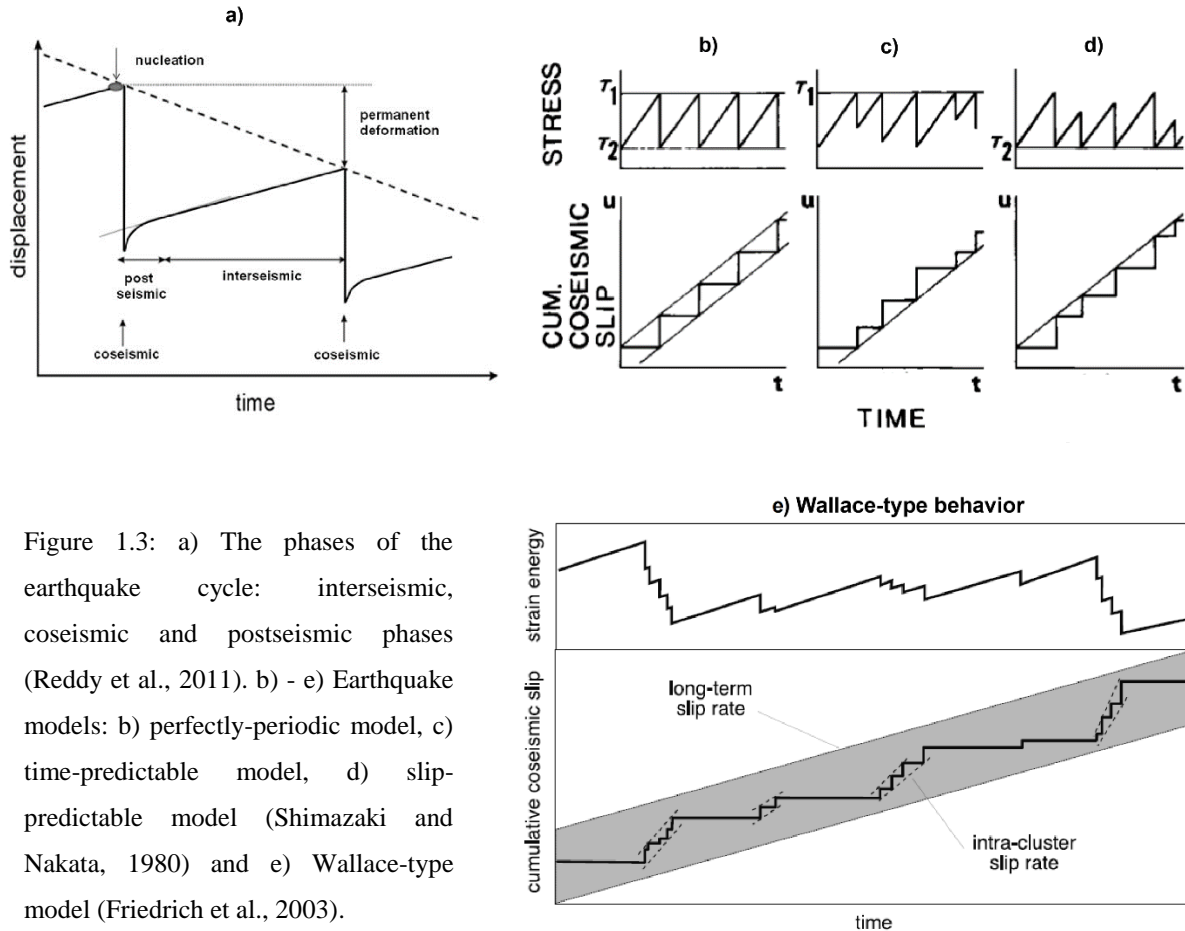
Figure 1.3: a) The phases of the earthquake cycle: interseismic, coseismic and postseismic phases (Reddy et al., 2011). b) - e) Earthquake models: b) perfectly-periodic model, c) time-predictable model, d) slip-predictable model (Shimazaki and Nakata, 1980) and e) Wallace-type model (Friedrich et al., 2003).

Several earthquake models with different approaches are defined to explain the complex behavior and recurrence of earthquakes over time (Reid, 1910; Shimazaki and Nakata, 1980; Wallace, 1987). Each earthquake model shown in Figure 1.3b – e represents the evolution of stress and the cumulative coseismic slip as a function of time. In the perfectly-periodic model (Figure 1.3b), the stress accumulates and drops at a constant rate and level (T_1 and T_2), which leads to periodic earthquakes of the same magnitude and recurrence interval. The time-predictable model (Figure 1.3c) describes a stress accumulation until a constant critical level (T_1), but the stress drop and hence the coseismic slip differs. Here, the time to the next earthquake but not the size is predictable. In the slip-predictable model (Figure 1.3d), the stress drops to a constant level (T_2) after a variable stress level is accumulated. The size of the next earthquake, but not the time point can be predicted. Figure 1.3e shows the Wallace-type model, which describes a clustered stress release and slip. Short-term periods with a high earthquake

6

recurrence alternate with long-term periods of infrequent earthquakes and low strain accumulation.

The earthquake models can be used to understand the behavior and recurrence of earthquakes in nature and some observations of earthquakes agree well with the models, e.g. the Nankaido earthquake sequence (Shimazaki and Nakata, 1980) or earthquake sequences in northeast India (Panthi et al., 2010). Generally, however, the earthquake models do not fully capture the complexity of the behavior of earthquakes in nature. Natural earthquakes are not perfectly periodic, the time as well as the size of an earthquake can vary widely and are not predictable due to changes in the rate of strain accumulation or other factors that affect the rupture process, similar as modelled in the Wallace model. Also, the current stress level and the status of the earthquake cycle are unknown. Additionally, fault systems are complex, with multiple faults interacting.

1.1.1.3 Earthquakes and fault interaction

If an earthquake on a fault releases the elastic stress built up from the interseismic phase, it not only affects the displacement field but also the stress field and leads to stress changes in the surrounding of the ruptured fault (source fault). This stress transfer can trigger or delay next earthquakes on adjacent faults (receiver faults) or even at greater distances (Freed, 2005; Scholz, 2019). Based on the Coulomb friction model for earthquakes, the potential to trigger or delay next earthquakes can be expressed by a change in the Coulomb failure stress, ΔCFS:

$$\Delta CFS = \Delta\tau - \mu \, (\Delta\sigma_n - \Delta p)$$

where $\Delta\tau$ is the change in shear stress, $\Delta\sigma_n$ and Δp are the changes in normal stress and pore pressure on the fault and μ is the friction coefficient (Scholz, 2019). An increasing shear stress or a decreasing effective normal stress ($\Delta\sigma_n - \Delta p$) and *vice versa* leads to increasing Coulomb failure stress (Freed, 2005). An increase in Coulomb stress (ΔCFS > 0) brings receiver faults closer to failure, whereas a Coulomb stress decrease (ΔCFS < 0) implies that the next earthquake is delayed. A Coulomb stress change of 0.1 MPa (1 bar) on the receiver faults, which is only a few percent of the coseismic stress drop on the source fault, is already high enough to potentially trigger another earthquake (King et al., 1994; Scholz, 2019; Stein, 1999). The analysis of Coulomb stress changes on faults is important to assess future seismic hazards, because it can be used to identify possible locations for future earthquakes. Hence, Coulomb stress changes are often calculated after major earthquakes (Bagge et al., 2019; Field et al., 2009; Freed et al., 2007; Luo and Liu, 2010; Parsons et al., 2008; Serpelloni et al., 2012; Stein,

7

2003; Toda et al., 2005; Wan and Shen, 2010; Wang et al., 2014). It is currently not possible to measure Coulomb stress changes on natural faults and the calculation depends on the geometry of the fault, the rheology of the region, the slip distribution of the earthquake, the rate and orientation of the regional stress field, and the friction coefficient.

Several earthquake-induced mechanisms may cause significant Coulomb stress changes in the vicinity of a ruptured fault, which act on different temporal and spatial scales. The sudden coseismic slip on the source fault leads to positive or negative coseismic (static) Coulomb stress changes on the receiver faults. Typical magnitudes of these static stress changes are in the range of a few percent of the coseismic stress drop and usually do not reach values of more than 1 MPa (Lin and Stein, 2004; Lin et al., 2011; Nostro et al., 1997; Ryder et al., 2012). Static Coulomb stress changes are routinely calculated to explain aftershock distributions and earthquake sequences (e.g., Hardebeck et al., 1998; Nostro et al., 1997; Parsons et al., 2008; Serpelloni et al. 2012; Stein et al., 1997; Wan and Shen, 2010; Wang and Chen, 2001).

Dynamic stress changes are triggered by the passage of seismic waves (Belardinelli et al., 1999; Pollitz et al., 2012; Scholz, 2019). Dynamic stress changes occur for up to several days over distances of hundreds to thousands of kilometers, depending on the wave properties. Seismic waves generate solely positive stress changes with typical values of one order of magnitude larger than static Coulomb stress changes (Belardinelli et al., 1999; Freed, 2005; Scholz, 2019).
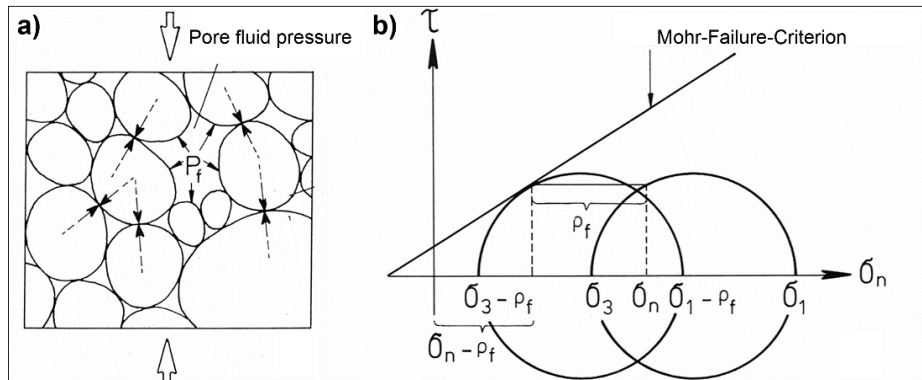
Figure 1.4: The effect of pore fluid pressure P_f. a) Illustration of the pore pressure in a porous rock. b) Effect of the pore pressure changes on the normal stress σ_n illustrated by a Mohr-diagram (Eisbacher, 1991).

Postseismic stress changes are caused by transient processes, which can trigger earthquakes after a time delay of days to decades. The earthquake on the fault in the brittle upper crust causes a stress increase that is coseismically imposed on the viscoelastic lower crust and lithospheric mantle, where it is relaxed by viscoelastic flow in the postseismic phase, which leads to considerable Coulomb stress changes in the upper crust (Freed and Lin 2001; Freed,

2005; Nur and Mavko, 1974). This process is called postseismic viscoelastic relaxation and it may trigger earthquakes over large distances of up to hundreds of kilometers away from the ruptured fault on timescales of years to many decades, depending primarily on the viscosity structure of the viscoelastic lithospheric layers (Bagge and Hampel, 2017; Bagge, et al., 2019; Chéry, 2001; Freed, 2005; Masterlark and Wang, 2002).

Postseismic Coulomb stress changes also arise from poroelastic effects in the porous, fluid-saturated crust. The coseismic movements lead to changes in pore fluid pressure and hence to considerable pore fluid pressure gradients within the upper crust. The pore fluid pressure is redistributed to its initial state by fluid flow from over-pressurized areas to under-pressurized areas, inducing significant stress changes. As Figure 1.4 shows, an increase in pore fluid pressure (P_f) brings a fault closer to failure by reducing all normal stresses by the amount of pore pressure. The shear stress is not affected. The Mohr-Coulomb-Criterion from section 1.1.1.2 is changed by the pore pressure (P_f):

$$\tau_{max} = c + \mu \, (\sigma_n - P_f)$$

where τ_{max} is the critical shear stress, c is the cohesion, μ the friction coefficient, σ_n is the normal stress and P_f is the pore fluid pressure. Poroelastic effects normally act on small spatial scales within 1-2 fault lengths around the source fault (Albano et al., 2017; Cocco and Rice, 2002; Piombo et al., 2005; Tung and Masterlark, 2018). The pore fluid pressure dissipation time varies between hours to years and depends, as well as the magnitude of the pore pressure change, on the elastic and hydraulic properties, e.g. the permeability, of the crust (Albano, 2017; Dempsey et al., 2013).

Other processes, which can lead to a Coulomb stress increase on faults are afterslip and interseismic stress accumulation. Afterslip is caused by unrelieved stress after an earthquake, which induces an aseismic slip within the rupture surface or at deeper regions of the fault (Freed, 2005). Interseismic stress accumulation is controlled by the regional deformation field and is continuously built-up stress on the fault zones (e.g., Bagge and Hampel, 2017; Bagge et al., 2019; Hearn and Thatcher, 2015).

1.2.2 State of the art

The calculation of Coulomb stress changes has become an important tool for the seismic hazard assessment and is routinely applied after major earthquakes to explain the distribution and evolution of aftershocks because Coulomb stress changes imply that next earthquakes will be

enhanced or retarded. That was shown by the first case studies of strike-slip faults, which demonstrated that most aftershocks after a major earthquake are located in areas of positive static Coulomb stress changes around the ruptured fault. For example, most aftershocks of the 1979 Homestead Valley Earthquake and the 1992 Joshua Tree Earthquake in California are concentrated in areas with a stress increase of at least 3 bars and are nearly absent in areas with negative stress changes, as shown in Figure 1.5 (King et al., 1994; Stein and Lisowski, 1983). The 1979 Homestead Valley, the 1986 North Palm Springs and the 1992 Joshua Tree Earthquakes increased the Coulomb stress changes in a region, which experienced the following 1992 Landers Earthquake (Figure 1.5c) and most aftershocks of the Landers Earthquake including the 1992 Big Bear Earthquake occur in areas with a stress increase (King et al., 1994; Stein et al., 1992).
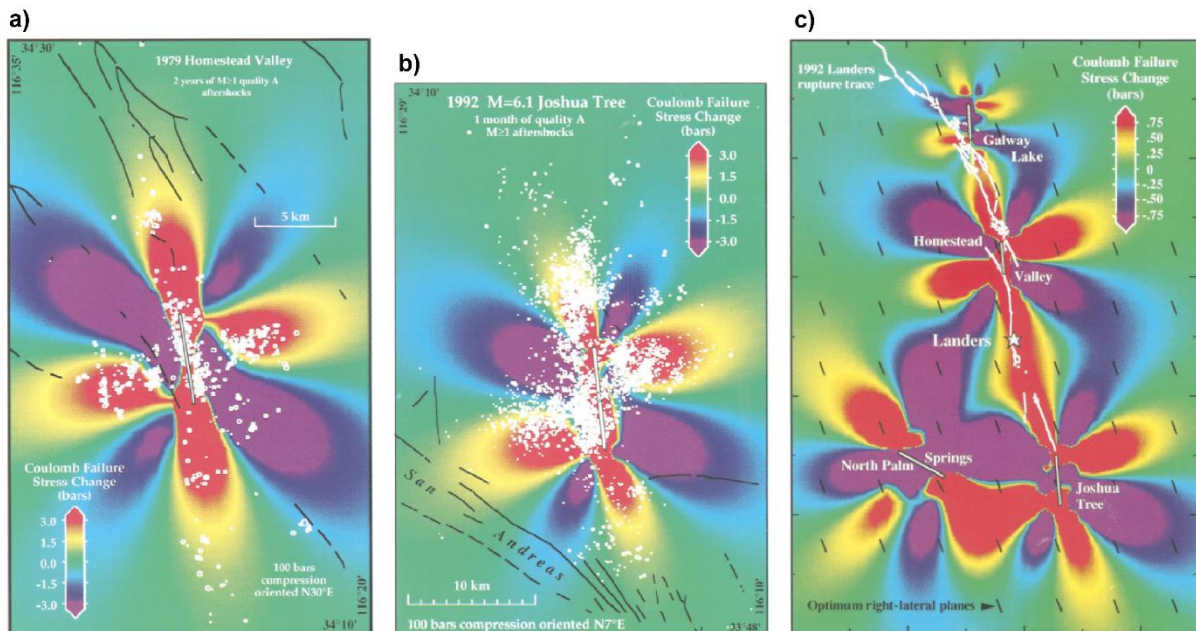
Figure 1.5: Static Coulomb stress changes of the earthquake sequence in California, modified from King et al., 1994: a) Coulomb stress changes and aftershock distribution associated with the 15 March 1979 Homestead Valley earthquake sequence, b) Coulomb stress changes and aftershock distribution associated for the 23 April 1992 Joshua Tree earthquake and c) Coulomb stress changes calculated for the four M > 5 earthquakes in the Caltech-USGS catalog within 50 km of the future Landers epicenter (ruptures enclosed as white lines). Each earthquake raised the stress at the future Landers epicenter (star).

Over the past two decades, most studies have focused on the calculation of static Coulomb stress changes, based on the analytical models of Okada (1985, 1992), which are able to calculate displacements and stress changes by dislocations in an isotropic, homogeneous elastic half-space (e.g., Chousianitis and Konca, 2021; Ganas et al., 2012; Nostro et al., 1997; Nostro et al., 2005; Serpelloni, 2012; Stein et al., 1992; Stein et al., 1997; Wan and Shen, 2010). The

slip distribution is required and can be derived from geodetic data. Investigations of intra-continental dip-slip earthquakes, for which static Coulomb stress changes are analyzed by this technique are e.g. the 1997 Umbria-Marche (Cocco et al., 2000; Nostro et al., 2005), the 2009 L'Aquila (Serpelloni et al., 2012) and the Emilia-Romagna sequence (Ganas et al., 2012) in Italy, the 2008 Wenchuan (Parsons et al., 2008; Wan and Shen, 2010) and 2013 Lushan earthquakes (Zhu and Miao, 2015) in China, the 2015 Gorkha earthquake in Nepal (Yang et al., 2018) or the 2020 Samos earthquake in the eastern Aegean Sea (Chousianitis and Konca, 2021). However, the application of the analytical models from Okada is limited to the calculation of static Coulomb stress changes, because only elastic deformation is considered. To include transient processes such as postseismic viscoelastic relaxation or poroelastic effects, other model techniques with much more technical and computational effort are required (Bagge and Hampel, 2017; Freed and Lin, 1998; Luo and Liu, 2010; Masterlark and Wang, 2002; Nostro et al., 2001; Wang et al., 2006).

As shown by many studies, however, the calculation of static stress changes alone is not sufficient in many cases (e.g., Bagge et al., 2019; Cocco et al., 2000; Masterlark and Wang, 2002; Piombo et al, 2005; Verdecchia et al., 2018; Zhu and Miao, 2015). Piombo et al. (2005) demonstrated, that there are regions where Coulomb stress changes vary after an earthquake from positive to negative and *vice versa* caused by transient mechanisms. Locations, that experience negative static stress changes after the main shock, become positive due to pore fluid pressure changes and fluid flow. Calculations of static Coulomb stress changes in California reveal, that it is not clear, if the 1999 Hector Mine Earthquake occur in an area of positive or negative stress changes caused by the 1992 Landers Earthquake (Masterlark and Wang, 2002) and that transient processes like postseismic viscoelastic relaxation (Freed and Lin, 2001; Polliz and Sacks, 2002) or poroelastic effects (Masterlark and Wang, 2002) played a crucial role for the triggering of the Hector Mine earthquake.

Investigations of postseismic deformations and stress changes under consideration of transient processes mostly focused on a specific time interval and hence on only one transient process, because they assume that the transient processes act on different spatial and temporal scales. Albano et al. (2017, 2019) and Tung et al. (2018a) investigated the aftershock evolution in the first months of the postseismic phase and hence neglected postseismic viscoelastic relaxation. They showed, that poroelastic effects play an important role for the transient stress transfer and the occurrence of aftershocks. For example, in Albano et al. (2017), the aftershocks in the early postseismic phase during the Emilia-Romagna sequence occur at areas with high pore pressure

changes due to the earthquake, and their evolution correlates spatially and temporally with the stress changes caused by the pore pressure diffusion process. Other studies focus on long-term analysis by considering only postseismic viscoelastic relaxation and no poroelastic effects (Bagge et al., 2019; Luo and Liu, 2010; Verdecchia et al., 2018; Wang et al., 2014) and demonstrated that viscoelastic relaxation may modify the stress field for up to several decades and trigger events over a long time and over large distances (Bagge et al.,2019; Verdecchia et al., 2018). The limited number of studies, which combined static Coulomb stress with both types of transient stress changes confirm the assumption of different timescales between the processes in their analysis of the Amatrice-Visso (Tung and Masterlark, 2018) and the Landers-Hector Mine (Freed and Lin, 2001; Masterlark and Wang, 2002) seismic sequences. However, the validity of this assumption has actually never been tested and studies with numerical models provide the evidence that viscoelastic relaxation may already occur in the early postseismic phase of the earthquake (e.g., Hampel and Hetzel, 2015) and may therefore overlap with the timescale of poroelastic effects. Most of the above-mentioned examples focus on individual earthquakes and faults in nature with a particular tectonic setting and rheological properties. Only a few studies investigated Coulomb stress changes by using theoretical models with a general setting (e.g., Bagge and Hampel, 2016, 2017; Cocco and Rice, 2002; Lin et al., 2011; Miao et al., 2021; Nostro et al., 2001).

1.2.3 Aim of this thesis

As mentioned above, several published studies showed that Coulomb stress calculations on natural faults can be ambiguous and caused by combinations of different transient and non-transient processes, which are usually not taken into account together in a combined analysis. The evolution of Coulomb stress changes caused by the combination of poroelastic effects and viscoelastic relaxation with static stress changes and interseismic stress accumulation in a generalized intra-continental model domain has not been systematically studied, yet. The hypothesis that the processes can be distinguished by their different temporal and spatial scales has never been tested for normal or thrust faults. This leads to the following research questions that are addressed in this work:

1. What is the relative importance of poroelastic effects and viscoelastic relaxation for the displacements and stress field of intra-continental normal and thrust faults?

2. How do the permeability and viscosity in the crust influence the pore fluid pressure changes and viscoelastic relaxation and thus the evolution of the displacements and stress field after an intra-continental earthquake?

3. What are the spatial and temporal scales of poroelastic effects and viscoelastic relaxation?

4. How do other parameters including the magnitude of coseismic slip, the friction coefficient and the total extension/shortening rate affect the Coulomb stress changes on normal and thrust faults?

The goal of this thesis is a systematic investigation of the interaction of pore fluid pressure changes and postseismic viscoelastic relaxation for the evolution of the displacements and stress field during the earthquake cycle of intra-continental normal and thrust faults by using finite-element models. The findings should lead to a better understanding of coseismic and transient Coulomb stress changes caused by coseismic slip, poroelastic effects, viscoelastic relaxation and interseismic stress accumulation. This offers insights into the relative importance of the different mechanisms for generating Coulomb stress changes on receiver faults and how quickly static Coulomb stress changes are altered by poroelastic effects and viscoelastic relaxation. By evaluating co- and postseismic velocity and stress change patterns independent of a specific earthquake, a detailed analysis of the spatial and temporal scales of the different processes is provided. Furthermore, a fundamental part of this thesis is to provide essential information for calculating Coulomb stress changes and analyzing postseismic velocity fields from geodetic data, which is crucial for earthquake hazard and risk assessment.

As a method, 2D and 3D finite-element models of normal and thrust faults with a generalized model setup independent of a particular fault geometry, specific earthquake and tectonic setting are used. All models consider gravity, isostasy, regional extension or shortening, pore fluid pressure and viscoelastic lithospheric layers. In a parameter study, several parameters in the models, including permeability, viscosity, friction coefficient, coseismic slip and deformation rate are varied to evaluate their influence on the model results.

The thesis is divided into four parts. In the first step, 2D finite-element models of normal and thrust faults with varied permeabilities and viscosities in the crust are used to analyze the co- and postseismic pore pressure changes as well as postseismic vertical and horizontal velocities (Chapter 2) at different time points. The next chapter (Chapter 3) includes the same parameter study with varied permeabilities and viscosities, but here, the co- and postseismic Coulomb stress changes for 3D finite-element models with a normal and thrust fault array are calculated

and evaluated. In addition, the results are linked to the postseismic surface deformation. The influence of the coseismic slip, the friction coefficient and the regional extension/shortening rate on the stress changes are presented in Chapter 4. In a final discussion, the main findings and limitations of this parameter study are evaluated and compared with published analyses for natural faults and earthquakes (Chapter 5).

1.2 Methods

1.2.1 Finite-element modeling

The finite-element method is a numerical model technique that can be used for complex mathematical problems, whose partial differential equations cannot be solved analytically. In geosciences, the finite-element method can be applied to model complex geological and geophysical systems and structures, such as e.g. earthquake and fault interaction, deformation and stress distributions, mechanical behavior of rocks, the flow of fluids or heat transfer. The finite element method is based on the principle of dividing a complex problem into a set of smaller, simpler sub-problems that are easier to solve. The continuous domain to be calculated is discretized by dividing it into small parts, i.e. a finite number of elements with a simple shape (e.g., triangular, tetrahedral, hexahedral). Depending on the element shape, each element consists of a varying number of element nodes, that connect the corners of neighboring elements and form the mesh. The properties and characteristics of the elements at each node are represented by a set of mathematical equations. After solving these equations for the nodes, the nodal values, which describe the behavior of the element, are interpolated to obtain a continuous solution over the entire domain.

The choice of the mesh size, the number and the shape of the elements depend on the type of problem being solved. For example, triangular-formed elements are commonly used in 2D simulations and are defined by three nodes, quadrilateral elements for 2D and 3D simulations have four nodes forming a quadrilateral shape and tetrahedral elements, which are commonly used in 3D simulations, are defined by four nodes that form a tetrahedron. The mesh size and the number of elements determine the accuracy of the simulation and computation time. In general, a smaller mesh size and a larger number of elements increase the number of equations and thus result in a more accurate solution, but also increase the computational costs of the analysis. For the best results, it is important to balance the trade-off between accuracy and computational efficiency. The mesh size is sufficient when further refinement does not have a significant influence on the accuracy of the calculation result.

1.2.2 General model setup and model run

The 2D and 3D numerical models in this thesis are created and calculated with the commercial finite-element analysis software ABAQUS (2018). This software allows including gravity, viscoelastic layers, the regional stress field, and interseismic stress accumulation, enables coupled pore fluid diffusion/stress analyses and captures the different temporal and spatial scales of poroelastic effects and postseismic viscoelastic relaxation. Different outputs are provided at pre-defined time intervals for different areas of the model, such as the fault planes or the model surface. The outputs used in this thesis are, for example, displacements, pore fluid pressure or normal and shear stress, which are used to calculate co- and postseismic Coulomb stress changes on the fault planes. Therefore, ABAQUS requires several input parameters and prescribed conditions, including the geometry and properties of the model domain, boundary conditions, interactions, loads, element size and shape. Different model analysis steps with different time lengths have to be defined, in which the loading, interaction and boundary conditions of the model can be varied.

All 2D and 3D normal and thrust fault models represent a 100 km thick and 500 km and 200 x 200 km wide continental lithosphere, respectively, subdivided into a 15 km thick elastic upper crust, a 15 km thick viscoelastic lower crust and a 70 km thick viscoelastic lithospheric mantle (Figure 1.6). The 2D models include a fault in the center of the upper crust. In the 3D models, a fault array is embedded in the upper crust comprising the source fault (SF) in the center and ten receiver faults (RF), such that postseismic Coulomb stress changes in the surrounding of the source fault can be captured. RF4, RF5, RF7 and RF8 are located in the footwall and hanging wall of the source fault, RF2 and RF10 are located along-strike of the source fault tips and RF1, RF3, RF9 and RF11 are located outside of the immediate hanging wall and footwall. The faults are integrated as frictional contact interfaces between footwall and hanging wall of each fault. As a fault dip, 60° and 30° are used for the normal and thrust fault, respectively. The faults within the 3D models are 40 km long and distances of ≥15 km in the x-direction and ≥5 km in the y-direction are applied between the faults. These dimensions reflect the natural spatial configuration of faults, for example, in the Basin and Range Province (Wesnousky et al., 2005), the Aegean region (Roberts and Michetti, 2004) and the foreland of the Tibetan Plateau (Hetzel et al., 2004; Meyer et al., 1998). The 2D models are meshed by second-order rectangular elements with an edge length of 1 km.

At the model sides of the 2D models and the model sides in the yz-plane of the 3D models a boundary condition is applied, which extends (normal fault models) or shortens (thrust fault

models) the model domain by 6 mm/a to simulate the tectonic background deformation and interseismic strain accumulation. The model sides in the xz-plane of the 3D models are fixed in y-direction. The model bottom is free to move in vertical and horizontal directions. The deformation rate will be varied in different experiments (cf. section 1.2.3).
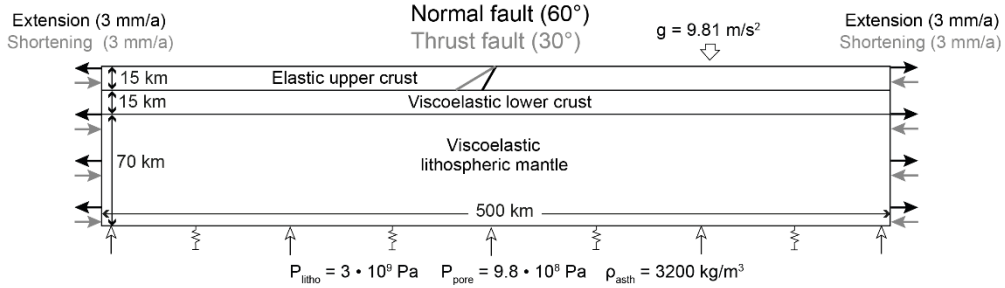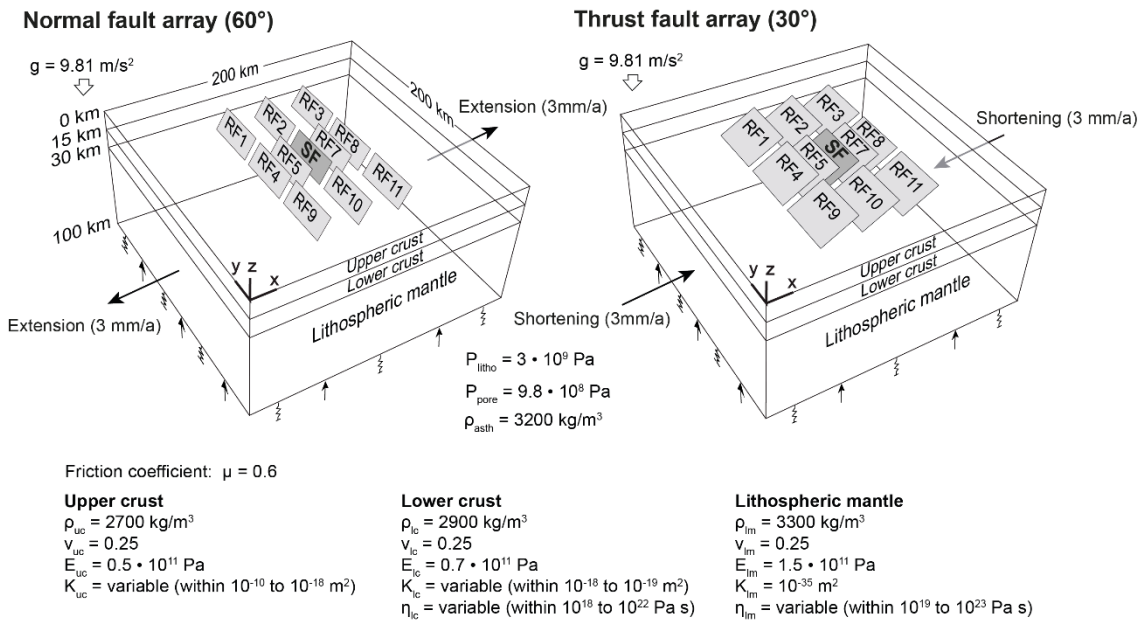
Figure 1.6: Setup of (a) the 2D finite-element normal and thrust fault reference model and (b) the 3D finite-element reference models with arrays of 40-km-long normal and thrust faults, respectively. Material properties are density (ρ), Young's modulus (E), Poisson's ratio (ν), viscosity (η) and permeability (K). Viscosity and permeability are varied in different experiments. Gravity is included as a body force. A lithostatic pressure and an elastic foundation, which represent the asthenosphere, are applied to the model bottom to implement isostatic effects (cf. Hampel et al., 2019). At the model sides, a velocity boundary condition is applied to extend or shorten the model at a total rate of 6 mm/a.

The rheological input parameters (Poisson's ratio ν, density ρ, Young's modulus E, permeability K and viscosity η) for the lithospheric layers in these principal models (reference models) are implemented in ABAQUS as material properties and represent typical values for

continental lithosphere (Chen and Molnar, 1983; Ingebritsen and Manning, 2010; Klemperer, 2006; Manning and Ingebritsen, 1999; Ryder et al., 2014; Shi et al., 2015; Stober and Bucher, 2015). For the viscosity, values of 10^{20} Pa s for the lower crust and 10^{23} Pa s for the lithospheric mantle are used. As permeabilities for the upper and lower crust, 10^{-12} m^2 and 10^{-18} m^2 are applied, the lithospheric mantle represents an impermeable layer with a permeability value of 10^{-35} m^2 (Tung et al., 2018a). The permeability is entered into ABAQUS as the hydraulic conductivity, which can be converted from $K_f = K * \rho_{fluid} * g / \eta_{fluid}$ (ρ_{fluid}: fluid density, 1000 kg/m^3; acceleration due to gravity, 9.81115 m/s^2; η_{fluid}: fluid viscosity, 998 x 10^{-6} kg m^{-1} s^{-1}). The viscosity values and the permeabilities in the upper and lower crust will be varied in different experiments (cf. Section 1.2.3). Viscoelastic behavior is implemented as linear, temperature-independent Maxwell viscoelasticity. Gravity is included as a body force, isostatic effects are simulated by applying a lithostatic pressure (P_{litho} = 3 x 10^9 Pa) as well as an elastic foundation, which represents the density of the asthenosphere (3200 kg/m^3) to the model bottom. The initial pore pressure distribution implemented at the model bottom is hydrostatic (P_{pore} = 9.8 x 10^8 Pa). For the coupled pore fluid diffusion/stress analysis in ABAQUS to simulate the coupling between solid and fluid phase, the saturation, which is 1 in our model and the void ratio are required. The void ratio describes the proportion between volumes of voids and solids in the medium and the volume of fluid trapped in the medium. Typically, it is a few percent for crystalline basement rocks (e.g. Masterlark and Wang 2002; Masterlark et al., 2003), in our models 0.06. Moreover, fluids cannot flow across the model boundaries and the faults, both are treated as impermeable (cf. Albano et al., 2017, 2019; Dempsey et al., 2013; Rudnicki, 1986; Tung and Masterlark, 2018).

Each model run consists of three model phases with different boundary conditions and time lengths, in which the model is divided into quasi-static analysis steps. In the first phase, during which the faults are unlocked, isostatic and hydrostatic equilibrium is established. In the second phase, extension/shortening is applied, slip accumulates on the faults until they reach constant slip rates. In both phases, the boundary conditions for the faults are set to unlock, which means slip on the faults is allowed. The slip on the model faults is initiated by the extending/shortening rate at the model sides and controlled by the Mohr-Coulomb criterion $\tau = C + \mu \sigma_n$, where τ is the shear stress, C is the cohesion (zero in the models), μ is the friction coefficient, which is 0.6 in the models and will be varied in different experiments and σ_n is the normal stress. The slip distribution develops freely and is not prescribed. Once the faults achieve a constant slip rate, the third model phase simulates the earthquake cycle. In the preseismic phase, extension/shortening continues, but the faults are switched to locked, no slip is allowed and slip

accumulation stops. Besides the extension/shortening rate and the rheological properties, the duration of the preseismic phase controls the magnitude of the model earthquake. Thus, the length of the preseismic phase must be chosen such that the coseismic slip is a maximum of 2 m, which corresponds to an earthquake with a magnitude of Mw = 6.9. In the coseismic phase, the source fault is unlocked (in the 3D models, all receiver faults remain locked) and experiences a sudden slip, which simulates the model earthquake. In the postseismic phase, all faults are locked again, while extension or shortening continues, to simulate the interseismic stress accumulation. The postseismic phase in all models lasts 100 years.

1.2.3 Parameter study

In order to test the influence of the different rheological parameters on the evolution of pore pressure changes, velocity field and Coulomb stress changes, the magnitude of the model earthquake, friction coefficient, extension/shortening rate, permeability and viscosity of the models are varied successively in different experiments. All models with varied parameters are shown in Table 1.1. The defined normal and thrust fault reference models consist of a permeability and viscosity structure typical of continental lithosphere (cf. Chapter 1.2.2; Chen and Molnar, 1983; Ingebritsen and Manning, 2010; Klemperer, 2006; Manning and Ingebritsen, 1999; Ryder et al., 2014; Shi et al., 2015; Stober and Bucher, 2015). The effects of pore fluid flow and viscoelastic relaxation are isolated by considering only poroelastic effects but no viscoelastic relaxation and *vice versa* during the postseismic phase. In the different sets of experiments, one parameter at a time is varied, while the other parameters are kept constant. For the viscosity, values from 10^{18} Pa s to 10^{22} Pa s for the lower crust and values from 10^{19} Pa s to 10^{22} Pa s for the lithospheric mantle are chosen, which reflect the range of viscosities derived for continental lithosphere (e.g., Burov and Watts, 2006; England et al., 2013; Gourmelen and Amelung, 2005; Henriquet et al., 2019; Kaufmann and Amelung, 2000; Klemperer, 2006; Nishimura and Thatcher, 2003). For the upper and lower crust, permeabilities between 10^{-10} m^2 and 10^{-18} m^2 and 10^{-16} m^2 and 10^{-19} m^2 are applied, respectively (Ingebritsen and Manning, 2010; Manning and Ingebritsen, 1999; Stober and Bucher, 2015). The lithospheric mantle with a permeability value of 10^{-35} m^2 is impermeable (Tung et al., 2018a). In addition, endmember models are configured, which combine different permeability and viscosity values in the upper and lower crust, respectively. To evaluate the effect of the interseismic stress accumulation on the stress change pattern, the total extension/shortening rate is varied between 2-8 mm/a, corresponding to typical deformation rates in tectonically active regions (e.g., Bennett et al., 2003; D'Agostino et al., 2001, 2008; Zhang et al., 2004). The

coseismic slip is varied between 0.5-3 m by adjusting the length of the preseismic phase. Different friction coefficients between 0.4 and 0.8 are used, which are common values for Coulomb stress calculations (Lin et al., 2011; Nostro et al., 1997; Ryder et al., 2012). The model results for postseismic deformation, pore pressure changes and Coulomb stress changes are shown in irregular time points between the first month up to the 50th year after the earthquake. This time interval covers the time scale in which poroelastic effects and viscoelastic relaxation are typically effective and the long-term alteration by interseismic stress accumulation can be represented.

Table 1.1: Overview of all calculated normal and thrust fault models with the successive varied parameters (red).

Coseismic slip (m)	Total ext./short. rate (mm/a)	Friction coefficient	Viscosity (Pa s)		Permeability (m^2)		Shown in:
			Lower crust	Lithospheric mantle	Upper crust	Lower crust	
Reference models							
2	6	0.6	10^{20}	10^{23}	10^{-12}	10^{-18}	Chapter 2, Chapter 3
2	6	0.6	10^{20}	10^{23}	-	-	Chapter 2, Chapter 3
2	6	0.6	-	-	10^{-12}	10^{-18}	Chapter 2, Chapter 3
Variation of viscosity (Pa s) of the lower crust							
2	6	0.6	10^{18}	10^{23}	10^{-12}	10^{-18}	Chapter 3
2	6	0.6	10^{19}	10^{23}	10^{-12}	10^{-18}	Chapter 2
2	6	0.6	10^{21}	10^{23}	10^{-12}	10^{-18}	not shown as figure
2	6	0.6	10^{22}	10^{23}	10^{-12}	10^{-18}	Chapter 2, Chapter 3
Variation of viscosity (Pa s) of the lower crust – without poroelastic effects							
2	6	0.6	10^{18}	10^{23}	-	-	not shown as figure
2	6	0.6	10^{19}	10^{23}	-	-	not shown as figure
2	6	0.6	10^{21}	10^{23}	-	-	not shown as figure
2	6	0.6	10^{22}	10^{23}	-	-	not shown as figure
Variation of viscosity (Pa s) of the lithospheric mantle							
2	6	0.6	10^{20}	10^{19}	10^{-12}	10^{-18}	not shown as figure
2	6	0.6	10^{20}	10^{20}	10^{-12}	10^{-18}	not shown as figure
2	6	0.6	10^{20}	10^{21}	10^{-12}	10^{-18}	not shown as figure
2	6	0.6	10^{20}	10^{22}	10^{-12}	10^{-18}	not shown as figure
Variation of viscosity (Pa s) of the lithospheric mantle – without poroelastic effects							
2	6	0.6	10^{20}	10^{19}	-	-	not shown as figure
2	6	0.6	10^{20}	10^{20}	-	-	not shown as figure
2	6	0.6	10^{20}	10^{21}	-	-	not shown as figure
2	6	0.6	10^{20}	10^{22}	-	-	not shown as figure
Variation of permeability (m^2) of the upper crust							
2	6	0.6	10^{20}	10^{23}	10^{-10}	10^{-18}	Chapter 3
2	6	0.6	10^{20}	10^{23}	10^{-11}	10^{-18}	Chapter 2
2	6	0.6	10^{20}	10^{23}	10^{-13}	10^{-18}	Chapter 2
2	6	0.6	10^{20}	10^{23}	10^{-14}	10^{-18}	Chapter 3
2	6	0.6	10^{20}	10^{23}	10^{-15}	10^{-18}	Chapter 2
2	6	0.6	10^{20}	10^{23}	10^{-16}	10^{-18}	Chapter 3
2	6	0.6	10^{20}	10^{23}	10^{-17}	10^{-18}	Chapter 2
2	6	0.6	10^{20}	10^{23}	10^{-18}	10^{-18}	not shown as figure
Variation of permeability (m^2) of the upper crust – without viscoelastic relaxation							

2	6	0.6	-	-	10^{-10}	10^{-18}	not shown as figure
2	6	0.6	-	-	10^{-11}	10^{-18}	not shown as figure
2	6	0.6	-	-	10^{-13}	10^{-18}	not shown as figure
2	6	0.6	-	-	10^{-14}	10^{-18}	not shown as figure
2	6	0.6	-	-	10^{-15}	10^{-18}	not shown as figure
2	6	0.6	-	-	10^{-16}	10^{-18}	not shown as figure
2	6	0.6	-	-	10^{-17}	10^{-18}	not shown as figure
2	6	0.6	-	-	10^{-18}	10^{-18}	not shown as figure
Variation of permeability (m^2) of the lower crust							
2	6	0.6	10^{20}	10^{23}	10^{-12}	10^{-16}	not shown as figure
2	6	0.6	10^{20}	10^{23}	10^{-12}	10^{-17}	Chapter 2
2	6	0.6	10^{20}	10^{23}	10^{-12}	10^{-19}	Chapter 2
Variation of permeability (m^2) of the lower crust – without viscoelastic relaxation							
2	6	0.6	-	-	10^{-12}	10^{-16}	not shown as figure
2	6	0.6	-	-	10^{-12}	10^{-17}	not shown as figure
2	6	0.6	-	-	10^{-12}	10^{-19}	not shown as figure
Endmember models with variable permeability and viscosity							
2	6	0.6	10^{19}	10^{23}	10^{-11}	10^{-18}	Chapter 2
2	6	0.6	10^{19}	10^{23}	10^{-17}	10^{-18}	Chapter 2
2	6	0.6	10^{22}	10^{23}	10^{-11}	10^{-18}	Chapter 2
2	6	0.6	10^{22}	10^{23}	10^{-17}	10^{-18}	Chapter 2
2	6	0.6	10^{18}	10^{23}	10^{-11}	10^{-18}	Chapter 3
2	6	0.6	10^{18}	10^{23}	10^{-16}	10^{-18}	Chapter 3
2	6	0.6	10^{22}	10^{23}	10^{-11}	10^{-18}	Chapter 3
2	6	0.6	10^{22}	10^{23}	10^{-16}	10^{-18}	Chapter 3
Variation of coseismic slip (m)							
0.5	6	0.6	10^{20}	10^{23}	10^{-12}	10^{-18}	not shown as figure
1	6	0.6	10^{20}	10^{23}	10^{-12}	10^{-18}	Chapter 4
1.5	6	0.6	10^{20}	10^{23}	10^{-12}	10^{-18}	not shown as figure
2.5	6	0.6	10^{20}	10^{23}	10^{-12}	10^{-18}	not shown as figure
3	6	0.6	10^{20}	10^{23}	10^{-12}	10^{-18}	Chapter 4
Variation of extension rate (mm/a)							
2	2	0.6	10^{20}	10^{23}	10^{-12}	10^{-18}	not shown as figure
2	4	0.6	10^{20}	10^{23}	10^{-12}	10^{-18}	Chapter 4
2	8	0.6	10^{20}	10^{23}	10^{-12}	10^{-18}	Chapter 4
Variation of friction coefficient							
2	6	0.4	10^{20}	10^{23}	10^{-12}	10^{-18}	Chapter 4
2	6	0.5	10^{20}	10^{23}	10^{-12}	10^{-18}	not shown as figure
2	6	0.7	10^{20}	10^{23}	10^{-12}	10^{-18}	not shown as figure
2	6	0.8	10^{20}	10^{23}	10^{-12}	10^{-18}	not shown as figure

2. Relative importance of poroelastic effects and viscoelastic relaxation for postseismic velocity fields after normal and thrust earthquakes: insights from 2D finite-element modelling

Jill Peikert[a], Andrea Hampel[a], Meike Bagge[b]*

[a]Institut für Geologie, Leibniz Universität Hannover, Callinstr. 30, 30167 Hannover, Germany
[b]GFZ German Research Centre for Geosciences, Telegrafenberg, 14473 Potsdam, Germany

Highlights

• 2D finite element modelling of poroelastic effects and viscoelastic relaxation
• Permeability and viscosity control temporal scales and interaction of both processes
• Poroelastic and viscoelastic effects may overlap in the early postseismic phase
• Poroelastic effects dominate the velocity field in the first postseismic months
• Viscoelastic relaxation influences the velocity field over decades

Abstract

Earthquakes on faults in the brittle upper crust evoke sudden changes in pore fluid pressure as well as postseismic viscoelastic flow in the lower crust and lithospheric mantle but the relative importance of these processes during the postseismic phase has not been systematically studied. Here, we use two-dimensional finite-element models to investigate how pore fluid pressure changes and postseismic viscoelastic relaxation interact during the earthquake cycle of an intracontinental dip-slip fault. To isolate the effects from pore fluid flow and viscoelastic relaxation from each other, we performed experiments with and without pore fluid flow and viscoelastic relaxation, respectively. In different experiments, we further varied the permeability of the crust and the viscosity of lower crust or lithospheric mantle. Our model results show poroelastic effects dominate the velocity field in the first months after the earthquake. In models considering poroelastic effects, the surfaces of both hanging wall and footwall of the normal fault subside at different velocities, while they move upwards in the thrust fault model. Depending on the permeability and viscosity values, viscoelastic relaxation dominates the velocity field from about the second postseismic year onward although poroelastic effects may still occur if the permeability of the upper crust is sufficiently low. With

respect to the spatial scales of poroelastic effects and viscoelastic relaxation, our results show that pore fluid pressure changes affect the velocity field mostly within 10-20 km around the fault, whereas the signal from viscoelastic relaxation is recognizable up to several tens of kilometres away from the fault. Our findings reveal that both poroelastic effects and viscoelastic relaxation may overlap earlier and over longer time periods than previously thought, which should be considered when interpreting aftershock distributions, postseismic Coulomb stress changes and surface displacements.

Keywords: Earthquake cycle, poroelastic effects, viscoelastic relaxation, finite-element modelling

2.1 Introduction

A fault ruptured by an earthquake experiences sudden coseismic slip and a stress drop. On the surrounding region, the earthquake has several effects. First, the sudden coseismic slip alters the pore pressure in the fluid-saturated crust (e.g. King and Muir-Wood, 1994; Nur and Booker, 1972; Sibson, 1994). These earthquake-induced poroelastic effects can lead to considerable pore fluid pressure gradients, which are subsequently relaxed in the postseismic phase by fluid flow from over-pressurized to under-pressurized regions given sufficient permeability (e.g., Antonioli et al., 2005; Chiarabba et al., 2009). The magnitude of the pore pressure change and the duration of the postseismic fluid migration depend on the elastic and hydraulic properties of the crust (Biot, 1941; Rice and Cleary, 1976). Poroelastic effects are typically strongest within 1-2 fault lengths around the source fault and act on timescales of days to a few years after the earthquake (Albano et al., 2017; Antonioli et al., 2005; Chiarabba et al., 2009; Tung and Masterlark, 2018). High pore fluid pressure gradients and the resulting postseismic pore fluid migration may trigger aftershocks by reducing the normal stress (Chiarabba et al., 2009; Malagnini et al., 2012; Nur and Booker, 1972). Second, the coseismic fault movement, which usually occurs in the brittle upper crust, causes a sudden stress increase below the brittle-ductile transition (e.g. Ellis and Stöckhert, 2004). This stress that is coseismically imposed on the lower crust and lithospheric mantle is relaxed by viscoelastic flow, a process called postseismic relaxation (Nur and Mavko, 1974). Postseismic viscoelastic relaxation in the lower crust and/or lithospheric mantle typically acts on local to regional spatial scales and on timescales of years to decades depending on the viscosity of the lithospheric layers (Freed and Lin, 1998; Gourmelen and Amelung, 2005; Hampel and Hetzel, 2015; Kenner and Segall, 1999; Masterlark and Wang, 2002; Pollitz, 1997).

Both pore fluid pressure changes and viscoelastic relaxation affect the stress and velocity fields in the crust (Barbot and Fialko, 2010). After major earthquakes, geodetic data provide information on the co- and postseismic surface deformation, which is then often used for calculating Coulomb stress changes induced on other faults in the region of the earthquake (e.g. Serpelloni et al., 2012). Based on the assumption that the spatial and temporal scales of the two processes are sufficiently different, analyses of geodetic data or Coulomb stress changes often neglect either pore fluid pressure changes (Freed and Lin, 2001; Luo and Liu, 2010) or viscoelastic relaxation (e.g. Albano et al., 2017, 2019, 2021; Nespoli et al., 2018). Only few studies considered the contributions of both processes to surface deformation and Coulomb stress changes after a major intracontinental earthquake (e.g. Masterlark and Wang, 2002; Ryder et al., 2007, 2010; Tung and Masterlark, 2018). With respect to the relative importance of poroelastic effects and viscoelastic relaxation, the studies came to different conclusions. While Tung and Masterlark (2018) argue that poroelastic effects were the primary trigger of the Visso earthquake following the 2016 Amatrice earthquake, Ryder et al. (2007, 2010) observed a prevalence of the viscoelastic relaxation signal in the interferometric synthetic aperture radar (InSAR) data from the 1997 Manyi and 2008 Nima-Gaize (Tibet) earthquakes. This suggest that viscoelastic relaxation may be important already during the early postseismic phase, as indicated also by the results from numerical models (Hampel and Hetzel, 2015). However, these earlier models did not include poroelasticity.

In this study, we investigate the relative importance of the poroelastic effects and postseismic viscoelastic relaxation during the earthquake cycle of an intracontinental normal or thrust fault. To achieve this, we use two-dimensional finite element models, which include gravity, pore fluid pressure, viscoelastic lithospheric layers and interseismic strain accumulation. By varying the permeability of the crust and the viscosity of the lithospheric layers in different experiments, we investigate the spatial and temporal evolution of poroelastic effects and viscoelastic relaxation in terms of co- and postseismic pore pressure changes as well as postseismic vertical and horizontal velocities. Our model results show that poroelastic effects and postseismic viscoelastic relaxation may overlap already in the early postseismic phase, with the consequence that the velocity field in the crust shows a combined signal of both processes. Our findings have important implications for the analysis of geodetic records of earthquakes and for the calculation of postseismic Coulomb stress changes.

2.2 Model setup and conducted experiments

2.2.1 Model setup

The two-dimensional finite-element models in this study are generated by the commercial software ABAQUS (version 2018). The models represent a 500-km-wide and 100-km-thick section of the lithosphere, which is divided into a 15-km-thick elastic upper crust, a 15-km-thick viscoelastic lower crust and a 70-km-thick viscoelastic lithospheric mantle (Figure 2.1). The general setup of the reference models with a 60°-dipping normal fault or 30°-dipping thrust fault and the rheological parameters of the layers (Poisson's ratio v, viscosity η, density ρ, Young's modulus E) are shown in Figure 2.1. The model fault is embedded in the model centre in the upper crust as a frictional contact interface between the footwall and the hanging wall (friction coefficient μ). The contact is implemented as surface-to-surface contact (cf. ABAQUS 2018 documentation), i.e. slip on the fault occurs by relative movement between the element surfaces of footwall and hanging wall. Whether slip on the model fault can occur during the model run, is controlled by the boundary conditions for the fault, which can be changed between locked (= no slip allowed) and unlocked (= slip is allowed) (cf. ABAQUS 2018 documentation). When the model fault is unlocked, slip initiation is controlled by the Mohr-Coulomb criterion $|\tau_{max}| = c + \mu\,\sigma_n$, where τ_{max} is the critical shear stress, c is the cohesion (zero in our model), σ_n is the normal stress and μ is the coefficient of friction. The sense of slip, i.e. normal or reverse, is controlled by either extending or shortening of the model domain, respectively, which is achieved by applying a velocity boundary condition to the model sides (Figure 2.1).

Viscoelastic behavior is implemented as linear, temperature-independent Maxwell viscoelasticity. To simulate the coupling between solid and fluid phase, we apply the coupled pore fluid diffusion/stress analysis in ABAQUS, which requires – besides the Young's modulus and Poisson ratio of the solid phase – the permeability, the void ratio and the saturation as input parameters. The permeability K enters ABAQUS as the hydraulic conductivity k_f that can be calculated from $k_f = K * \rho_{fluid} * g / \eta_{fluid}$ (ρ_{fluid}: fluid density, 1000 kg/m^3; acceleration due to gravity, 9.81 m/s^2; η_{fluid}: fluid viscosity, 998 x 10^{-6} kg m^{-1} s^{-1}). The void ratio is defined as the proportion between the volume of voids and solids in the medium and the volume of fluid trapped in the medium. The void ratio typically is a few per cent for crystalline basement rocks (cf. Masterlark and Wang, 2002; Masterlark, 2003). In our models, we use a void ratio of 0.06 and a saturation of 1. The fault is treated as impermeable, i.e. fluid cannot flow across it (cf. Albano et al., 2017, 2019; Dempsey et al., 2013; Rudnicki, 1986). This is supported by observations from natural faults as well as by results from experiments, which show that faults

act as a barrier to fluid flow once an impermeable fault gouge layer has developed (Ingebritsen and Manning, 2010; Parsons et al., 1999; Piombo 2005; Scholz, 1987). Moreover, no pore fluid flow will occur across the model boundaries. The initial pore pressure (P_{pore}) distribution in the models is hydrostatic. Gravity is included as a body force in all models, as well as isostatic effects, which are simulated by applying a lithostatic pressure (P_{litho}) of 3×10^9 Pa and an elastic foundation to the model bottom (marked as arrows and springs in Figure 2.1) (cf. Hampel et al., 2019). The property of the elastic foundation represents an asthenosphere with a density of 3200 kg/m^3. The stiffness of the elastic foundation is calculated from the product of density of the asthenosphere ρ_{asth} and gravitational acceleration g. As initial condition, a lithostatic stress field is defined. All models are meshed by second-order rectangular elements with an average edge length of ~1 km.
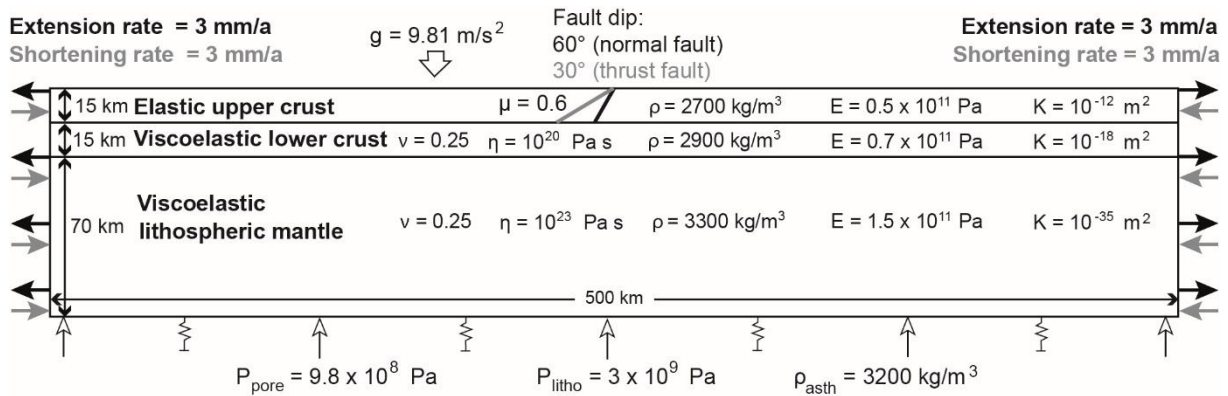

Figure 2.1: Setup of the two-dimensional finite-element reference models (R1nf, R1tf) with a 60°-dipping normal fault or a 30°-dipping thrust fault. The lithosphere is subdivided into an elastic upper crust, viscoelastic lower crust and viscoelastic lithospheric mantle. The fault (friction coefficient μ) is embedded in the upper crust. Material properties are density (ρ), Young's modulus (E), Poisson's ratio (v), viscosity (η) and permeability (K). Viscosity and permeability are varied in different experiments. Gravity is included as a body force. A lithostatic pressure and an elastic foundation, which represent the asthenosphere, are applied to the model bottom to implement isostatic effects (cf. Hampel et al., 2019). The model bottom is free to move in the vertical and horizontal directions; the model sides are free to move in the vertical direction. At the model sides a velocity boundary condition is applied to extend or shorten the model at a total rate of 6 mm/a.

Each model run consists of three model phases (Table 2.1) (cf. Bagge and Hampel, 2016, 2017; Hampel and Hetzel, 2012, 2015; Hampel et al., 2013). Viscoelastic behaviour and pore fluid flow are activated during the first model phase and remain active until the end of each model run. During the first model phase, the frictional contact between the fault hanging wall and footwall, lithostatic and hydrostatic pressure distributions as well as a state of isostatic equilibrium are established in the model. The model fault is unlocked but slip, i.e. relative

movement between footwall and hanging wall, is not yet initiated. The first model phase lasts 300 ka to ensure that pore fluid flow and viscoelastic deformation triggered solely by applying gravity has ceased before the next model phase. During the second model phase, the model is extended or shortened, which initiates slip on the fault. Once slip is initiated, the fault is allowed

Table 2.1: Overview of model phases.

Model phase	Description	Applied model components	State of fault
1	Establishment of contact along fault and of isostatic and hydrostatic equilibrium	Gravity, isostasy, pore fluid flow, viscoelastic material behaviour	Unlocked (but slip not yet initiated)
2	Extension or shortening of model domain until fault reaches constant slip rate	Gravity, isostasy, pore fluid flow, viscoelastic material behaviour, extension/shortening	Unlocked (continuous slip)
3	Preseismic phase Coseismic phase Postseismic phase	Gravity, isostasy, pore fluid flow, viscoelastic material behaviour, extension/shortening	Locked Unlocked Locked

to continuously accumulate slip until it reaches a constant slip rate. Continuous fault slip at a constant slip rate simulates slip accumulation integrated over many earthquake cycles and ensures that the results obtained from the subsequent third model phase do not depend on the number of previous earthquake cycles (cf. Hampel and Hetzel, 2012, 2015; Hampel et al., 2013). The model time needed to achieve a constant slip rate depends primarily on the fault dip and the viscosity structure of the lithosphere (cf. Hampel et al., 2010). In the present study, the second model phase lasts ca. 250 ka in the normal fault model and 950 ka in the thrust fault, respectively. Extension or shortening continues through the third model phase, which comprises the preseismic, coseismic and postseismic phases. During the preseismic phase, during which the fault is locked, slip accumulation stops. The length of the preseismic phase is chosen such that the fault experiences 2 m of coseismic slip during subsequent coseismic phase. Depending on the slip rate of the fault, the length of the preseismic phase varies between ca. 3800 and 4200 a in the different experiments. At the beginning of the coseismic phase (30 s), the fault is switched from locked to unlocked, which causes sudden slip on the fault. The slip distribution is not prescribed but develops freely. The size of the earthquake is controlled by the applied far-field extension or shortening rate, the rheological properties of the model, and the duration of the preseismic phase. In this study, we define the duration of the preseismic phase such that the maximum coseismic slip is 2 m, which would be the typical slip of an $M_w \sim 7$ intraplate earthquake if we assume a fault length of 40 km (Wells and Coppersmith, 1994). During the postseismic phase (50 model years), we lock the fault again while extension or shortening

continues to simulate the interseismic deformation and the related stress increase. Note that potential afterslip is not considered because our intention is to evaluate the effects from pore fluid pressure changes and viscoelastic relaxation.

2.2.2 Conducted experiments

To investigate the relative importance of poroelastic effects and postseismic viscoelastic relaxation during the coseismic and postseismic phases, we conducted the following experiments. First, we computed normal and thrust fault reference models ($R1_{nf}$, $R1_{tf}$), in which we used permeability values and a viscosity structure typical of continental lithosphere (Figure 2.1, Table 2.2) (Chen and Molnar, 1983; Ingebritsen and Manning, 2010; Klemperer, 2006; Manning and Ingebritsen, 1999; Ryder et al., 2014; Shi et al., 2015; Stober and Bucher, 2015).

Table 2.2: Overview of numerical models of this study.

Model name[a]	Permeability of upper crust K_{uc} (m^2)	Permeability of lower crust K_{lc} (m^2)	Viscosity of lower crust η_{lc} (Pa s)	Viscosity of lithospheric mantle η_{lm} (Pa s)	Results shown in figure(s)
Reference models					
$R1_{nf}$, $R1_{tf}$	10^{-12}	10^{-18}	10^{20}	10^{23}	2-5
$R2_{nf}$, $R2_{tf}$	10^{-12}	10^{-18}	-	-	3-5
$R3_{nf}$, $R3_{tf}$	-	-	10^{20}	10^{23}	3-5
Models with variable permeability					
$P1_{nf}$, $P1_{tf}$	10^{-11}	10^{-18}	10^{20}	10^{23}	6a, S1a
$P2_{nf}$, $P2_{tf}$	10^{-13}	10^{-18}	10^{20}	10^{23}	6b, S1b
$P3_{nf}$, $P3_{tf}$	10^{-15}	10^{-18}	10^{20}	10^{23}	7a, S2a
$P4_{nf}$, $P4_{tf}$	10^{-17}	10^{-18}	10^{20}	10^{23}	7b, S2b
$P5_{nf}$, $P5_{tf}$	10^{-12}	10^{-17}	10^{20}	10^{23}	S3a, S4a
$P6_{nf}$, $P6_{tf}$	10^{-12}	10^{-19}	10^{20}	10^{23}	S3b, S4b
Models with variable viscosity					
$V1_{nf}$, $V1_{tf}$	10^{-12}	10^{-18}	10^{19}	10^{23}	8a, S5a
$V2_{nf}$, $V2_{tf}$	10^{-12}	10^{-18}	10^{22}	10^{23}	8b, S5b
$V3_{nf}$, $V3_{tf}$	10^{-12}	10^{-18}	10^{20}	10^{22}	S6
Endmember models with variable permeability and viscosity					
$PV1_{nf}$, $PV1_{tf}$	10^{-11}	10^{-18}	10^{19}	10^{23}	9a, S7a
$PV2_{nf}$, $PV2_{tf}$	10^{-17}	10^{-18}	10^{19}	10^{23}	9b, S7b
$PV3_{nf}$, $PV3_{tf}$	10^{-11}	10^{-18}	10^{22}	10^{23}	10a, S8a
$PV4_{nf}$, $PV4_{tf}$	10^{-17}	10^{-18}	10^{22}	10^{23}	10b, S8b

[a] Subscripts nf and tf refer to normal fault and thrust fault, respectively.

To isolate the effect of pore fluid flow and viscoelastic relaxation, we performed additional runs of the reference models, in which we switched off either viscoelastic behaviour ($R2_{nf}$, $R2_{tf}$) or pore fluid flow ($R3_{nf}$, $R3_{tf}$) during the postseismic phase. Second, we computed models, in

which we varied the permeability of the crust from 10^{-11} to 10^{-17} m^2 for the upper crust and 10^{-17} to 10^{-19} m^2 for the lower crust while keeping the viscosity structure constant (P1-6$_{nf}$, P1-6$_{tf}$, Table 2.2) (Ingebritsen and Manning, 2010; Manning and Ingebritsen, 1999; Stober and Bucher, 2015). For the lithospheric mantle, we apply a permeability of K = 10^{-35} m^2, which represents an impermeable layer (Tung et al., 2018a). Third, we ran experiments, in which we varied the viscosity for the lower crust and lithospheric mantle between 10^{19} and 10^{22} Pa s and between 10^{22} and 10^{23} Pa s, respectively (V1-3$_{nf}$, V1-3$_{tf}$, Table 2.2). These values represent the range of viscosities derived for continental lithosphere (Burov and Watts, 2006; England et al., 2013; Gourmelen and Amelung, 2005; Henriquet et al., 2019; Kaufmann and Amelung, 2000; Klemperer, 2006; Nishimura and Thatcher, 2003). Fourth, we calculated selected end-member model configurations, in which we varied both permeability and viscosity values (PV1-4$_{nf}$, PV1-4$_{tf}$, Table 2.2).

2.3 Results

In the following, we first show the results from the normal and thrust fault reference models for the coseismic (Section 3.1) and postseismic phase (Section 3.2.1). In Sections 3.2.2 to 3.2.4, we present the postseismic velocity fields and pore pressure distributions from the models, in which we varied the permeability of the crust and/or the viscosity of the lower crust or lithospheric mantle (Table 2.2).

2.3.1 Coseismic phase

Figure 2.2 illustrates the coseismic vertical and horizontal displacement fields as well as the coseismic pore pressure changes, as obtained from the normal and thrust fault reference models (R1$_{nf}$, R1$_{tf}$). The sudden slip on the model fault causes footwall uplift and hanging wall subsidence in the normal fault model and hanging wall uplift and footwall subsidence in the thrust fault model (Figure 2.2a, b). In the normal fault model, horizontal surface displacements are directed away from the fault (Figure 2.2c, d), indicating extension across the fault. Within the fault footwall, shortening prevails, while alternating zones of extension and shortening occur within the hanging wall (Figure 2.2e) (cf. Hampel and Hetzel, 2015; see Section 4.1 for
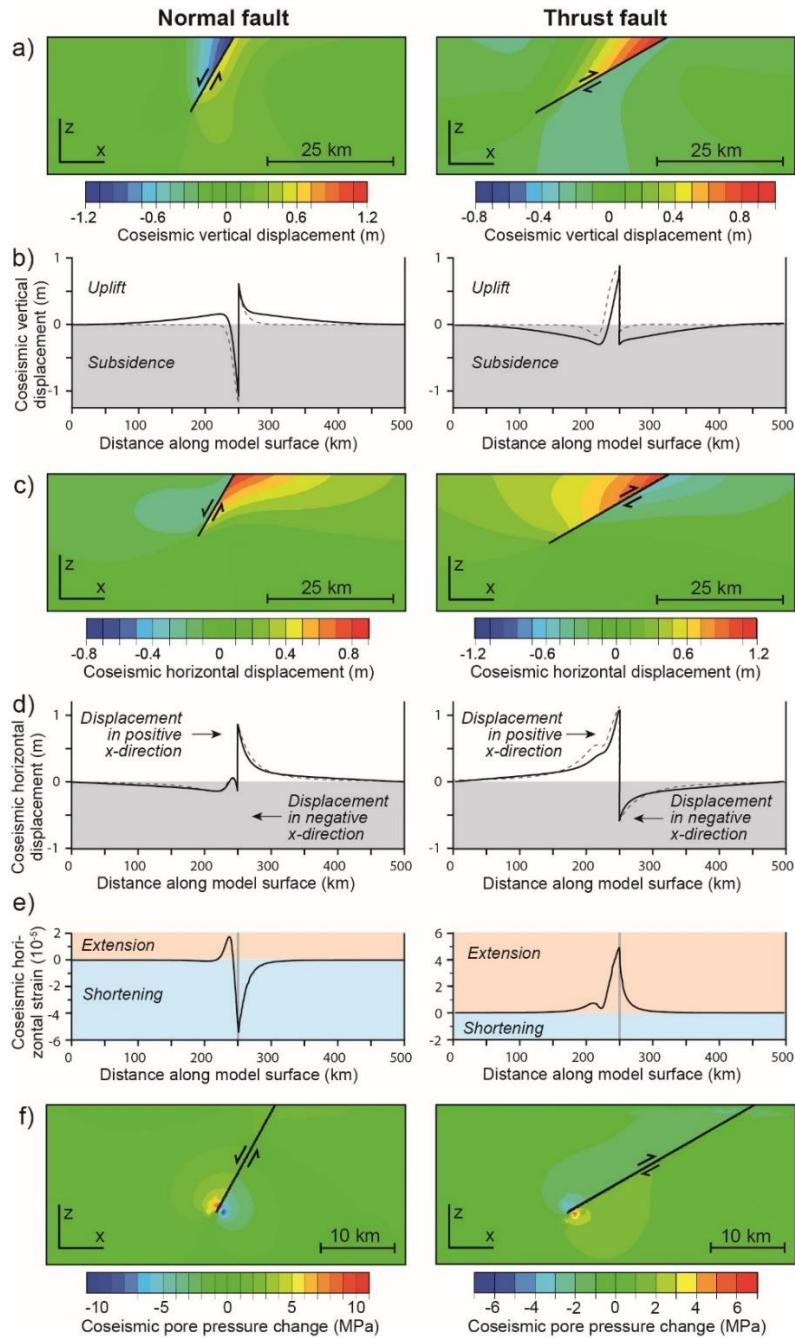
Figure 2.2: Model results for the coseismic phase in the normal fault reference model (left column) and thrust fault reference model (right column). a) Vertical displacement field around the fault. b) Vertical displacement for a profile along the model surface. c) Horizontal displacement field around the fault. b) Horizontal displacement for a profile along the model surface. e) Horizontal strain for a profile along the model surface. f) Pore pressure changes with respect to hydrostatic values. Model sections around the fault in figure parts a, c and f are shown without vertical exaggeration. Dashed lines in figure parts b and d represent curves based on the analytical solution (Okada, 1985; Beauducel, 2022).

across the fault, while footwall and hanging wall experience extension (Figure 2.2d, e). For comparison, vertical and horizontal displacements obtained from analytical solutions for an elastic half-space (Okada, 1985) are shown as dashed lines in Figures 2.2b and 2.2d (cf.

Beauducel, 2022) (see Section 2.4.1 for discussion). Coseismic pore pressure changes occur mainly in the lower part of the fault and reach highest positive or negative values around the fault tip with a radius of 1-2 km (Figure 2.2f). In the normal fault reference model, the coseismic slip leads to an over-pressurization of the hanging wall (~11 MPa) and an under-pressurization of the footwall by ~10 MPa with respect to the hydrostatic pressure. In contrast, the pore pressure decreases by ~5 MPa in the thrust fault hanging wall and increases by ~6 MPa in the footwall relative to the hydrostatic values. The zone of negative pore pressure changes in the thrust fault hanging wall expands from the fault tip to the surface of the model.

2.3.2 Postseismic phase

2.3.2.1 Reference models

In this section, we analyse the postseismic vertical and horizontal velocity fields derived from the reference models ($R1_{nf}$, $R1_{tf}$) together with the results from the model runs without viscoelastic behaviour ($R2_{nf}$, $R2_{tf}$) or without pore fluid flow ($R3_{nf}$, $R3_{tf}$), respectively (Figures 2.3, 2.4). Afterwards, we present the postseismic pore pressure evolution at different time intervals in the normal and thrust fault reference models with and without viscoelastic relaxation (Figure 2.5). To account for the generally non-linear evolution of the postseismic deformation, the model results are shown at irregular time intervals, i.e. for model stages between which the largest changes occur. In general, these are the first months and years after the earthquake.

Figure 2.3 shows the evolution of the vertical and horizontal velocity fields derived from the normal fault reference models ($R1_{nf}$, $R2_{nf}$, $R3_{nf}$). In the reference model $R1_{nf}$ (Figure 2.3a), high vertical and horizontal velocities with absolute values ranging from ca. -1400 to 700 mm/a occur in the upper crust in the first month after the earthquake. Notably, the model surface subsides on both sides of the fault. Horizontal movements of the hanging wall and footwall are directed toward the fault. In the second month after the earthquake, the principal patterns of the velocity fields are similar to the first month, but the vertical and horizontal velocities decrease to -70 and 10 mm/a and -45 and 30 mm/a, respectively. From the third month onwards, the velocities further decrease. The hanging wall shows subsidence at a rate of -4 mm/a near the surface while the footwall is uplifted at the fault tip by the same rate. The horizontal movements of the hanging wall and footwall change direction, with the highest velocities occurring in the hanging wall near the fault. The velocity patterns integrated over the first year largely reflect
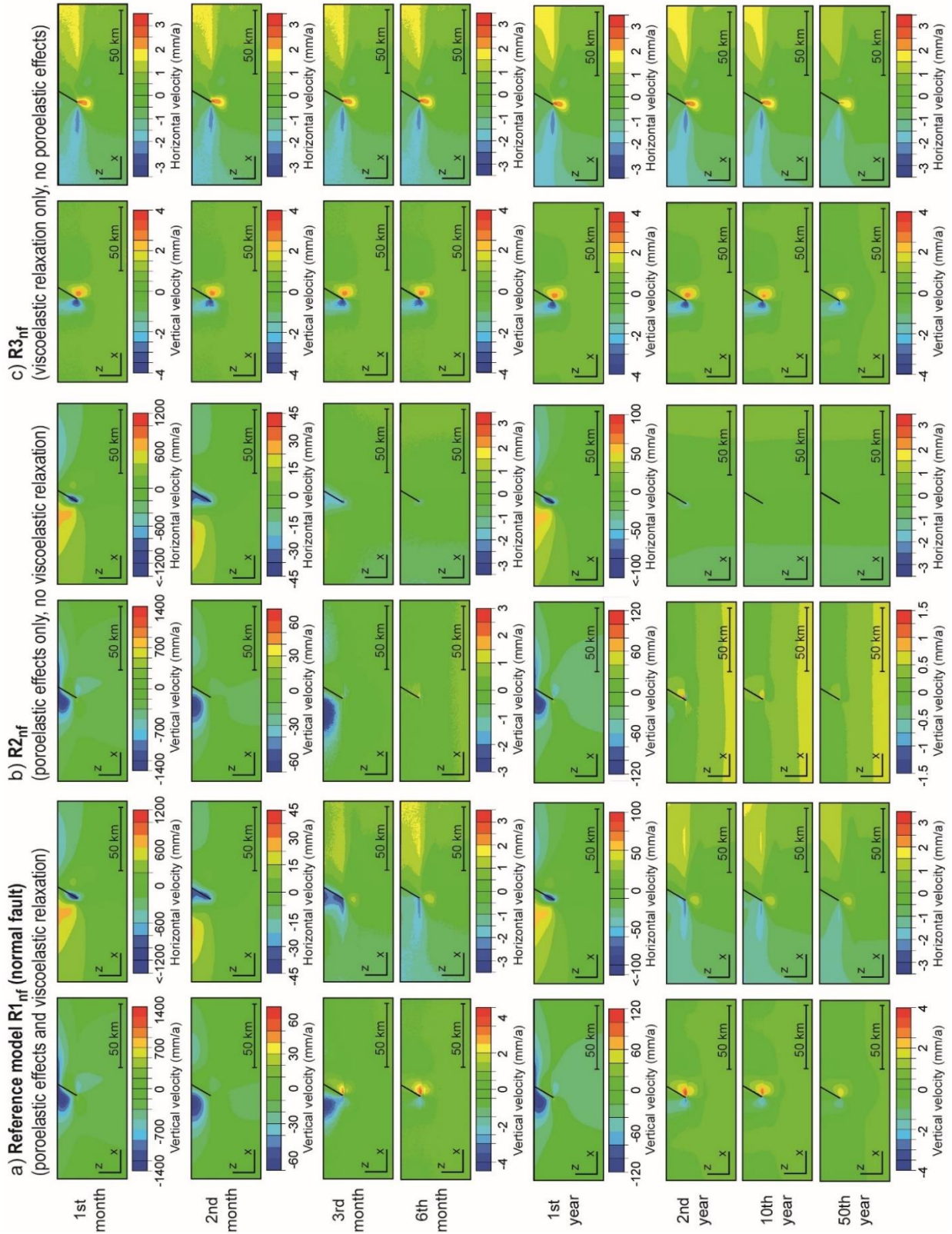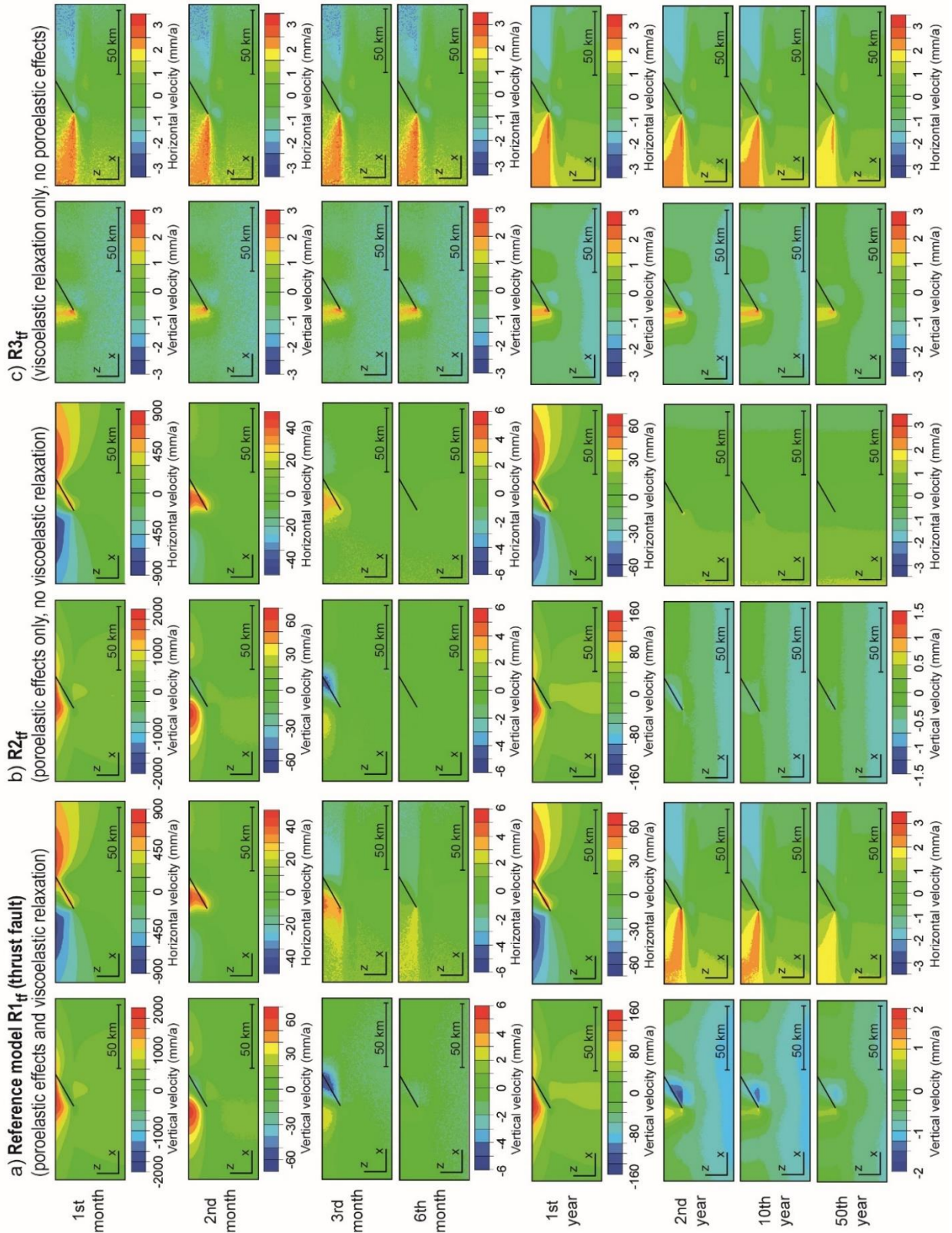
Figure 2.3: Postseismic velocity fields from the normal fault reference model (a) R1$_{nf}$ (with both poroelastic and viscoelastic effects), (b) R2$_{nf}$ (poroelastic effects, no viscoelastic relaxation) and (c) R3$_{nf}$ (viscoelastic relaxation, no poroelastic effects). Shown is a section in the model centre around the fault (no vertical exaggeration). Note that the velocity fields at all time points are averaged over the respective time interval, i.e. the velocity field for the first postseismic year is integrated over the time period between the beginning and the end of the first year after the earthquake.

Figure 2.4: Postseismic velocity fields from the thrust fault reference model (a) R1$_{tf}$ (with both poroelastic and viscoelastic effects), (b) R2$_{tf}$ (poroelastic effects, no viscoelastic relaxation) and (c) R3$_{tf}$ (viscoelastic relaxation, no poroelastic effects). Shown is a section in the model centre around the fault. No vertical exaggeration. Note that the velocity fields at all time points are averaged over the respective time interval, i.e. the velocity field for the first postseismic year is integrated over the time period between the beginning and the end of the first year after the earthquake.

the patterns observed in the early stage of the year (see Section 4.1 for discussion). In the following years, higher vertical velocities only occur within a few kilometres around the fault and slightly decrease over the next 50 years. The horizontal velocities also decrease over time but remain elevated up to distances of ~60 km compared to the undisturbed velocity field. The model without viscoelastic behaviour (R2$_{nf}$, Figure 2.3b) shows the same velocity patterns in the early postseismic phase as the reference model R1$_{nf}$, but from the third month onwards, perturbations of both vertical and horizontal velocities become weaker. The vertical velocity field shows hanging wall subsidence (-3 mm/a) in the third month after the earthquake, which largely disappears in the following month, and slight footwall uplift near the fault tip (0.7 mm/a) in the following 50 years appears. From the sixth month onwards, the horizontal velocity field is dominated by the regional extension. In contrast to models R1$_{nf}$ and R2$_{nf}$, the model without pore fluid flow (R3$_{nf}$; Figure 2.3c) shows footwall uplift and hanging wall subsidence at maximum rates of 3 and -4 mm/a, respectively, near the fault tip from the first month onwards. The horizontal velocity field shows extension across the fault and velocity perturbations at distances of up to 60 km with highest velocities of 3 mm/a near the fault tip. Over the entire period, the vertical and horizontal velocity patterns remain similar, with a gradual decrease in the velocities over the next 50 years.

The thrust fault reference model R1$_{tf}$ (Figure 2.4a) shows high vertical and horizontal velocities ranging from -400 to 2000 mm/a and from -900 to 900 mm/a, respectively, in the first month after the earthquake. On both sides of the fault, the model surface is uplifted. The horizontal movements of the hanging wall and footwall are directed away from the fault. Over the next months, the velocity patterns change, with the footwall starting to subside and the horizontal movements changing to shortening across the fault. Similar to the normal fault reference model R1$_{nf}$, the velocity patterns of the first year are dominated by the high velocities of the early postseismic phase. From the second year onwards, the hanging wall is uplifted and the footwall subsides at rates of up to 1 and -2 mm/a, respectively. The largest horizontal velocity perturbations occur around the fault tip and in a >50 km wide zone in the footwall and hanging wall. The velocities slightly decrease over the period of 50 years after the earthquake.

The thrust fault model without viscoelastic behaviour (R2$_{tf}$, Figure 2.4b) shows the same velocity patterns in the early postseismic stage as model R1$_{tf}$. In the third month, the velocity fields are still disturbed near the fault, but these perturbations dissipate over the next few years. After the second year, the velocity field induced by the regional shortening dominates. In the model without pore fluid flow (R3$_{tf}$; Figure 2.4c), the vertical and horizontal velocity fields are
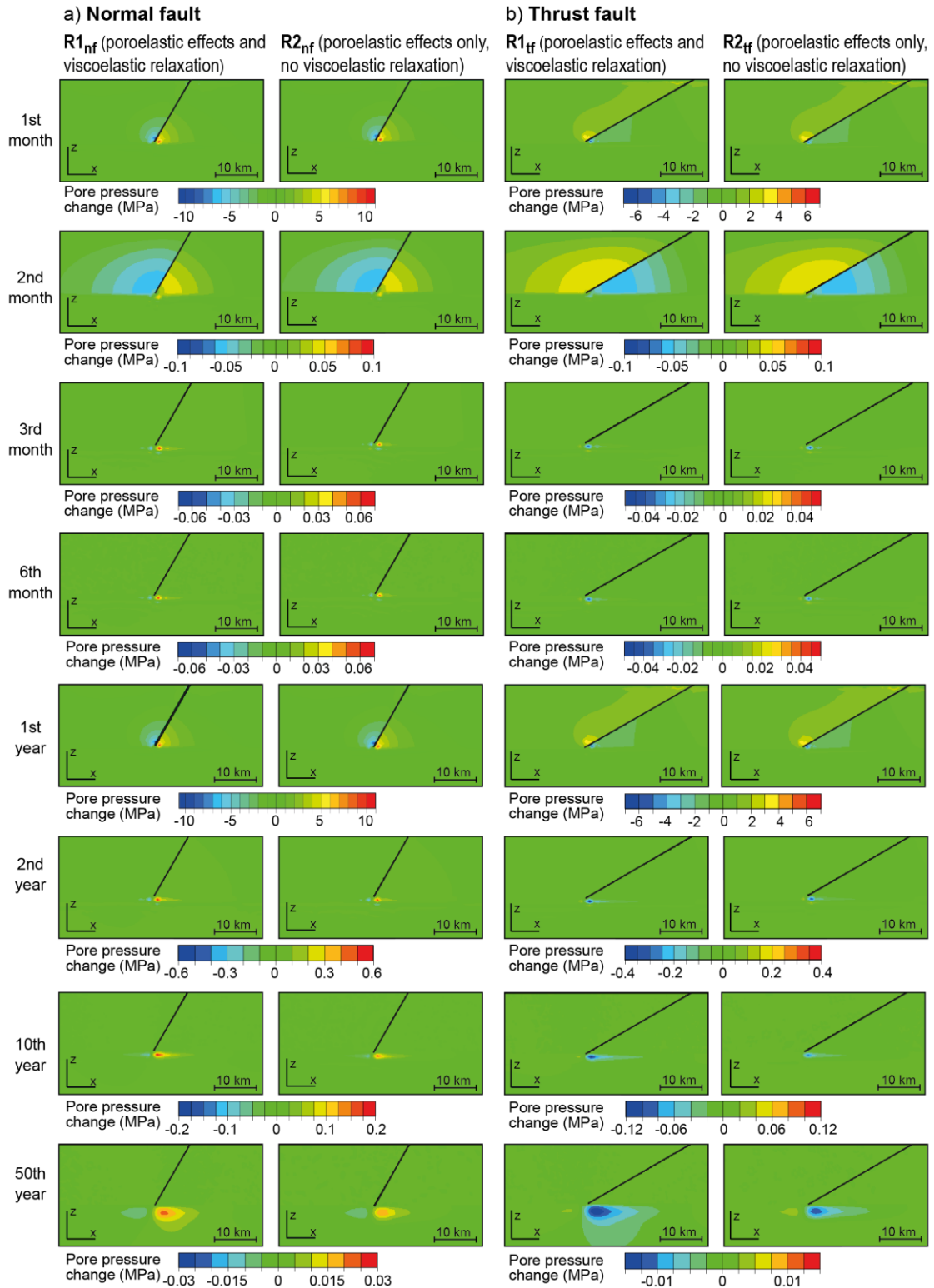
33

Figure 2.5: Postseismic pore pressure changes with respect to hydrostatic values for (a) the normal fault reference model R1$_{nf}$ and (b) the thrust fault reference model R1$_{tf}$ and for the reference models without viscoelastic relaxation (R2$_{nf}$, R2$_{tf}$). Shown is a section in the model centre around the fault (no vertical exaggeration). Note that the pore pressure changes at all time points are averaged over the respective time interval, i.e. the pore pressure change for the first postseismic year is integrated over the time period between the beginning and the end of the first year after the earthquake. Reference models R3$_{nf}$ and R3$_{tf}$ are not shown here as they do not consider pore pressure effects.

disturbed up to several kilometres away from the fault, with highest velocities occurring near the fault tip (3 mm/a) from the first month onwards. In contrast to models $R1_{tf}$ and $R2_{tf}$, which show uplift on both sides of the fault, model $R3_{tf}$ shows hanging wall uplift and footwall subsidence. The velocity patterns of model $R3_{tf}$ remain similar over the 50 years after the earthquake, with only negligible velocity changes.

The postseismic evolution of the pore pressure in the normal and thrust fault reference models with and without viscoelastic relaxation ($R1_{nf}$, $R2_{nf}$, $R1_{tf}$, $R2_{tf}$) is illustrated in Figure 2.5. A comparison with the coseismic phase (Figure 2.2) shows that the pore pressure changes are inverted relative to the coseismic distribution, i.e. zones with previously positive values now exhibit negative values and *vice versa*. In the first month, the magnitudes of the pore pressure changes are almost equivalent to the ones in the coseismic phase (i.e. +/-11 MPa in the normal fault model $R1_{nf}$ and +/-6 MPa in the thrust fault model $R1_{tf}$), which implies that the coseismically induced pore pressure changes have largely dissipated. In other words, the hydrostatic pore pressure distribution is almost recovered in both models already in the early postseismic phase. In the second month, the pore pressure changes decrease rapidly by two orders of magnitude and expand within the upper crust towards the surface because of the fluid diffusion. The pore pressure changes during the first year after the earthquake reflects the pore pressure pattern of the first month. Over the next 50 years, the values decrease by up to three orders of magnitude. Notable, while the pore pressure changes are concentrated around the fault during the first two years after the earthquake, zones of small positive and negative pore pressure changes develop in the lower crust beneath the fault during the late postseismic phase. Compared to the reference models $R1_{nf}$ and $R1_{tf}$ (left column of Figure 2.5a and 2.5b), the models without viscoelastic relaxation ($R2_{nf}$, $R2_{tf}$) (right column of Figure 2.5a and 2.5b) show a similar pore pressure evolution. Differences between the models occur mainly in the late postseismic phase, where the models without viscoelastic relaxation ($R2_{nf}$, $R2_{tf}$) show smaller zones with negative and positive pore pressure changes in the lower crust than the reference models $R1_{nf}$ and $R1_{tf}$.

2.3.2.2 Models with variable permeability

In this section, we show the results for selected normal and thrust fault models, in which we varied the permeability of the upper or lower crust while keeping the viscosity structure constant (Table 2.2; Figures 2.6-2.7 and S1-S4). Compared to the reference models $R1_{nf}$ and $R1_{tf}$ the models with upper-crustal permeabilities of 10^{-11} m^2 ($P1_{nf}$, $P1_{tf}$) and 10^{-13} m^2 ($P2_{nf}$, $P2_{tf}$) show
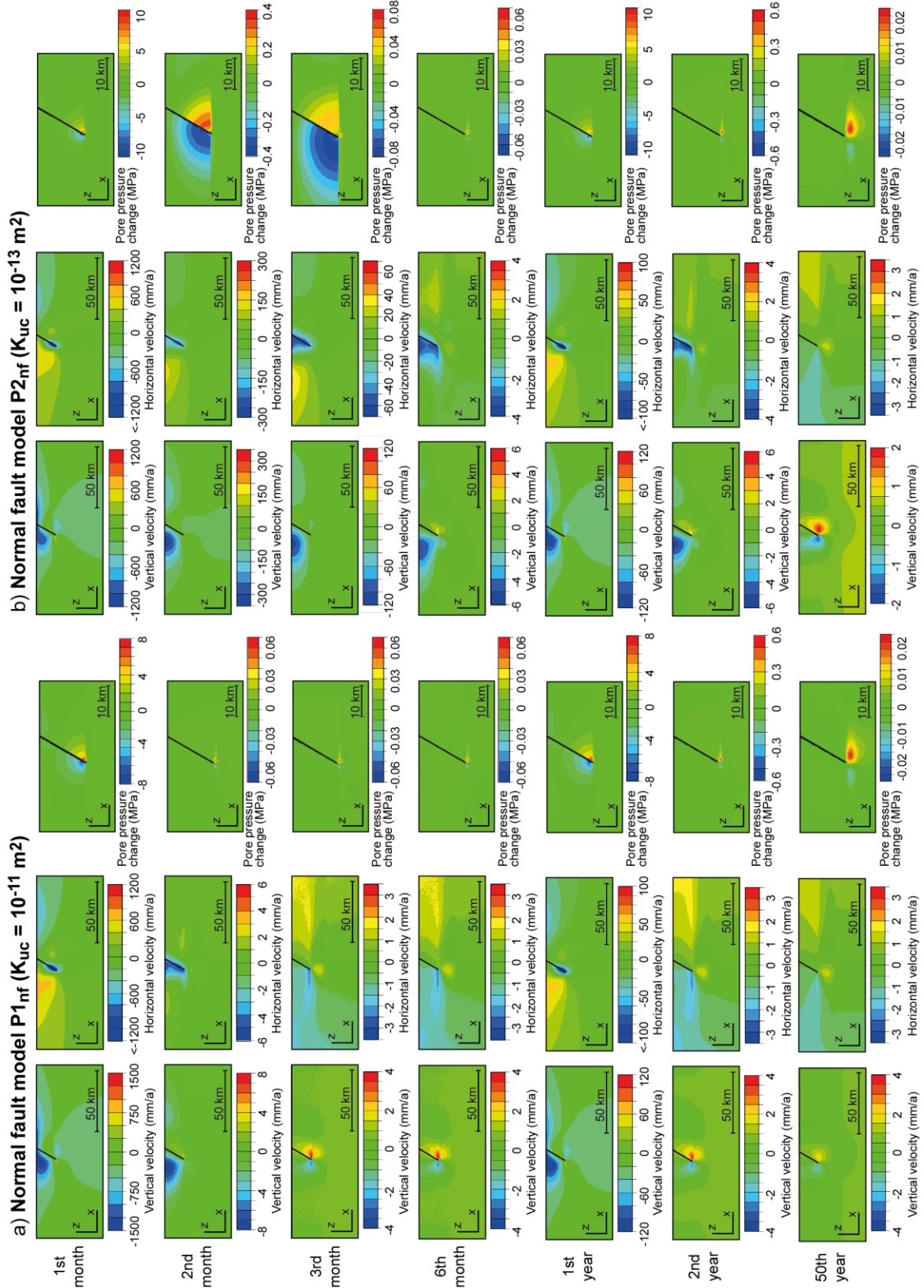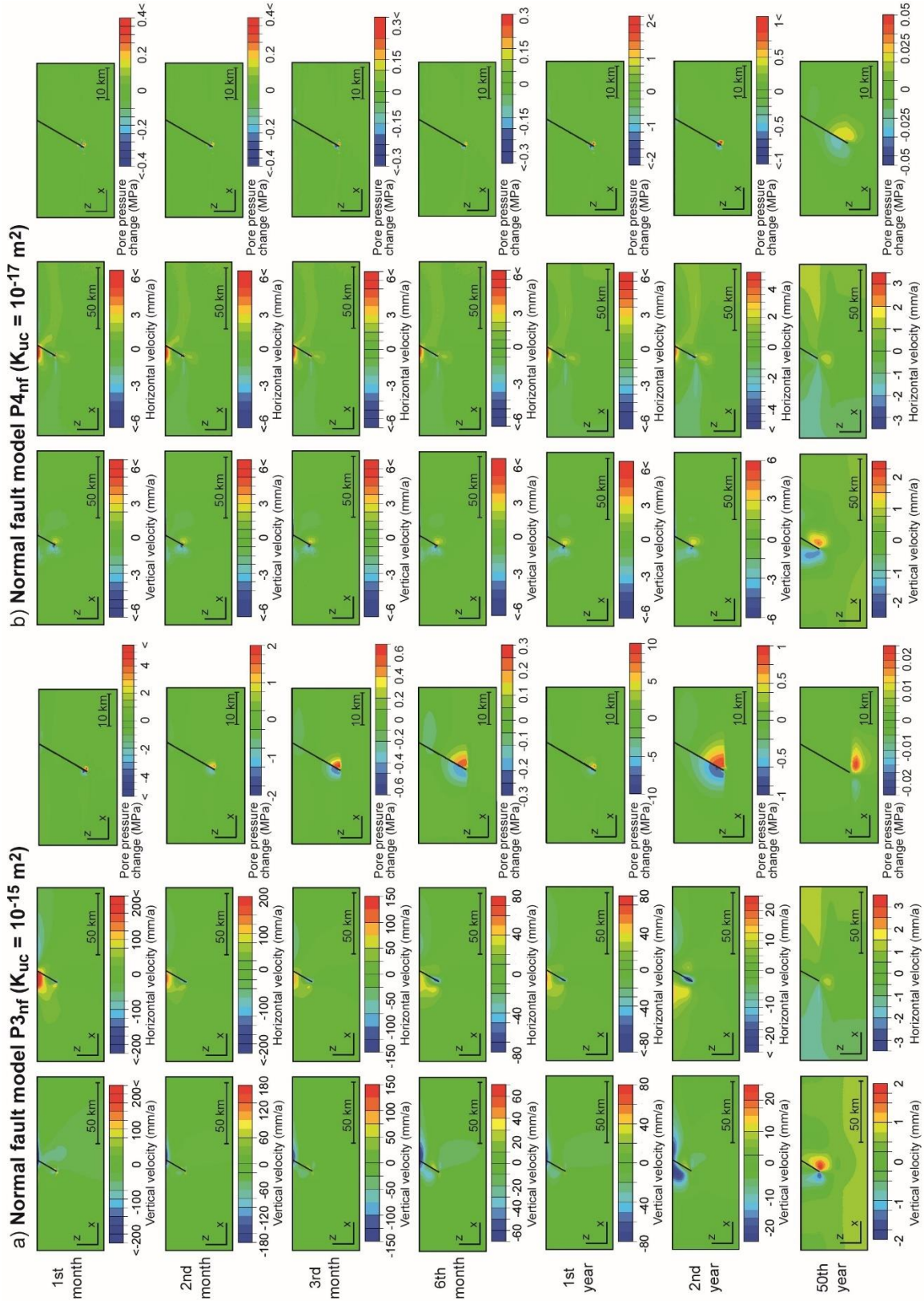
Figure 2.6: Postseismic velocity fields and pore pressure changes from normal fault models (a) P1$_{nf}$ with an upper-crustal permeability of K$_{uc}$ = 10^{-11} m^2 and (b) P2$_{nf}$ with an upper-crustal permeability of K$_{uc}$ = 10^{-13} m^2. No vertical exaggeration. Note that the velocity fields and pore pressure changes at all time points are averaged over the respective time interval, i.e. the velocity field and pore pressure change for the first postseismic year is integrated over the time period between the beginning and the end of the first year after the earthquake.

Figure 2.7: Postseismic velocity fields and pore pressure changes from normal fault models (a) P3$_{nf}$ with an upper-crustal permeability of K$_{uc}$ = 10^{-15} m^2 and (b) P4$_{nf}$ with an upper-crustal permeability of K$_{uc}$ = 10^{-17} m^2. No vertical exaggeration. Note that the velocity fields and pore pressure changes at all time points are averaged over the respective time interval, i.e. the velocity field and pore pressure change for the first postseismic year is integrated over the time period between the beginning and the end of the first year after the earthquake.

a similar evolution of the velocity fields over the time interval of 50 years, with some minor differences in the early postseismic stage. These differences include slightly higher velocities during the first month in models $P1_{nf}$ and $P1_{tf}$ followed by a stronger decrease than in the reference models $R1_{nf}$ and $R1_{tf}$ (Figures 2.6a, S1a), whereas models $P2_{nf}$ and $P2_{tf}$ show slightly lower initial postseismic velocities than the reference models ($R1_{nf}$, $R1_{tf}$) but velocities remain higher until the sixth month (Figures 2.6b, S1b). Hydrostatic conditions in the pore fluid pressure changes are largely reached during the first month in the models $P1_{nf}$ and $P1_{tf}$ and during the second month in models $P2_{nf}$ and $P2_{tf}$.

For a permeability of $10^{-15}\,m^2$ ($P3_{nf}$, $P3_{tf}$), the postseismic velocities are overall lower than in the reference models ($R1_{nf}$, $R1_{tf}$) and show a different evolution (Figures 2.7a, S2a). In the first month and until the fifth year, the velocity fields are only perturbed around the fault tip and at the model surface on both sides of the fault, which show subsidence in the normal fault model ($P3_{nf}$) and uplift in the thrust fault model ($P3_{tf}$). The horizontal movements are directed toward the normal fault and away from the thrust fault, which persist until the second year after the earthquake. After the fifth year, the horizontal velocity field switches back to movements directed away from the normal fault and toward the thrust fault, respectively. With respect to the pore pressure changes, models $P3_{nf}$ and $P3_{tf}$ show a prolonged relaxation, i.e. in the first month, the pore pressure changes by only +/-8 MPa in the normal fault model and by up to -5 MPa in the thrust fault model. The pore pressure expands within the upper crust towards the surface in the fifth year in both models ($P3_{nf}$, $P3_{tf}$). The migration of the pore pressure changes along the boundary between upper and lower crust and into the lower crust is recognizable in the tenth year in both models.

In the models with an upper-crustal permeability of $10^{-17}\,m^2$ ($P4_{nf}$, $P4_{tf}$), the magnitudes of the vertical and horizontal velocities are one order lower during the first year after the earthquake than in the reference models $R1_{nf}$ and $R1_{tf}$ but the velocity decrease after this first year occurs more gradually (Figures 2.7b, S2b). Regarding the horizontal movements and the resulting shortening or extension, the velocity field evolution resembles those of models $P3_{nf}$ and $P3_{tf}$. The pore pressure changes decrease by up to +/-4 MPa and +/-3 MPa in the normal and thrust fault model, respectively. As a result, the coseismically induced pore pressure changes are not completely dissipated in the first year after the earthquake. Until the 50th year after the earthquake, the pore pressure changes decrease further and slowly expand around the fault tip.

Changes in the permeability of the lower crust have only minor influence on the postseismic velocity fields (Supplementary Figures S3, S4). Compared to the reference models ($R1_{nf}$, $R1_{tf}$),

a higher permeability of 10^{-17} m^2 (P5$_{nf}$, P5$_{tf}$) leads to a slower change of the velocity patterns after the second month (Figures S3a, S4a). Up to the fifth year, velocities remain high in an area around the fault tip. Horizontal movements directed toward the normal fault (P5$_{nf}$) and away from the thrust fault (P5$_{tf}$) prevail already from the third month onwards. After the fifth year, the evolution of the velocity fields largely resembles the one of the reference models R1$_{nf}$ and R1$_{tf}$. Pore pressure changes in the models P5$_{nf}$ and P5$_{tf}$ are similar to the reference models (R1$_{nf}$, R1$_{tf}$) during the first month while they are higher around the fault tip until the second year. In the following years, the pore pressure changes migrate into the lower crust. Using a permeability of 10^{-19} m^2 for the lower crust (P6$_{nf}$, P6$_{tf}$) does not change the evolution of the velocity field over the entire model time of 50 years relative to the reference models R1$_{nf}$ and R1$_{tf}$ (Figures S3b, S4b). The pattern of the pore pressure changes develops largely similar to the reference models, however, the gradual decrease after the first month and from the first year onward as well as the magnitude and the extent of the pore pressure changes into the lower crust differ from the reference models (R1$_{nf}$, R1$_{tf}$).

2.3.2.3 Models with variable viscosity

In the next model series, we varied the viscosity of the lower crust or lithospheric mantle while keeping the permeability structure constant (Table 2.2; Figures 2.8 and S5-S6). Generally, a change in viscosity affects the magnitudes but not the patterns of the postseismic velocities during the first year. The pore pressure changes are largely similar to the reference models R1$_{nf}$ and R1$_{tf}$ during the first postseismic year, with their magnitude being somewhat higher.

For a lower-crustal viscosity of 10^{19} Pa s (V1$_{nf}$, V1$_{tf}$), the maximum vertical and horizontal velocities during the third and sixth month are up to one magnitude higher than in the reference model R1$_{nf}$ and R1$_{tf}$ (Figures 2.8a, S5a). In both models (V1$_{nf}$, V1$_{tf}$), the horizontal velocity field is highly disturbed around the fault tip but also more than 100 km away from the fault in both upper crust and upper part of the lower crust. In the 20th year, both models still show maximum velocities of 7-9 mm/a. Thus, a lower viscosity in the lower crust leads to higher velocities than in the reference models R1$_{nf}$ and R1$_{tf}$ until the 20th year. After 20 years, a new zone of subsidence (normal fault model V1$_{nf}$) and uplift (thrust fault model V1$_{tf}$) develops 50 km away from the fault. Below this zone, horizontal movements are directed toward the normal fault and away from the thrust fault, which is in contrast to the prevailing horizontal velocity fields induced by the regional deformation. With respect to the pore pressure, changes by

Figure 2.8: Postseismic velocity fields and pore pressure changes from normal fault models (a) V1$_{nf}$ with a lower-crustal viscosity of $\eta_{lc} = 10^{19}$ Pa s and (b) V2$_{nf}$ with a lower-crustal viscosity of $\eta_{lc} = 10^{22}$ Pa s. No vertical exaggeration. Note that the velocity fields and pore pressure changes at all time points are averaged over the respective time interval, i.e. the velocity field and pore pressure change for the first postseismic year is integrated over the time period between the beginning and the end of the first year after the earthquake.

+/-12 MPa in the normal fault model (V1$_{nf}$) and +/-6 MPa in the thrust fault model (V1$_{tf}$) can be observed in the first month, which decrease by up to two orders of magnitude in the following month and expand into the upper crust towards the surface. Hydrostatic conditions are largely reached after the second month. Until the end of the model runs, the pore pressure changes migrate into the lower crust and the magnitude decreases.

In the models with a viscosity of 10^{22} Pa s in the lower crust (V2$_{nf}$, V2$_{tf}$), high velocity perturbations similar to the reference model R1$_{nf}$ and R1$_{tf}$ occur until the second month after the earth-quake (Figures 2.8b, S5b). In the third month, the largest velocity perturbations can be found in the hanging wall of both normal and thrust fault (V2$_{nf}$, V2$_{tf}$), similar to the third month of the reference model without viscoelastic relaxation (R2$_{nf}$, R2$_{tf}$). From the sixth month onwards and in the following years, the velocities decrease and the velocity fields slowly transition to the patterns induced by the regional deformation with weak perturbations occurring around the fault tip and at the transition between upper and lower crust up to 150 km away from the fault. The pore pressure changes in the first month reach +/-15 MPa (normal fault model V2$_{nf}$) and +/-12 MPa (thrust fault model V2$_{tf}$). Until the 50th model year, the pore pressure distribution in both models evolves – with a slight temporal delay and a higher magnitude – similarly to the reference model R1$_{nf}$ and R1$_{tf}$.

In contrast to variations in the lower-crustal viscosity, varying the viscosity of the lithospheric mantle in our models (V3$_{nf}$, V3$_{tf}$: 10^{22} Pa s) does not have a large effect on the velocities and pore pressure distribution around the fault (Figures S6). Both temporal evolution and spatial patterns of the velocity field and the pore pressure changes are similar to the reference model (R1$_{nf}$, R1$_{tf}$).

2.3.2.4 Endmember models with variable viscosity and permeability

Based on the model results described in sections 3.2.1-3.2.3, this section presents four endmember models, in which we combined a high/low permeability of the upper crust with a low/high viscosity of the lower crust to maximize or minimize the effects from the interaction between pore pressure changes and viscoelastic relaxation (Table 2.2, Figures 2.9-2.10 and S7-S8).

In models PV1$_{nf}$ and PV1$_{tf}$ we combine a high permeability of 10^{-11} m^2 in the upper crust with a low viscosity of 10^{19} Pa s in the lower crust (Figures 2.9a, S7a). In the first month after the earthquake, the results show the same velocity distributions as in the reference model R1$_{nf}$ and R1$_{tf}$, models P1$_{nf}$ and P1$_{tf}$ with the same permeability and models V1$_{nf}$ and V1$_{tf}$ with the same
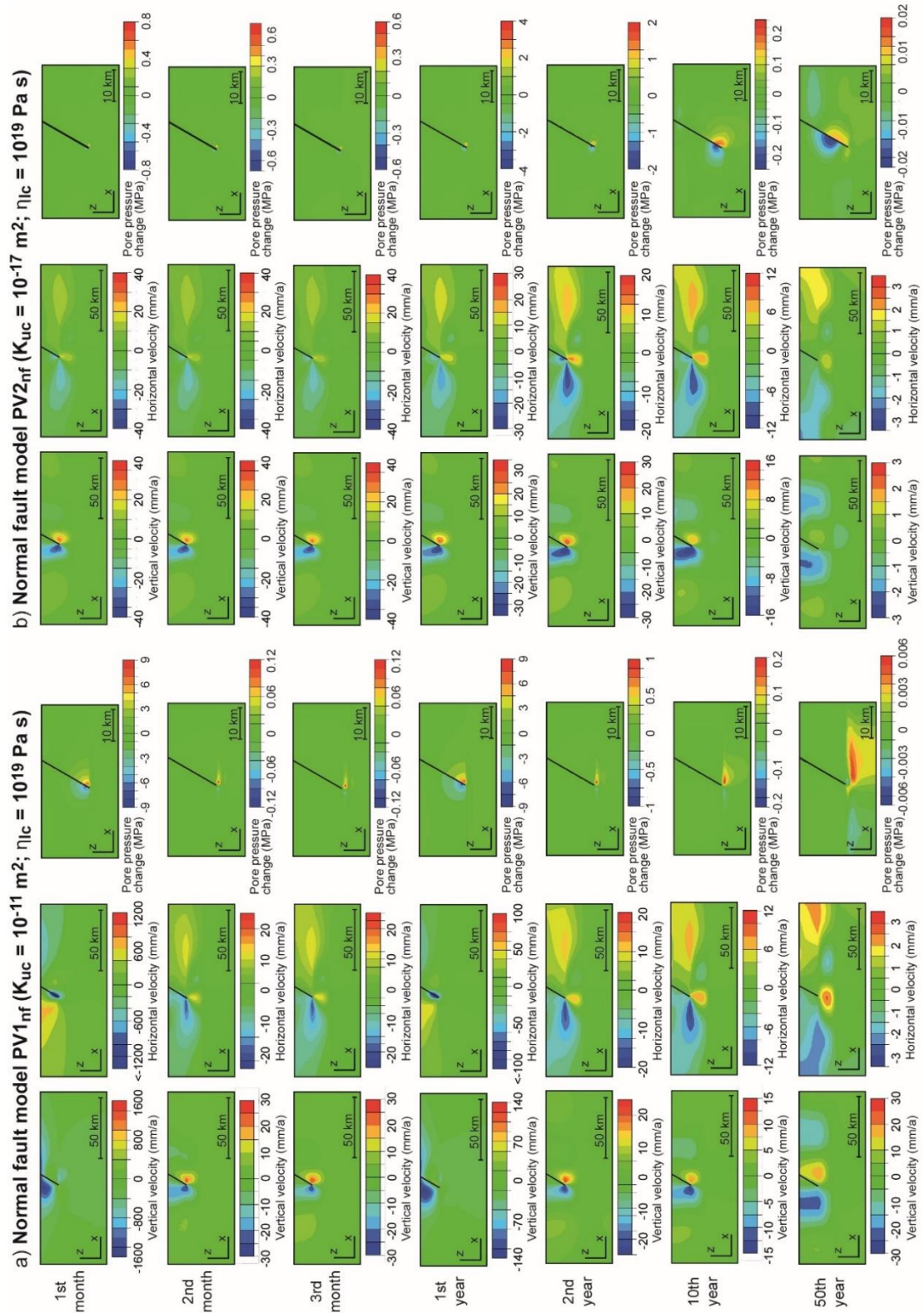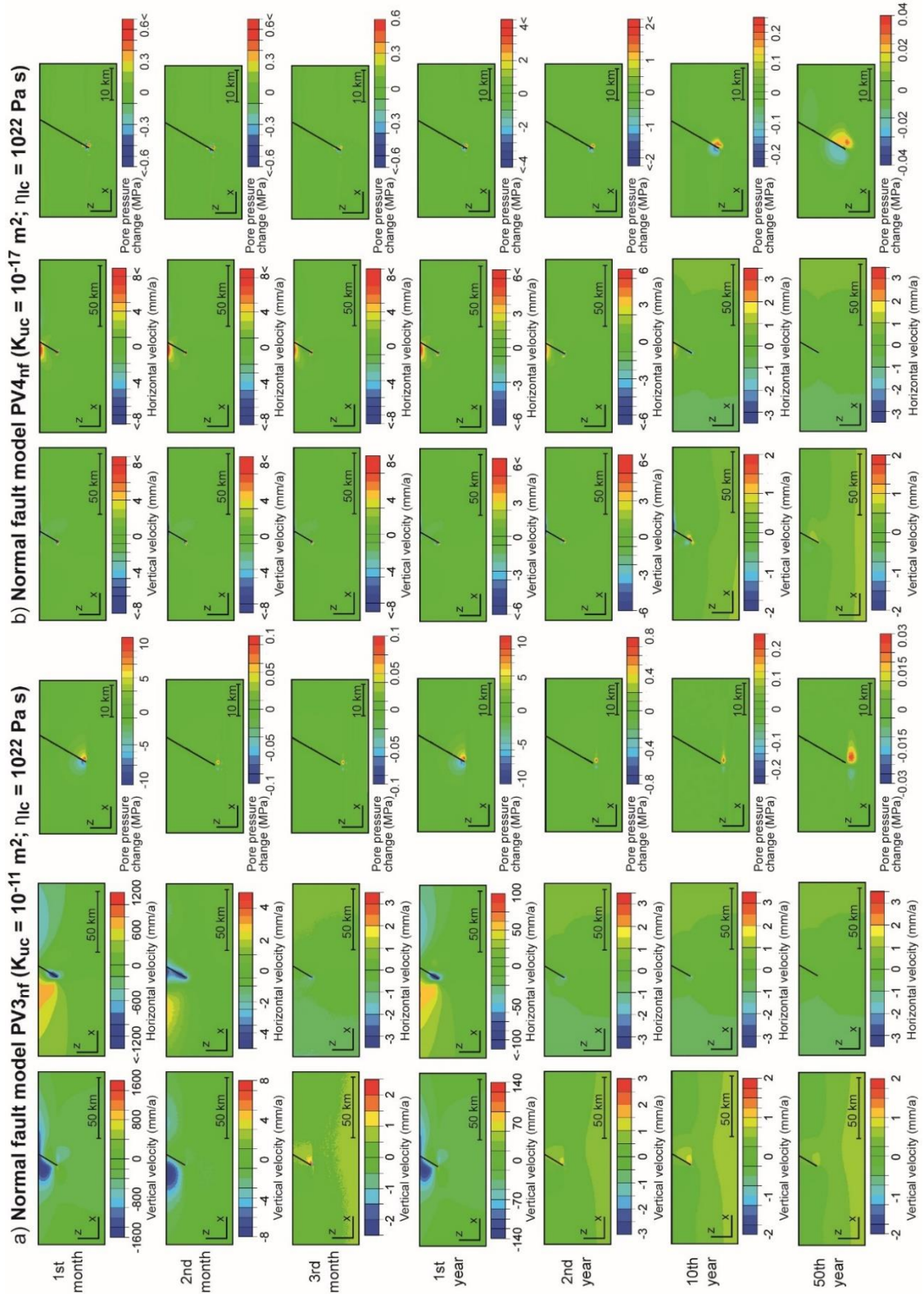
41

Figure 2.9: Postseismic velocity fields and pore pressure changes from normal fault models (a) PV1$_{nf}$ with an upper-crustal permeability of K$_{uc}$ = 10^{-11} m^2 and a lower-crustal viscosity of η$_{lc}$ = 10^{19} Pa s and (b) PV2$_{nf}$ with an upper-crustal permeability of K$_{uc}$ = 10^{-17} m^2 and a lower-crustal viscosity of η$_{lc}$ = 10^{19} Pa s. No vertical exaggeration. Note that the velocity fields and pore pressure changes at all time points are averaged over the respective time interval, i.e. the velocity field and pore pressure change for the first postseismic year is integrated over the time period between the beginning and the end of the first year after the earthquake.

42

Figure 2.10: Postseismic velocity fields and pore pressure changes from normal fault models (a) PV3$_{nf}$ with an upper-crustal permeability of K$_{uc}$ = 10^{-11} m^2 and a lower-crustal viscosity of η_{lc} = 10^{22} Pa s and (b) PV4$_{nf}$ with an upper-crustal permeability of K$_{uc}$ = 10^{-17} m^2 and a lower-crustal viscosity of η_{lc} = 10^{22} Pa s. No vertical exaggeration. Note that the velocity fields and pore pressure changes at all time points are averaged over the respective time interval, i.e. the velocity field and pore pressure change for the first postseismic year is integrated over the time period between the beginning and the end of the first year after the earthquake.

viscosity but the magnitudes of the velocities best agree with models $P1_{nf}$ and $P1_{tf}$. This also applies to the pore pressure changes in the first month. Already in the second month, the velocities strongly decrease. Hanging wall subsidence, footwall uplift and extension across the normal fault as well as hanging wall uplift and footwall subsidence and shortening across the thrust fault already start in the second month onwards. The velocity fields and also the pore pressure distributions now resemble the results obtained for third month of models $V1_{nf}$ and $V1_{tf}$. The further evolution of $PV1_{nf}$ and $PV1_{tf}$ is similar to models $V1_{nf}$ and $V1_{tf}$.

Models $PV2_{nf}$ and $PV2_{tf}$ have a low viscosity of 10^{19} Pa s combined with a low permeability of 10^{-17} m^2 (Figures 2.9b, S7b). This parameter combination yields considerably lower velocities in the first month and velocity fields comparable to the third month of models $V1_{nf}$ and $V1_{tf}$. Like in models $P4_{nf}$ and $P4_{tf}$, no major changes occur in the velocity fields during the following months until the fifth year. Until the 50th year, models $PV2_{nf}$ and $PV2_{tf}$ show a similar evolution of the velocity distributions as $V1_{nf}$ and $V1_{tf}$, but with different magnitudes.

The pore pressures develop comparable to models $P4_{nf}$ and $P4_{tf}$, with slightly higher pore pressure changes around the fault tip in the first months and year after the earthquake and pore pressure expansion over the following years.

The combination of a high permeability in the upper crust (10^{-11} m^2) and a high viscosity in the lower crust (10^{22} Pa s) in models $PV3_{nf}$ and $PV3_{tf}$ (Figures 2.10a, S8a) leads to similar velocity fields in the first month, that occur in the reference models ($R1_{nf}$, $R1_{tf}$), the models with the same permeability ($P1_{nf}$, $P1_{tf}$) and viscosity structure ($V2_{nf}$, $V2_{tf}$). The pore pressure distributions are similar to models $V2_{nf}$ and $V2_{tf}$ for the first month and year after the earthquake. In the second month, velocities strongly decrease. While the patterns of the velocity fields are similar to models $V2_{nf}$ and $V2_{tf}$, their magnitudes are one order of magnitude lower. The velocity patterns of the third month resemble the ones observed in the sixth month in models $V2_{nf}$ and $V2_{tf}$, with a similar evolution over the following years, i.e. the velocity fields are dominated by the regional deformation and only weakly perturbed around the fault. The pore pressure changes of the second month in models $PV3_{nf}$ and $PV3_{tf}$ are equivalent to the ones occurring in the third month in model $V2_{nf}$ and $V2_{tf}$. Afterwards, they develop similarly as in models $V2_{nf}$ and $V2_{tf}$.

Finally, models $PV4_{nf}$ and $PV4_{tf}$ combine a high viscosity (10^{22} Pa s) with a low permeability (10^{-17} m^2) (Figures 2.10b, S8b). The results show the least pronounced perturbations in the velocities and pore pressure distributions of all models. During the first year, the velocity fields are mainly perturbed around the fault tip and at the surface near the fault, similar to models $P4_{nf}$

and P4$_{tf}$. Until the tenth year, the models PV4$_{nf}$ and PV4$_{tf}$ also show slight opposite movements in the horizontal direction. On both sides of the fault, subsidence occurs in the normal fault model and uplift in the thrust fault model until the 50th year. The velocity perturbations around the fault tip and at the surface slowly dissipate over the years, similar to models V2$_{nf}$ and V2$_{tf}$. The pore pressure evolution in models PV4$_{nf}$ and PV4$_{tf}$ is similar to model set P4$_{nf}$ and P4$_{tf}$ from the first month onwards, with the magnitudes of the pore pressure changes being slightly higher.

2.4 Discussion

Our parameter study reveals that both poroelastic effects and viscoelastic relaxation modify the postseismic pore pressure changes and velocities through space and time, depending on the permeability and viscosity, respectively. In the following, we discuss the main findings and limitations of our models and evaluate the relative importance of poroelastic effects and postseismic viscoelastic relaxation for the velocity and pore pressure distributions (Section 4.1). In Section 4.2, we qualitatively compare our findings with data and models from natural normal and thrust fault earthquakes. Note that the application of our models to data from specific earthquakes is beyond the scope of our study, because the main purpose of our study is advancing the general understanding of the underlying processes. Also, specific models including poroelastic and/or viscoelastic effects are already available for a number of earthquakes (e.g. Albano et al., 2017, 2019, 2021; Freed and Lin, 2001; Luo and Liu, 2010; Masterlark and Wang, 2002; Nespoli et al., 2018; Ryder et al., 2007, 2010; Tung and Masterlark, 2018).

2.4.1 Discussion of model results, model limitations and implications for the relative importance of viscoelastic relaxation and poroelastic effects

During the coseismic phase, the sudden slip on the model fault causes crustal movements typical of normal and thrust fault earthquakes, i.e. hanging wall subsidence and footwall uplift in the normal fault model and hanging wall uplift and footwall subsidence in the thrust fault model (Figures 2.2a, b). Horizontal movements in the footwall and hanging wall are directed away from the normal fault and toward the thrust fault (Figures 2.2b, d). Compared to the analytical solutions by Okada (1985), the vertical displacements occur in broader zones on both sides of the fault whereas the horizontal displacements are largely similar (Figures 2.2b, d). The differences between the displacements can be attributed to the fact that Okada (1985) simplifies the crust as an isotropic, homogeneous elastic half-space, whereas our models account for

gravity, isostatic effects, rheological layering of the lithosphere and poroelastic effects. Furthermore, Okada (1985) assumes a constant amount of slip on a rectangular fault plane, whereas the slip distribution in our finite-element models is tapered, i.e. it goes to zero at the lower fault tip. As shown by previous studies, the consideration of tapered fault slip, isostatic effects and/or rheological layering in finite-element models leads to more realistic surface displacements in agreement with geodetically measured surface displacement patterns (e.g. Hampel and Hetzel, 2015; Hsu et al., 2011; Tung et al., 2018b).

With respect to the strain regime, the coseismic horizontal displacements indicate extension across the normal fault and to shortening across the thrust fault (Figure 2.2). In the footwall and hanging wall, however, shortening prevails in the normal fault model and extension in the thrust fault model (Figure 2.2e). The phenomenon of coseismic shortening in the footwall of normal faults and of coseismic extension in the hanging wall of thrust faults is well known from geological field observations from natural earthquakes (e.g. Crone et al., 1987; King and Vita-Finzi, 1981; Lin et al., 2009; Liu-Zeng et al., 2009; Meghraoui et al., 1988; Myers and Hamilton, 1964; Philip and Meghraoui, 1983; Slemmons, 1957; Yu et al. 2010). As shown in a previous numerical modelling study (Hampel and Hetzel, 2015), the coseismic strain patterns are also recognizable in GPS data from intra-continental dip-slip faults (e.g. Cheloni et al., 2010; Chen et al. 2006; Serpelloni et al., 2012; Yu et al., 2001). During the postseismic phase, the coseismically induced strain fields are gradually altered by the combined effect of viscoelastic flow and interseismic strain accumulation (Hampel and Hetzel, 2015). Again, the spatiotemporal evolution of the strain field is also visible in GPS data (e.g. Cheloni et al., 2010; Yu et al., 2003).

In contrast to the coseismic vertical displacements, the vertical movements during the early postseismic phase depends on whether poroelastic effects are considered in the respective experiment. Models including poroelastic effects (e.g. $R1_{nf}$, $R1_{tf}$ and $R2_{nf}$, $R2_{tf}$) reveal that the footwall and hanging wall move in the same vertical direction, i.e. both experience subsidence in the normal fault model and uplift in the thrust fault model, respectively (Figures 2.3, 2.4). In contrast, models including only viscoelastic relaxation but no fluid flow ($R3_{nf}$, $R3_{tf}$) do not show this pattern (Figures 2.3c, 2.4c). This implies that vertical movements are caused by the poroelastic effects, i.e. they are driven by pore fluid diffusion and depend on the permeability. The dependence of the vertical movements near the fault on the presence or absence of pore fluid flow in a numerical model is supported by a comparison with models that either considered (e.g. Albano et al., 2017, 2019, 2021) or neglected pore fluid flow (e.g. Barbot and Fialko,

2010; Hampel and Hetzel, 2015; Pollitz, 1997). To further evaluate if the postseismic vertical movements of hanging wall and footwall in the same direction are indeed indicative of poroelastic effects, detailed geodetic data from both fault-bounding blocks at different time intervals after the earthquake would be desirable. So far, the available geodetic data from intra-continental earthquakes do not yield a consistent picture, partly because of the larger uncertainty involved with measurements of vertical movements. For example, 60 days after the 2009 L'Aquila normal fault earthquake, the 8 GPS stations on the hanging wall of the Paganica fault show subsidence of up to 50 mm while the one station located on the footwall showed 5.4 mm of uplift (Cheloni et al., 2010). In contrast, the postseismic deformation field of the 2016 Amatrice-Norcia earthquakes was characterized by primarily subsidence of the hanging wall but subsidence and uplift in the footwall (Mandler et al., 2021). After the 2003 Chengkung (Taiwan) thrust fault earthquake, the 3 GPS stations located near the fault surface trace recorded uplift (Chen et al., 2006).

The further spatio-temporal evolution of the postseismic velocity field depends on the permeability of the crust. Models with upper-crustal permeabilities higher than 10^{-15} m^2 show elevated vertical and horizontal velocities and strong velocity perturbations in the first month after the earthquake, which decrease rapidly in the following few months. The velocities are highest in a small area around the fault of up to 20 km away from the fault. For lower permeabilities, the velocities in the first month show lower initial values but a slower decrease over time. Note that, although both vertical and horizontal velocities generally decrease over time, the specific velocity values and patterns depend on the time interval over which the velocities are integrated. In Figures 2.3-2.10 and S1-S8, we illustrate this by showing the velocities for the first months and integrated over the first year after the earthquake. If the velocities are integrated over a month, the highest velocities occur during the first month but generally decrease until the sixth month after the earthquake. If the velocity field integrates over the entire first year after the earthquake, elevated values are obtained and the velocity pattern of the first year generally resembles the one of the first month. This indicates that a velocity field integrated over the first postseismic year may be dominated by the signal from poroelastic effects rather than by the signal from incipient viscoelastic relaxation (see Section 4.2 for a discussion of the relative importance of the two processes). Caution is therefore advised when choosing the time interval for analysing postseismic velocity fields obtained, for example, from geodetic data. Sometimes, postseismic velocity fields integrated over the early postseismic phase are interpreted to reflect the signal from incipient viscoelastic relaxation, under the assumption that poroelastic effects have largely disappeared (e.g. Aoudia et al., 2003;

Liu-Zeng et al., 2020; Mandler et al., 2021), which may not always be the case.

The return to velocity patterns typical of normal and thrust faults occurs within the first few months in models $P1_{nf}$ and $P1_{tf}$ and $R1_{nf}$ and $R1_{tf}$ and in the second and after the fifth year in models $P2_{nf}$ and $P2_{tf}$ and $P3_{nf}$ and $P3_{tf}$, respectively. For lower permeabilities (e.g. model $P4_{nf}$, $P4_{tf}$), the unusual movements are only slightly recognizable. Models $R2_{nf}$ and $R2_{tf}$, which considers poroelastic effects but no viscoelastic relaxation shows the same velocity evolution in the first two months after the earthquake as the reference models $R1_{nf}$ and $R1_{tf}$. In the third month, the velocity fields are still disturbed, and in the following months and years, only the regional velocity fields largely remain, without significant velocity perturbations. Hence, models $R2_{nf}$ and $R2_{tf}$ show that in absence of postseismic viscoelastic relaxation, poroelastic effects seem to affect the velocity fields until the third month.

With respect to the pore pressure distribution, we observe in all models that the areas with maximum and minimum pore pressure changes are mostly located within a few kilometres around the fault tip. Relative to the coseismic phase, the postseismic pore pressure changes are inverted. Because of the higher magnitude, this dominant pattern of pore pressure changes in our models overprints the pore pressure changes with alternating zones of negative and positive pore pressure changes that may be expected from a double-couple earthquake source function with conjugate zones of extension and shortening. The alternating zones of negative and positive pore pressure changes can be made visible by limiting the colour scale to a narrower range of values (Supplementary Figure S9; Zhou and Burvey, 2014). As noted by previous studies, deformation patterns may differ from the theoretically expected conjugate pattern if, for example, anisotropy, pore pressure and the background stress state are considered (e.g. Foulger and Julian, 2015; Hamiel et al., 2005; Vavrycuk 2005; Wang, 1997). Notably, non-double-couple components in seismic moment tensors have been reported for natural and induced earthquakes and related, for example, to anisotropies, pore pressure and/or stress state (e.g. Frohlich, 1994; Martinez-Garzon et al., 2017; Miller et al; 1998).

The pore pressure changes normalize during the postseismic phase at different rates and slowly migrate into the lower crust over the years. Models $P1_{nf}$ and $P1_{tf}$ and $P2_{nf}$ and $P2_{tf}$ with high permeabilities in the upper crust ($K_{uc} = 10^{-11}$ m^2 and $K_{uc} = 10^{-13}$ m^2) show pore pressure changes of the same magnitude as the pore pressure changes of the coseismic phase of the reference models $R1_{nf}$ and $R1_{tf}$, followed by pore pressure migration into the lower crust with only low magnitude, i.e. hydrostatic conditions are reached already in the first month (Figures 2.6a, 2.6b, S1a and S1b). With decreasing permeability in the upper crust (lower than $K_{uc} = 10^{-13}$ m^2), the

magnitude of the pore pressure changes decreases in the first month, but remains higher in the following months and years, indicating that fluids diffuse slower within the upper crust, pore fluid pressure normalization lasts longer and hydrostatic conditions are therefore only reached after years or decades, respectively. In models $P4_{nf}$ and $P4_{tf}$ ($K_{uc} = 10^{-17}$ m^2, Figures 2.7b and S2b), this slow fluid diffusion is particularly well illustrated over the entire 50-year period.
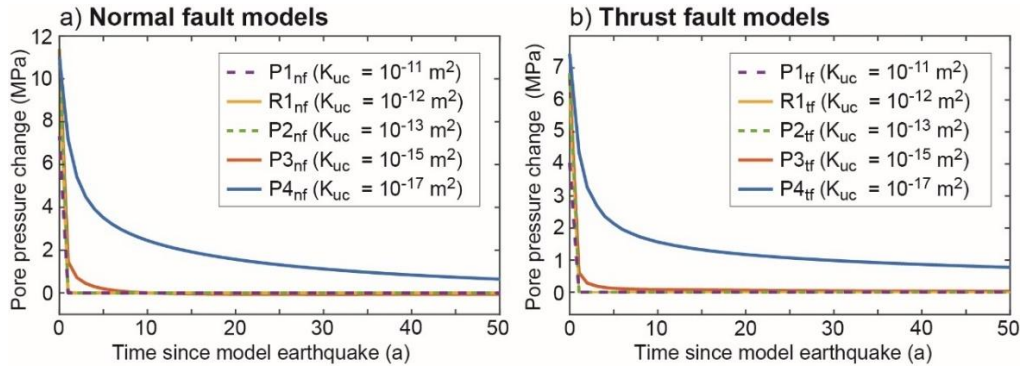

Figure 2.11: Temporal evolution of the postseismic pore pressure changes in (a) normal fault and (b) thrust fault models.

Figure 2.11 shows the temporal evolution of the pore pressure in the over-pressurized model area near the fault tip for different permeabilities in the upper crust. With respect to the temporal decrease of the pore pressure changes, we note that dissipation times in 2D finite-element models may somewhat differ from those in 3D models because the fluid flow is forced to occur in two dimensions only. A comparison between the 2D models presented in this study and the results from preliminary 3D models suggests that the difference in dissipation times effect may become recognizable for permeabilities lower than ca. 10^{-15} m^2. However, the observed difference in dissipation times in 2D and 3D models is small and does not affect our conclusions obtained from the 2D models regarding the timescale of the interaction of poroelastic effects with viscoelastic relaxation. In the reference models $R1_{nf}$ and $R1_{tf}$, the pore pressure changes decrease exponentially and reach largely hydrostatic conditions within four days. In models with permeabilities higher than 10^{-14} m^2, the pore pressure normalizes within the first year after the earthquake. For a permeability of $K_{uc} = 10^{-15}$ m^2 (models $P3_{nf}$, $P3_{tf}$), the pore pressure relaxation lasts ~10 years. In the models with a permeability of $K_{uc} = 10^{-17}$ m^2 (models $P4_{nf}$, $P4_{tf}$), the pore pressure relaxes very slowly, with the result that the hydrostatic pore pressure of the preseismic phase is still not fully recovered after 50 years. Thus, our results underline that the permeability of the upper crust has a strong effect on the pore fluid diffusion during the postseismic phase. The lower the permeability, the weaker is the fluid flow and the longer takes the pore pressure normalization. In contrast, the permeability of the lower crust has a negligible

effect on the pore pressure evolution in the upper crust. However, an increase of the permeability in the lower crust may lead to an increased fluid flow into the lower crust.

In summary, a high permeability in the upper crust causes strong poroelastic effects with large pore pressure changes and velocity perturbations, but these effects last only for a few days to a few months after the earthquake. A low permeability in the upper crust leads to weak, but long-lasting poroelastic effects, which are still recognizable several years after the earthquake. Therefore, the poroelastic effects observed in our models act on timescales that overlap with the spatio-temporal evolution of the postseismic viscoelastic relaxation process. A change in the viscosity in the lower crust compared to the reference models may therefore affect the model results already for the early postseismic phase. For example, a viscosity of 10^{19} Pa s leads to larger velocity perturbations, which slightly change over the period of 50 years, mainly in an area of 10-20 km around the fault, but up to several tens of kilometres away from the fault (models $V1_{nf}$, $V1_{tf}$). The vertical and horizontal velocities are high in the first years after the earthquake and decrease over the following years. For a higher viscosity (models $V3_{nf}$, $V3_{tf}$; 10^{22} Pa s), only weak velocity perturbations with low velocities occur, which are recognizable several tens of kilometres away from the fault and only change negligibly over the decades. Hence, as can be expected, an increase of the viscosity in the lower crust leads to slower but more prolonged viscoelastic relaxation. As illustrated by the models $R3_{nf}$ and $R3_{tf}$, which considers viscoelastic relaxation but no pore fluid pressure (Figures 2.3c and 2.4c), velocity perturbations occur from the first month onward, with only negligible changes over the next 50 years. This underlines that a signal from viscoelastic relaxation is already recognizable in the first month after the earthquake. In presence of pore fluid flow (models $R1_{nf}$, $R1_{tf}$ and $R2_{nf}$, $R2_{tf}$), however, the signal from viscoelastic relaxation is overprinted by the signal from the poroelastic effects, which strongly influence the velocity fields in the early postseismic phase if the permeability is sufficiently high. As soon as the poroelastic effects decay, the viscoelastic relaxation signal starts to dominate the velocity fields, which is the case already in the third month in models with high permeabilities (e.g. models $PV1_{nf}$, $PV1_{tf}$ and $PV3_{nf}$, $Pv3_{tf}$). Models with a low permeability and a low viscosity ($PV2_{nf}$, $PV2_{tf}$) highlight the possibility that viscoelastic relaxation may dominate the velocity fields with pronounced velocity perturbations already from the first month onwards because the poroelastic effects are weak. For the combination of a low permeability and a high viscosity, the signals from both effects are weak but long-lasting, with the result that they overlap over several decades and cause weak velocity perturbations (models $PV4_{nf}$, $PV4_{tf}$).

2.4.2 Comparison with data and models for natural intra-continental earthquakes

A key region where a wealth of studies has investigated poroelastic effects after normal and thrust earthquakes with magnitudes of up to M_w ~7 are the Apennines and Emilia-Romagna region (Italy) (e.g. Albano et al., 2019, 2021; Antonioli et al., 2005; Chiarabba et al., 2009; Nespoli et al., 2018; Tung and Masterlark, 2018). In addition, a few studies used geodetic data from the postseismic phase to determine the rheological structure of the lithosphere beneath the Apennines and found low viscosities (~10^{18} Pa s) for the lower crust (Aoudia et al., 2003; Riva et al., 2007). Based on our model results, we would therefore expect an interaction between poroelastic effects and viscoelastic relaxation during the postseismic phase. Most studies, however, focussed on a specific time interval after the earthquake and therefore neglected either viscoelastic relaxation (e.g. Albano et al., 2017, 2019, 2021; Chiarabba et al., 2009; Nespoli et al., 2018) or poroelastic effects (Aoudia et al., 2003; Riva et al., 2007). In the following, we evaluate the results from the previous studies on earthquakes in the Apennines and Emilia-Romagna region in the light of our model results.

Poroelastic effects were studied, for example, by Albano et al. (2017, 2019, 2021) for the 2009 L'Aquila, 2012 Emilia-Romagna and the 2016 Amatrice-Visso-Norcia seismic sequences. Their finite-element models were either based on a simplified cross-section (Albano et al., 2019, 2021) or adjusted to the respective region (Albano et al., 2017) and used permeabilities between 10^{-12} and 10^{-17} m^2. Similar to our results, their findings indicate that the coseismic pore pressure changes are completely dissipated by fluid diffusion in the postseismic phase. Hydrostatic conditions are reached within a few days to up to one year, depending on the permeability in the crust. Compared to these results, our models indicate even longer pore pressure dissipation times of several years if the upper crust has a permeability of 10^{-17} m^2. Notably, Albano et al. (2017, 2019, 2021) obtain postseismic surface subsidence for the 2009 L'Aquila and 2016 Amatrice-Visso-Norcia normal fault earthquakes and uplift for the 2012 Emilia-Romagna thrust fault earthquakes, which agrees well with our model results obtained for an idealized fault geometry. In addition, our models show that these unusual surface displacements are largest in the first year after the earthquake in models with high permeabilities.

The spatial distribution and dissipation time of the fluid overpressure is closely related to the spatio-temporal distribution of aftershocks. Seismological data from the 1997 Umbria-Marche earthquake sequence revealed that most of the main shocks and aftershocks occurred in areas where the pore pressure increased around the fault (Antonioli et al., 2005; Chiarabba et al., 2009). For the 2016 Amatrice-Visso-Norcia earthquakes, Albano et al. (2019) showed that the

26 October 2016 earthquake occurred when the fluid overpressure induced by the 24 August 2016 Amatrice earthquake had not yet dissipated. Over-pressurization and pore pressure dissipation may trigger aftershocks, with the stress increase being related to the pore pressure dissipation time and hence to the permeability. In accordance with Albano et al. (2019)'s findings, our models indicate that the pore pressure may not fully dissipate within a few months after the earthquake if the permeability is lower than 10^{-13} m^2. For the crust beneath the Apennines, a permeability of 10^{-16} m^2 was derived by Tung and Masterlark (2018), who carried out modelling and Coulomb stress change calculations for the 2016 Amatrice-Visso-Norcia earthquakes. For such a permeability value, our model results indicate pore fluid dissipation times of more than a few months after the earthquake. With respect to the relative importance of poroelastic effects and viscoelastic relaxation for aftershock triggering, Tung and Masterlark (2018) argued that the postseismic Coulomb stress changes are dominated by poroelastic effects and that the contribution from viscoelastic relaxation is negligible. However, their model only considered viscoelastic behaviour in the mantle but not the low viscosity of the lower crust that was reported by Aoudia et al. (2003) and Riva et al. (2007).

Our model results support the notion that poroelastic effects dominate the velocity field during the early postseismic phase, i.e. when the probability of strong aftershocks is high. However, our findings indicate that the velocity field may also contain a signal from viscoelastic relaxation for sufficiently low viscosities of the lower crust (Figures 2.8a, 2.9, S5a, S7). This is in accordance with the findings by Riva et al. (2007), who analysed the postseismic deformation after the 1997 Umbria-Marche earthquake sequence based on campaign GPS data from the time period between 1999-2003. Based on forward modelling, Riva et al. (2007) found that the observed postseismic deformation requires a contribution of viscoelastic relaxation. Their preferred model included a viscosity of ~10^{18} Pa s for the lower crust. In additional models, Riva et al. (2007) also evaluated a possible contribution by poroelastic effects, which they found to be small for the time period covered by the GPS data. Therefore, they disregarded poroelastic effects in their final forward models of the GPS data. Our model results agree with Riva et al. (2007)'s observation that poroelastic effects decrease within 2-3 years after the earthquake, however, poroelastic effects should not be neglected completely because for the observed permeability and viscosity values poroelastic and viscoelastic effects may overlap for years after an earthquake in the Apennines.

Compared to Italy, data on coseismically triggered poroelastic and viscoelastic effects are relatively sparse for other region with intra-continental dip-slip earthquakes. In Taiwan, for

example, the 1999 Chi-Chi thrust fault earthquake triggered fluid flow and considerable changes in groundwater levels and river discharges (Lai et al. 2004; Wang et al., 2001, 2004). For the postseismic deformation field, however, poroelastic effects apparently did not play a major role (e.g. Hsu et al., 2007; Rousset et al. 2012; Zhu and Cai, 2009). Instead, the postseismic deformation field was largely dominated by viscoelastic relaxation due the presence of layers with low viscosities in the lithosphere (Rousset et al. 2012; Zhu and Cai, 2009). Based on inversion of GPS data, Zhu and Cai (2009) derived viscosities of the lower crust and the upper mantle of 2.7 x 10^{18} and 4.2x10^{20} Pa s, respectively, while Rousset et al. (2012) obtained viscosities of 5 x 10^{17} and 0.5-1 x 10^{19} Pa s at mid-crustal and lower crustal levels. As our models indicate, the absence of a major poroelastic signal in the early postseismic deformation field may be related to a low permeability in the upper crust, in particular when combined with low lower-crustal viscosities (Figure S7). This may apply to Taiwan where a permeability of ca. 4 x 10^{-15} m^2 at a crustal depth of 10-20 km was derived from a seismological analysis of aftershocks and fluid migration after the 2016 Meinong earthquake (Hsu et al., 2020). Even lower permeabilities (10^{-16} to 10^{-18} m^2) were obtained from drill core samples of the host rock of the Chelungpu fault (Doan et al. 2006; Scibek, 2020). Taiwan may therefore provide an example of a region with thrust fault earthquakes where the timescales of poroelastic and viscoelastic effects overlap in a way that the resulting postseismic deformation is dominated by viscoelastic relaxation.

2.5 Conclusions

Based on two-dimensional finite-element models, we investigated the relative importance of poroelastic effects and postseismic viscoelastic relaxation during the earthquake cycle of intracontinental dip-slip faults and evaluated the results in terms of co- and postseismic pore pressure changes as well as vertical and horizontal velocities. Our experiments with variable permeabilities in the crust and variable viscosities in the lower crust or lithospheric mantle demonstrate that the earthquake induces pore fluid pressure changes especially around the fault tip, which dissipate by fluid diffusion within a few days to decades, depending on the permeability of the crust. These poroelastic effects dominate in the first few months, but still affect the velocity field years after the earthquake if the permeability of the upper crust is sufficiently low. Viscoelastic relaxation already occurs in the early postseismic phase, dominates the velocity field from about the second postseismic year onward and persists for several decades. Viscoelastic relaxation acts on spatial scales of up to several tens of kilometres

away from the fault, whereas poroelastic effects occur mainly within 10-20 km around the fault. Our results show that poroelastic effects and postseismic viscoelastic relaxation may overlap in the early postseismic phase for up to several years, depending primarily on the combination of upper-crustal permeability and lower-crustal viscosity. Therefore, both processes should be considered when analysing geodetic data on postseismic surface deformation or calculating postseismic Coulomb stress changes. In future investigations, we will use 3D numerical models that will include fault arrays as well as poroelastic effects and viscoelastic relaxation to evaluate the combined effect of both processes on Coulomb stress changes.

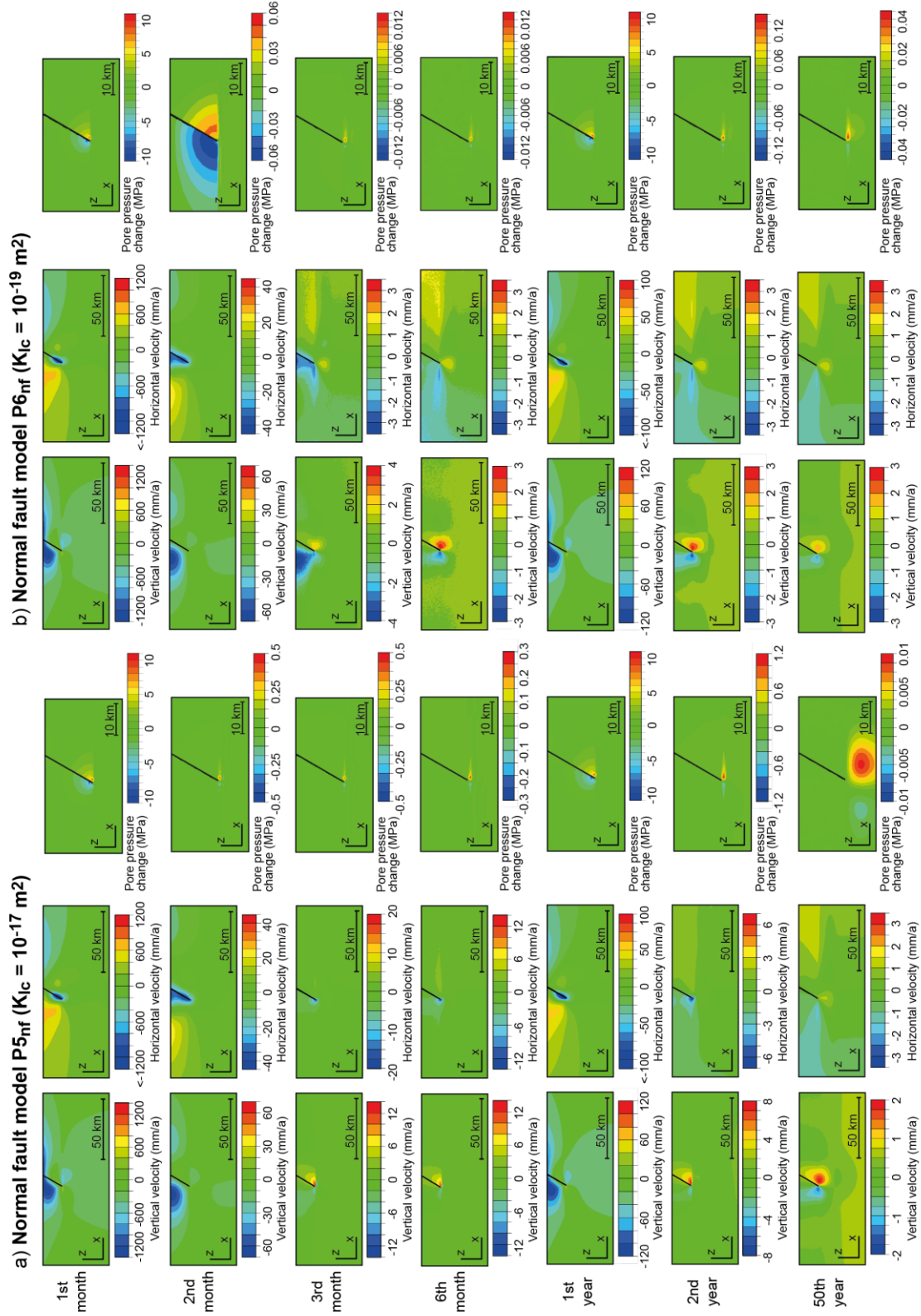## 2.6 Acknowledgements

Supplement
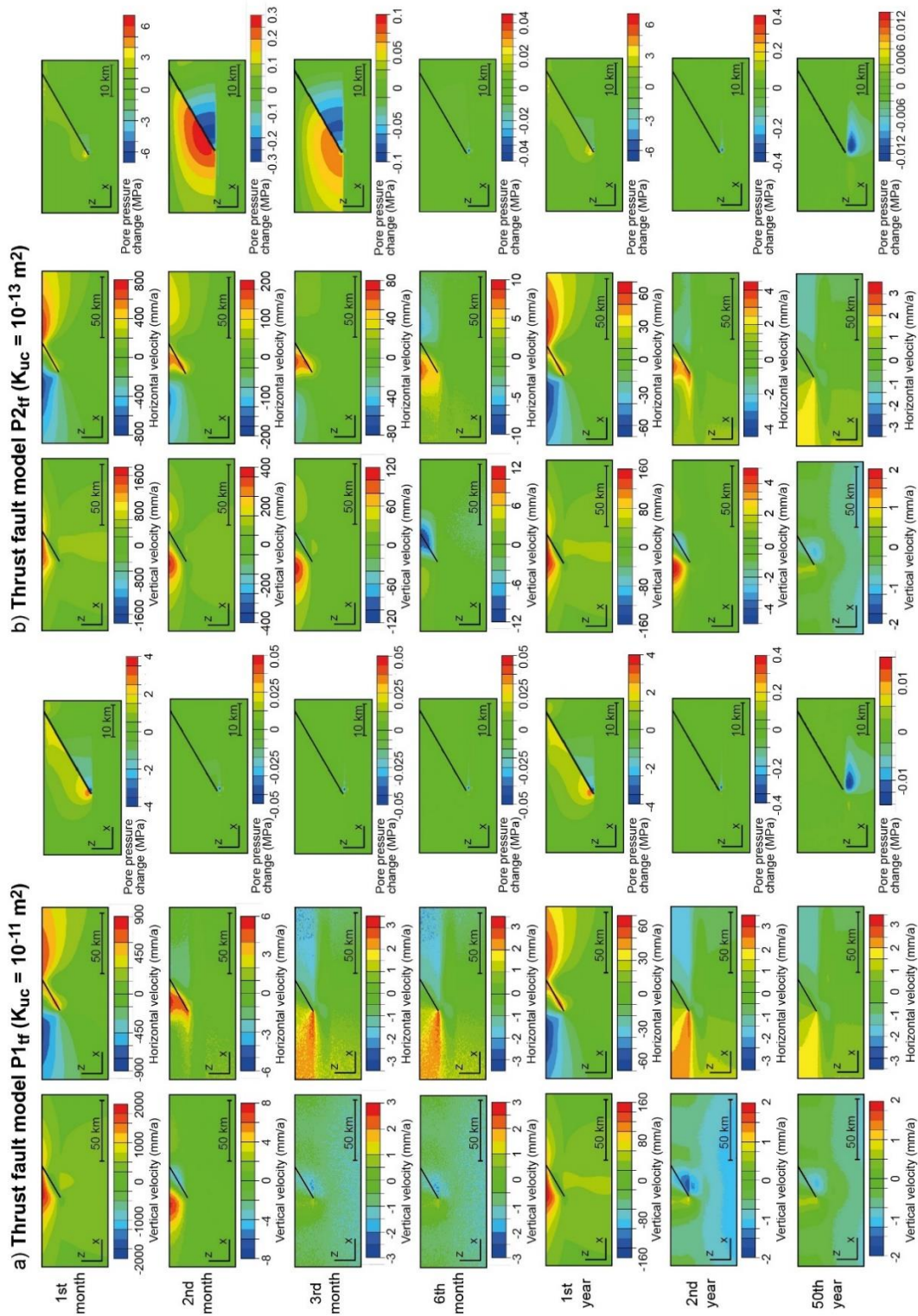
Figure S1: Postseismic velocity fields and pore pressure changes from thrust fault models (a) P1$_{tf}$ with an upper-crustal permeability of $K_{uc} = 10^{-11}$ m^2 and (b) P2$_{tf}$ with an upper-crustal permeability of $K_{uc} = 10^{-13}$ m^2. No vertical exaggeration. Note that the velocity fields and pore pressure changes at all time points are averaged over the respective time interval, i.e. the velocity field and pore pressure change for the first postseismic year is integrated over the time period between the beginning and the end of the first year after the earthquake.
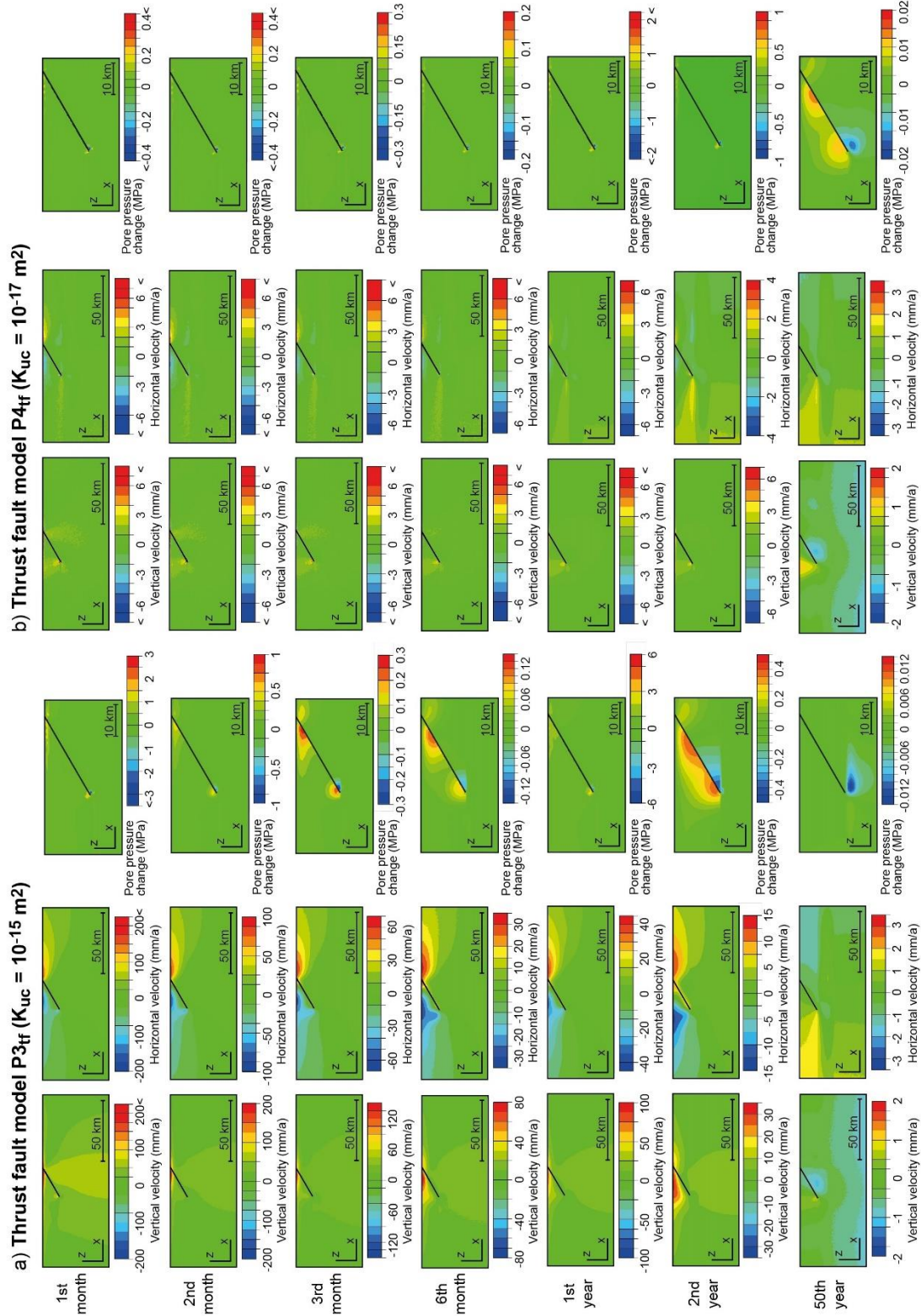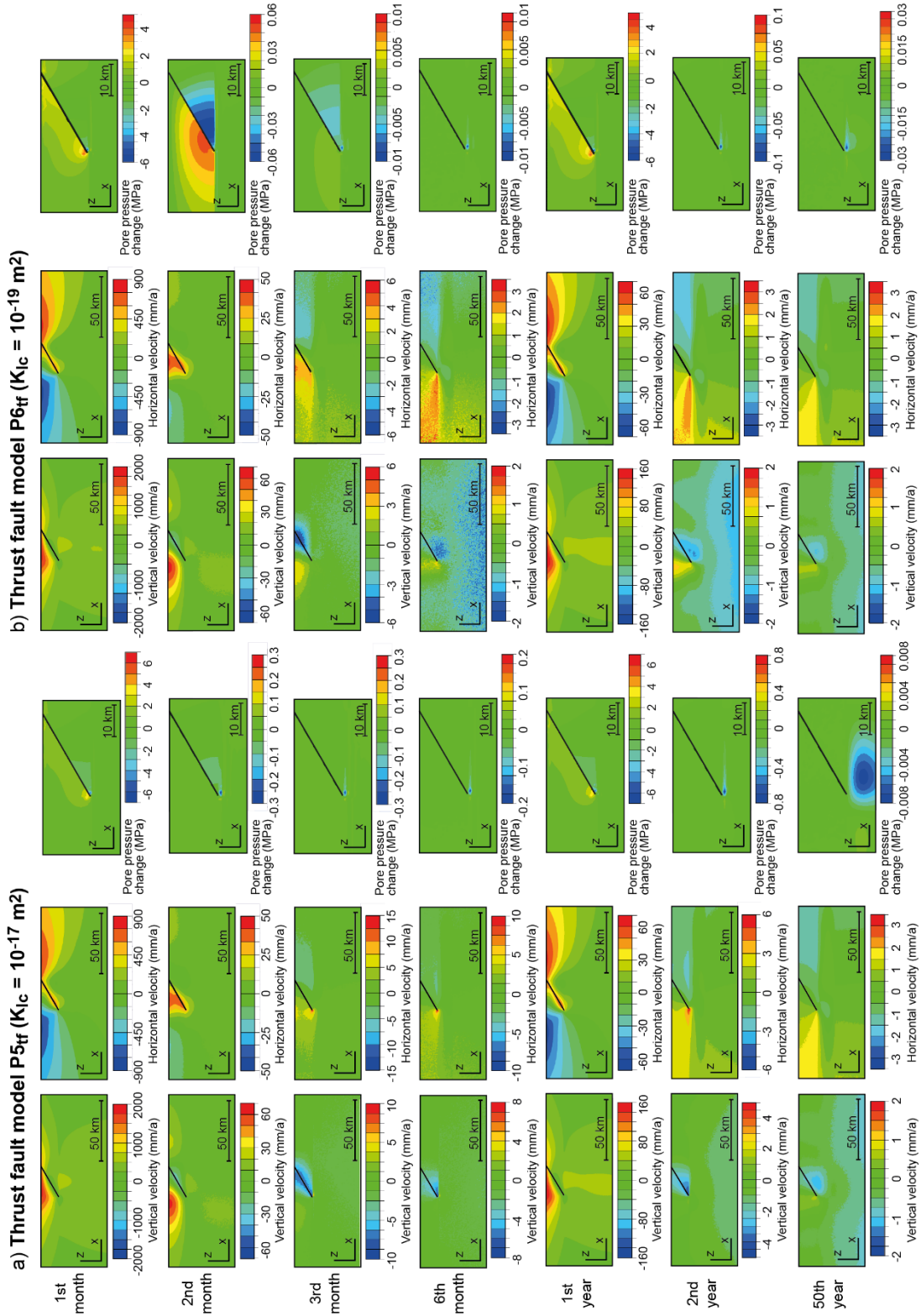
Figure S2: Postseismic velocity fields and pore pressure changes from thrust fault models (a) P3$_{tf}$ with an upper-crustal permeability of K$_{uc}$ = 10^{-15} m^2 and (b) P4$_{tf}$ with an upper-crustal permeability of K$_{uc}$ = 10^{-17} m^2. No vertical exaggeration. Note that the velocity fields and pore pressure changes at all time points are averaged over the respective time interval, i.e. the velocity field and pore pressure change for the first postseismic year is integrated over the time period between the beginning and the end of the first year after the earthquake.
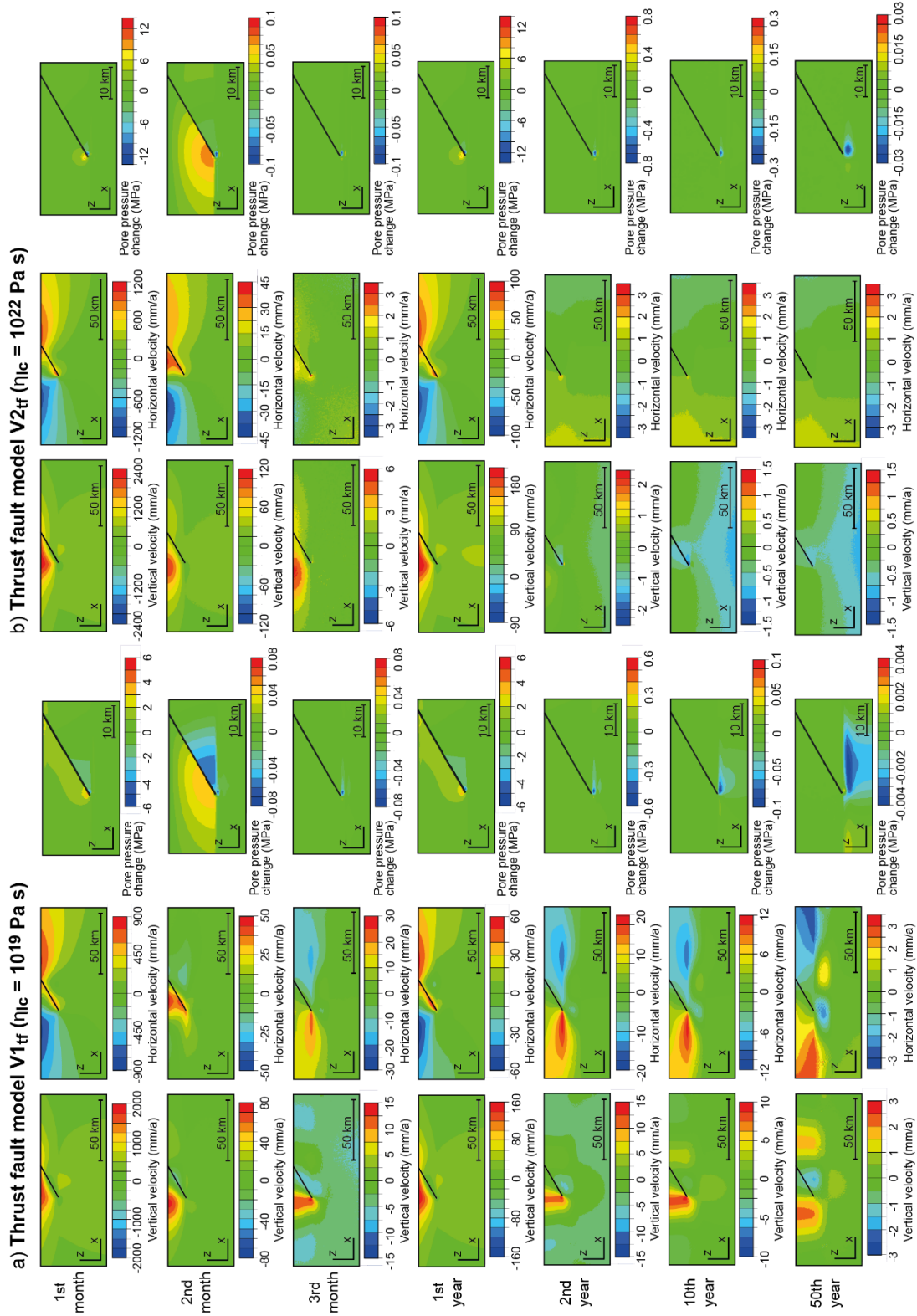
Figure S3: Postseismic velocity fields and pore pressure changes from normal fault models (a) P5$_{nf}$ with a lower-crustal permeability of K$_{lc}$ = 10^{-17} m^2 and (b) P6$_{nf}$ with a lower-crustal permeability of K$_{lc}$ = 10^{-19} m^2. No vertical exaggeration. Note that the velocity fields and pore pressure changes at all time points are averaged over the respective time interval, i.e. the velocity field and pore pressure change for the first postseismic year is integrated over the time period between the beginning and the end of the first year after the earthquake.
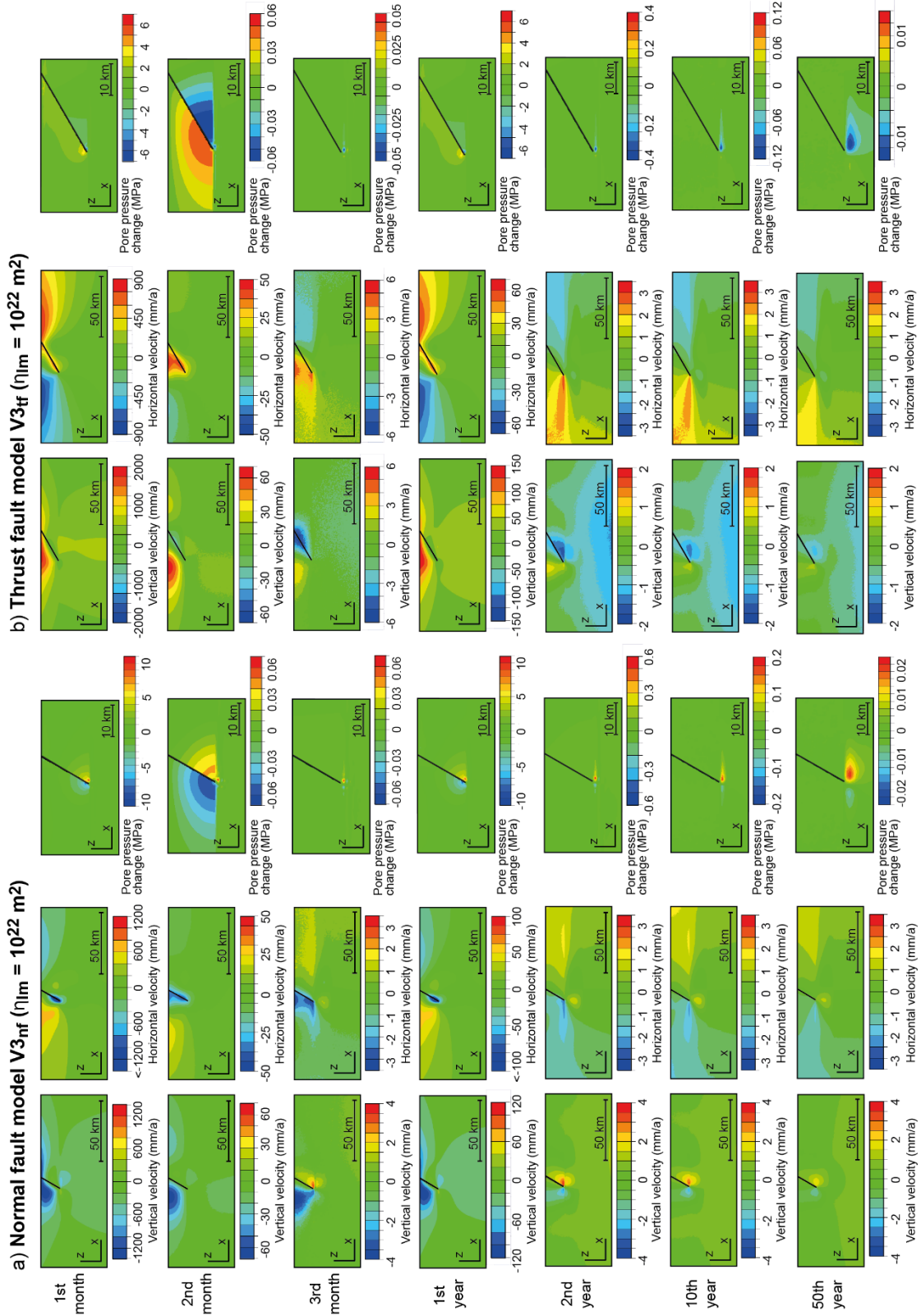
Figure S4: Postseismic velocity fields and pore pressure changes from thrust fault models (a) P5$_{tf}$ with a lower-crustal permeability of K$_{lc}$ = 10^{-17} m^2 and (b) P6$_{tf}$ with a lower-crustal permeability of K$_{lc}$ = 10^{-19} m^2. No vertical exaggeration. Note that the velocity fields and pore pressure changes at all time points are averaged over the respective time interval, i.e. the velocity field and pore pressure change for the first postseismic year is integrated over the time period between the beginning and the end of the first year after the earthquake.
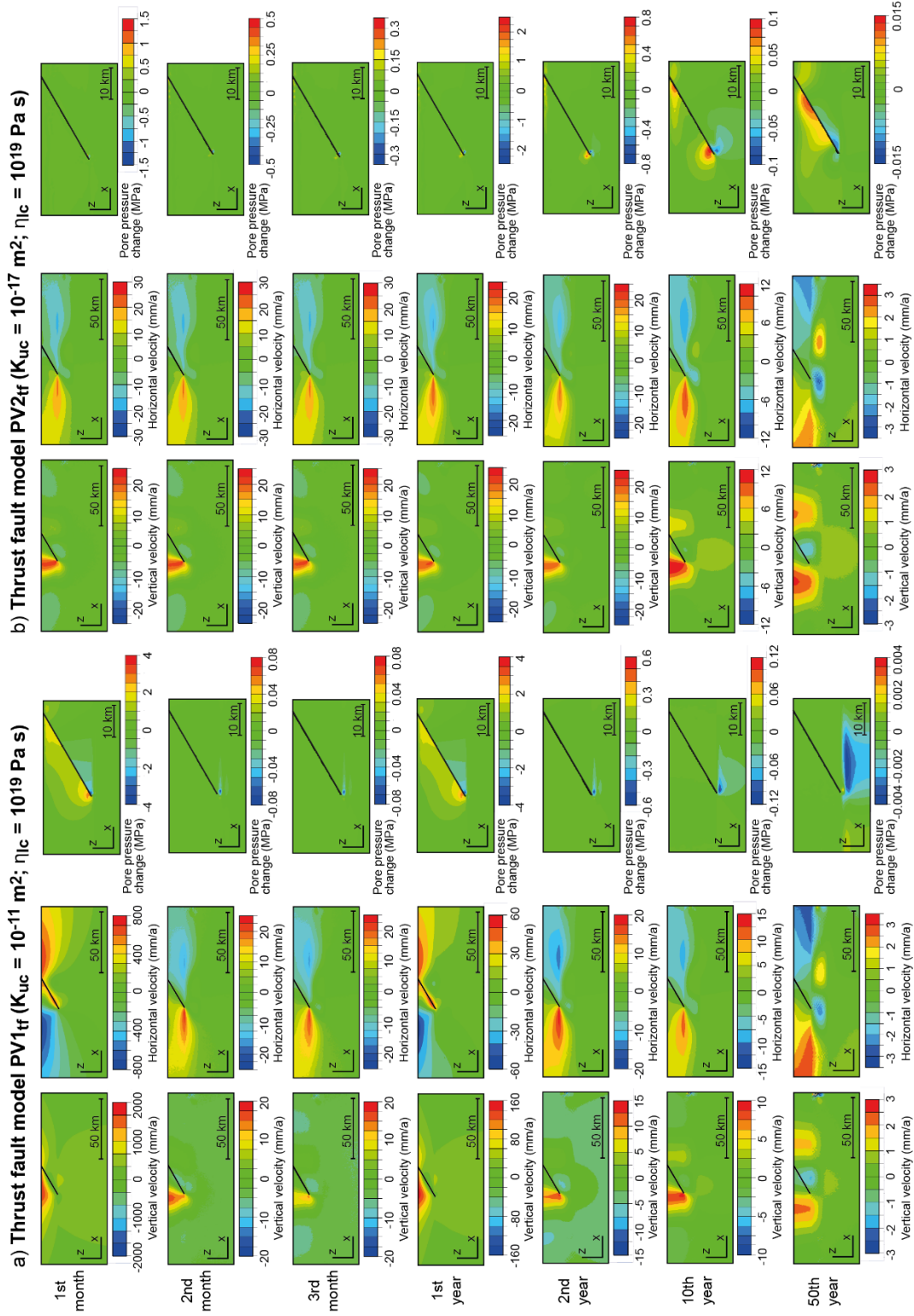
Figure S5: Postseismic velocity fields and pore pressure changes from thrust fault models (a) $V1_{tf}$ with a lower-crustal viscosity of $\eta_{lc} = 10^{19}$ Pa s and (b) $V2_{tf}$ with a lower-crustal viscosity of $\eta_{lc} = 10^{22}$ Pa s. No vertical exaggeration. Note that the velocity fields and pore pressure changes at all time points are averaged over the respective time interval, i.e. the velocity field and pore pressure change for the first postseismic year is integrated over the time period between the beginning and the end of the first year after the earthquake.

Figure S6: Postseismic velocity fields and pore pressure changes from (a) the normal fault model V3$_{nf}$ and (b) the thrust fault model V3$_{tf}$, each with a viscosity of the lithospheric mantle of $\eta_{lm} = 10^{22}$ Pa s. No vertical exaggeration. Note that the velocity fields and pore pressure changes at all time points are averaged over the respective time interval, i.e. the velocity field and pore pressure change for the first postseismic year is integrated over the time period between the beginning and the end of the first year after the earthquake.
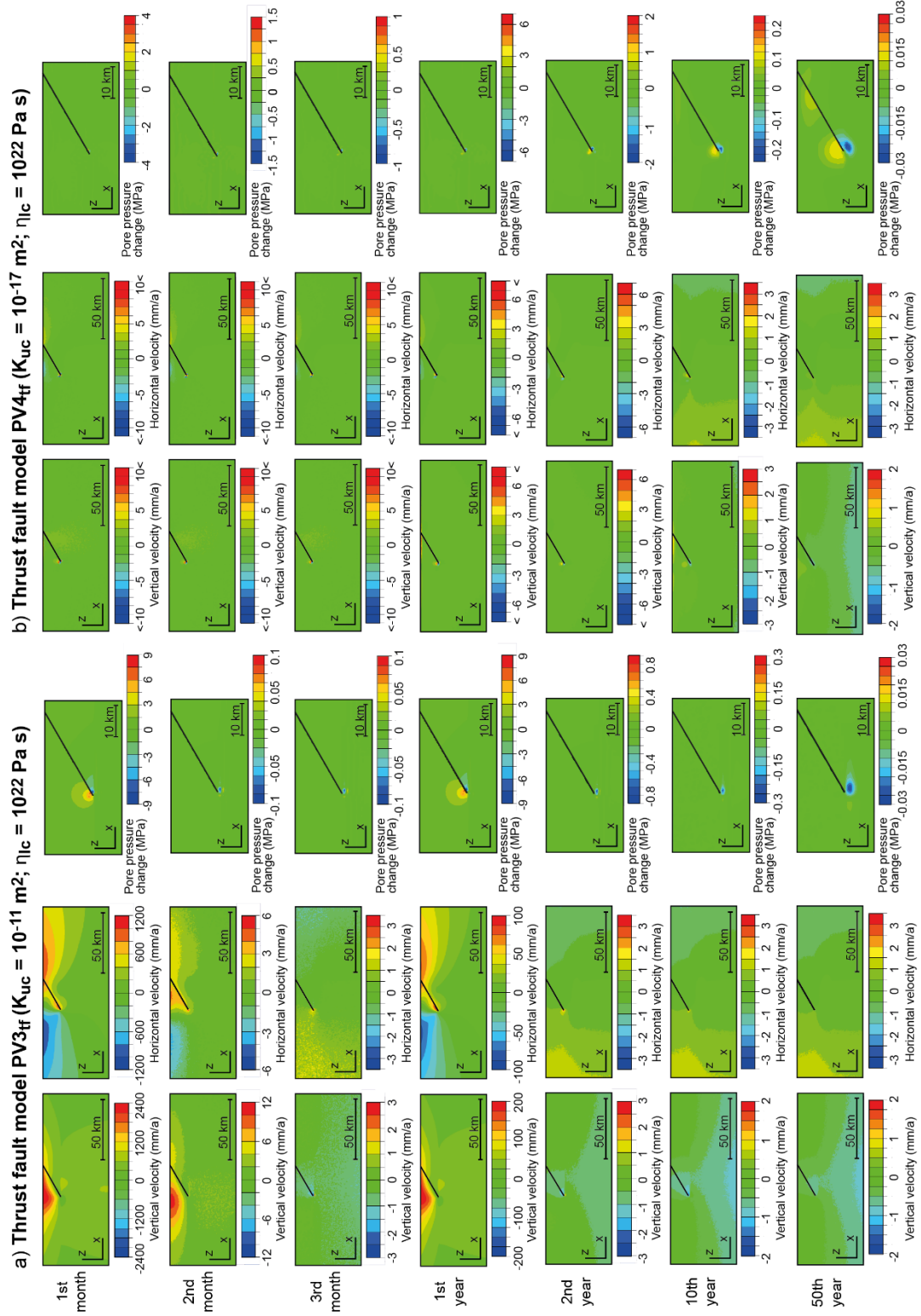
Figure S7: Postseismic velocity fields and pore pressure changes from thrust fault models (a) PV1$_{tf}$ with an upper-crustal permeability of $K_{uc} = 10^{-11}$ m^2 and a lower-crustal viscosity of $\eta_{lc} = 10^{19}$ Pa s and (b) PV2$_{tf}$ with an upper-crustal permeability of $K_{uc} = 10^{-17}$ m^2 and a lower-crustal viscosity of $\eta_{lc} = 10^{19}$ Pa s. No vertical exaggeration. Note that the velocity fields and pore pressure changes at all time points are averaged over the respective time interval, i.e. the velocity field and pore pressure change for the first postseismic year is integrated over the time period between the beginning and the end of the first year after the earthquake.

61

Figure S8: Postseismic velocity fields and pore pressure changes from thrust fault models (a) PV3$_{tf}$ with an upper-crustal permeability of $K_{uc} = 10^{-11}$ m^2 and a lower-crustal viscosity of $\eta_{lc} = 10^{22}$ Pa s and (b) PV4$_{tf}$ with an upper-crustal permeability of $K_{uc} = 10^{-17}$ m^2 and a lower-crustal viscosity of $\eta_{lc} = 10^{22}$ Pa s. No vertical exaggeration. Note that the velocity fields and pore pressure changes at all time points are averaged over the respective time interval, i.e. the velocity field and pore pressure change for the first postseismic year is integrated over the time period between the beginning and the end of the first year after the earthquake.
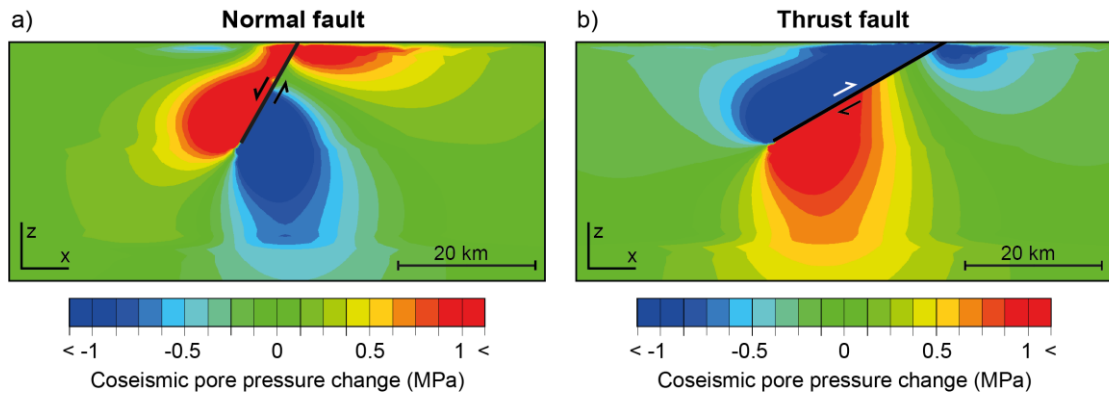
Figure S9: Coseismic pore pressure changes with respect to hydrostatic values for the normal fault and thrust fault reference models. No vertical exaggeration. Note that the maximum and minimum values of the color scales are adjusted to reflect alternating zones with positive and negative pore pressure changes.

3. 3D finite-element modeling of Coulomb stress changes on normal and thrust faults caused by pore fluid pressure changes and postseismic viscoelastic relaxation

Jill Peikert[1], Andrea Hampel[1], and Meike Bagge[2]

[1]Institut für Geologie, Leibniz Universität Hannover, Callinstr. 30, 30167 Hannover, Germany

[2]GFZ German Research Centre for Geosciences, Telegrafenberg, 14473 Potsdam, Germany

Abstract

The analysis of Coulomb stress changes has become an important tool for seismic hazard evaluation because such stress changes may trigger or delay next earthquakes. Processes that can cause significant Coulomb stress changes include coseismic slip, earthquake-induced poroelastic effects and transient postseismic processes such as viscoelastic relaxation. However, the combined influence of poroelastic effects and viscoelastic relaxation on co- and postseismic Coulomb stress changes has not been systematically studied so far. Here, we use three-dimensional finite-element models with arrays of normal and thrust faults to investigate how pore fluid pressure changes and viscoelastic relaxation interact during the postseismic phase. In different experiments, we vary the permeability of the crust and the viscosity of the lower crust or lithospheric mantle, while keeping the other parameters constant. Our results show that the coseismic (= static) Coulomb stress changes are immediately altered by the signal from poroelastic effects and viscoelastic relaxation during the first month after the earthquake. For sufficiently low viscosities, the Coulomb stress change patterns show a combined signal from poroelastic and viscoelastic effects already during the first postseismic year. For sufficiently low permeabilities, Coulomb stress changes induced by poroelastic effects overlap with the signals from viscoelastic relaxation and interseismic stress accumulation for decades. Our results imply that poroelastic and viscoelastic effects have a strong impact on the magnitudes and patterns of Coulomb stress changes and should therefore be considered together when analyzing Coulomb stress transfer between faults.

3.1 Introduction

Large earthquakes affect the stress state on faults in the vicinity of the source fault that ruptured during the seismic event in a way that the next earthquake on the neighboring faults (called "receiver faults") may be promoted or delayed. It is therefore crucial for seismic hazard evaluation to analyze the earthquake-induced stress changes, which are usually expressed in terms of Coulomb stress changes ΔCFS (King et al., 1994; Stein, 2003; Freed, 2005; Scholz, 2010):

$$\Delta CFS = \Delta\tau - \mu\,(\Delta\sigma_n - P)$$

where $\Delta\tau$ is the change in shear stress (positive in direction of slip of the source fault), μ is the friction coefficient, $\Delta\sigma_n$ is the change in normal stress (positive if fault is clamped) and P is the pore pressure. An increase in the Coulomb stress implies that receiver faults are brought closer to failure, whereas a stress decrease indicates that the next earthquake may be delayed (King et al., 1994; Stein, 1999). Hence, the analysis of Coulomb stress changes can be used to identify possible locations of future earthquakes and has become an important tool for the evaluation of seismic hazard in a region (e.g., Stein, 2003; Toda et al., 2005; Freed et al., 2007; Parsons et al., 2008; Field et al., 2009; Luo and Liu, 2010; Wan and Shen, 2010; Serpelloni et al., 2012; Wang et al., 2014; Bagge et al., 2019).

Coulomb stress changes on receiver faults may be generated by a variety of earthquake-induced mechanisms, including static stress changes caused by the coseismic slip (King et al., 1994; Stein, 1999, Ryder et al., 2012) and dynamic stress changes caused by seismic waves (Belardinelli et al., 1999; Gomberg et al., 2001; Oglesby et al., 2003; Pollitz et al., 2012). Transient Coulomb stress changes may be caused by pore fluid pressure changes and postseismic viscoelastic relaxation. Pore fluid pressure changes result from the coseismic slip on the source fault and may trigger aftershocks by reducing the normal stress (Cocco et al., 2000; Chiarabba et al., 2009; Malagnini et al., 2012; Piombo et al., 2005; Chiaraluce, 2012). During the postseismic phase, coseismically induced pore fluid pressure gradients are relaxed by fluid flow if rocks are sufficiently permeable (e.g., Albano et al., 2017; Nespoli et al., 2018; Tung and Masterlark, 2018). Postseismic viscoelastic relaxation refers to the process by which the coseismically imposed stress is relaxed due to viscous flow in the lower crust and lithospheric mantle (Nur and Mavko, 1974). Depending on the viscosity of the lower crust and lithospheric mantle, postseismic viscoelastic relaxation may cause considerable stress changes on faults in the brittle upper crust (Pollitz 1997; Freed and Lin, 1998; Kenner and Segall, 1999;

Nostro et al., 2001; Masterlark and Wang, 2002; Gourmelen and Amelung, 2005; Bagge and Hampel, 2017; Verdecchia et al., 2018).

Since the recognition that the stress transfer between source and receiver faults may trigger earthquakes (King et al., 1994; Stein, 1999, 2003), static Coulomb stress changes have been routinely calculated after major earthquakes (e.g., Wang and Chen, 2001; Parsons et al., 2008; Wan and Shen, 2010; Serpelloni et al. 2012). In addition, static Coulomb stress changes were used to explain past earthquake sequences (e.g., Nostro et al., 1997; Stein et al., 1997; Hardebeck et al., 1998). Analyses solely based on static Coulomb stress changes neglect, however, that transient processes, as well as interseismic strain accumulation, may considerably affect the magnitude and distribution of Coulomb stress changes on receiver faults during the postseismic phase (e.g., Cocco et al., 2000; Freed and Lin, 2001; Pollitz and Sacks, 2002; Masterlark and Wang, 2002; Cianetti et al., 2005; Verdecchia et al., 2018; Bagge et al., 2017, 2019). So far, studies that consider transient processes in Coulomb stress calculations typically account either for poroelastic effects (e.g., Albano et al. 2017, 2018; Nespoli et al., 2018; Tung et al., 2018a; Miao et al., 2021) or viscoelastic relaxation (e.g., Luo and Lui, 2010; Verdecchia et al., 2018; Bagge et al., 2019), based on the assumption that the two processes act on sufficiently different temporal and spatial scales. Only a limited number of studies has considered transient Coulomb stress changes arising from both poroelastic and viscoelastic effects (Freed and Lin, 2001; Masterlark and Wang, 2002; Barbot and Fialko, 2010; Tung and Masterlark, 2018).

The validity of the assumption that poroelastic effects and viscoelastic relaxation act on different timescales has been challenged by inversions of geodetic data from intra-continental earthquakes and numerical models, which showed that viscoelastic relaxation may already occur in the early postseismic phase (e.g., Ryder et al., 2007, 2010; Barbot and Fialko, 2010; Hampel and Hetzel, 2015; Bagge and Hampel, 2017; Mandler et al., 2021) and hence on the timescale of poroelastic effects (Dempsey et al., 2013; Albano et al. 2017, 2019; Tung et al., 2018a). This temporal overlapping of poroelastic and viscoelastic effects is reflected in the postseismic velocity and stress fields (Peikert et al., 2022) but the consequences for Coulomb stress changes on receiver faults have not been systematically studied so far.

Here, we use 3D finite-element models with a generalized setup of intra-continental normal and thrust fault arrays to gain insights into Coulomb stress change patterns arising from coseismic slip, poroelastic effects, postseismic viscoelastic relaxation and interseismic stress accumulation. Due to this implementation of transient and non-transient processes in the

models, we are able to evaluate their relative importance for the magnitude and distribution of the Coulomb stress changes on the receiver faults in the model fault array. We investigate the spatial and temporal scales of poroelastic and viscoelastic effects and the resulting impact on the Coulomb stress changes by conducting experiments with variable permeability and viscosity structure of the crust and the lithospheric mantle.

3.2 Setup of the 3D finite-element models

3.2.1 Principal model setup

In this study, we use 3D finite-element models created with the commercial software ABAQUS (version 2018). All models consist of a 200 x 200 km wide and 100 km thick lithosphere, which is subdivided into an elastic upper crust, a viscoelastic lower crust and a viscoelastic lithospheric mantle. The principal model setup of the normal and thrust fault reference models including the elastic parameters (Poisson's ratio v, Young's modulus E), density ρ, viscosity η and permeability K of the layers are shown in Figure 3.1. Viscoelastic behavior is implemented as linear, temperature-independent Maxwell viscoelasticity. The viscosity values applied in our models (Figure 3.1, Table 3.1) reflect the range of viscosity estimates of continental lithosphere (Kaufmann and Amelung, 2000; Nishimura and Thatcher, 2003; Gourmelen and Amelung, 2005; Burov and Watts, 2006; Klemperer, 2006; England et al., 2013; Ryder et al., 2014; Shi et al., 2015 Henriquet et al., 2019).

The permeability enters ABAQUS as the hydraulic conductivity k that can be calculated from $k = K * \rho_{fluid} * g / \eta_{fluid}$ (ρ_{fluid}: fluid density, 1000 kg/m^3; acceleration due to gravity, 9.81 m/s^2; η_{fluid}: fluid viscosity, 998 x 10^{-6} kg m^{-1} s^{-1}). For the upper and lower crust, we use permeabilities in the range of values derived for the upper and lower crust, respectively (Figure 3.1, Table 3.1) (Manning and Ingebritsen, 1999; Ingebritsen and Manning, 2010; Stober and Bucher, 2015). For the lithospheric mantle, we apply a permeability of 10^{-35} m^2 to simulate an impermeable layer (Tung et al., 2018a). The initial pore pressure distribution in the models is hydrostatic; as a boundary condition, a pore pressure (P_{pore}) of 9.8 x 10^8 Pa is applied at the model bottom. We simulate the coupling between solid and fluid phase by applying the coupled pore fluid diffusion/stress analysis in ABAQUS (ABAQUS Documentation 2018). To specify the proportion between volumes of voids and solids in the medium and the volume of fluid trapped in the medium, ABAQUS uses the void ratio, which is a few percent for crystalline basement rocks (e.g., Masterlark and Wang, 2002; Masterlark et al., 2003). In our models, we use a void
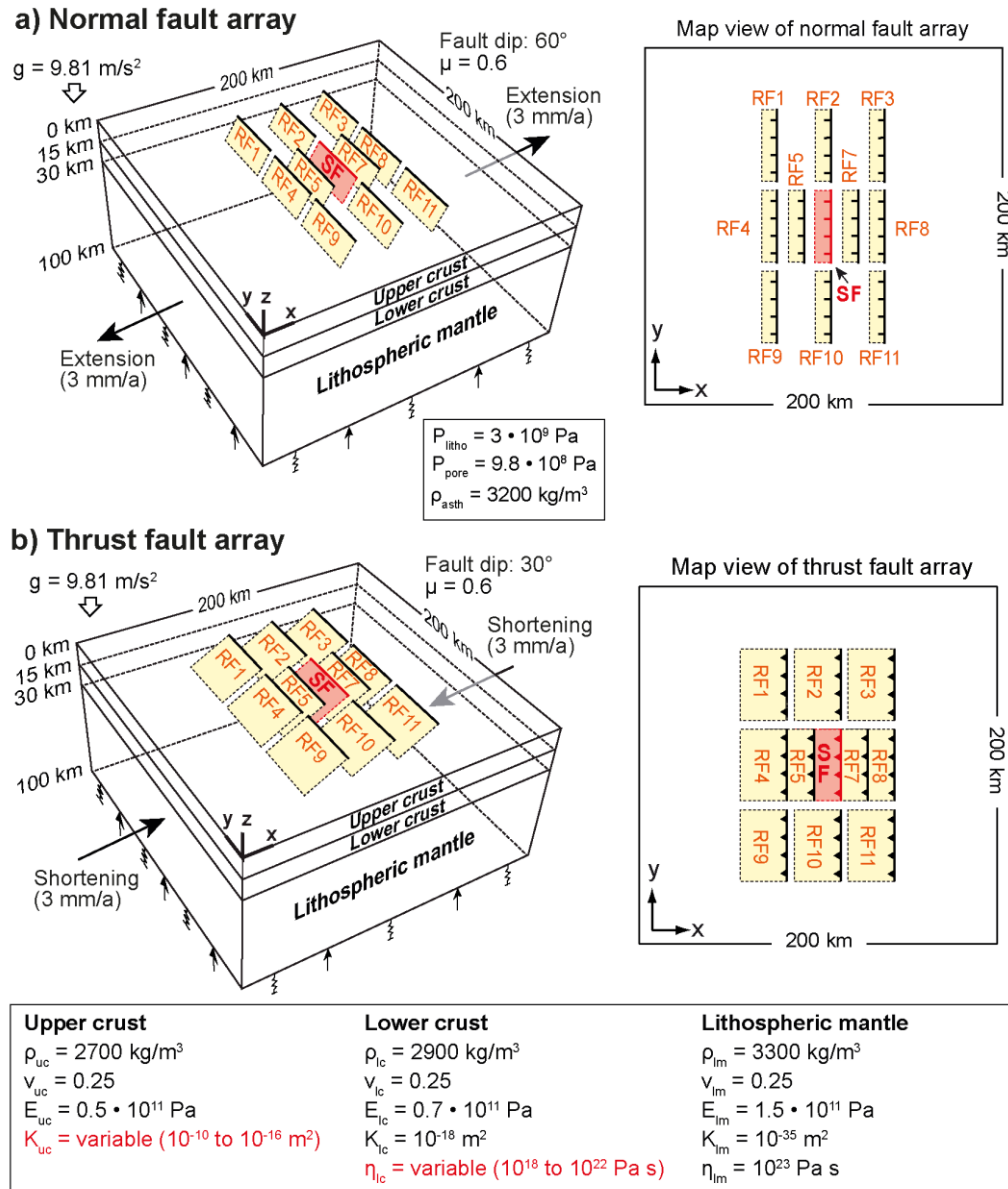
Figure 3.1: Principal setup of the 3D finite-element models with an array of a) normal faults and b) thrust faults. Abbreviations are SF source fault and RF receiver fault. The rheological parameters are ρ density, E Young's modulus, ν Poisson's ratio, η viscosity, μ friction coefficient and K permeability. Indices uc, lc and lm refer to upper crust, lower crust and lithospheric mantle, respectively.

ratio of 0.06 and a saturation of 1. No pore fluid flow will occur across the model boundaries and the fault is treated as impermeable, i.e. fluid cannot flow across it (cf. Rudnicki, 1986; Dempsey et al., 2013; Albano et al., 2017, 2019; Peikert et al., 2022). Gravity is included in all models as a body force. Isostatic effects are implemented by adding a lithostatic pressure (P_{litho}) of 3×10^9 Pa and an elastic foundation to the model bottom (cf. Hampel et al., 2019). The property of the elastic foundation represents an asthenosphere with a density of 3200 kg/m^3. The model bottom is free to move in vertical and horizontal directions; model sides in the xz-plane are fixed in the y-direction. By applying a velocity boundary condition to the model sides

in the yz-plane, the model domain is either extended or shortened to simulate the interseismic strain accumulation.

In the model center, a source fault (SF), which experiences the coseismic slip during the analysis, and ten surrounding receiver faults are embedded in the upper crust as frictional contact interfaces between footwall and hanging wall of each fault (Figure 3.1). All faults are 40 km long and extend from the top to the bottom of the upper crust. A dip of 60° and 30° is used for normal and thrust faults, respectively. The positions of the receiver faults with respect to the source fault have been chosen to capture the postseismic Coulomb stress changes in the surrounding of the source fault: four receiver faults are located in the footwall and hanging wall of the source fault (RF4, RF5, RF7, RF8), two faults are located along-strike of the source fault's tips (RF2, RF10), and four other faults are located outside of the immediate hanging wall and footwall of the source fault (RF1, RF3, RF9, RF11). We apply distances between the faults of $\geq$15 km in the x-direction and $\geq$5 km in the y-direction, following natural spatial configurations of faults, for example, in the Basin and Range Province (Wesnousky et al., 2005), the Aegean region (Roberts and Michetti, 2004) and the foreland of the Tibetan Plateau (Meyer et al., 1998; Hetzel et al., 2004). Slip on the model faults is initiated by extending or shortening the model domain at a total rate of 6 mm/a and controlled by a Mohr-Coulomb criterion $|\tau_{max}| = c + \mu \, \sigma_n$, where τ_{max} is the shear stress, c is cohesion (zero in the models), μ is the friction coefficient (0.6 in the models) and σ_n is the normal stress. Note that although the fault planes are pre-defined with a rectangular shape, the spatial slip distribution on the fault plane is not prescribed and develops freely in response to the extension or shortening of the model.

3.2.2 Model phases

Each model run consists of three model phases. In the first model phase, viscoelastic behavior and pore fluid flow are activated and lithostatic and hydrostatic pressure distributions as well as isostatic equilibrium are established in the model. During the second model phase, slip on the faults is initiated by extension or shortening of the model in the x-direction (Figure 3.1). The faults are unlocked and allowed to accumulate slip until they reach a constant slip rate, depending primarily on the fault dip and the viscosity structure of the lithosphere (cf. Hampel et al., 2010; Bagge and Hampel, 2017; Peikert et al., 2022). Once all faults achieved a constant slip rate, the earthquake cycle is simulated in the third model phase, which comprises the preseismic, coseismic and postseismic phases. In the preseismic phase, all faults are locked and

slip accumulation stops, while the extension or shortening of the model continues. At the beginning of the coseismic phase, the source fault (fault 6) is unlocked, which causes a sudden slip (= model earthquake). All receiver faults remain locked during the coseismic phase. The coseismic slip on the source fault is controlled by the applied far-field extension or shortening rate, the rheological properties of the model and the length of the preseismic phase (cf. Hampel and Hetzel, 2012). In this study, we have chosen a duration of the preseismic phase such that the fault experiences a maximum coseismic slip of 2 m (Figure 3.2a), which represents a typical value of an Mw ≈ 7 earthquake on a 40-km-long fault (Wells and Coppersmith, 1994). During the postseismic phase, all faults including the source fault are locked again, while extension or shortening continues to simulate interseismic strain accumulation.

3.2.3 Coseismic displacement and Coulomb stress changes

Figure 3.2 illustrates the model state at the end of the coseismic phase (cf. Hampel et al., 2013; Bagge and Hampel, 2016, 2017). Note that the coseismic slip, surface displacements and Coulomb stress changes are similar in all models of our study (Table 3.1) because the coseismic deformation does not depend on the permeability of the crust or the viscosity structure of the lithosphere. In all models, the source fault experiences a total coseismic slip of ~2 m (Figure 3.2a). The vertical surface displacements show coseismic footwall uplift and hanging wall subsidence in the normal fault model and primarily hanging wall uplift in the thrust fault model (Figure 3.2b), in accordance with geological and geodetical observations from normal and thrust fault earthquakes in nature (e.g., Yu et al., 2001; Chen et al., 2006; Lin et al., 2009; Liu-Zeng et al., 2009; Cheloni et al., 2010; Yu et al., 2010; Serpelloni et al., 2012). The horizontal displacement fields in the x-direction indicate surface movements away from the normal fault and toward the thrust fault (Figure 3.2b), which implies extension and shortening across the normal and thrust source faults, respectively. Within the footwall of the normal fault, shortening occurs because the magnitude of the horizontal displacements in the positive x-direction decreases with distance from the source fault (cf. Hampel and Hetzel, 2015; Peikert et al., 2022). In contrast, the direction and magnitude of the horizontal movements in the thrust fault model are such that extension occurs within the hanging wall and footwall (cf. Hampel and Hetzel, 2015; Peikert et al., 2022). Both, coseismic shortening in normal fault footwalls and coseismic extension near thrust faults are in accordance with geological and geodetic observations from natural earthquakes (e.g., Slemmons, 1957; Myers and Hamilton, 1964; King and Vita-Finzi, 1981; Philip and Meghraoui, 1983; Crone et al., 1987; Meghraoui et al., 1988; Yu et al., 2001;

Chen et al., 2006; Lin et al., 2009; Liu-Zeng et al., 2009; Cheloni et al., 2010; Yu et al., 2010; Serpelloni et al., 2012). Figure 3.2c shows the distribution of the coseismic Coulomb stress changes on the source and receiver faults in our models (cf. Bagge and Hampel, 2016). For our model earthquake with a coseismic slip of ~2 m and a magnitude of $M_w \approx 7$, the coseismic stress drop is on the order of 20-30 MPa and hence within the range of coseismic stress drop derived for natural intra-plate earthquakes (Kanamori and Anderson, 1975; Hanks, 1977; Scholz, 2002). In both, the normal and thrust fault models, the receiver faults located in footwall and hanging wall of the source fault mostly show negative Coulomb stress changes (RF4, RF5, RF7, RF8). The largest positive Coulomb stress changes are obtained for receiver faults RF2 and RF10, which are located along strike of the source fault tips, as well as on RF5 located in the hanging wall of the source fault. Mixed patterns of positive and negative stress changes occur on receiver faults RF1, RF3, RF9 and RF11.
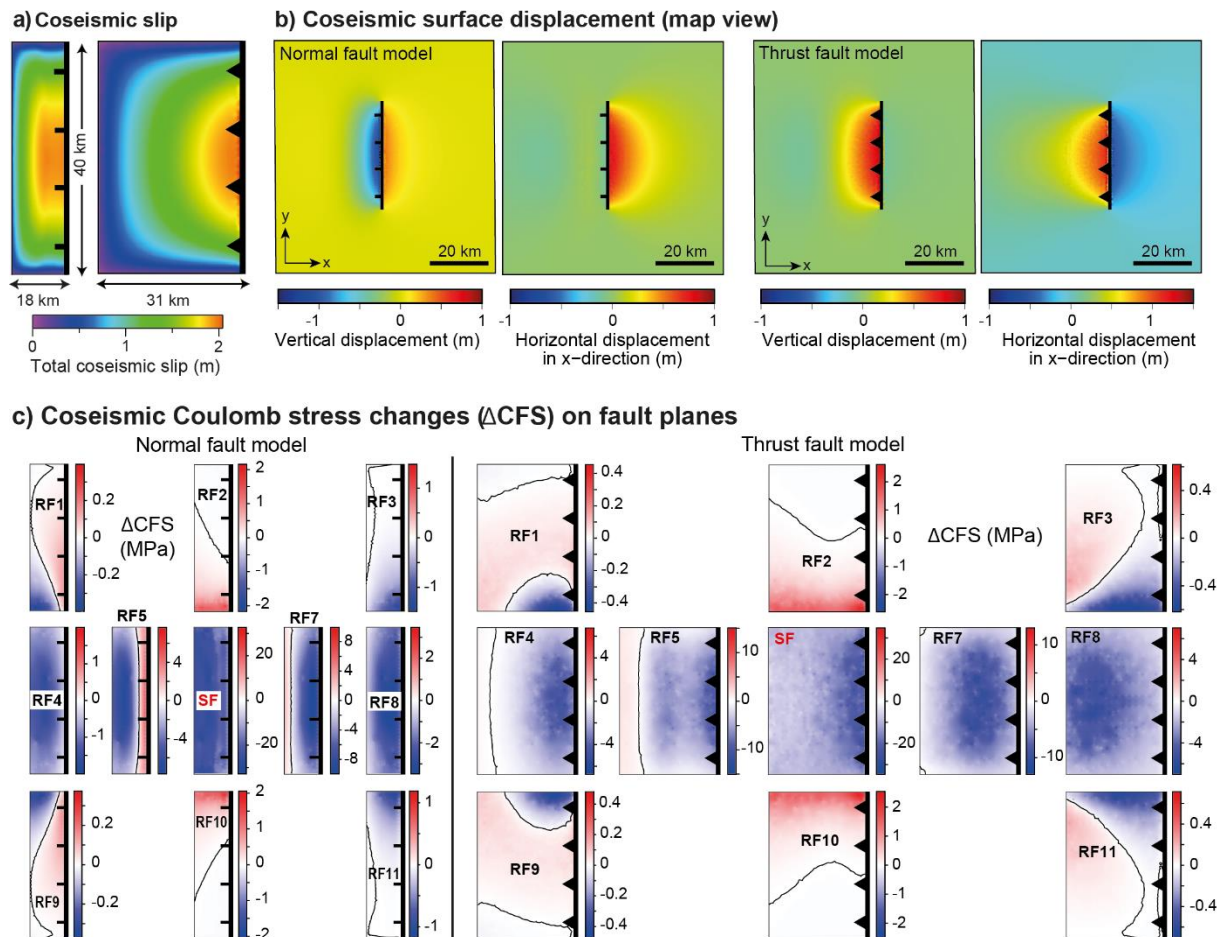
Figure 3.2: Model state at the end of the coseismic phase (cf. Hampel et al. 2013; Bagge and 1178 Hampel, 2016). a) Coseismic total slip on the fault. b) Coseismic surface displacement in vertical and x-direction. c) Coseismic (=static) Coulomb stress changes. The type of model fault is indicated by ticks (normal faults) and black triangles (thrust faults) pointing toward hanging wall. Slip, surface displacements and Coulomb stress changes are extracted from reference models RF1nf and RF1tf but representative also for all other models (Table 3.1).

71

3.2.4 Experiments conducted for parameter study

For our parameter study, we defined three reference models for each fault array (Table 3.1). Reference models $R1_{nf}$ (normal fault array) and $R1_{tf}$ (thrust fault array) include both poroelastic effects and viscoelastic relaxation. The second type of reference models ($R2_{nf}$, $R2_{tf}$) considers poroelastic effects but no viscoelastic relaxation during the postseismic phase. Models $R3_{nf}$ and $R3_{tf}$ include postseismic viscoelastic relaxation but no poroelastic effects. For our sensitivity analyses, we first performed a series of experiments, in which we varied one parameter a time, i.e. we varied either the permeability of the upper crust ($P1-3_{nf}$, $P1-3_{tf}$) or the viscosity of the lower crust ($V1-2_{nf}$, $V1-2_{tf}$) (Table 3.1). The second set of experiments consists of four endmember configurations, for which we combined high and low permeability and viscosity values, respectively (Table 3.1; $PV1-4_{nf}$; $PV1-4_{tf}$).

Table 3.1. Overview of experiments presented in this study

Model name[a]	Permeability of upper crust k_{uc} (m^2)	Permeability of lower crust k_{lc} (m^2)	Viscosity of lower crust η_{lc} (Pa s)	Viscosity of lithospheric mantle η_{lm} (Pa s)	Results shown in figures
Reference models					
$R1_{nf}$, $R1_{tf}$	10^{-12}	10^{-18}	10^{20}	10^{23}	3, 4, 5, 6, 7, 10
$R2_{nf}$, $R2_{tf}$	10^{-12}	10^{-18}	-	-	3, 4, 5, 6, 8, 10
$R3_{nf}$, $R3_{tf}$	-	-	10^{20}	10^{23}	3, 4, 5, 6, 9, 10
Models with variable permeability					
$P1_{nf}$, $P1_{tf}$	10^{-10}	10^{-18}	10^{20}	10^{23}	11, 14, 17
$P2_{nf}$, $P2_{tf}$	10^{-14}	10^{-18}	10^{20}	10^{23}	12, 15, 17
$P3_{nf}$, $P3_{tf}$	10^{-16}	10^{-18}	10^{20}	10^{23}	13, 16, 17
Models with variable viscosity					
$V1_{nf}$, $V1_{tf}$	10^{-12}	10^{-18}	10^{18}	10^{23}	18, 20, 22
$V2_{nf}$, $V2_{tf}$	10^{-12}	10^{-18}	10^{22}	10^{23}	19 21, 22
Endmember models with variable permeability and viscosity					
$PV1_{nf}$, $PV1_{tf}$	10^{-11}	10^{-18}	10^{18}	10^{23}	23, 27
$PV2_{nf}$, $PV2_{tf}$	10^{-16}	10^{-18}	10^{18}	10^{23}	24, 28
$PV3_{nf}$, $PV3_{tf}$	10^{-11}	10^{-18}	10^{22}	10^{23}	25, 29
$PV4_{nf}$, $PV4_{tf}$	10^{-16}	10^{-18}	10^{22}	10^{23}	26, 30

[a] Subscripts nf and tf refer to normal fault and thrust fault, respectively.

3.3 Results

In the following section, the postseismic Coulomb stress changes for the different normal and thrust fault models are shown for different time points between the first months and 50th year after the earthquake. First, we present the results for the normal and thrust fault reference models (R1-3$_{nf}$, R1-3$_{tf}$) in Figures 3.3-3.6 and Figures 3.7-3.10, respectively. Afterwards, we show the results from models with variable permeability (Figures 3.11-3.17), variable viscosity (Figures 3.18-3.22) and endmember configurations (Figures 3.23-3.30).

3.3.1 Reference models

In the first month after the earthquake, most normal and thrust faults show Coulomb stress change patterns that are inverse to the coseismic (static) stress changes, i.e. areas with positive coseismic stress changes now show negative stress changes and *vice versa*. In the normal fault model R1$_{nf}$ with both poroelastic and viscoelastic effects (Figures 3.3a-3.5a), most faults exhibit positive Coulomb stress changes with values of 7 MPa on the source fault and 0.15 MPa (RF1 and RF9) to 2.5 MPa (RF7) on the receiver faults. A mixed pattern of positive and negative stress changes occurs on the receiver faults closest to the source fault (RF2, RF5, RF7 and RF10). In the thrust fault model R1$_{tf}$ (Figure 3.7), all faults, except RF3 and RF11, show positive as well as negative Coulomb stress changes along the lower part of the fault of up to 9 MPa on the source fault and 0.25 MPa (RF3 and RF11) to 4 MPa (RF5) on the receiver faults. In the following months, the magnitude of Coulomb stress changes decreases on all faults. In the second month, all normal faults, except RF1, RF4 and RF9 in the hanging wall, and all thrust faults experience a stress decrease along the upper and/or lower part of the fault. In both models, the areas with negative stress changes shifted their position on the fault plane to the upper part of the fault or to the outer edges (RF2 and RF10) in the third month, the source faults show solely positive stress changes of 0.2 MPa. Notably, RF5 shows a higher magnitude of stress changes than the source fault in both, normal and thrust fault models, of 0.3 MPa and 0.4 MPa, respectively. In the sixth month, the receiver faults located in the hanging wall (RF4 and RF5) in the normal fault model and all faults in the hanging wall and footwall (RF4, RF5, RF7, RF8) as well as RF1 and RF9 in the thrust fault model still experience positive and negative Coulomb stress changes. All other faults experience positive stress changes. The stress change pattern of the first year is dominated by the stress change pattern of the first month in the normal fault model, with similar magnitudes on the source fault and the receiver faults on its footwall (RF3, RF7, RF8, RF11) and higher magnitudes on the other receiver faults. In the thrust fault

73

model, the magnitudes of the stress changes are similar to the first month, but the position of negative stress changes on some faults, which experience positive and negative stress changes, is different and located at the upper and/or lower part of the fault plane. In the second year after the earthquake, the Coulomb stress changes decreased by 1-2 orders of magnitude. Most of the normal faults show solely positive stress changes between 0.2 MPa (SF) and 0.025 (RF1, RF9). RF5 still experiences positive and negative Coulomb stress changes of 0.15 MPa. In the thrust fault model, all receiver faults in the hanging wall (RF1, RF4, RF5, RF9) and RF7 and RF8 in the footwall parallel to the source fault still show zones of negative stress changes along the upper part of the fault plane. All other faults are positive with magnitudes between 0.25 MPa on the source fault and 0.025 MPa on RF1, RF3, RF9 and RF11. The highest positive stress changes on the receiver faults are located on RF5 (0.2 MPa). From the fifth year onward, the values of the stress increase on the source fault of the normal and thrust fault models slowly decrease until the 50th year, from 0.2 MPa to 0.1 MPa and 0.1 to 0.07 MPa, respectively. Most of the receiver faults show a homogeneous Coulomb stress distribution with an average stress increase of 0.02 MPa (normal fault) and 0.015 MPa (thrust fault) until the 50th year. On RF4 in the normal fault model, the positive stress changes remain constant at a value of 0.02 MP, but the distribution is not homogeneous and RF5 exhibit positive and negative stress changes by a similar value until the 50th year. In the thrust fault model, all faults located parallel to the source fault in the hanging wall and footwall shows positive and negative stress changes on faults RF4 and RF5 over the years with magnitudes of 0.015 MPa and 0.04 MPa, respectively. On the fault planes of RF7 and RF8 the stress increase is not homogeneous and slowly decreases until the 50th year from 0.05 MPa to 0.04 MPa and 0.04 MPa to 0.03 MPa, respectively.

The normal and thrust fault reference models with poroelastic effects but no viscoelastic relaxation $R2_{nf}$ (Figures 3.3b-3.5b) and $R2_{tf}$ (Figure 3.8) show the same evolution as the reference models with both processes ($R1_{nf,tf}$) with the same pattern and similar stress change magnitudes until the fifth year after the earthquake. From the sixth month onward until the 50th year, a homogeneous stress increase of average 0.02 MPa and 0.015 MPa in the normal and thrust fault model, respectively, can be observed on all receiver faults. The source fault experiences positive stress changes of 0.05 MPa in the normal fault model and 0.1 MPa in the thrust fault model in the fifth year, which decrease to a value of 0.025 MPa and 0.02 MPa in the 50th year.

In models with viscoelastic relaxation but no pore fluid pressure changes ($R3_{nf}$, Figures 3.3c-3.5c and $R3_{tf}$, Figure 3.9), the postseismic Coulomb stress changes are 2-3 orders of magnitude lower than in the reference models with both processes ($R1_{nf,tf}$) already from the first month

onward. In the normal fault model, solely positive Coulomb stress changes occur on all faults in the first six months, except RF5, with constant values of maximum 0.002 MPa. Only RF5 shows positive stress changes in the lower part and negative stress changes in the upper part of the fault plane, which doesn't change until the 50th year. From the first year until the 50th year, the positive stress change pattern and magnitude on all other receiver faults remain constant and homogeneous at a value of 0.02 MPa on all faults. Also the source fault exhibits a stress increase over the years between 0.15 MPa in the first year and 0.08 MPa in the 50th year after the earthquake. RF1, RF2, RF3, RF9, RF10 and RF11 of the thrust fault model show a homogeneous stress increase with a constant value of maximum 0.002 MPa in the first six months and 0.02 MPa from the first to the 50th year after the earthquake. On the source fault, RF7 and RF8 positive stress changes can be observed from the first month onward with a slowly decreasing magnitude over the years. RF4 experiences a zone of negative stress changes in the first months after the earthquake, which turn into positive stress changes in the first year. RF5 shows a mixed pattern of positive and negative stress changes over the years.

Figure 3.6 illustrates the vertical and horizontal velocity fields at the surface of all three normal fault reference models (R1-3$_{nf}$). in the first month, the horizontal velocity field in R1$_{nf}$ and R2$_{nf}$ indicate shortening across the source fault, whereas extension occurs within the hanging wall and footwall, the highest velocities are found around RF5 and RF7. Around the source fault, the surface subsides and shows small areas of uplift at the source fault tips near RF2 and RF10. The maximum velocities range between 500 and 1000 mm/a, in horizontal and vertical directions, respectively. In the following months, the position of the velocity patterns changes such that the shortening in x-direction and subsidence occur across RF5, the hanging wall and footwall still extend by a constant rate of 3 mm/a. The strongest movements in vertical direction can be found around RF5. Until the sixth month, the velocities decrease to 3 mm/a and 4 mm/a in horizontal and vertical direction, respectively. Both models show the same velocity patterns of the first month and in the first year after the earthquake, with velocities of up to 45 mm/a in the horizontal direction and 100 mm/a in the vertical direction. The pattern and the values of the velocity fields of the second year are similar to those of the sixth month. R3$_{nf}$ shows a different evolution. From the first month until the end of the model run, extension occurs across the source fault and the velocity field is only slightly disturbed on both sides around the source fault. Subsidence occurs around RF5 and uplift around the source fault at an average rate of 1 mm/a. From the fifth year onward, the movements in model R1$_{nf}$ and R2$_{nf}$ change directions to extension across the source fault. In contrast to model R2$_{nf}$, in R1$_{nf}$, the footwall near the source fault still shows subsidence, the hanging wall around the source fault uplift and the

horizontal velocity field remains slightly disturbed in the footwall and hanging wall around the source fault, similar to model R3$_{nf}$. The velocity patterns and values remain constant in all three models until the 50th year with velocities up to 3 mm/a in horizontal direction and 0.8 mm/a (R1, R3$_{nf}$) and 0.03 mm/a (R2$_{nf}$) in vertical direction. The horizontal and vertical velocity fields of the thrust fault reference models (R1-3$_{tf}$) in Figure 3.10 evolve similar to the normal fault model, with some small differences. All movements occur in opposite directions, i.e. zones of shortening or uplift in the normal fault model are zones of extension and subsidence in the thrust fault models and *vice versa*. The values and pattern of velocities in the thrust fault models differ only slightly from the normal fault models.

3.3.2 Models with variable permeability

We now varied the permeability of the upper crust while keeping the viscosity of the lower crust constant (Figures 3.11-3.17). In both models with a higher permeability (P1$_{nf,tf}$) (Figures 3.11a, 3.14), the Coulomb stress distribution in the first month and first year after the earthquake resemble the stress distribution of the second month in the reference models (R1$_{nf,tf}$) with mixed patterns of positive and negative stress changes on all faults, except RF1, RF4 and RF9 in the normal fault model and RF8 in the thrust fault model. The magnitudes of the stress changes reach values of 4 MPa on the source fault and up to 2.5 MPa on the receiver faults (RF5) in both models. Already in the second month, the stress changes in P1$_{nf}$ and P1$_{tf}$ decrease by two orders of magnitude and the pattern resembles the Coulomb stress pattern of R1$_{nf}$ and R1$_{tf}$ in the second year, in which only RF5 of the normal fault model and RF1, RF4, RF5, RF7, RF8 and RF9 of the thrust fault model show zones of negative stress changes. In the thrust fault model, these zones turned into zones of stress increase in the third month, and new zones of negative stress changes appear on the lower part of RF4 and RF5. From the second year onward up to the 50th year, both models evolve similarly to R1$_{nf,tf}$ from the fifth year. The receiver faults of the normal fault model show an average stress increase of 0.02 MPa over the years and a homogeneous Coulomb stress distribution, except RF4, RF5 and the source fault. On RF5, a second zone of negative stress changes appear at the lower part of the fault plane in the fifth year until the 20th year and the upper part of RF5 remains negative until the end of the time period. In the thrust fault model, RF1-3 and RF9-11 experience a homogenous stress increase of up to 0.02 MPa, which remains constant over the following years. RF4 and RF5 still show a negative stress zone in the lower part of the fault planes, which disappears in the 20th year on RF4 and becomes smaller on RF5 over the decades.
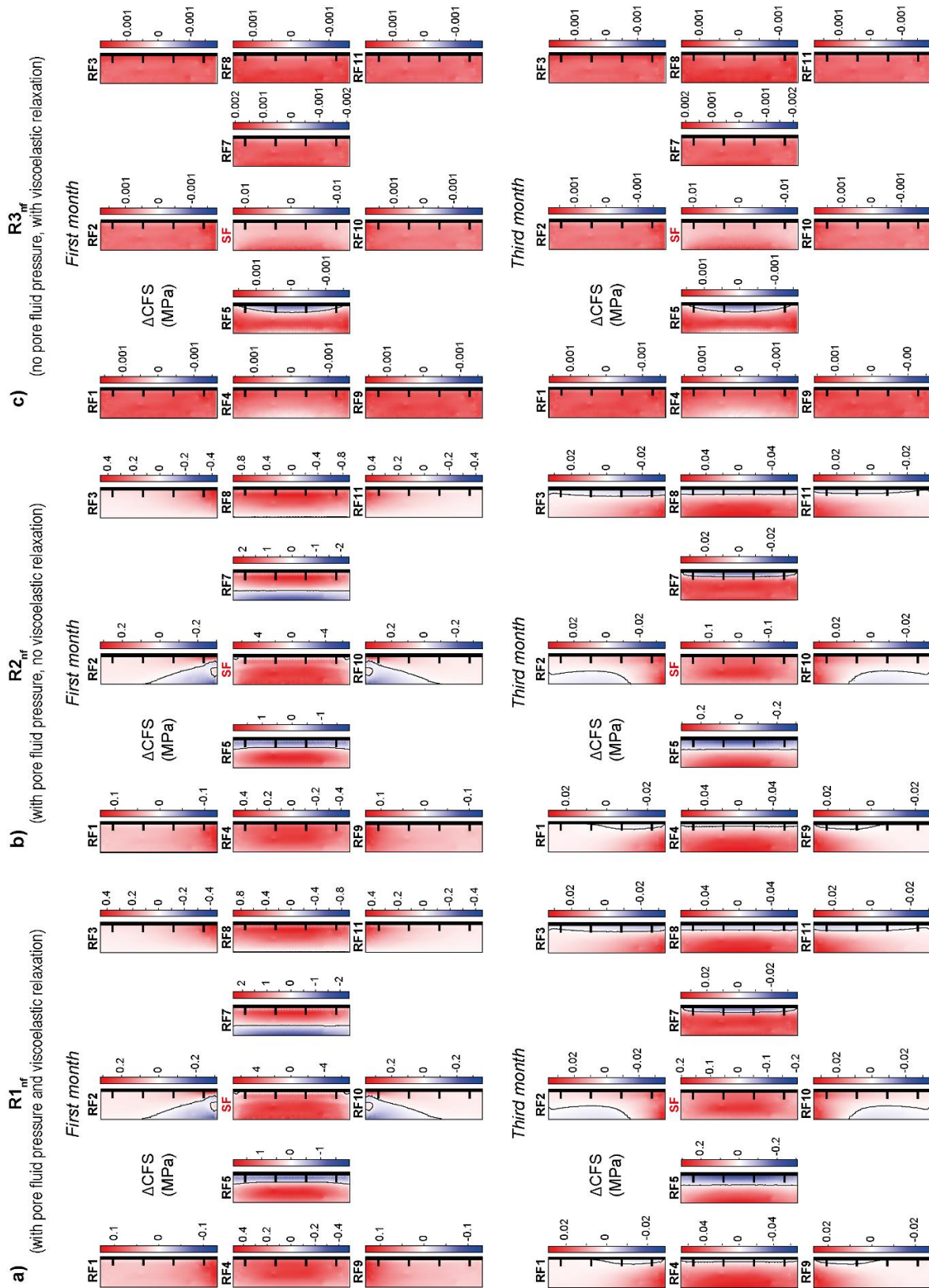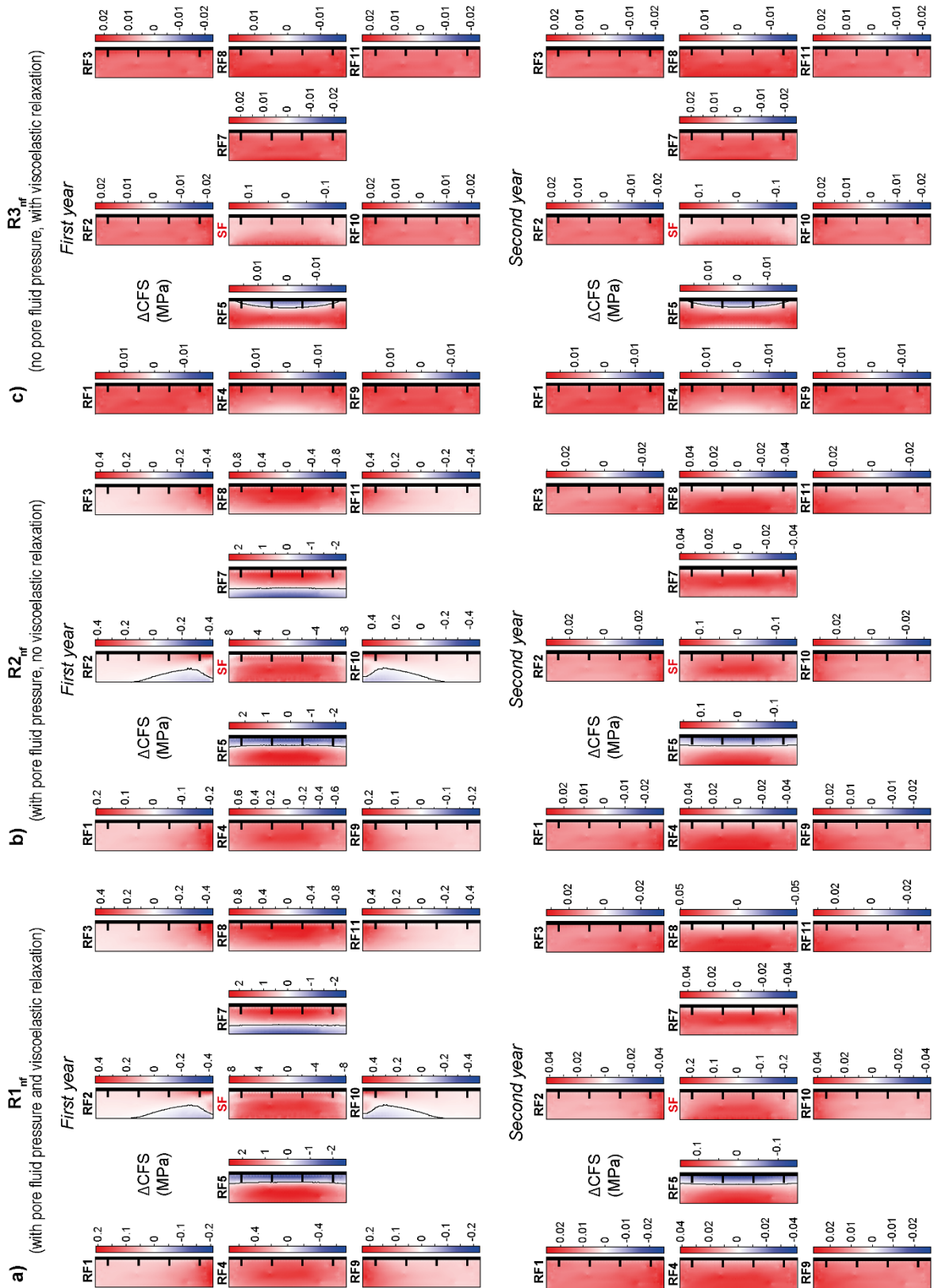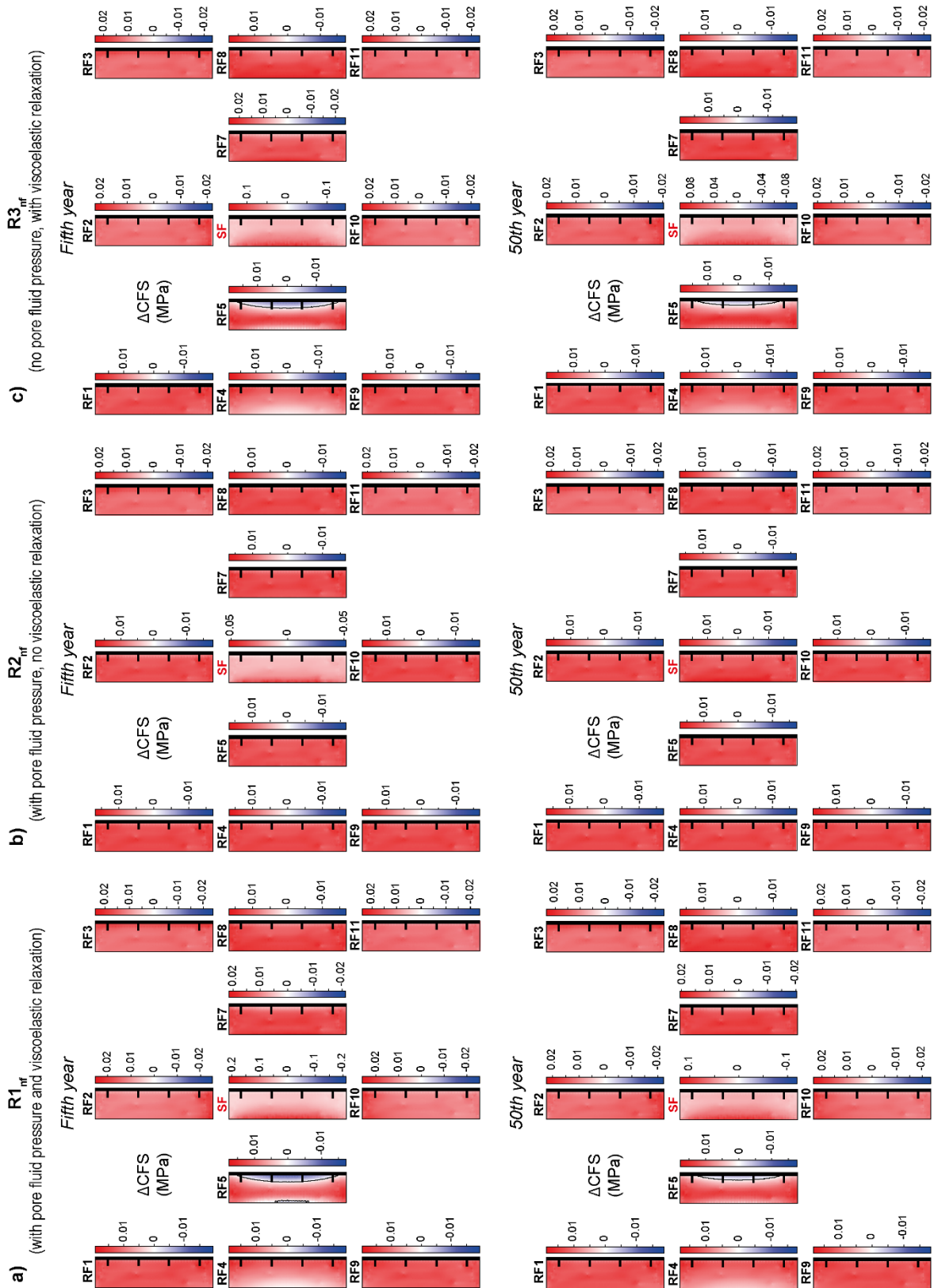
Figure 3.3: Postseismic Coulomb stress changes for the first and third month from the normal fault reference models a) with pore fluid pressure changes and viscoelastic relaxation (R1$_{nf}$), b) with pore fluid pressure changes but without viscoelastic relaxation (R2$_{nf}$) and c) with viscoelastic relaxation but without pore fluid pressure changes (R3$_{nf}$). Distances between faults in fault array are not to scale (Model stages selected from interactive Figure 3 from Peikert et al., Geosphere, in review).
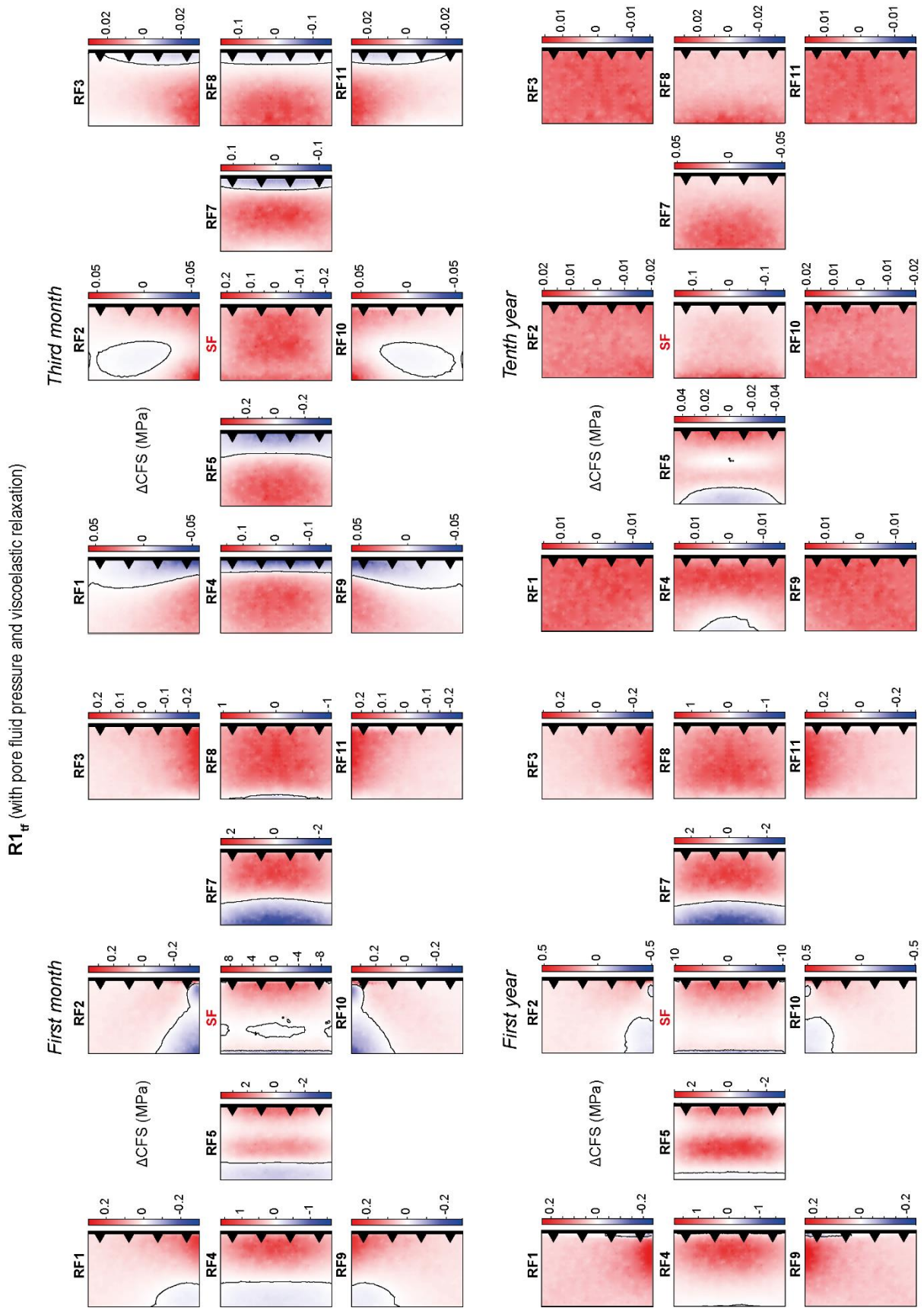
Figure 3.4: Postseismic Coulomb stress changes for the first and second year from the normal fault reference models a) with pore fluid pressure changes and viscoelastic relaxation (R1$_{nf}$), b) with pore fluid pressure changes but without viscoelastic relaxation (R2$_{nf}$) and c) with viscoelastic relaxation but without pore fluid pressure changes (R3$_{nf}$). Distances between faults in fault array are not to scale. (Model stages selected from interactive Figure 3 from Peikert et al., Geosphere, in review).
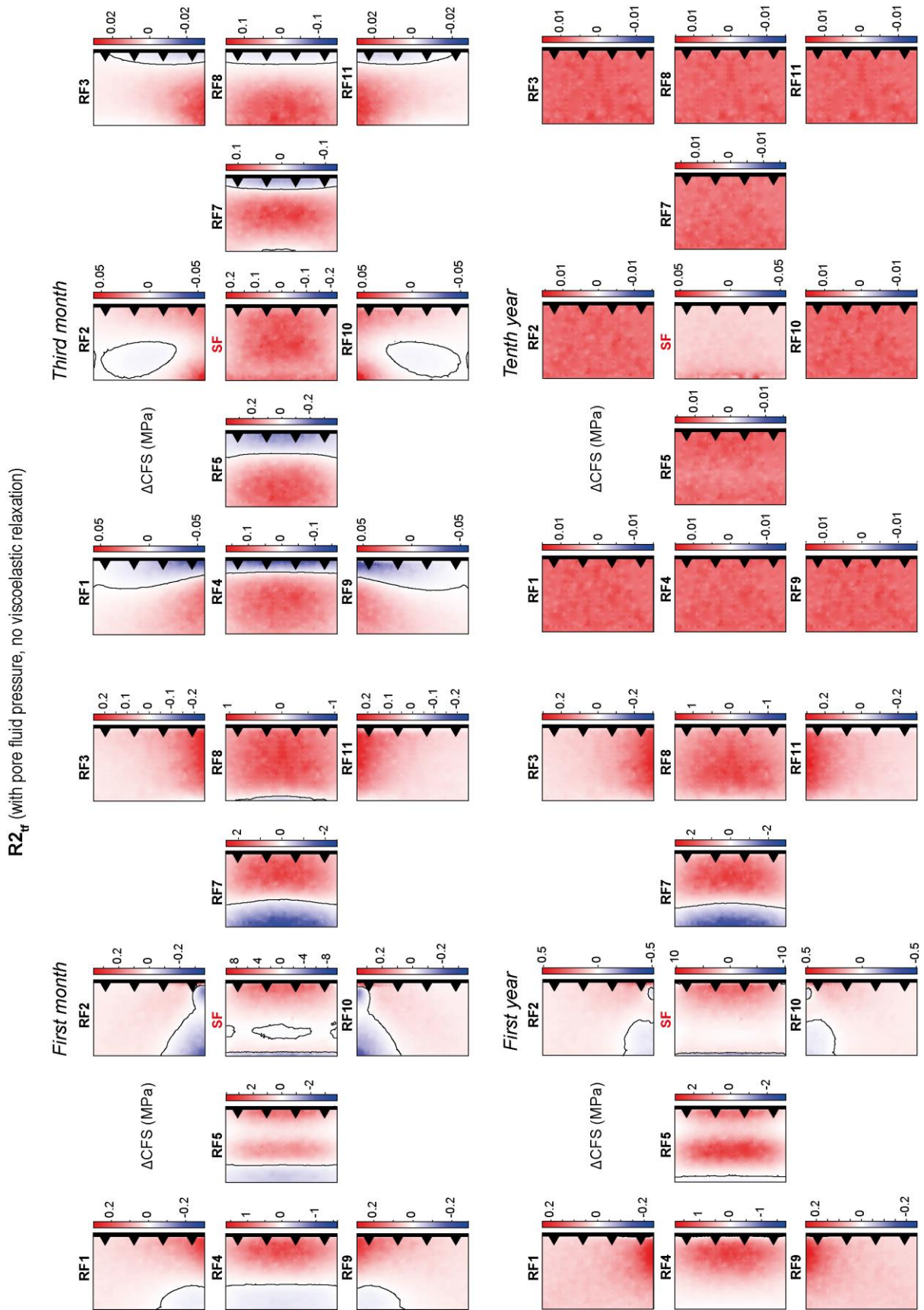
Figure 3.5: Postseismic Coulomb stress changes for the fifth and 50th year from the normal fault reference models a) with pore fluid pressure changes and viscoelastic relaxation (R1$_{nf}$), b) with pore fluid pressure changes but without viscoelastic relaxation (R2$_{nf}$) and c) with viscoelastic relaxation but without pore fluid pressure changes (R3$_{nf}$). Distances between faults in fault array are not to scale. (Model stages selected from interactive Figure 3 from Peikert et al., Geosphere, in review).
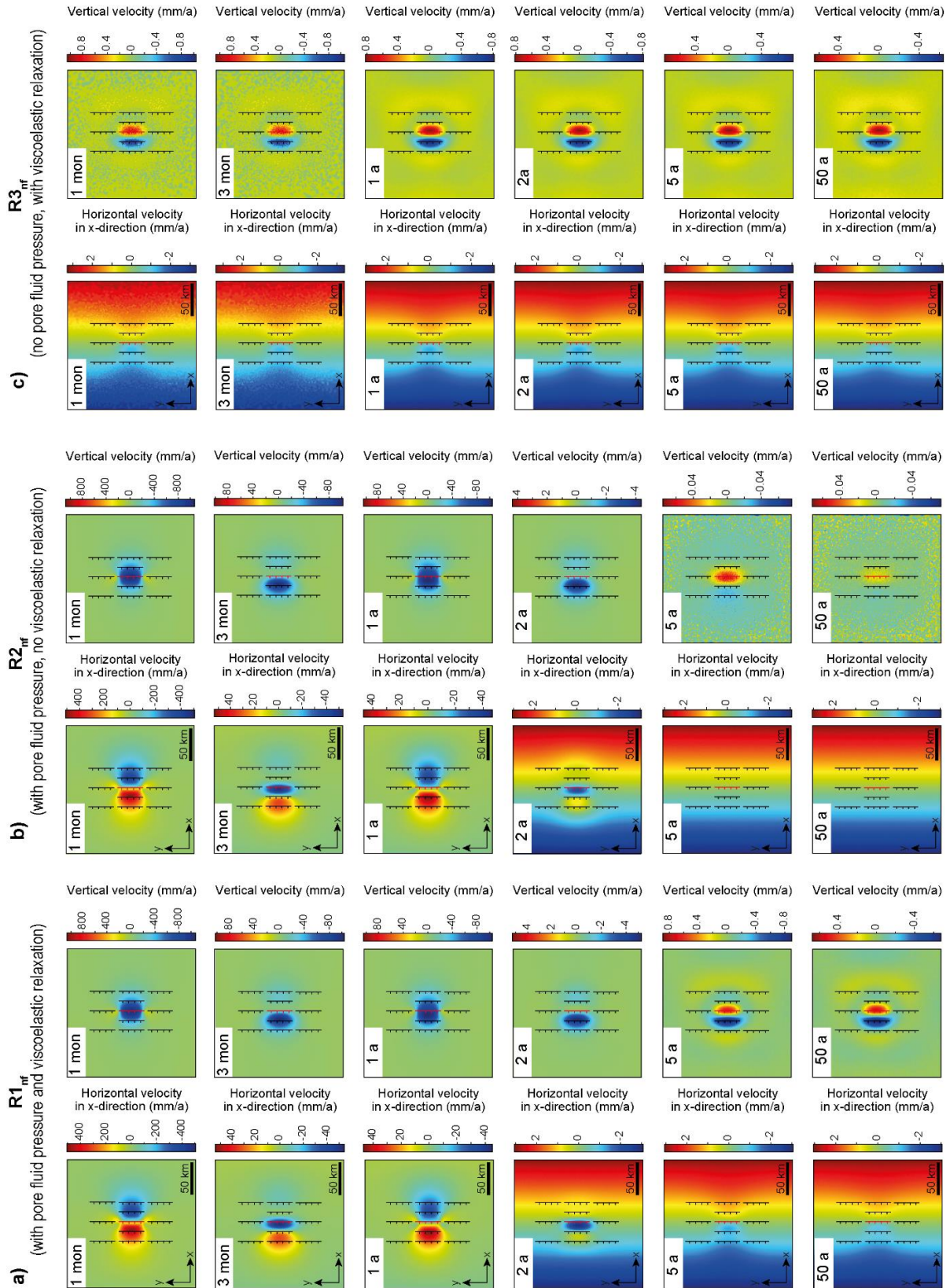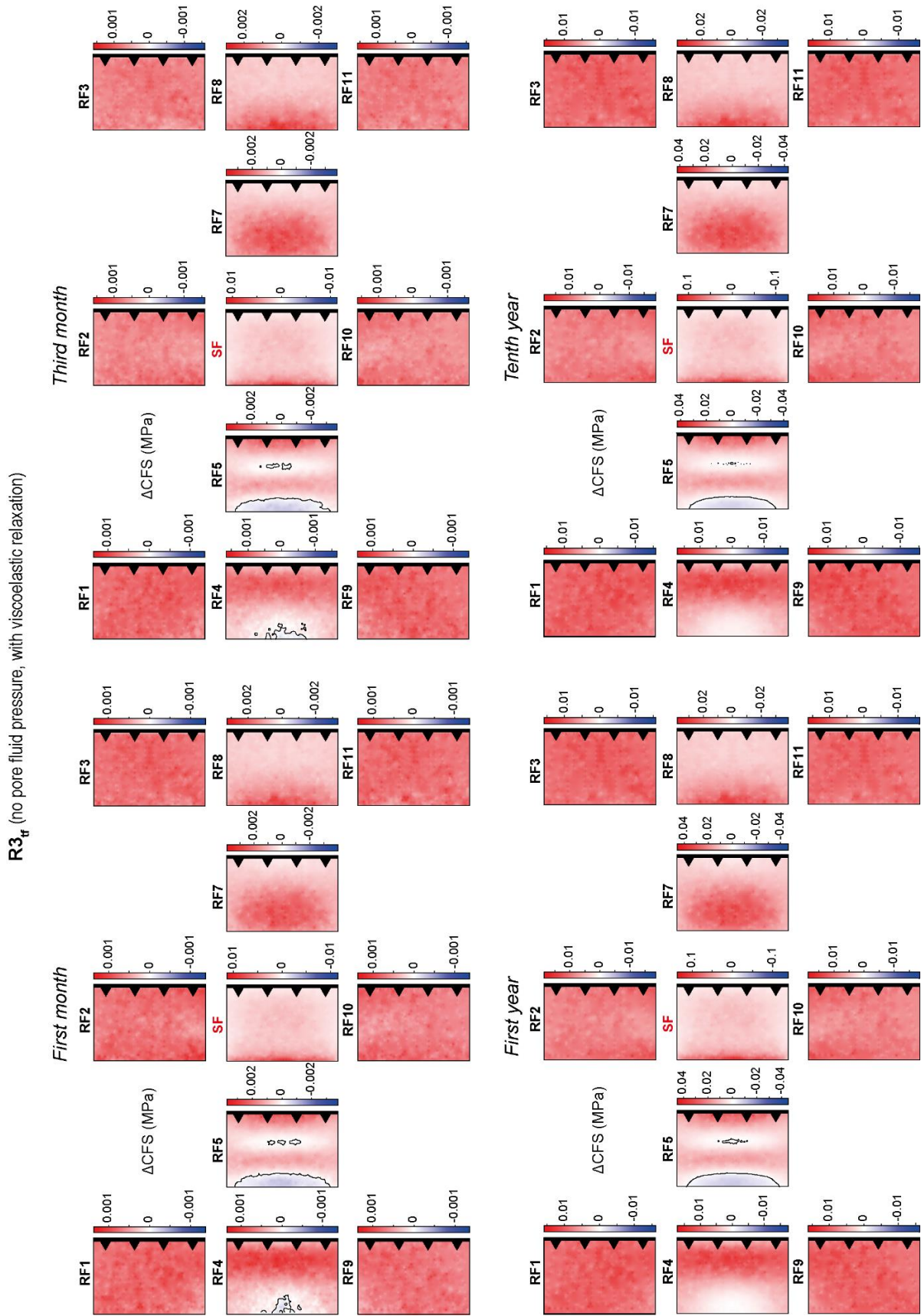
Figure 3.6: Horizontal velocity field in the x-direction and vertical velocity from the normal fault reference models a) with pore fluid pressure changes and viscoelastic relaxation (R1_{nf}), b) with pore fluid pressure changes but without viscoelastic relaxation (R2_{nf}) and c) with viscoelastic relaxation but without pore fluid pressure changes (R3_{nf}). Distances between faults in fault array are not to scale. (Model stages selected from interactive Figure 3 from Peikert et al., Geosphere, in review).
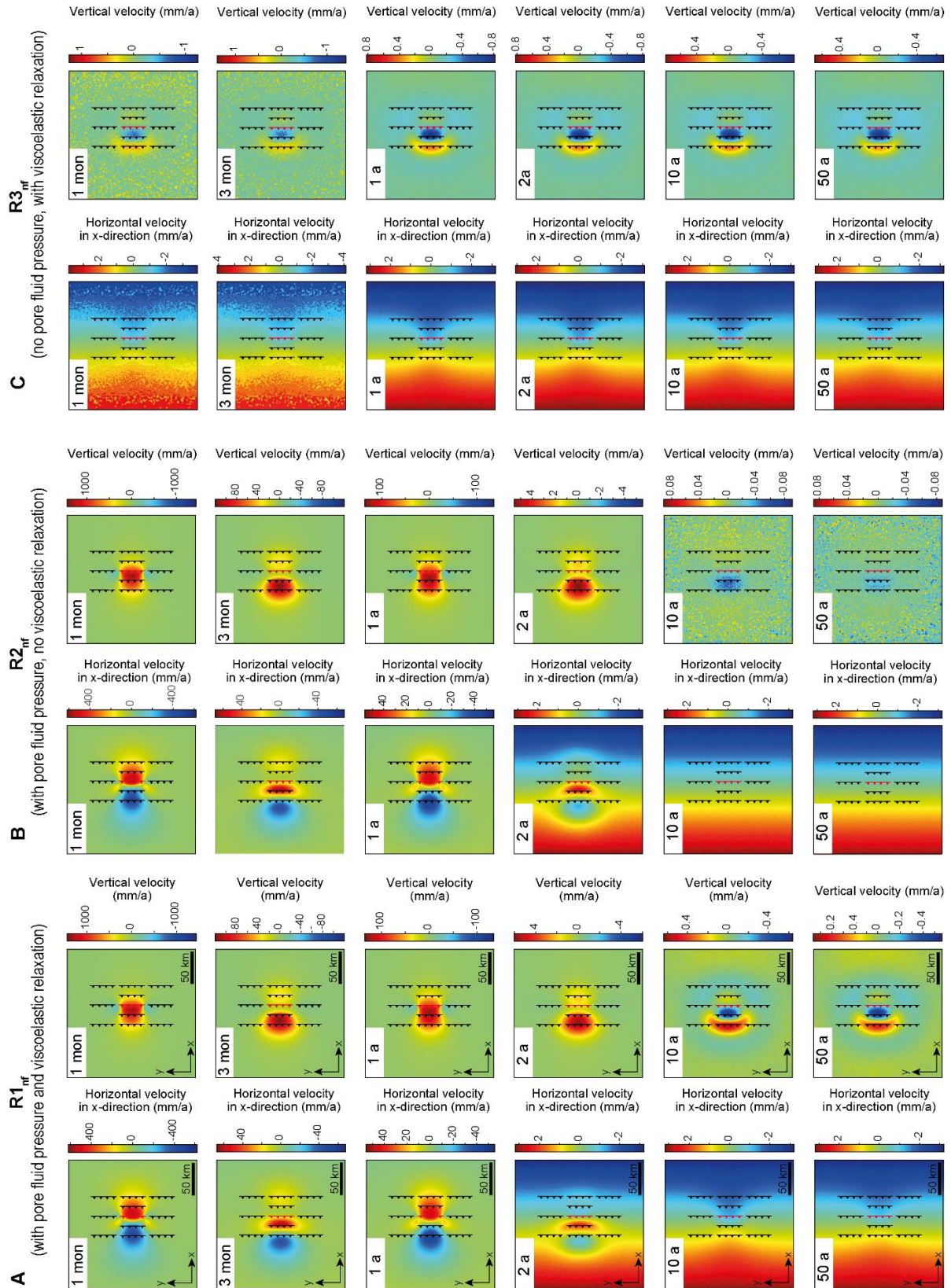
80

Figure 3.7: Postseismic Coulomb stress changes from the thrust fault reference model with pore fluid pressure changes and viscoelastic relaxation (R1$_{nf}$). Distances between faults in fault array are not to scale. (Model stages selected from interactive Figure 4 from Peikert et al., Geosphere, in review).

Figure 3.8: Postseismic Coulomb stress changes from the thrust fault reference model with pore fluid pressure changes but without viscoelastic relaxation (R2$_{nf}$). Distances between faults in fault array are not to scale. (Model stages selected from interactive Figure 4 from Peikert et al., Geosphere, in review).

82

Figure 3.9: Postseismic Coulomb stress changes from the thrust fault reference model with viscoelastic relaxation but without pore fluid pressure changes (R3_nf). Distances between faults in fault array are not to scale. (Model stages selected from interactive Figure 4 from Peikert et al., Geosphere, in review).

Figure 3.10: Horizontal velocity field in the x-direction and vertical velocity from the thrust fault reference models a) with pore fluid pressure changes and viscoelastic relaxation (R1$_{tf}$), b) with pore fluid pressure changes but without viscoelastic relaxation (R2$_{tf}$) and c) with viscoelastic relaxation but without pore fluid pressure changes (R3$_{tf}$). Distances between faults in fault array are not to scale. (Model stages selected from interactive Figure 4 from Peikert et al., Geosphere, in review).
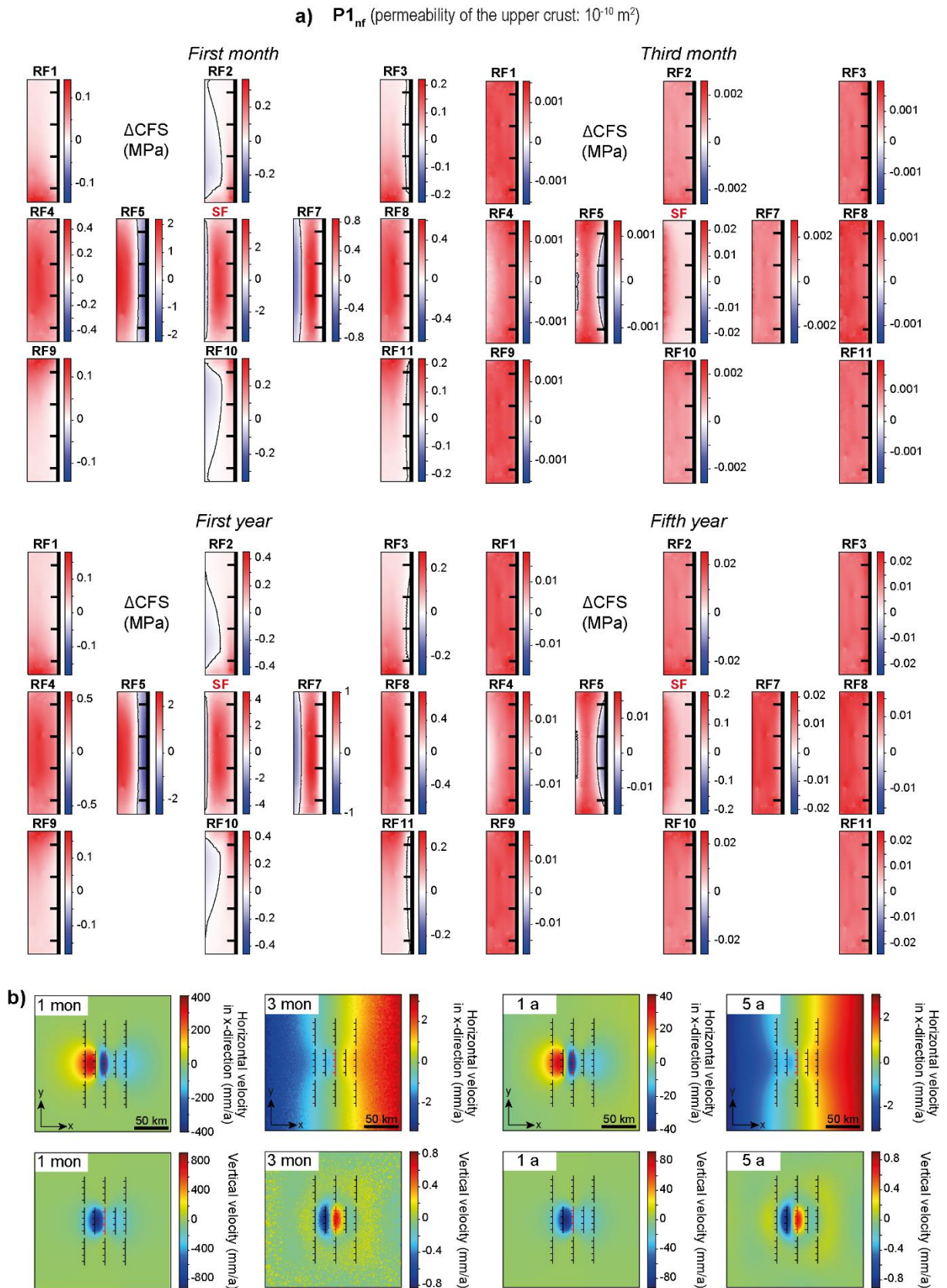
Figure 3.11: Normal fault model with a lower permeability $P1_{nf}$ 10^{-10} m^2 for the upper crust than in the reference model. Distances between faults in fault array are not to scale. a) Postseismic Coulomb stress changes b) Horizontal velocity field in the x-direction and vertical velocity field. (Model stages selected from interactive Figure 5 from Peikert et al., Geosphere, in review).
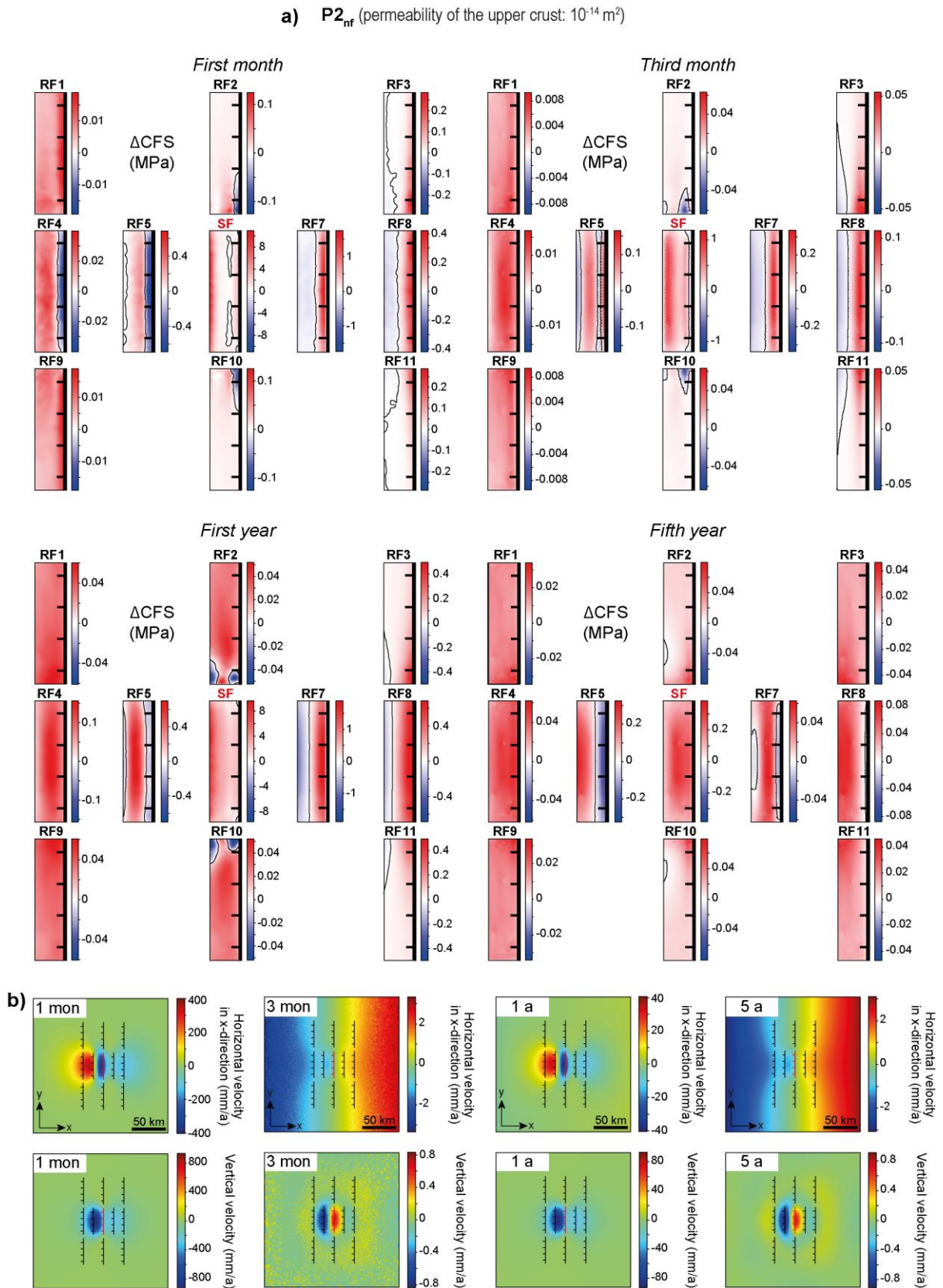
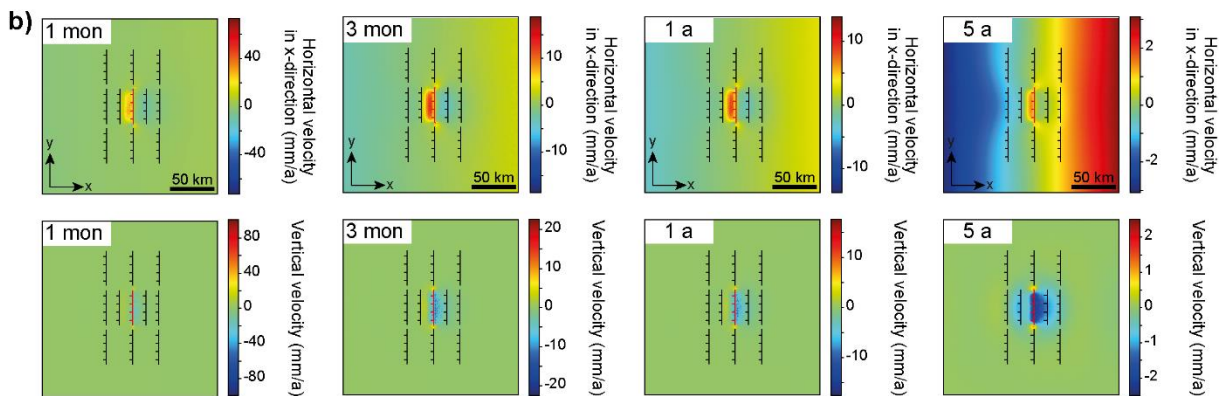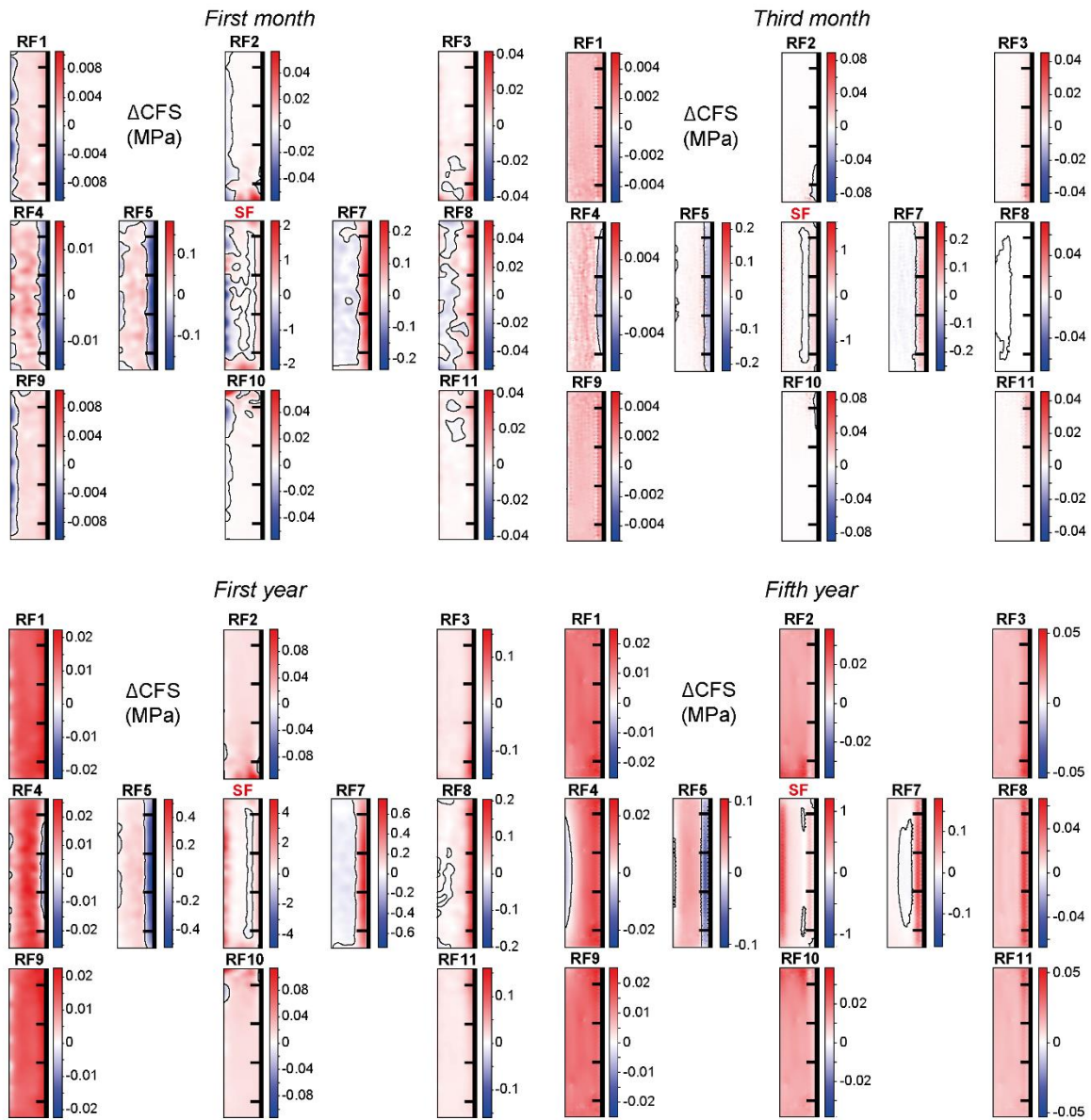**Figure 3.12:** Normal fault model with a higher permeability P2$_{nf}$ 10^{-14} m^2 for the upper crust than in the reference model. Distances between faults in fault array are not to scale. a) Postseismic Coulomb stress changes b) Horizontal velocity field in the x-direction and vertical velocity field. (Model stages selected from interactive Figure 5 from Peikert et al., Geosphere, in review).

Figure 3.13: Normal fault model with a higher permeability P3$_{nf}$ 10^{-16} m^2 for the upper crust than in the reference model. Distances between faults in fault array are not to scale. a) Postseismic Coulomb stress changes b) Horizontal velocity field in the x-direction and vertical velocity field. (Model stages selected from interactive Figure 5 from Peikert et al., Geosphere, in review).
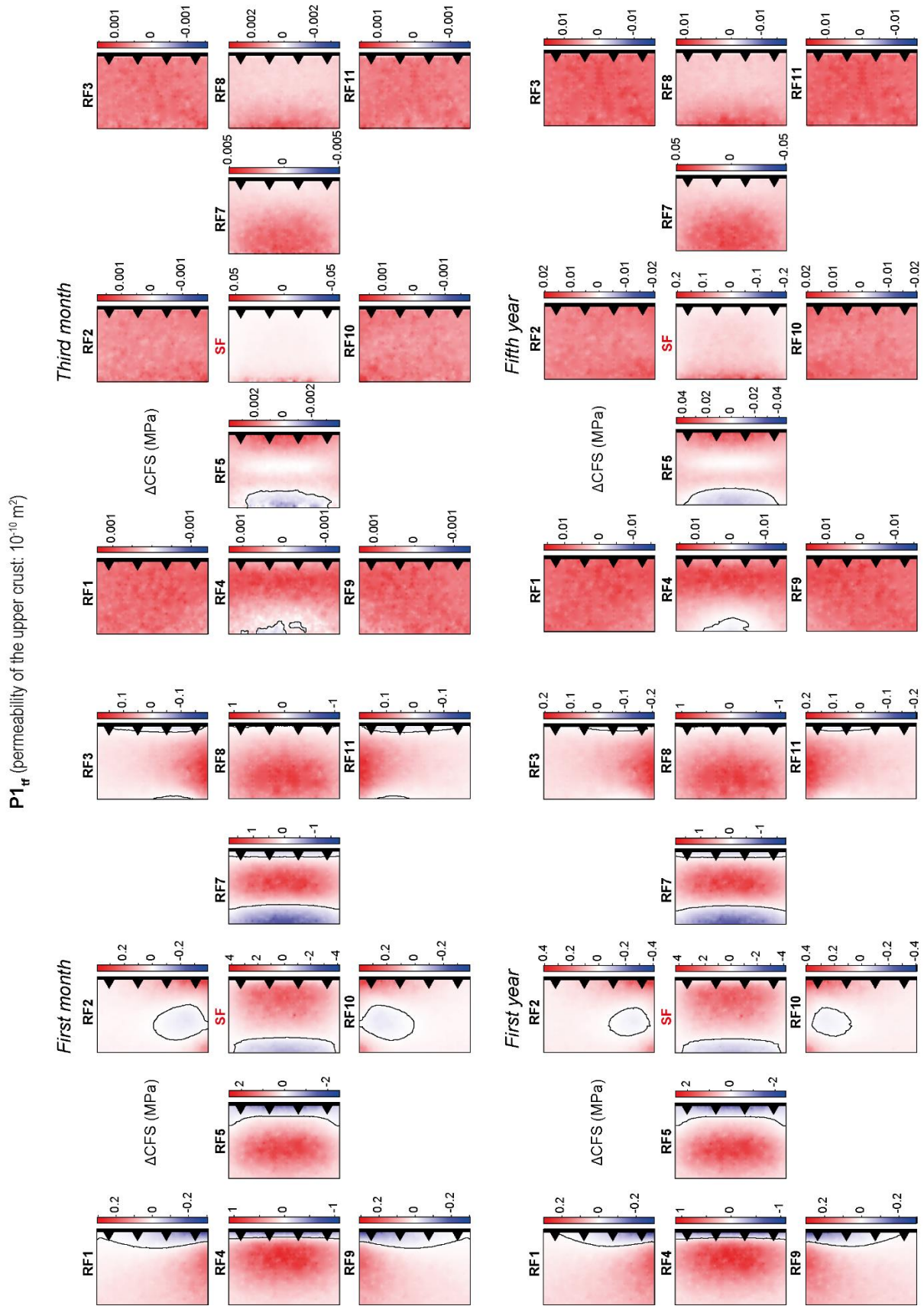
Figure 3.14: Postseismic Coulomb stress changes for the thrust fault model with a lower permeability $P1_{tf}$ 10^{-10} m^2 for the upper crust than in the reference model. Distances between faults in fault array are not to scale. (Model stages selected from interactive Figure 6 from Peikert et al., Geosphere, in review).
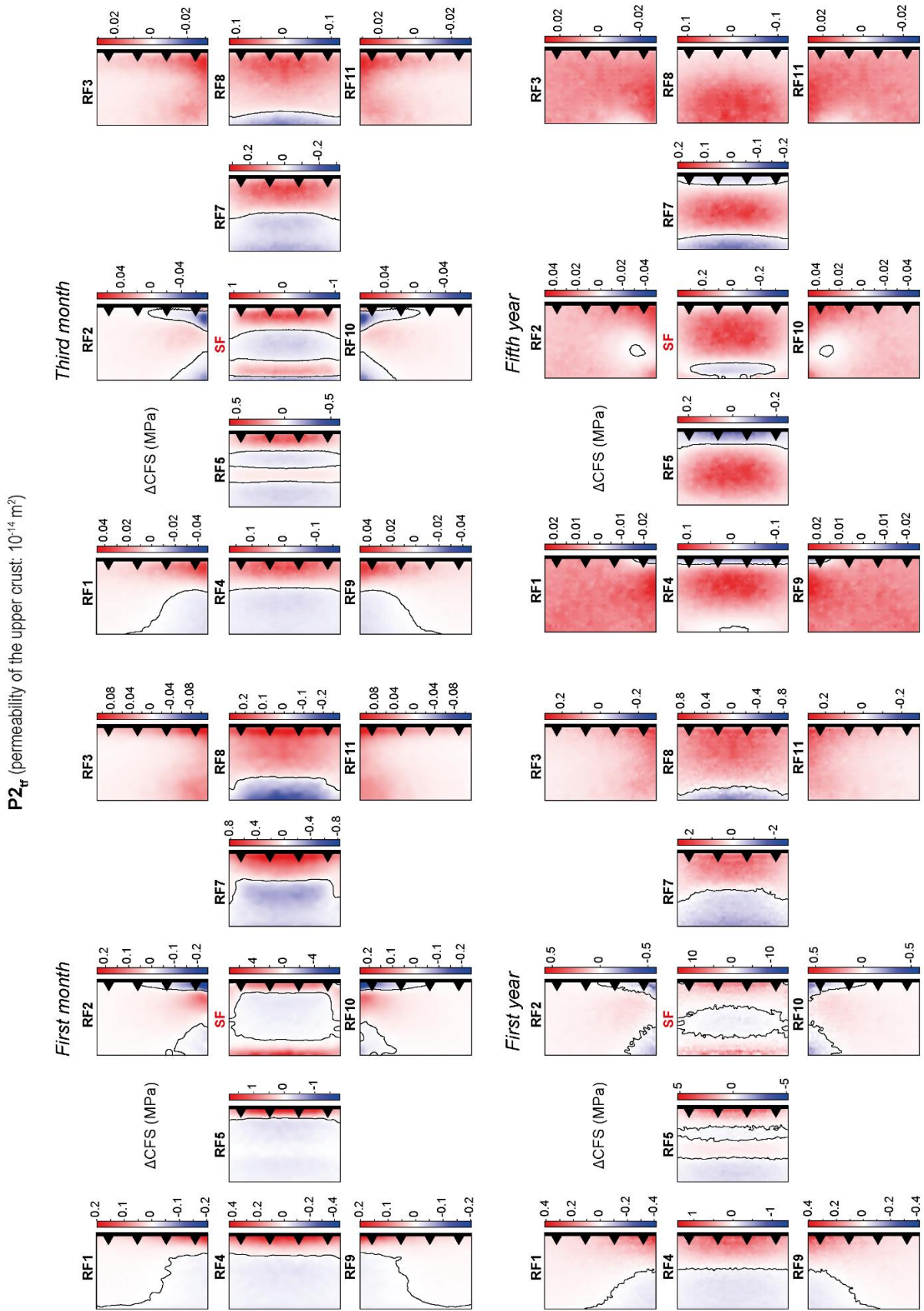
Figure 3.15: Postseismic Coulomb stress changes for the thrust fault model with a higher permeability P2t$_f$ 10^{-14} m^2 for the upper crust than in the reference model. Distances between faults in fault array are not to scale. (Model stages selected from interactive Figure 6 from Peikert et al., Geosphere, in review).

Figure 3.16: Postseismic Coulomb stress changes for the thrust fault model with a higher permeability P3$_{tf}$ 10^{-16} m^2 for the upper crust than in the reference model. Distances between faults in fault array are not to scale. (Model stages selected from interactive Figure 6 from Peikert et al., Geosphere, in review).
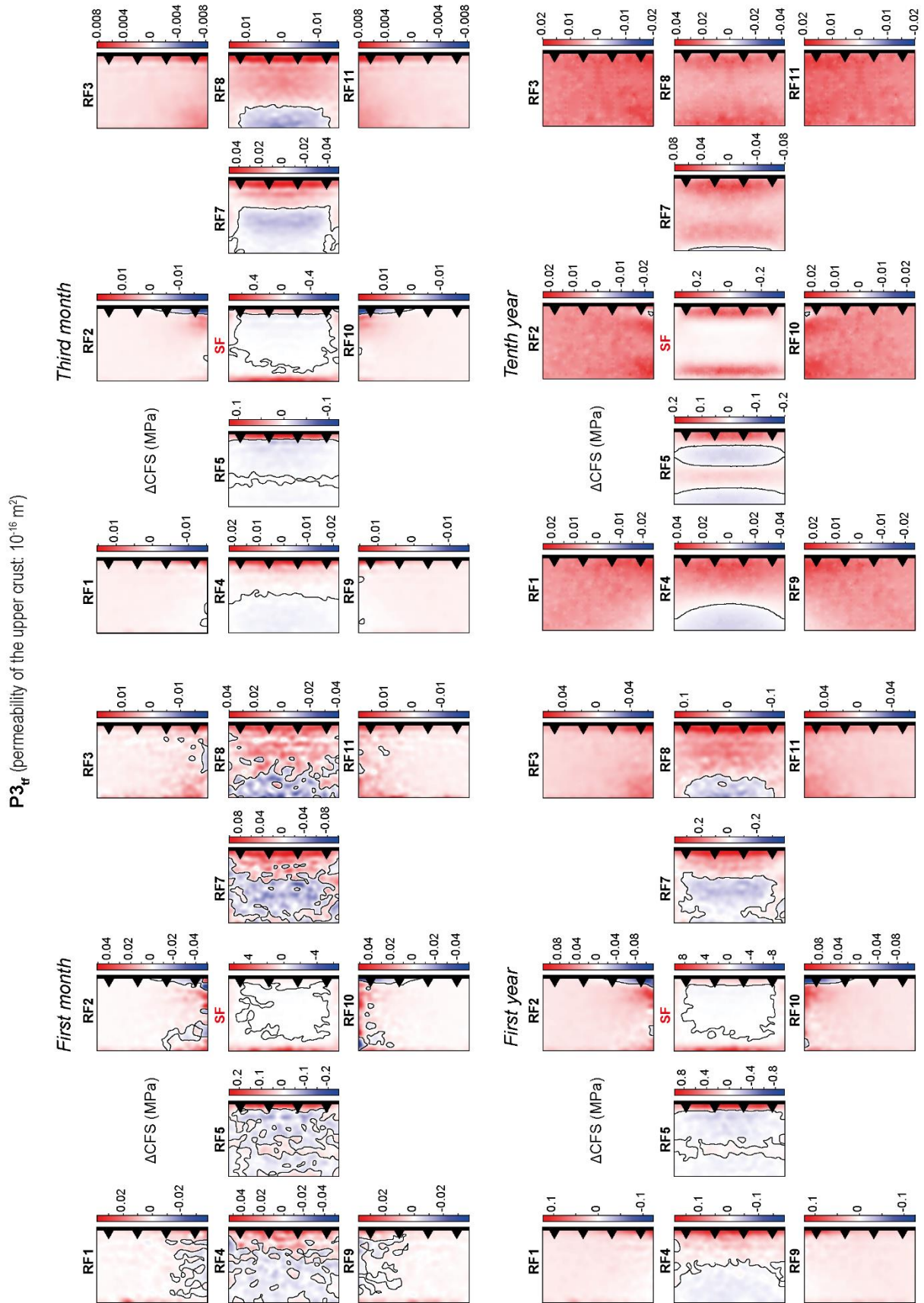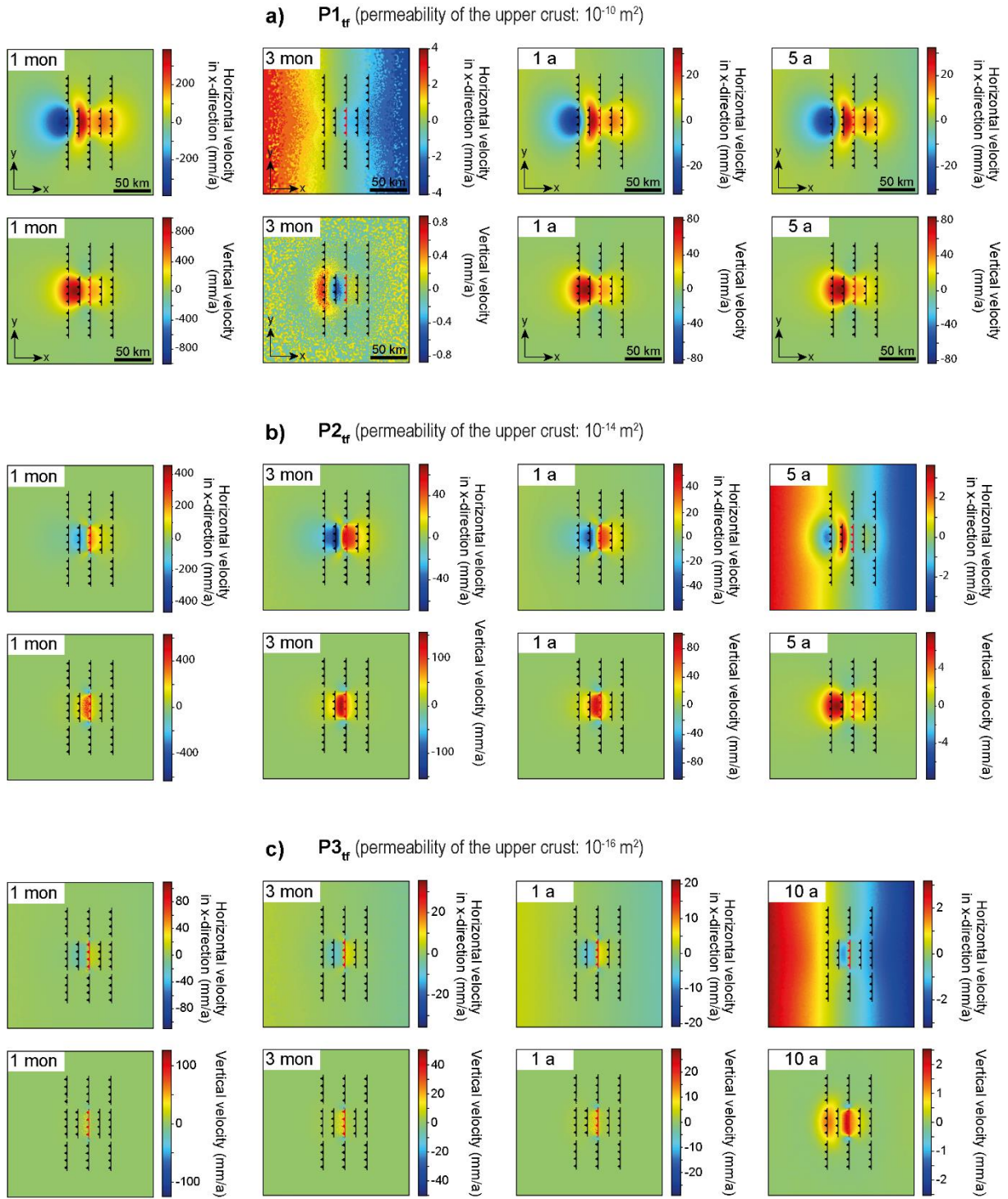
Figure 3.17: Horizontal velocity field in the x-direction and vertical velocity field for the thrust fault models with varied permeabilities. a) P1$_{tf}$ 10^{-10} m^2 for the upper crust. b) P2$_{tf}$ 10^{-14} m^2 for the upper crust. c) P3$_{tf}$ 10^{-16} m^2 for the upper crust. (Model stages selected from interactive Figure 6 from Peikert et al., Geosphere, in review).

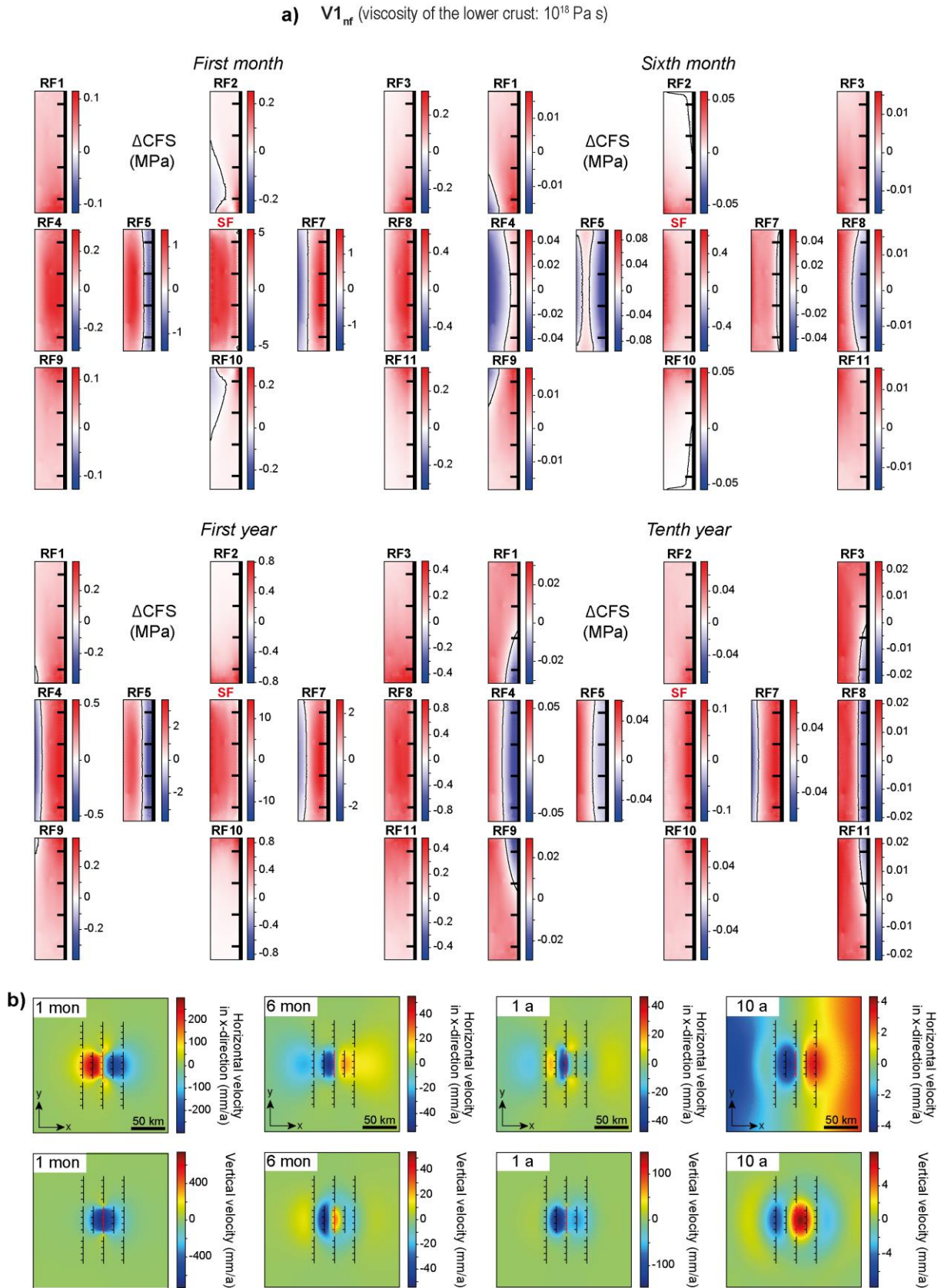**Figure 3.18:** Normal fault model with a lower viscosity V1$_{nf}$ 10^{18} Pa s for the lower crust than in the reference model. Distances between faults in fault array are not to scale. a) Postseismic Coulomb stress changes b) Horizontal velocity field in the x-direction and vertical velocity field. (Model stages selected from interactive Figure 7 from Peikert et al., Geosphere, in review).

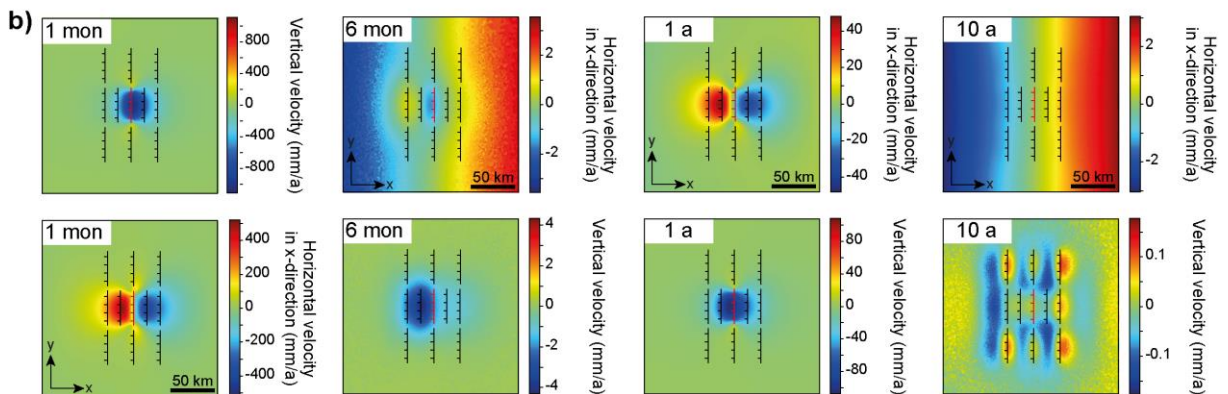**Figure 3.19:** Normal fault model with a higher viscosity $V2_{nf}$ 10^{22} Pa s for the lower crust than in the reference model. Distances between faults in fault array are not to scale. a) Postseismic Coulomb stress changes b) Horizontal velocity field in the x-direction and vertical velocity field. (Model stages selected from interactive Figure 7 from Peikert et al., Geosphere, in review).

Figure 3.20: Postseismic Coulomb stress changes for the thrust fault model with a lower viscosity V1$_{tf}$ 10^{18} Pa s for the lower crust than in the reference model. Distances between faults in fault array are not to scale. (Model stages selected from interactive Figure 8 from Peikert et al., Geosphere, in review).
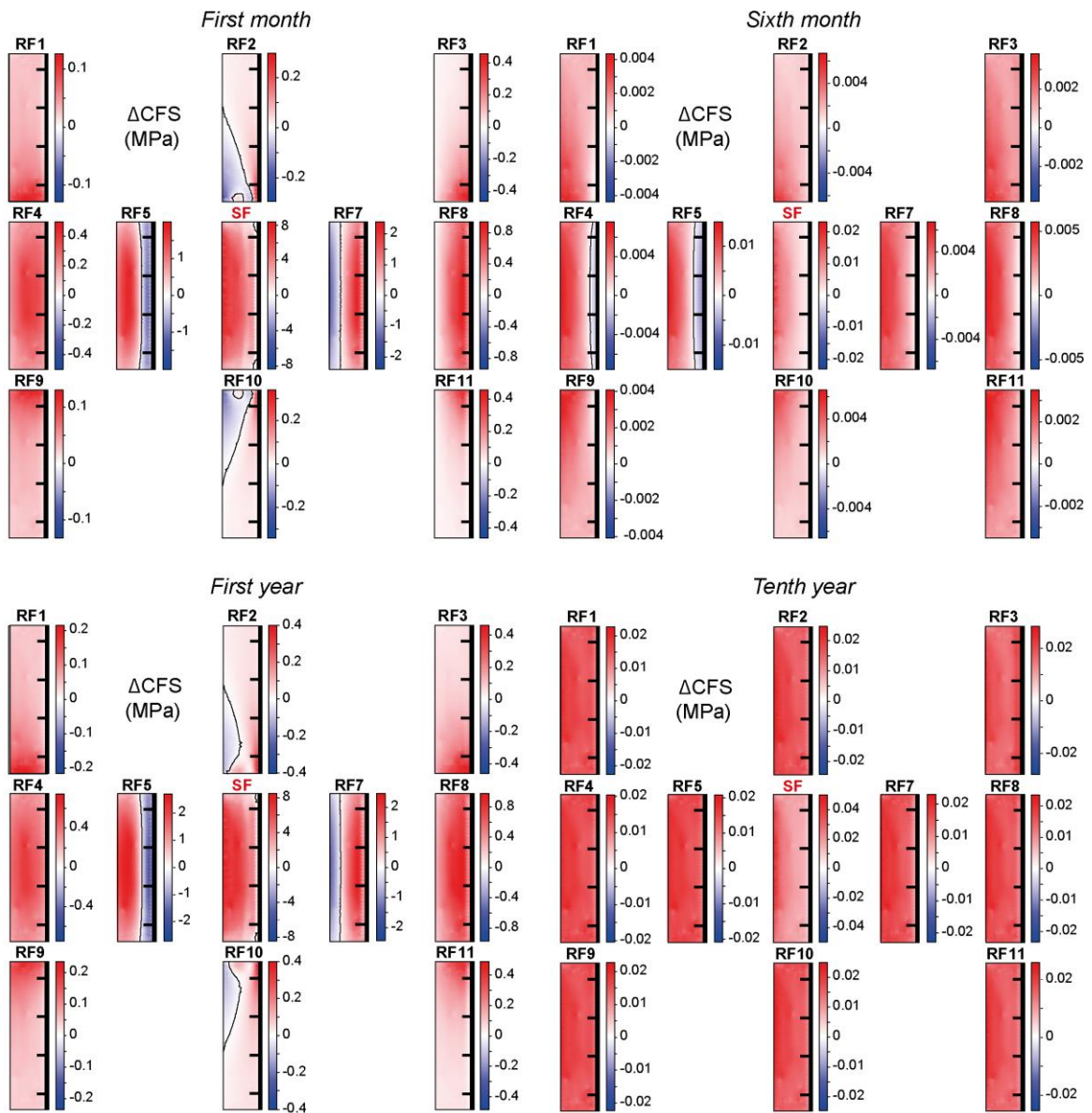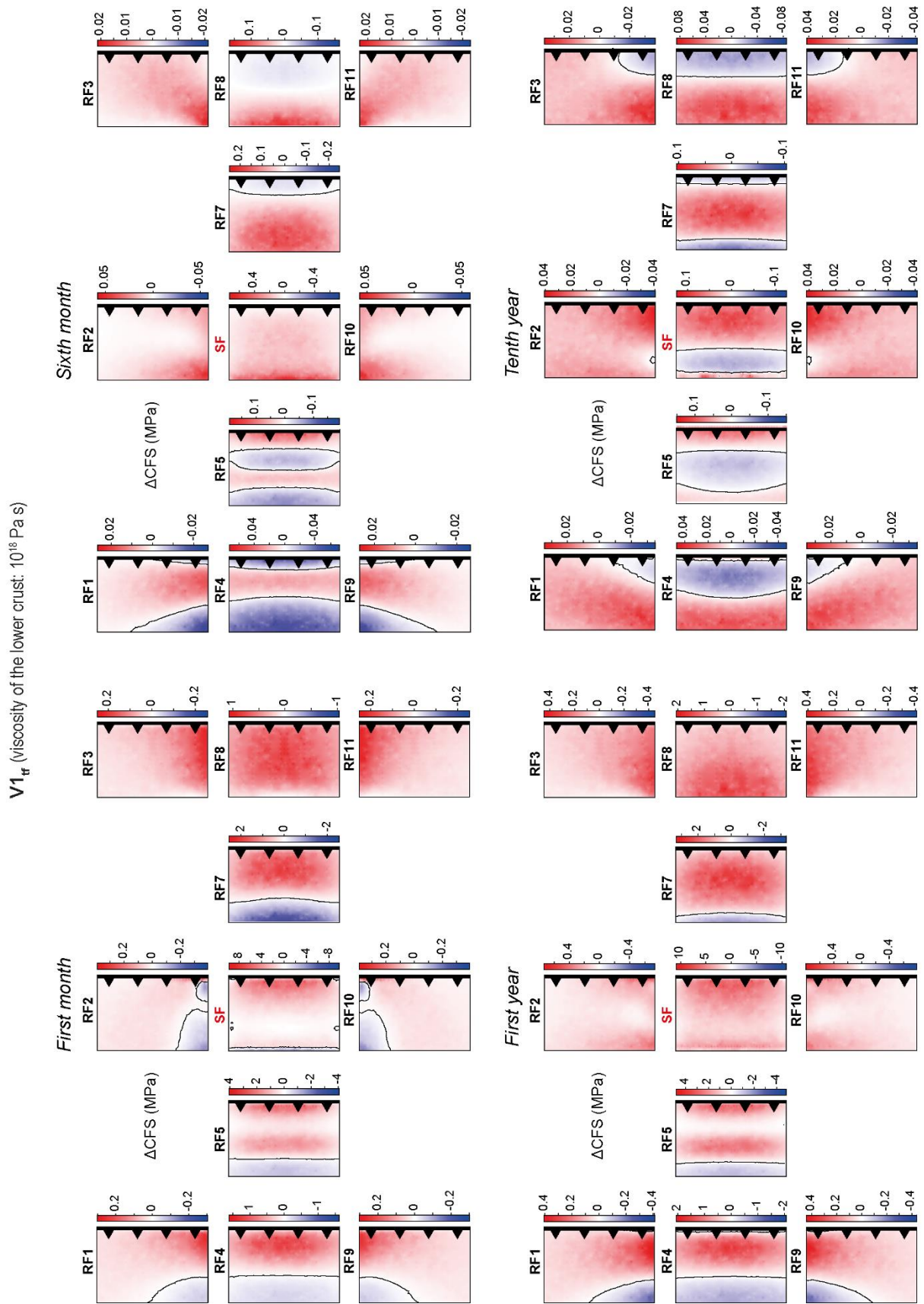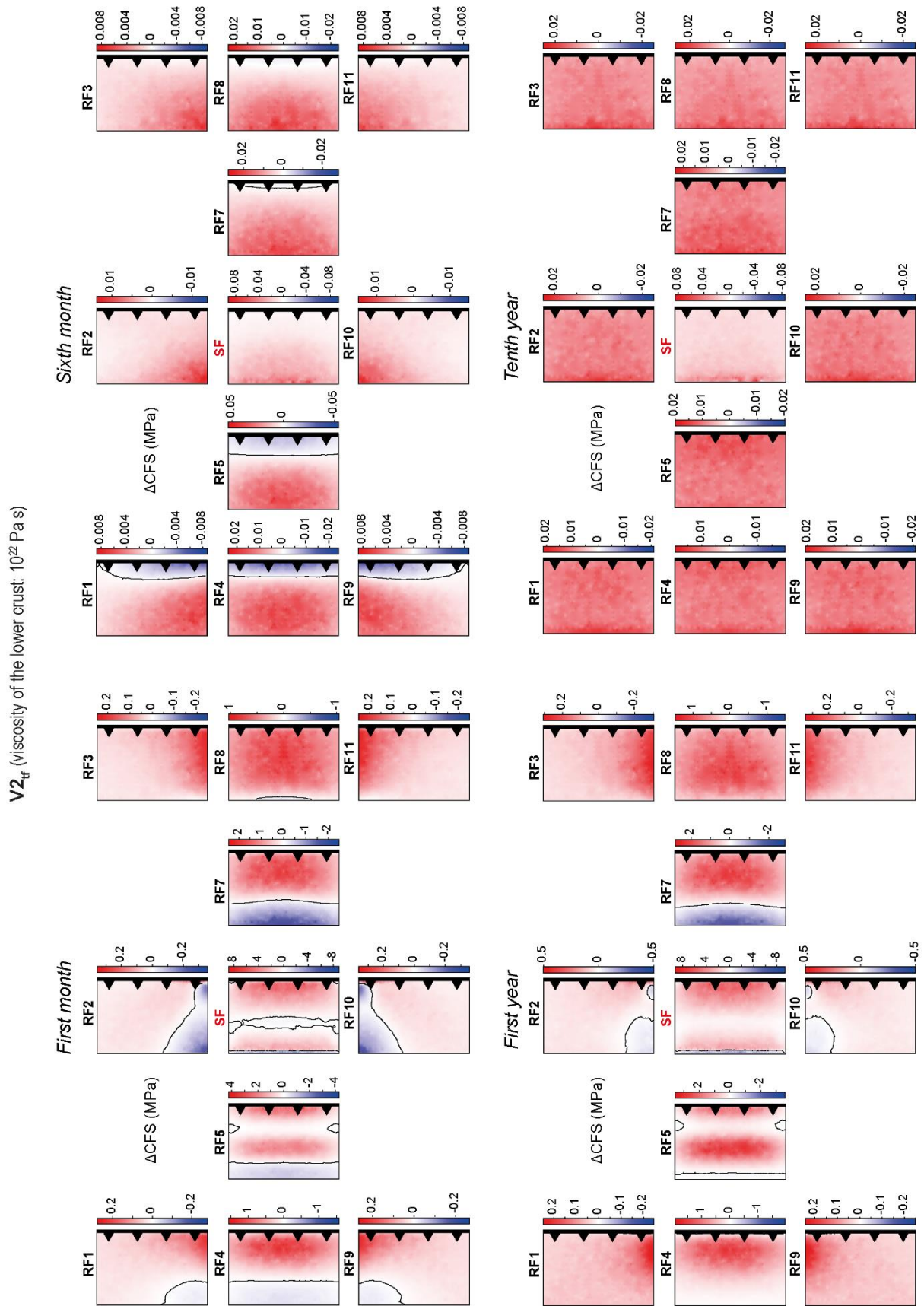
Figure 3.21: Postseismic Coulomb stress changes for the thrust fault model with a higher viscosity V2$_{tf}$ 10^{22} Pa s for the lower crust than in the reference model. Distances between faults in fault array are not to scale. (Model stages selected from interactive Figure 8 from Peikert et al., Geosphere, in review).

Figure 3.22: Horizontal velocity field in the x-direction and vertical velocity field for the thrust fault models with varied viscosities. a) V1$_{tf}$; 10^{18} Pa s for the lower crust. b) V2$_{tf}$; 10^{22} Pa s for the lower crust. (Model stages selected from interactive Figure 8 from Peikert et al., Geosphere, in review).

Figure 3.23: Postseismic Coulomb stress changes from normal fault models with endmember configurations of a high permeability of the upper crust with a low viscosity of the lower crust (PV1$_{nf}$). Distances between faults in fault array are not to scale. (Model stages selected from interactive Figure 9 from Peikert et al., Geosphere, in review).

Figure 3.24: Postseismic Coulomb stress changes from normal fault models with endmember configurations of a low permeability of the upper crust with a low viscosity of the lower crust (PV2$_{nf}$). Distances between faults in fault array are not to scale. (Model stages selected from interactive Figure 9 from Peikert et al., Geosphere, in review).

PV3$_{nf}$ (permeability of the upper crust: 10^{-10} m^2; viscosity of lower crust: 10^{22} Pa s)

Figure 3.25: Postseismic Coulomb stress changes from normal fault models with endmember configurations of a high permeability of the upper crust with a high viscosity of the lower crust (PV3$_{nf}$). Distances between faults in fault array are not to scale. (Model stages selected from interactive Figure 9 from Peikert et al., Geosphere, in review).
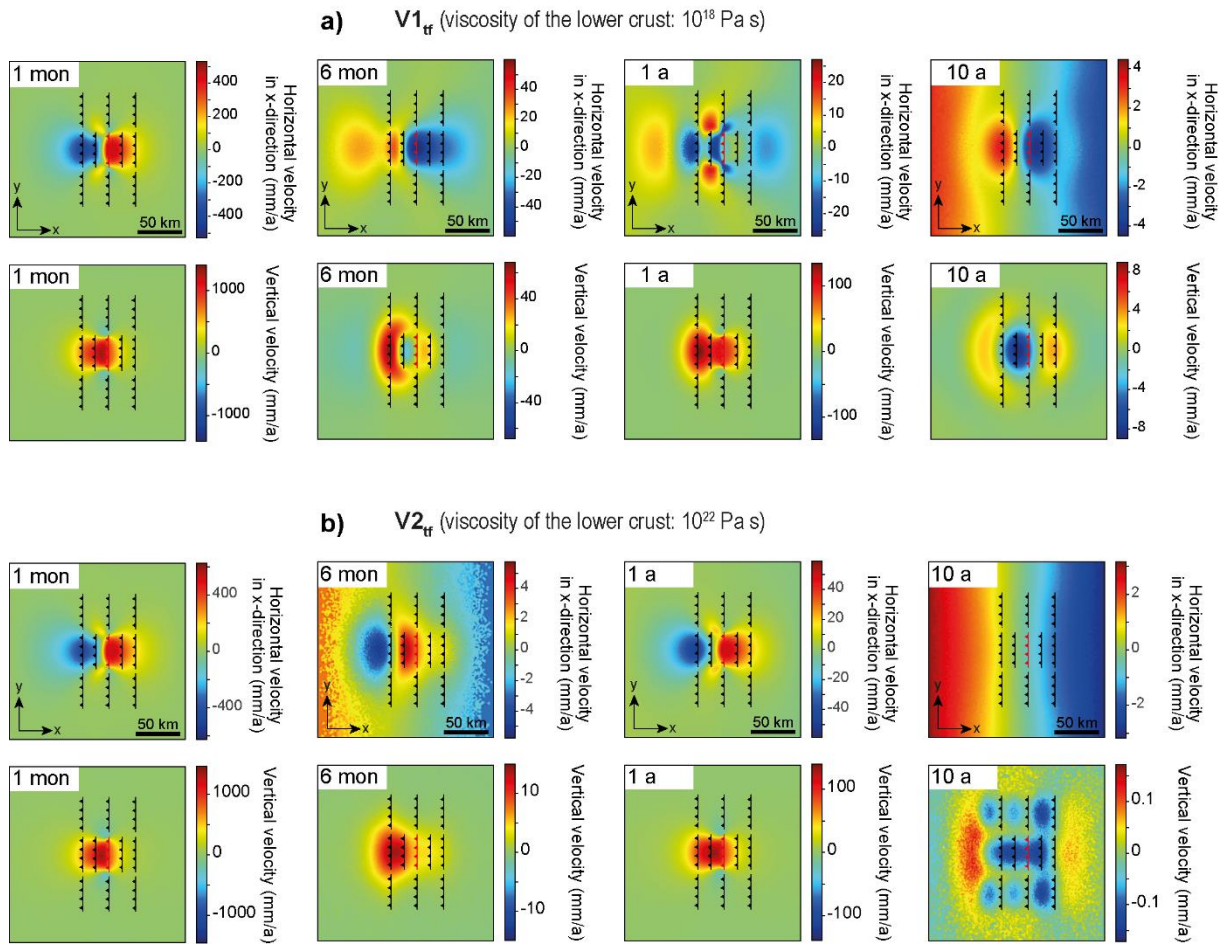
$PV4_{nf}$ (permeability of the upper crust: 10^{-16} m²; viscosity of lower crust: 10^{22} Pa s)

Figure 3.26: Postseismic Coulomb stress changes from normal fault models with endmember configurations of a low permeability of the upper crust with a high viscosity of the lower crust ($PV4_{nf}$). Distances between faults in fault array are not to scale. (Model stages selected from interactive Figure 9 from Peikert et al., Geosphere, in review).
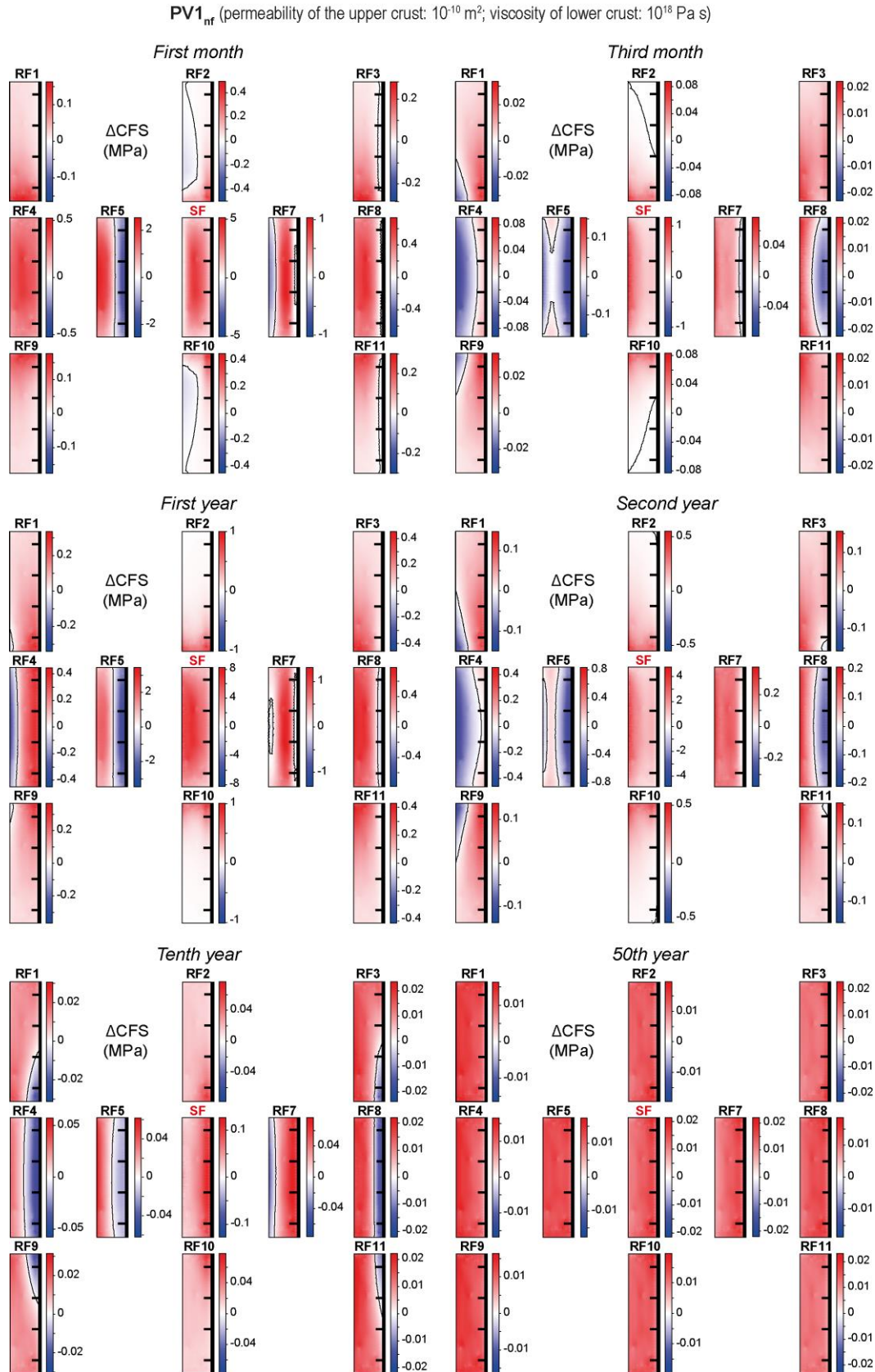
100

Figure 3.27: Postseismic Coulomb stress changes from thrust fault models with endmember configurations of a high permeability of the upper crust with a low viscosity of the lower crust (PV1$_{tf}$). Distances between faults in fault array are not to scale. (Model stages selected from interactive Figure 10 from Peikert et al., Geosphere, in review).
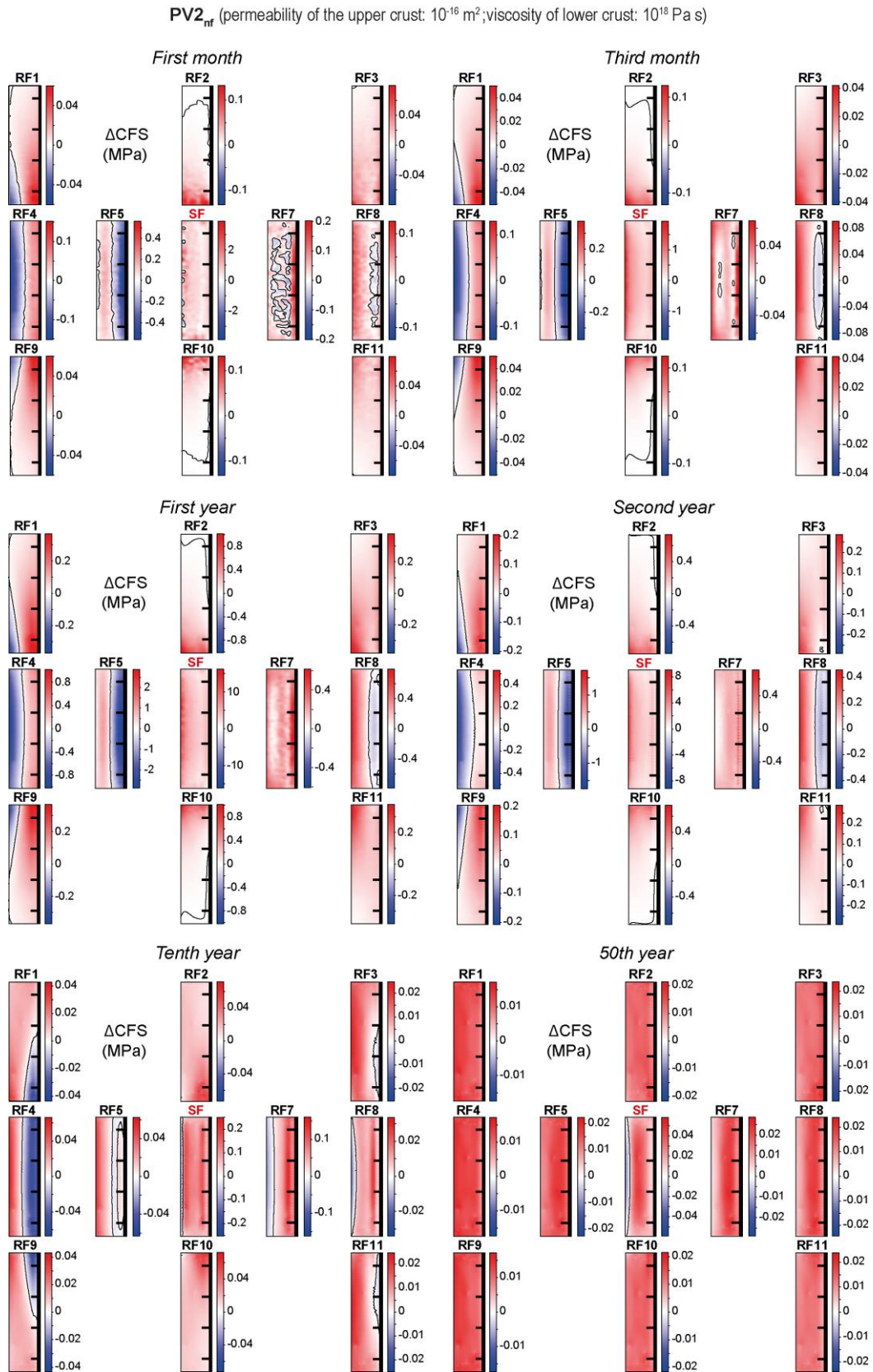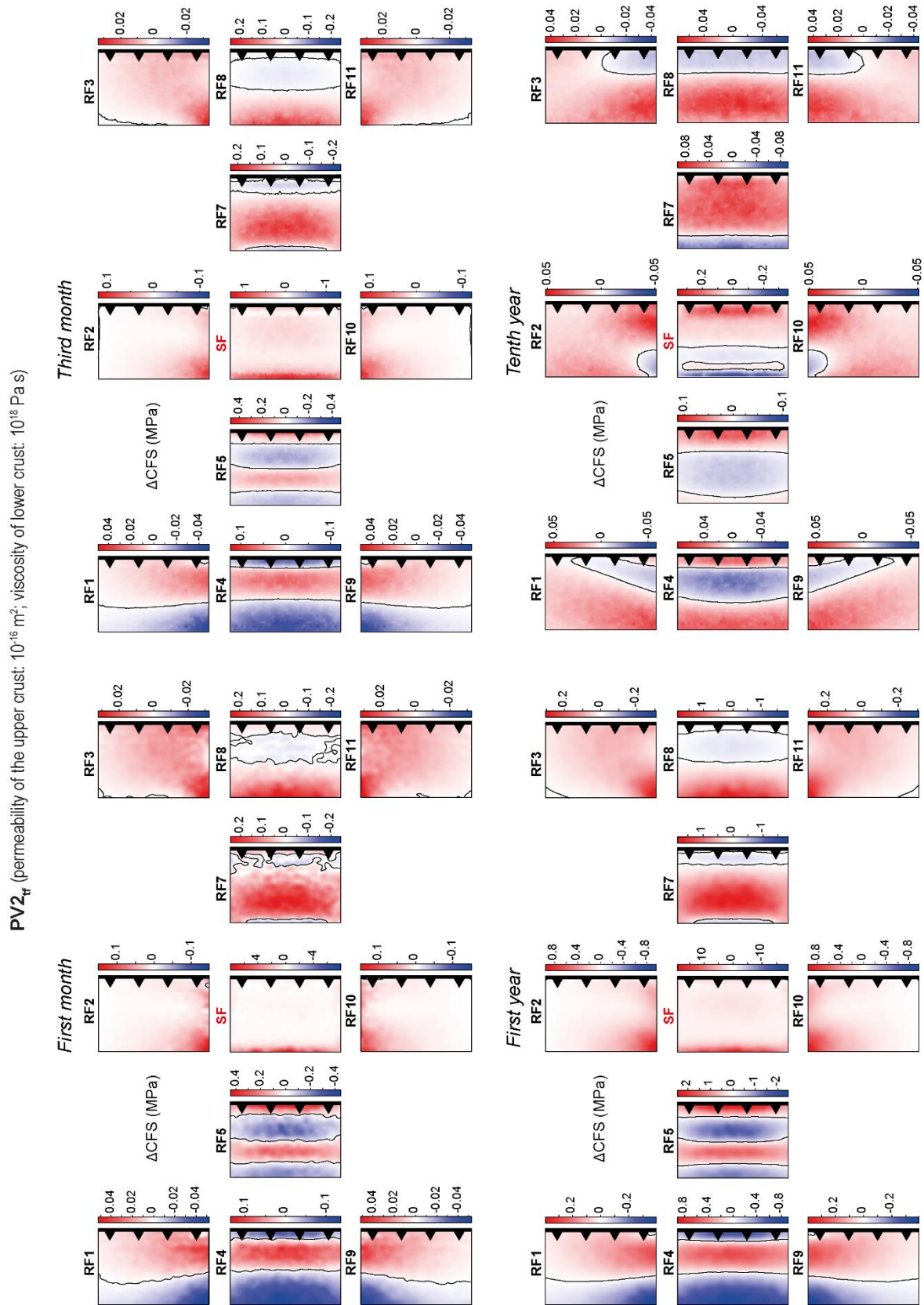
Figure 3.28: Postseismic Coulomb stress changes from thrust fault models with endmember configurations of a low permeability of the upper crust with a low viscosity of the lower crust (PV2$_{tf}$). Distances between faults in fault array are not to scale. (Model stages selected from interactive Figure 10 from Peikert et al., Geosphere, in review).
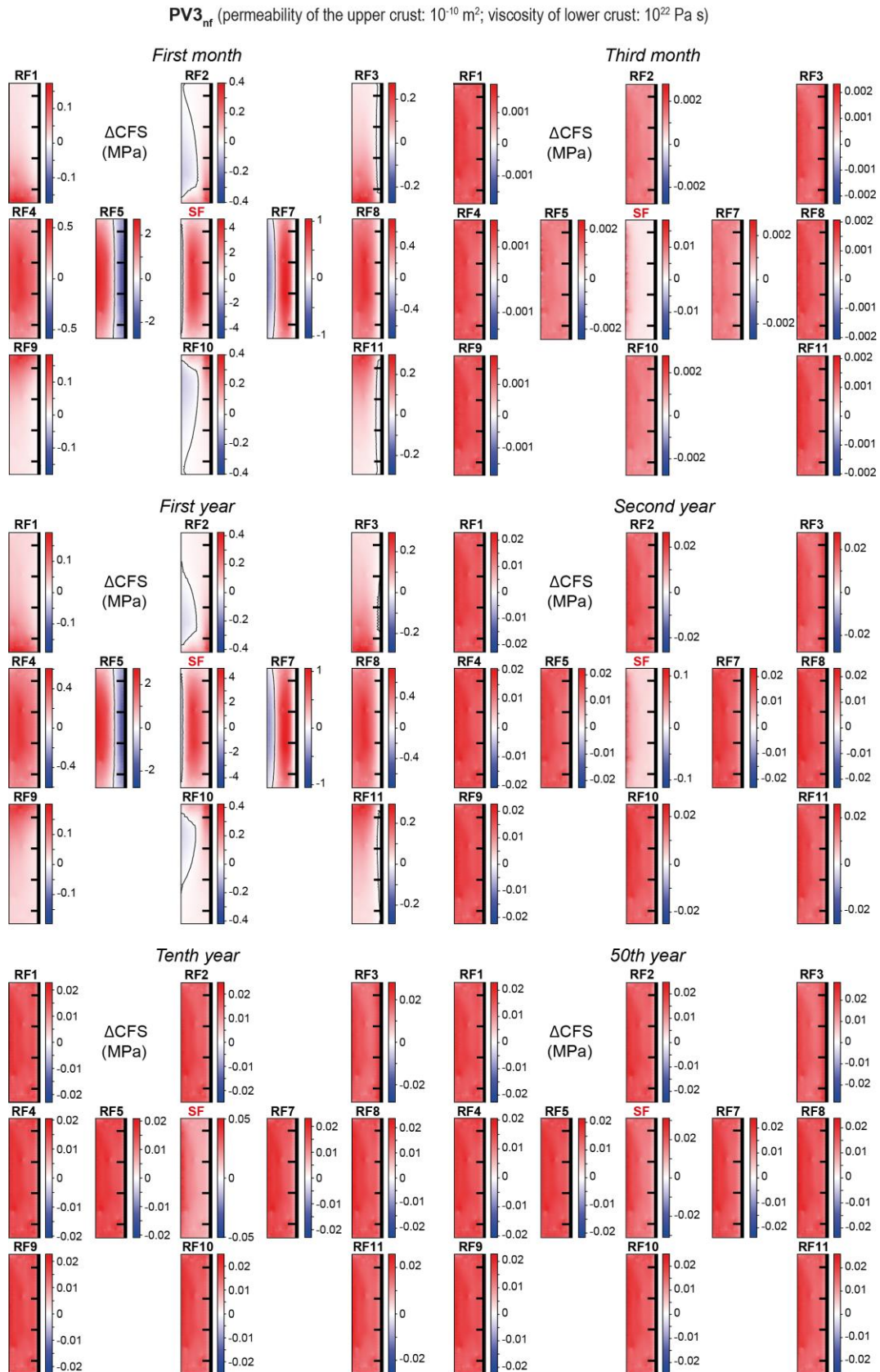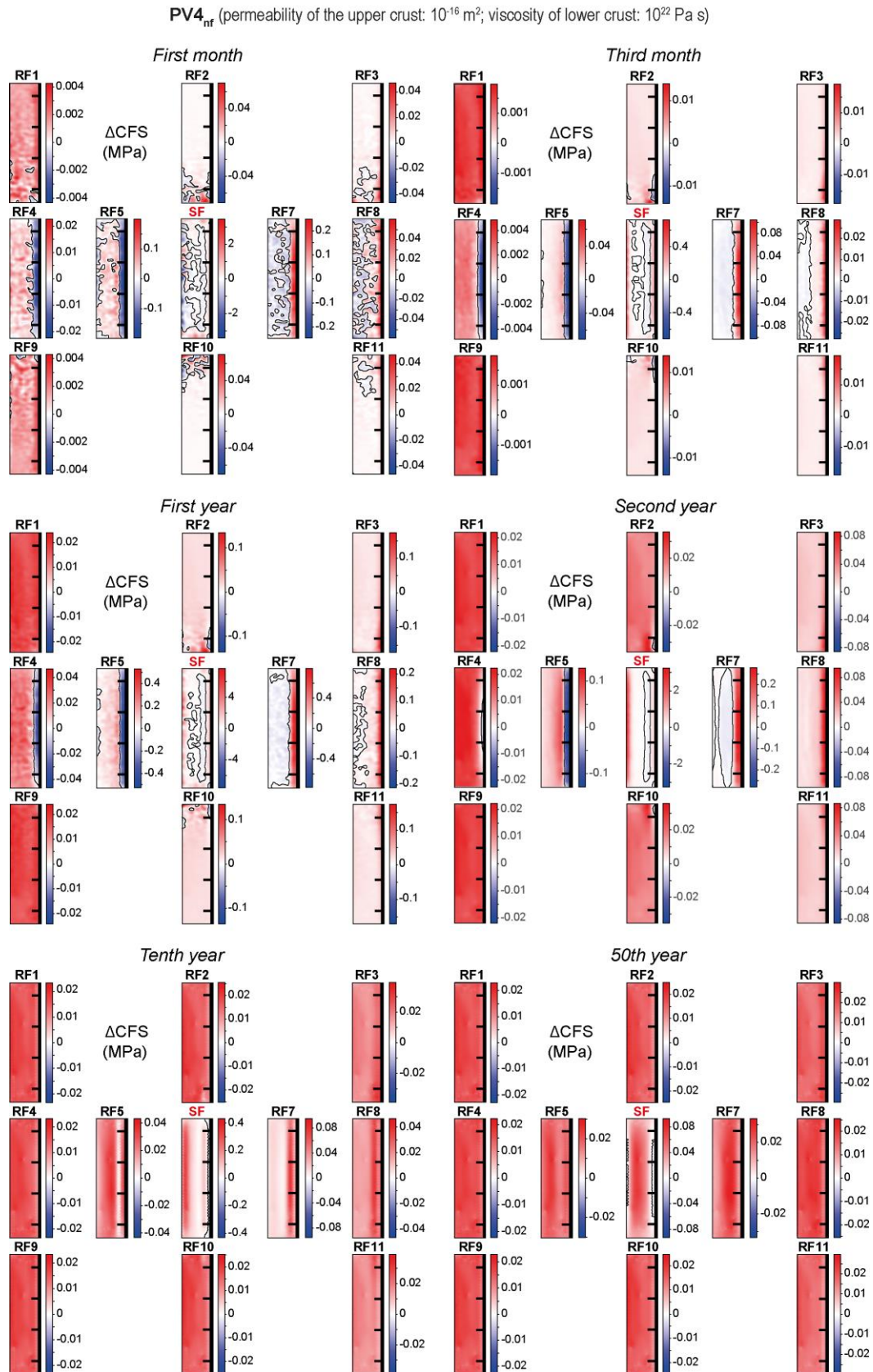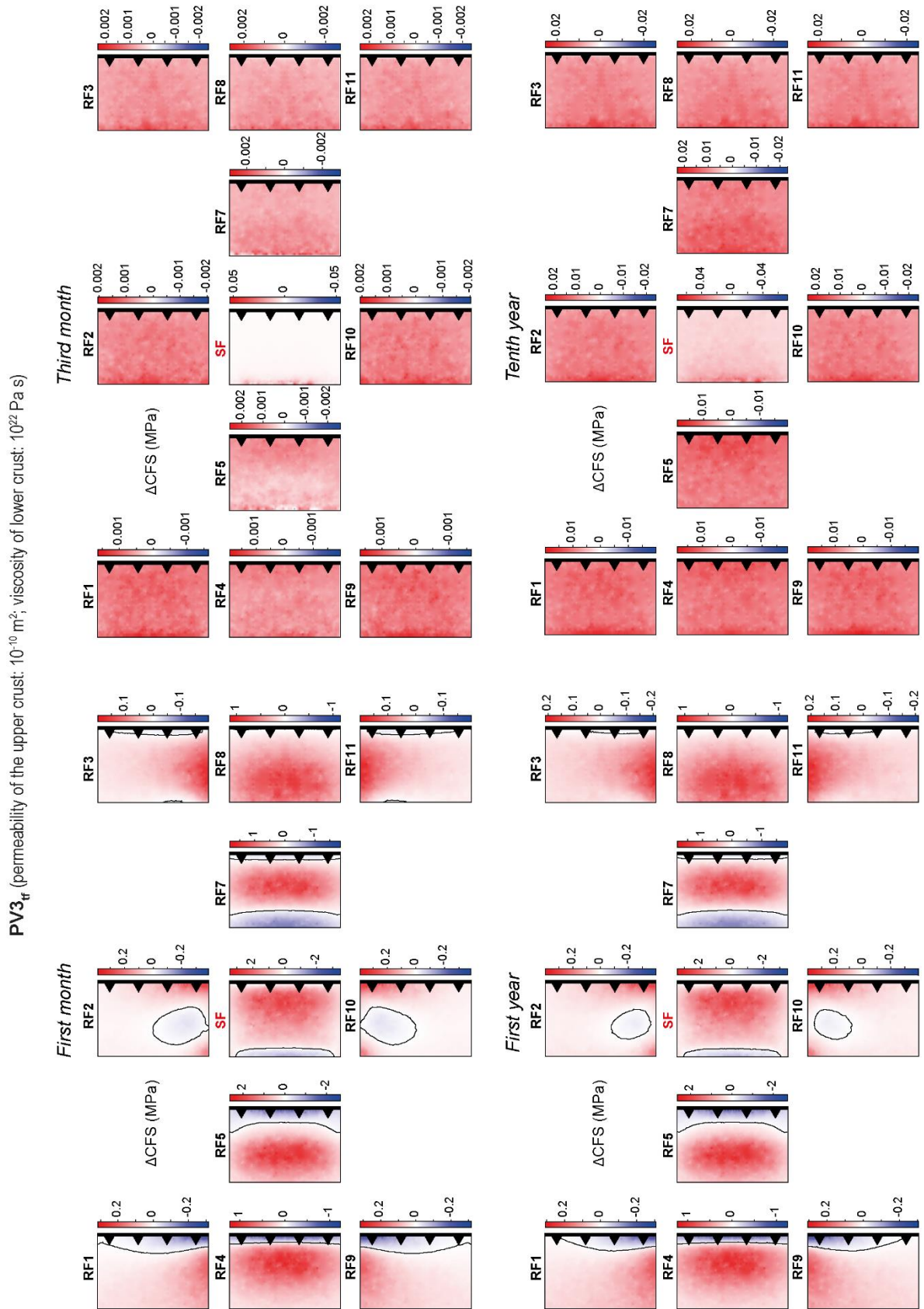
Figure 3.29: Postseismic Coulomb stress changes from thrust fault models with endmember configurations of a high permeability of the upper crust with a high viscosity of the lower crust (PV3$_{tf}$). Distances between faults in fault array are not to scale. (Model stages selected from interactive Figure 10 from Peikert et al., Geosphere, in review).

103

Figure 3.30: Postseismic Coulomb stress changes from thrust fault models with endmember configurations of a low permeability of the upper crust with a high viscosity of the lower crust (PV4$_{tf}$). Distances between faults in fault array are not to scale. (Model stages selected from interactive Figure 10 from Peikert et al., Geosphere, in review).
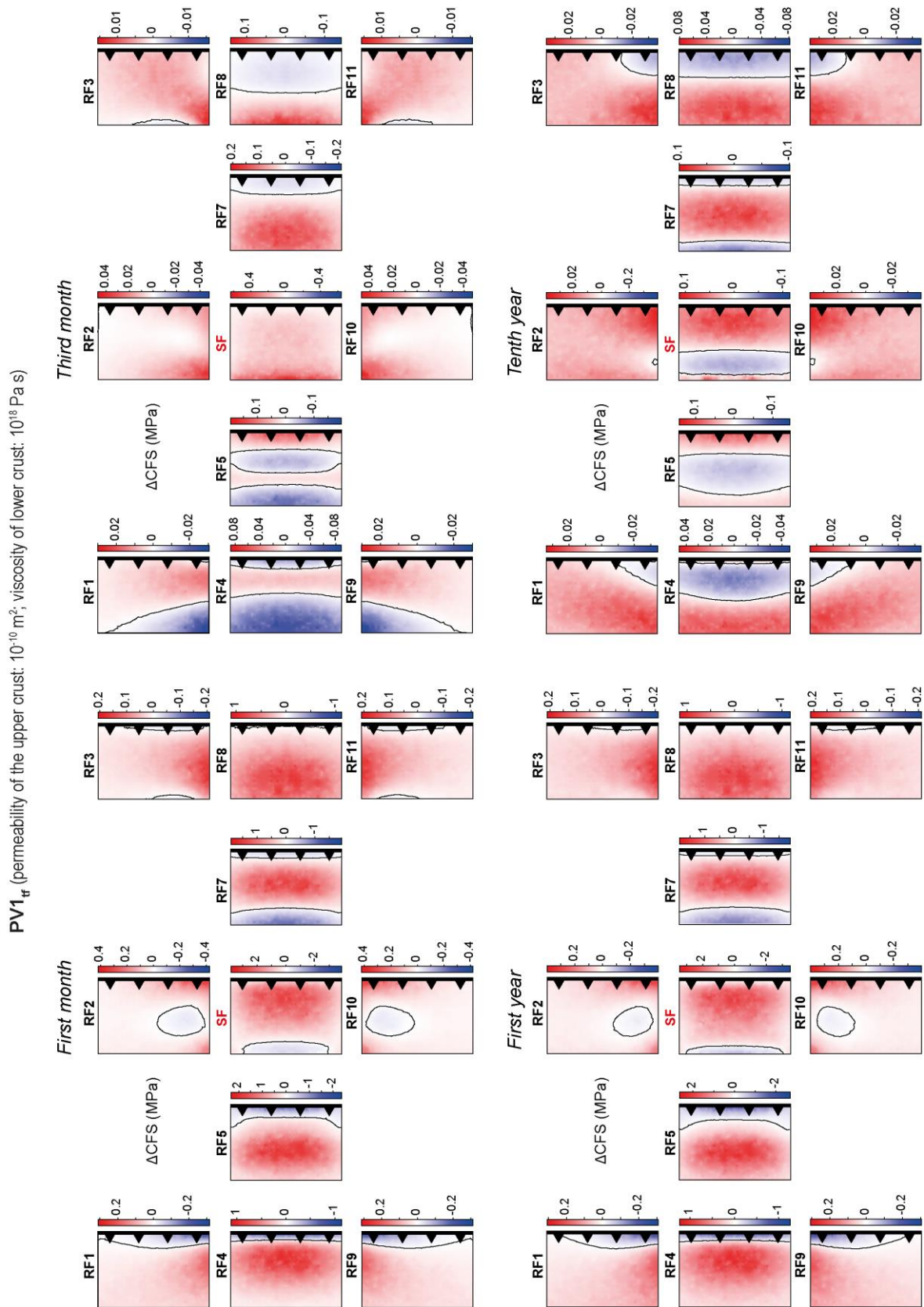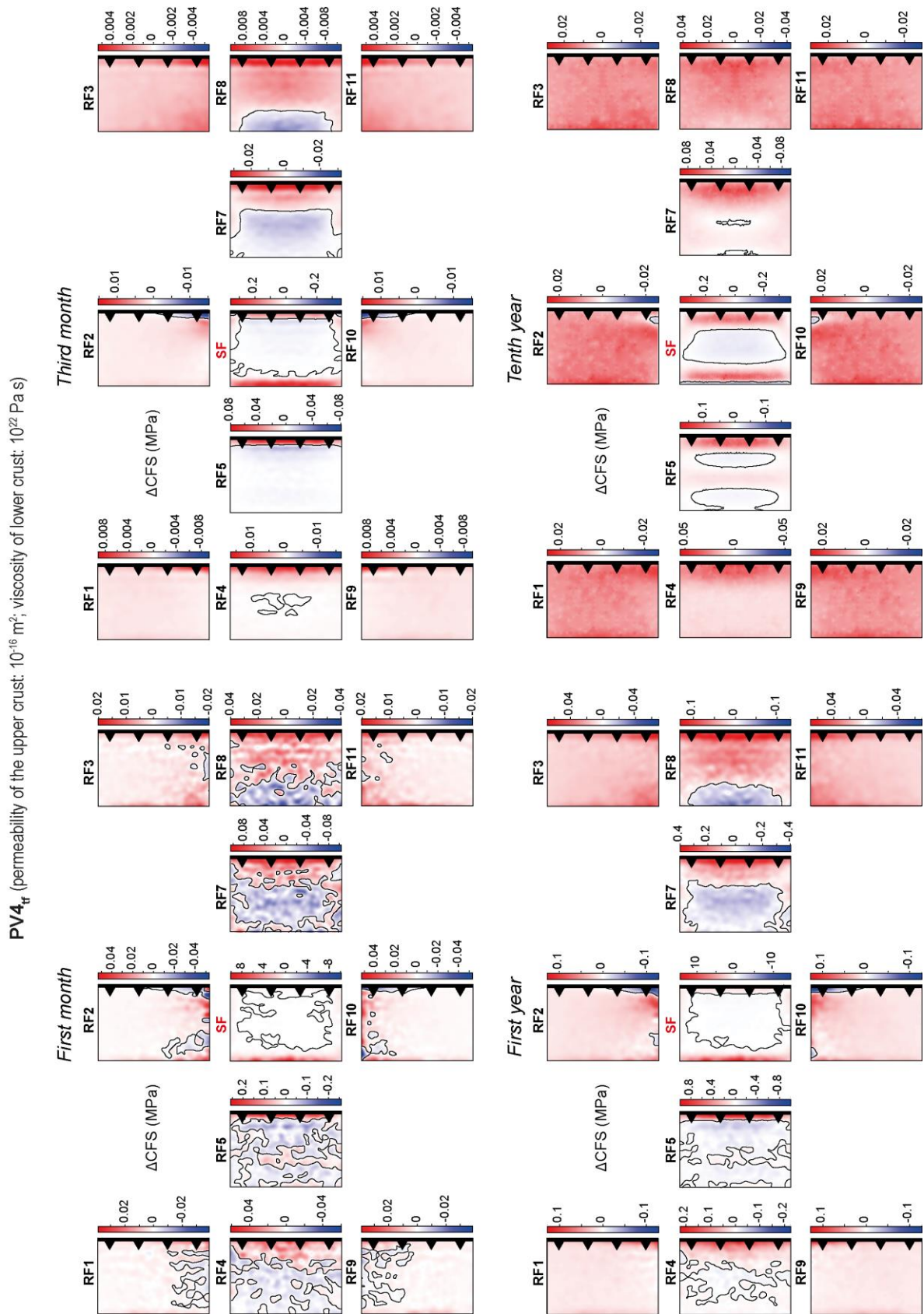
104

Almost all receiver faults of the normal and thrust fault model with a lower permeability in the upper crust (P2$_{nf,tf}$) (Figures 3.12a, 3.15) experience both positive and negative stress changes, except RF1 and RF9 of the normal fault and RF3 and RF11 of the thrust fault model, which solely increase. The highest stress changes occur on RF7 (3 MPa) and RF5 (4 MPa) and on the source fault, the stress change reaches a value of 20 MPa and 15 MPa, in the normal and thrust fault model, respectively. The negative zone on RF4 of the normal fault model disappears in the second month and the magnitudes of the stress changes decrease, but the patterns on the faults do not considerably alter in the following months in both models. The Coulomb stress distribution of the first year after the earthquake resembles the pattern of the second month and the magnitudes of the first month. In the second year, the normal source fault and the adjacent receiver faults (RF2, RF5, RF7 and RF10) show a mixed pattern of positive and negative stress changes, similar to the first year in R1$_{nf}$, with 2 MPa on the source fault and up to 0.5 MPa on RF7. In the thrust fault model, the pattern of the second year resembles the pattern of the first year of model R1$_{tf}$, the magnitudes range between 8 MPa on the source fault and up to 4 MPa on the receiver faults (RF5). In the fifth year, the zones of negative stress changes on the normal source fault disappear and become smaller on the thrust source fault and on the receiver faults in both models, a second zone appears on RF7. From the 10th year onward, the evolution of the stress change distribution in the normal fault model is similar to R1$_{nf}$, with the same pattern, but higher magnitudes. The homogeneous Coulomb stress distribution with an average stress increase of 0.02 MPa on all other receiver faults can be observed from the 20th year onward. The stress field pattern in the 10th year in the thrust fault model resembles the stress field pattern of the second year of R1$_{tf}$, but it evolves differently in the following years. Whereas a homogeneous stress change distribution with values up to 0.025 MPa already occurs on RF1-3 and RF9-11, a zone of negative stress changes can be found in the 20th year on RF4 and in the 50th year on RF5. RF7 still shows higher values of 0.04 MPa in the 50th year.

Model P3$_{nf}$ and P3$_{tf}$ with a permeability of 10^{-16} m^2 (Figures 3.13a, 3.16) show positive and negative stress changes of up to 2 MPa on the normal source fault, up to 6 MPa on the thrust source fault and between 0.2 MPa (RF7) and 0.008 MPa (RF1, RF9) on the normal receiver faults and between 0.2 (RF5) and 0.02 (RF3, RF11) on the thrust receiver faults in the first month. Over the following months, the negative zones on the outermost receiver faults (RF1, RF3, RF9, RF11) disappear and become smaller on the other faults, the magnitudes slightly decrease to values between 0.1 MPa (RF7) and 0.002 (RF1, RF9) MPa and between 0.08 MPa (RF5) and 0.004 MPa on the receiver faults in the normal and thrust fault model, respectively. In the first year after the earthquake, all faults parallel to the source fault experience positive

and negative stress changes in the normal fault model. The highest stress changes on the receiver fault can be found in RF7 (0.7 MPa). The thrust fault model shows a mix of positive and negative stress changes on faults parallel and along-strike to the source fault with the highest value on RF5 (0.9 MPa). Over the years, the negative stress zones become smaller and slowly turn into positive stress changes. From the first to the 10th year in the normal fault model and the 20th year in the thrust fault model, the stress changes decrease by one order of Magnitude and RF4 and RF5 still show negative stress changes on one or two parts of the fault. In the 50th year, solely positive stress changes can be found on all faults in the normal fault model, except RF5. A homogeneous stress change distribution with values up to 0.025 MPa occurs on most faults. RF5 and RF7 still show higher values of 0.03 MPa. In the thrust fault model, RF4 and RF5 still experience negative stress changes and higher values between 0.03 MPa and 0.05 MPa can be observed on the faults parallel to the source fault.

The horizontal and vertical surface velocities in the first month and the first year in model P1$_{nf}$ (Figure 3.11b) are similar to the reference model R1$_{nf}$, and somewhat lower in model P1$_{tf}$ (Figure 3.17a) than in R1$_{tf}$, but the velocity pattern of both models P1$_{nf,tf}$ resembles the second month of R1$_{nf,tf}$. The velocities decrease by two orders of magnitude in the second month. In the third month, similar to the sixth month of the reference models, the horizontal velocity field switches direction back to extension across the normal source fault and shortening across the thrust source fault. Around the normal source fault, the model surface starts to show uplift, whereas it still subsides near RF5. In the thrust fault model, zones of uplift occur near the source fault and RF4 and subsidence near RF5. In the following years, the velocity field remains similar with only small changes.

Model P2$_{nf}$ (Figure 3.12b) shows in the first month shortening across the source fault. Extension occurs at the surface of the hanging wall and in the footwall with the highest movements between the source fault and RF5. The area with disturbed velocities is smaller compared to the reference model R1$_{nf}$. Near the source fault and RF7, the model surface subsides, whereas uplift can be found around RF5 and the source fault tips. P2$_{tf}$ (Figure 3.17b) shows extension across the source fault and shortening within the hanging wall and footwall. Uplift of the model surface can be observed between the source fault and RF5, whereas subsidence occurs around the source fault tips. In the following months, the horizontal and vertical velocities decrease from 350 mm/a and 400 mm/a in the first month to 40 mm/a and 50 mm/a in the sixth month in the normal fault model, respectively and from 450 mm/a and 500 mm/a to 35 mm/a and 75 mm/a in the thrust fault model. The velocity patterns do not considerably change over the months. In

the second year in both models, the disturbed areas extend and the velocity pattern in horizontal and vertical directions resembles the first year of the reference models with maximum velocities of 9 mm/a and 20 mm/a in the normal fault model and 8 mm/a and 25 mm/a in the thrust fault model, respectively. In the fifth year, horizontal movements switched positions, shortening can now be found across RF5 and extension on the footwall between the source fault and RF7 in the normal fault model. The surface around RF5 and RF8 still subsides, while the source fault starts to show uplift. The fifth and 10th year of the thrust fault model and the 10th year of the normal fault model resemble the velocity field of the second year in the reference model and both models evolve similar in the following years.

In models $P3_{nf}$ and $P3_{tf}$, (Figures 3.13b, 3.17c) in the first month, the surface velocity field is disturbed in a smaller area around the source fault tips and between RF5 and RF7. The normal fault model shows shortening across the source fault and extension within the footwall and hanging wall with velocities of 40 mm/a. The area between RF7 and the source fault subsides with a velocity of 20 mm/a, uplift of 20 mm/a can be found around the source fault tips. In the thrust fault model, the surface across the source fault extends, shortening of maximum 30 mm/a occurs within the footwall and hanging wall. In vertical direction, the area around the source fault shows uplift and the source fault tips subsidence with values of around 40 mm/a. The surface velocity pattern of both models only slightly changes and the velocities slowly decrease in the next six months. The regional extension and shortening in the normal and thrust fault model, respectively, start to dominate the horizontal velocity field in the 20th year, but remain slightly disturbed around the faults. The vertical velocity field still shows subsidence in the normal fault model and uplift in the thrust fault model within the hanging wall and footwall in the 50th year.

3.3.3 Models with variable viscosity

In this section, we describe the results from models, in which we used either lower ($V1_{nf,tf}$) or higher ($V2_{nf,tf}$) viscosities for the lower crust compared to the reference models while keeping the permeability constant (Figures 3.18-3.19, 3.20-3.22). The results show that Coulomb stress changes in the first month in the normal fault model $V1_{nf}$ (Figure 3.18a) are slightly lower compared to the normal fault reference model with values of 5 MPa on the source fault and a maximum of 1.7 MPa on RF7 and minimum 0.1 MPa on RF1 and RF9 and in the thrust fault model $V1_{tf}$ (Figure 3.20) the magnitudes are similar to the thrust fault reference model. The stress change pattern evolves similarly to the reference model in the first two months in both

models, but on the source faults, the stress solely increases in the second month. In the third month, RF1, RF9 and the source fault of the normal fault model still show solely positive stress changes, whereas all other faults experience a mixed pattern of positive and negative stress changes, similar to the reference model, but in model $V1_{nf}$ the magnitudes of the stress changes are higher and the zones of negative stress changes are smaller or located on a different position on some faults. In the thrust fault model, one or two zones of negative stress changes can be found on different locations on the fault planes of all receiver faults in the second and third month, with higher magnitudes than in the reference model. After six months, the zones of negative stress changes on receiver faults RF2-3 and RF10-RF11 in both normal and thrust fault models become smaller or disappear, whereas the zones of negative stress changes on all receiver faults of the source fault's hanging wall and RF8 expand. RF7 shows two zones of stress decrease in both models. Until the sixth month, the magnitudes of the stress changes decrease to 0.6 MPa on the source fault and between 0.09 MPa on RF5 and 0.017 MPa on the outermost receiver faults in the normal fault model. The magnitudes in the thrust fault model range between 0.8 MPa on the source fault and 0.25 MPa (RF7) to 0.02 MPa (RF3 and RF11). In the first year after the earthquake, the magnitudes of stress changes are higher than in the reference model on the source fault (15 MPa in $V1_{nf}$ and 11 MPa in $V1_{tf}$) and on most of the receiver faults. All the receiver faults on the hanging wall side (RF1, RF4, RF9, RF5) and RF7 on the footwall show negative stress change zones along the lower or upper part of the fault planes in both models. The stress solely increases on the other faults. In the following years, the magnitudes of the stress change decrease, but are still one order of magnitude higher in the second year than in the reference model. The zones of stress decrease become larger on the receiver faults of the hanging wall. In the thrust fault models, two zones of stress decrease can be found on all receiver faults of the hanging wall. On the footwall side, new zones of negative stress changes occur on RF3, RF8 and RF11 in both models, but in the normal fault model, the negative zone on RF7 disappears. In the fifth year after the earthquake, all faults in the normal fault model, except RF2 and RF10, experience both positive and negative stress changes, also the source fault, which showed solely positive stress changes in the years before and after the fifth year. The stress field pattern on the receiver faults does not change in the 10th year, but the magnitudes decrease further and the stress change magnitude of the source fault is one magnitude smaller than in the reference model. In the 20th year, some zones of negative stress change still remain on RF1, RF4, RF7 and RF9, on all other faults, the Coulomb stress changes increase. In the thrust fault model, the zones of negative stress changes on the receiver faults in the hanging wall and footwall expand in the fifth year. In the 10th year, a mixed pattern of

positive and negative stress changes can be observed on all faults, including the source fault, which becomes smaller on most faults or disappears on RF1 and RF9 in the 20th year. The magnitude of the Coulomb stress changes on the source fault is one order smaller than in the reference model, whereas all other faults show higher values. In the 50th year, a homogeneous Coulomb stress distribution with an average stress increase of 0.02 MPa can be found on all faults in the normal fault model and on most of the faults in the thrust fault model.

The velocity patterns of the first month in model V1$_{nf}$ and V1$_{tf}$ (Figures 3.18b, 3.22a) resemble the patterns of the first month in the reference models R1$_{nf}$ and R1$_{tf}$, with lower velocities in model V1$_{nf}$ compared to Rf1$_{nf}$. In the second month, the velocities and the pattern of the vertical velocities of V1$_{nf,tf}$ and R1$_{nf,tf}$ are similar, the horizontal velocity patterns slightly differ. Shortening occurs across RF5 and extension within the hanging wall in model V1$_{nf}$, similar to the reference model, but extension can be observed across the area between the source fault and RF7 and shortening within the footwall. In the thrust fault model (V1$_{tf}$), shortening can be found within the hanging wall, and across the source fault, but extension across RF4 and within the hanging wall. In the third month, the velocity field in the normal fault model already shows extension across the source fault and a zone of uplift at the same area. In the sixth month, the velocities of the normal fault model are one magnitude higher compared to the reference model. In the thrust fault model, shortening occurs across RF5 and a zone of subsidence appears between RF5 and the source fault.

The velocity field of the first year shows two zones of subsidence around RF5 and RF7 in the normal fault model, shortening across RF5 and extension within the footwall and hanging wall, with velocities similar to the reference model. The thrust fault model shows extension across the source fault as well as several zones of either extension or shortening around the receiver faults. The vertical velocity field shows major zones of uplift. In the second year, the surface extends across the source fault and subsides around the faults in the normal fault model and *vice versa* in the thrust fault model, while a zone of uplift appears at the normal source fault and subsidence between the thrust source fault and RF5. Until the 50th year, in both models, the velocities slowly decrease and the velocity field remains strongly disturbed around the faults and the disturbed areas expand. In the 50th year, the velocity field is dominated by the regional deformation.

In both normal and thrust fault models with a higher viscosity (V2$_{nf,tf}$, Figures 3.19a and 3.21), an almost identical evolution of the stress field patterns and magnitudes as in the reference models can be observed in the first five years after the earthquake. From the fifth year onward,

homogeneously distributed positive stress changes occur on all receiver fault planes with values of up to 0.025 MPa in both models, which remain constant over the following years. The source fault also shows solely a stress increase in both models with decreasing magnitudes from the fifth to the 50th year of 0.07 MPa to 0.03 MPa in the normal fault model and 0.2 MPa to 0.03 MPa in the thrust fault model. The velocity fields of both models (V2$_{nf,tf}$, Figures 3.19b and 3.22b) evolve similarly to the corresponding reference models R1$_{nf}$ and R1$_{tf}$ in the first two years after the earthquake. From the fifth year onward, the velocity fields of V2$_{nf}$ and V2$_{tf}$ do not show any considerable perturbations and the horizontal velocity field is dominated by the regional extension and shortening, respectively.

3.3.4 Endmember models with variable permeability and viscosity

In this model series, we present endmember models (PV1-4) with a combination of a high/low permeability of the upper crust with a low/high viscosity of the lower crust, based on the results of the previous sections to maximize or minimize the effects from the interaction of poroelastic effects and viscoelastic relaxation (Figures 3.23-3.26, 3.27-3.30).

The stress field pattern of the normal fault model PV1$_{nf}$ with a high permeability and a low viscosity (Figure 3.23) mostly resembles the stress field pattern of model P1$_{nf}$ in the first month, with the difference that the stress on the source fault and RF1, RF4 and RF9 solely increases. The magnitudes of the Coulomb stress changes on the receiver faults on the hanging wall are similar to model P1$_{nf}$ and the stress changes on the other faults are similar or slightly higher than in model V1$_{nf}$. The highest stress increase can be found on RF5 (2.5 MPa). The stress field pattern and magnitudes of the thrust fault model PV1$_{tf}$ (Figure 3.27) are similar to model P1$_{tf}$. In the second month the stress changes on the receiver faults of both models decrease by one order of magnitude and the pattern resembles the stress field pattern of the sixth month of model V1$_{nf}$ and V1$_{tf}$ with one or two zones of negative stress changes on most faults. The thrust fault model shows additional zones of stress decrease on RF2-3 and RF10-11. There are no significant changes of the stress field in the following months in both models. From the first to the 50th year after the earthquake, the stress field of PV1$_{nf}$ evolves similarly to model V1$_{nf}$. Differences can be found in the first year and the fifth year. The magnitudes of the stress changes are slightly lower on some faults of model PV1$_{nf}$ in the first year and RF7 and RF8 show a different stress field pattern with a mix of positive and negative stress changes. In the fifth year, the Coulomb stress pattern on the source fault, on RF1, RF4, RF7 and RF9 differs from model V1$_{nf}$. RF1 and RF9 show two areas of negative stress changes near RF4 and RF4

exhibits solely negative stress changes. The magnitudes are lower on all three faults. The stress on the source fault and RF7 solely increases with higher magnitudes on the source fault. In the thrust fault model, the stress field pattern of the first year after the earthquake mostly resembles model $V1_{tf}$, but the stress change magnitudes are lower and the stress change distribution differs on most faults. All faults, except the source fault, experience a mixed pattern of positive and at least a small area of negative stress changes. From the second year until the 50th year, the Coulomb stress changes evolve similarly to model $V1_{tf}$, showing the same pattern and magnitudes.

In models $PV2_{nf,tf}$ (Figures 3.24, 3.28) we combined a low permeability with a high viscosity. In the first month, the stress field shows a mixed pattern of positive and negative stress changes on almost all normal receiver faults, except RF3 and RF11 and on all thrust receiver faults within the hanging wall and RF7 and RF8. The patterns in both models change only negligible over the next months, and resembles the patterns of model $V1_{nf,tf}$ in the sixth month, RF7 on the normal fault turns into solely positive stress changes. The magnitudes are lower than the magnitudes in Model $V1_{nf,tf}$ in the first month, but the decrease of magnitudes is slower, hence, the magnitudes are higher compared to models $V1_{nf,tf}$ in the sixth month. In the first year in the normal fault model, RF8, the receiver faults on the hanging wall and along-strike of the source fault show positive and negative stress changes, the magnitudes are similar to the magnitudes of model $V1_{nf}$ on most faults, but lower on RF7. Over the years, the evolution of the stress change pattern mostly resembles model $V1_{nf}$, but the magnitudes always remain higher. In the thrust fault model, all receiver faults except RF2 and RF10 experience both, positive and negative stress changes in the first month, with magnitudes lower compared to model $V1_{tf}$. From the second year onward, the stress field pattern and evolution resemble model $V1_{tf}$, but with higher magnitudes. In the 50th year, the source fault still shows parts of negative stress changes.

Both models with a high permeability and a high viscosity ($PV3_{nf,tf}$, Figures 3.25, 3.29) resemble the Coulomb stress evolution of model $P1_{nf,tf}$ with the same stress change magnitudes in the first two months and in the first year after the earthquake. In the following months and decades, solely positive Coulomb stress changes can be observed on all faults in both models, similar to model $V1_{nf,tf}$ from the fifth year onward. The source faults still show higher values of 0.1 and 0.2 MPa in the normal and thrust fault model, respectively, which decrease over the years. The receiver faults exhibit a homogeneous Coulomb stress change distribution with a stress increase between 0.015 to 0.025 MPa in both models.

Models PV4$_{nf,tf}$ with a low permeability and a high viscosity (Figures 3.26, 3.30), mostly resemble the stress field evolution of model P3$_{nf,tf}$ in the early postseismic phase. From the second year onwards, the zones of negative stress changes on the receiver faults parallel to the source fault turn into positive stress zones in the 10th year in the normal fault model. The stress change magnitudes are lower compared to model P3$_{nf}$ in the second up to the 10th year, but again similar from the 10th year onward. In the thrust fault model, RF5 and the source fault still show parts of negative stress changes until the 50th year and the magnitudes evolve similarly to model P3$_{tf}$.

3.4 Discussion

Our models with different permeabilities and viscosities provide insights into Coulomb stress changes arising from coseismic slip, poroelastic effects, postseismic viscoelastic relaxation and interseismic stress accumulation. In the following, we evaluate the main findings of our models and the relative importance of poroelastic effects and postseismic viscoelastic relaxation for the generation and evolution of postseismic Coulomb stress changes. We also link the postseismic Coulomb stress changes to the postseismic surface deformation. Afterwards, we compare our modeled Coulomb stress change patterns with stress change analyses for natural faults and earthquakes.

3.4.1 Relative importance of poroelastic effects and viscoelastic relaxation

The model results show that the static Coulomb stress changes are significantly altered through space and time by both, poroelastic effects and viscoelastic relaxation immediately after the earthquake. The distribution, magnitude and evolution of the postseismic Coulomb stress changes are controlled by the permeability of the upper crust, the viscosity of the lower crust as well as the position of the receiver faults relative to the source fault. In the first months after the earthquake, models considering poroelastic effects with and without viscoelastic relaxation (R1$_{nf,tf}$ and R2$_{nf,tf}$, respectively) reach stress change magnitudes of up to two orders higher compared to models that include only viscoelastic relaxation (R3$_{nf,tf}$) (Figures 3.3-3.10). The highest stress changes occur on the receiver faults closest to the source fault (up to 3 MPa, R1$_{tf}$), but the outermost receiver faults also show higher values of up to 0.4 MPa (R1$_{nf}$), which could be high enough to trigger another earthquake (King et al., 1994). Both models (R1$_{nf,tf}$ and R2$_{nf,tf}$), show the same stress field evolution in the first two years after the earthquake, which

indicate that poroelastic effects dominate the stress field in the early postseismic phase. In almost all models, the postseismic stress field is dominated by poroelastic effects in the early postseismic phase, leading to strong and spatially large signals, which overlap the signals from viscoelastic relaxation and interseismic stress accumulation for months to several years, if the viscosity is high enough. How long the poroelastic effects persist and cause Coulomb stress changes that are high enough to trigger earthquakes depends on the permeability of the crust and the associated pore pressure dissipation time. While poroelastic effects decay within two months in models with high permeabilities of 10^{-10} m^2 (P1$_{nf,tf}$, PV1$_{nf,tf}$, PV3$_{nf,tf}$) due to the fast fluid flow, they can be observed for two and more than ten years in models with a permeability of 10^{-12} m^2 (R1-2$_{nf,tf}$, V2$_{nf,tf}$) and 10^{-14} m^2 (P2$_{nf,tf}$), respectively. During these times, the Coulomb stress changes on RF5 are still high enough (>0.1 MPa) to potentially trigger another earthquake. The magnitudes of stress changes due to poroelastic effects decrease with decreasing permeabilities by one order of magnitude between permeabilities of 10^{-12} m^2 and 10^{-16} m^2. In models with a permeability of 10^{-16} m^2 (P3$_{nf,tf}$, PV2$_{nf,tf}$, PV4$_{nf,tf}$), poroelastic effects still overlap with viscoelastic relaxation and interseismic stress accumulation for up to 50 years, but are only high enough to trigger another earthquake on RF5 or RF7 up to the 10th (normal fault) and 20th year (thrust fault). Therefore, the poroelastic effects observed in our models act on timescales that overlap with the spatio-temporal evolution of the postseismic viscoelastic relaxation process. The Coulomb stress distribution of the models including only viscoelastic relaxation but no fluid flow (R3$_{nf,tf}$) indicates that the influence of viscoelastic relaxation on the stress field is already recognizable in the first month, but the Coulomb stress changes due to viscoelastic relaxation are lower and hence overlapped by the stress changes caused by poroelastic effects. As soon as the poroelastic effects decay, the viscoelastic relaxation signal starts to dominate the stress field (Figures 3.3-3.10). High viscosities in the lower crust of 10^{22} Pa s (V2$_{nf,tf}$, PV3-4$_{nf,tf}$) lead to increasing Coulomb stress changes, which remain constant over decades on all receiver faults with average values of 0.02 MPa and thus slightly higher than the values of the interseismic stress accumulation (0.01–0.02 MPa in our models). Models with a viscosity of 10^{20} Pa s additionally show negative stress changes on RF5 for decades. Both viscosity values lead to Coulomb stress changes, which still outweigh the continuous interseismic stress increase in the 50th year after the earthquake. In models with a low viscosity of 10^{18} Pa s (V1$_{nf,tf}$, PV1-2$_{nf,tf}$), the viscoelastic relaxation causes positive and negative Coulomb stress changes on all faults with higher values and a significant change of distribution and magnitude over time. The Coulomb stress changes are until the fifth year (normal fault) on RF2, RF5, RF7 and RF10 and until 10th year (thrust fault) on RF5 and RF7 high enough, to trigger

another earthquake on the receiver faults nearest to the source fault if the permeability is sufficiently high at the same time ($V1_{nf,tf}$, $PV1_{nf,tf}$). In these models, the viscosity is low enough that the signal from viscoelastic relaxation already starts to dominate the stress field from the third month onwards and overlaps the signal from poroelastic effects. Between the 20th and 50th year, the interseismic stress increase prevails the stress field. If the low viscosity is combined with a low permeability ($PV2_{nf,tf}$), viscoelastic relaxation dominates the stress field from the first month onward and the Coulomb stress changes are still high enough in the 10th year, to trigger another earthquake on RF7 (normal fault) and RF5 (thrust fault). This combination of permeability and viscosity in the crust highlight the possibility that viscoelastic relaxation may dominate already in the early postseismic phase. In models, which combine a low permeability with a high viscosity, the signals from both effects are weak but long-lasting, with the result that the Coulomb stress changes are still a superposition of stress changes caused by poroelastic effects, viscoelastic effects and interseismic stress accumulation in the 50th year. Based on our model results, poroelastic effects may affect the stress field for decades, if the permeability is sufficiently low and viscoelastic relaxation is already recognizable in the first month after the earthquake. Hence, poroelastic effects and viscoelastic relaxation interact over longer timescales than expected (e.g., Freed and Lin, 2001; Luo and Liu, 2010; Albano et al., 2017, 2019, 2021; Nespoli et al., 2018), which should be considered for the calculation of postseismic Coulomb stress changes.

3.4.2 Coulomb stress changes and surface deformation

Both, poroelastic effects and viscoelastic relaxation lead to considerable crustal movements around the source fault (cf. Peikert et al., 2022), which leave a signal in the vertical and horizontal surface displacement fields and cause the Coulomb stress changes and influence the stress field through space and time (Figures 3.11-3.30). The magnitudes of the stress changes strongly correlate with the velocities. If a model shows high surface velocities, it also experiences high Coulomb stress changes in the same area. A velocity decrease by one order of magnitude generally leads to a decrease of the stress change magnitude by one order. The movements in horizontal directions control the distribution of the Coulomb stress changes on the faults. Extension leads to positive stress changes on normal faults and negative stress changes on thrust faults, whereas areas of shortening experience negative stress changes on normal faults and positive stress changes on thrust faults (Bagge and Hampel, 2017). The

velocities and spatiotemporal evolution of the surface deformations strongly depend on the permeability and viscosities of the crust (Peikert et al., 2022).

Models with high permeabilities (R1$_{tf,nf}$, R2$_{tf,nf}$, P1$_{tf,nf}$, V2$_{tf,nf}$) show high surface velocities in the early postseismic phase, which are two magnitudes higher than surface velocities caused by only viscoelastic relaxation (R3$_{tf,nf}$). The highest movements can be found on RF5 and RF7, which experience the highest stress changes. In the early postseismic phase in the normal fault models, shortening between RF5 and the source fault as well as between RF7 and the source fault leads to negative stress changes on the upper part of RF5 and the lower part of RF7. In contrast, the other parts of these faults show positive stress changes due to the extension within the footwall and hanging wall. In most models, high velocity perturbations occur between the source fault and the receiver faults along strike to the source fault (RF2, RF10) in the early postseismic phase, caused by poroelastic effects. This leads to higher Coulomb stress changes at the parts of RF2 and RF10 near to the source fault. Due to the fast pore pressure diffusion, the velocities strongly change and the velocity field is dominated by the signal from viscoelastic relaxation and the regional extension and shortening from the third month (P1$_{nf,tf}$) and the fifth year (R1-2 $_{nf,tf}$, V2 $_{nf,tf}$) onwards. The model considering only viscoelastic relaxation but no pore fluid pressure (R3$_{nf,tf}$) shows velocity perturbations with low velocities from the first month onward, which negligible changes over the next 50 years. This underlines that a signal from viscoelastic relaxation is already recognizable in the first month.

A lower permeability leads to prolonged pore pressure diffusion and hence to a slower change of the velocity and stress field magnitudes and pattern. The velocity field is affected by poroelastic effects until the 10th year in models with a permeability of 10^{-14} m^2 and until the 20th year in models with 10^{-16} m^2. As a result, the stress field shows a similar evolution. The areas without significant velocity perturbations generally do not experience high Coulomb stress changes. For example, in the normal fault model with a permeability of 10^{-14} m^2, the velocity perturbations on the hanging wall of the source fault are limited to the area between the source fault and RF5, resulting in low Coulomb stress changes on the outer receiver faults of the hanging wall (RF1 and RF9). Caused by the strong viscoelastic relaxation, the surface velocity field is highly disturbed in models with a low viscosity (V1 $_{tf,nf}$), showing higher velocities until the 10th year and a pattern of several areas of extension and shortening, resulting in a mixed pattern of positive and negative stress changes on all faults parallel to the source fault. The surface velocity field is dominated by the signal from viscoelastic relaxation already in the third month and strongly changes within 20 years, similar to the stress field. In normal

fault models with a viscosity of 10^{20} Pa s in the upper crust, an area of shortening occurs within the hanging wall around RF5, after the poroelastic effects decayed, resulting in negative Coulomb stress changes on the upper part of RF5 until the 50th year. Both only change negligibly over time and overlap the regional extension field over 50 years. The rest of the model domain indicates enhanced extension similar to the regional extension field and hence solely positive stress changes with magnitudes, which are typical for the interseismic stress accumulation, controlled by the regional deformation (Bagge and Hampel 2017). A high viscosity of 10^{22} Pa s ($V2_{tf,nf}$) leads to weak, but long-lasting viscoelastic relaxation, which results in weak velocity perturbation and slow surface velocities over decades. The surface velocity field changes only negligibly over time. The Coulomb stress change magnitudes and distribution also do not change significantly over the decades. The velocity field pattern only slightly differs from the velocity field pattern caused by the regional extension and shortening and hence only experiences positive stress changes.

In most models, the surface velocity and stress field are dominated by poroelastic effects in the early postseismic phase (except $V1_{tf,nf}$ and $PV2_{tf,nf}$). The highest movements and stress changes can be found in the first month after the earthquake, following by a strong decrease of the velocities and stress change magnitudes in the following months, if the permeability is sufficiently high. As a result, the postseismic velocity and stress field integrated over one year, show elevated values and resemble the velocity and stress field of the first month, if the permeability is higher than 10^{-14} m^2 and hence include a strong signal from poroelastic effects, which overlap and is much stronger than the signal from incipient viscoelastic relaxation. Therefore, it is important to choose the right time interval for the calculation of Coulomb stress changes and for the analysis of postseismic velocity fields derived from geodetic data. In some cases, the poroelastic effects do not have largely disappeared in the early postseismic phase (Peikert et al., 2022) and the postseismic velocity field cannot be interpreted to reflect solely the signal from incipient viscoelastic relaxation (e.g., Aoudia et al., 2003; Liu-Zeng et al., 2020; Mandler et al., 2021).

3.4.3 Comparison with Coulomb stress changes for natural intra-continental earthquakes

To evaluate the seismic hazard of a region, Coulomb stress changes are routinely calculated after major earthquakes, mostly focusing on static Coulomb stress changes. Aftershocks, however, can may occur a few days to months to years after the main earthquake, which requires to consider postseismic transient processes, as demonstrated by our study. Most previous

studies, however, focused on a specific time interval and therefore restricted their analysis to a combination of static stress changes with either pore fluid pressure changes (Albano et al., 2017, 2019; Antonioli et al., 2005; Tung et al., 2018a) or postseismic viscoelastic relaxation (e.g., Luo and Lui, 2010; Bagge and Hampel, 2017, Wang et al., 2014). Only a limited number of studies considered static and both types of transient Coulomb stress changes in their analyses (Freed and Lin, 2001; Masterlark and Wang, 2002; Barbot and Fialko, 2010; Tung and Masterlark, 2018; Zhu and Miao, 2015). In the following, we qualitatively compare our findings with Coulomb stress calculations from natural dip-slip earthquakes with respect to the relative importance and spatio-temporal evolution of poroelastic effects and viscoelastic relaxation for aftershock triggering.

For example, Zhu and Miao (2015) analyzed the six months aftershock sequence of the 2013 Lushan Earthquake, concentrated in a 40 x 15 km wide, NE-SW oriented area around the mainshock at depths between 10 and 22 km. They showed that most of the aftershocks occurred in areas with negative static Coulomb stress changes and hence, were not directly triggered by coseismic static Coulomb failure stress changes due to the Lushan mainshock. The authors assumed that aftershocks may have been triggered by postseismic stress transfer produced by changes of pore pressure and fluid flow but they excluded viscoelastic relaxation as a mechanism. Our models indicate that poroelastic effects strongly alter the stress field immediately after the earthquake and positive stress changes are found in areas on the receiver faults near the source fault, which experience negative static stress changes before (cf. Piombo et al., 2005). The area investigated by Zhu and Miao (2015) is comparable to the position of the receiver faults RF2, RF5, RF7 and RF10 in our models. In most of our models, these faults experience a considerable stress increase at the corresponding depths caused by poroelastic effects in the first six months.

Other examples of dip-slip earthquakes, for which aftershock triggering by static versus transient stress changes was evaluated, include the 1997 Umbria-Marche and the 2016 Amatrice-Visso-Norcia earthquake sequences in the Central Apennines, Italy. As shown by Cocco et al. (2000), the three largest earthquakes of the 1997 Umbria-Marche sequence may have been triggered solely by static Coulomb stress changes. However, the agreement between modeled and observed spatial patterns of the entire earthquake series was further increased by considering enhanced fluid flow (Cocco et al., 2000). Later, Antonioli et al. (2005) confirmed that postseismic pore pressure relaxation played a crucial role in the evolution of aftershocks during the 1997 Umbria-Marche earthquake sequence, as most of the main shocks and

aftershocks occurred in areas where the pore pressure increased around the fault. The authors used a permeability of 7.4 x 10^{-12} m^2 for this area. As shown by our models, permeabilities of this order of magnitude may lead to strong poroelastic effects, which dominate the stress field from the first month to until at least the second year after the earthquake (Figures 3.3-3.6). Our finding agrees with the model results from Albano et al. (2017, 2019), who showed that considerable poroelastic effects with a strong impact on the stress field may occur in the early postseismic phase because earthquake-induced pore pressure gradients fully dissipate after a few days to a few months for sufficiently high permeability (Albano et al., 2017, 2019). In the Amatrice-Norcia earthquake sequence, the 26 October 2016 event occurred even before the fluid overpressure induced by the 24 August Amatrice event had fully dissipated (Albano et al., 2019).

In contrast, a low permeability of 10^{-16} m^2 for the crust beneath the Central Apennines was derived by Tung and Masterlark (2018), who calculated Coulomb stress changes for the 2016 Amatrice-Norcia earthquakes and found that poroelastic effects dominate the postseismic stress field and are responsible for the aftershock triggering. For such a permeability value, our model results indicate a considerably slower dissipation of the pore pressure with the consequence that poroelastic effects cause stress changes for several years if the viscosity of the lower crust is sufficiently high. However, Tung and Masterlark (2018) only considered viscoelastic behavior in the mantle and assumed that the contribution from viscoelastic relaxation is negligible. As Riva et al. (2007) and Aoudia et al. (2003) derived a viscosity of 10^{18} Pa s for the lower crust beneath the Central Apennines from the postseismic deformation after the 1997 Umbria-Marche earthquake sequence, we argue that viscoelastic relaxation has also contributed to aftershock triggering. This is illustrated by our model PV2$_{nf}$, which has a low permeability of 10^{-16} m^2 combined with a low viscosity of 10^{18} Pa s. For such a combination, poroelastic effects influence the stress field for several years due to slow pore pressure dissipation but are overprinted by the signal from viscoelastic relaxation already in the first month up to decades. This leads to higher Coulomb stress changes over larger distances, especially on the receiver faults along-strike and parallel to the source fault.

In summary, our findings imply that the analysis of static Coulomb stress changes may not be a reliable tool for predicting stress transfer after major earthquakes because poroelastic effects and viscoelastic relaxation may alter both the magnitude and spatial distribution of the coseismically induced Coulomb stress changes already during the first month after the earthquake. Both poroelastic effects and viscoelastic relaxation should be considered when

calculating Coulomb stress changes and analyzing geodetic measurements of earthquake-induced surface deformation. Transient processes should also be considered in the analysis of paleo-earthquake sequences (e.g., Verdecchia et al., 2018, Bagge et al., 2019) when the subsequent events occur on timescales of years to decades. As shown by our model results, such models should also account for interseismic stress accumulation because this process dominates the Coulomb stress change patterns after the signal from the transient process has disappeared.

3.5 Conclusions

We used 3D finite-element models of intra-continental normal and thrust faults including coseismic slip, poroelastic effects, postseismic viscoelastic relaxation and interseismic stress accumulation to investigate the relative importance of these processes for the spatio-temporal evolution of postseismic Coulomb stress changes. The models show that coseismic stress changes do not persist through the early postseismic phase but are considerably altered by poroelastic effects and viscoelastic relaxation within the first month after the earthquake. Poroelastic effects cause high Coulomb stress changes and dominate in the early postseismic phase, but may still influence the stress and surface velocity field several years after the earthquake for sufficiently low permeability. Postseismic viscoelastic relaxation can affect the surface deformation patterns and the stress field already in the first few months after the earthquake if the viscosity of the lower crust is low enough. Depending on the combination of upper-crustal permeability and lower-crustal viscosity, our results indicate that the signals from poroelastic effects and postseismic viscoelastic relaxation may overlap in the early postseismic phase for up to several years. Poroelastic effects and viscoelastic relaxation have a strong influence on the magnitudes and distribution of postseismic Coulomb stress changes and should be considered together with interseismic stress accumulation when analyzing Coulomb stress transfer between faults and analyzing geodetic data on postseismic surface deformation.

3.6 Acknowledgements

4. 3D finite-element modeling of the influence of friction coefficient, coseismic slip and deformation rate on Coulomb stress changes

In additional models, the importance of the friction coefficient, coseismic slip and deformation rate for co- and postseismic Coulomb stress changes are evaluated by varying these parameters. A friction coefficient of 0.4 is used, which is in the range of a typical value for intra-continental faults and Coulomb stress calculations (Collettini et al., 2009, Lin et al., 2011; Nostro et al., 1997; Ryder et al., 2012). Experiments with a lower slip of 1 m and a higher slip of 3 m are shown, which represent earthquakes of $M_w = 6.7$ and of $M_w = 7.0$, respectively. As alternative deformation rates, a value of 4 mm/a and 8 mm/a are used, representing typical deformation rates in tectonically active continental interiors (e.g., Bennett et al., 2003; D'Agostino et al. 2001, 2008; Zhang et al. 2004). In previous studies, all parameters had only a minor effect on the stress field and influenced mainly the magnitude of the stress changes (Bagge and Hampel, 2016). The coseismic Coulomb stress distributions of all models presented here are similar to the coseismic Coulomb stress change distribution of the reference model in Chapter 3 (Figure 3.2) and immediately changed in the first month, similar to the models in Chapter 3. Only the models with a lower or higher coseismic slip show lower or higher coseismic stress changes, respectively. Hence, only the postseismic Coulomb stress changes for different time intervals are shown. The models are compared to the 3D reference models $R1_{nf}$ and $R1_{tf}$ in Chapter 3 (Figures 3.3-3.6 and 3.7, 3.10).

4.1 Models with variable friction coefficient

A reduction of the friction coefficient to 0.4 (Figure 4.1a) leads to higher stress changes than in the reference model $R1_{nf}$ on the receiver faults of the hanging wall (RF1, 4, 5, 9) and along-strike to the source fault (RF2, 10). On the other faults, the magnitudes are lower or similar. The highest stress changes can be found on RF5 (2 MPa), the lowest stress changes occur on RF1 and RF9 (0.08 MPa). The thrust fault model (Figure 4.2a) shows a mixed pattern of positive and negative stress changes on RF2, RF5, RF7, RF10 and the source fault, the values on most receiver faults are slightly lower or higher compared to the thrust fault reference model $R1_{tf}$. Values between 3 MPa on RF5 and 0.25 MPa on RF1 and RF9 can be observed. In the second month, all receiver faults in the normal fault model turn into solely negative stress changes, except RF5. The stress changes decrease by up to two orders of magnitude to 0.1 on

120

RF5 and 0.02 on RF1 and RF9. In the third and sixth months, the stress changes further decrease, the patterns do not change. In the thrust fault model, the stress changes decrease by one order of magnitude in the second month and the patterns change, all receiver faults of the hanging wall and RF7 show positive and negative stress changes. In the following months, the magnitudes further decrease, in the third month, all faults except RF5, and in the sixth month,
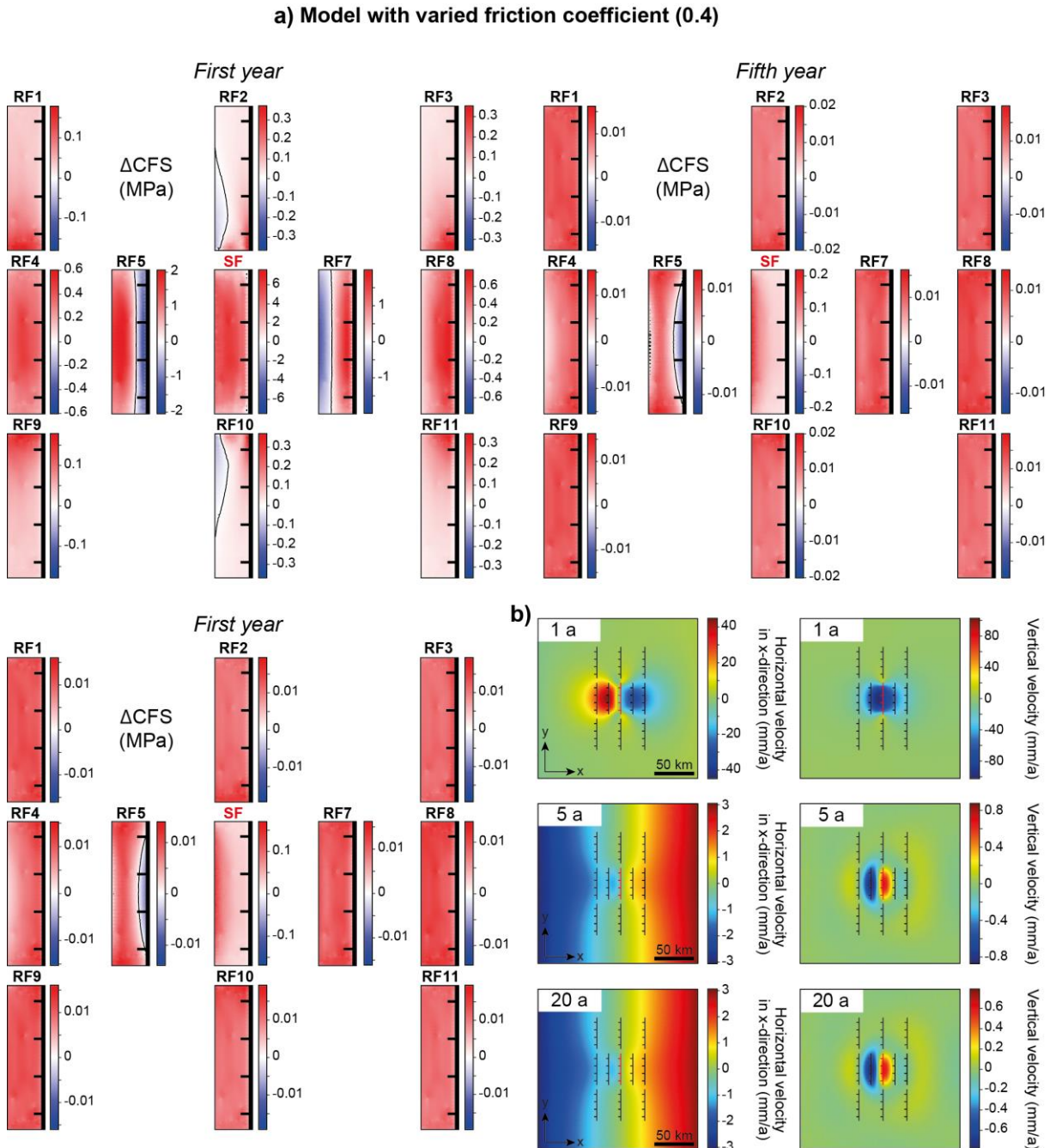

Figure 4.1: Normal fault model with a friction coefficient of 0.4 at different time intervals. **a)** Postseismic Coulomb stress changes. Distances between faults in the fault array are not to scale. **b)** Postseismic horizontal velocity field in x-direction and vertical velocity field.
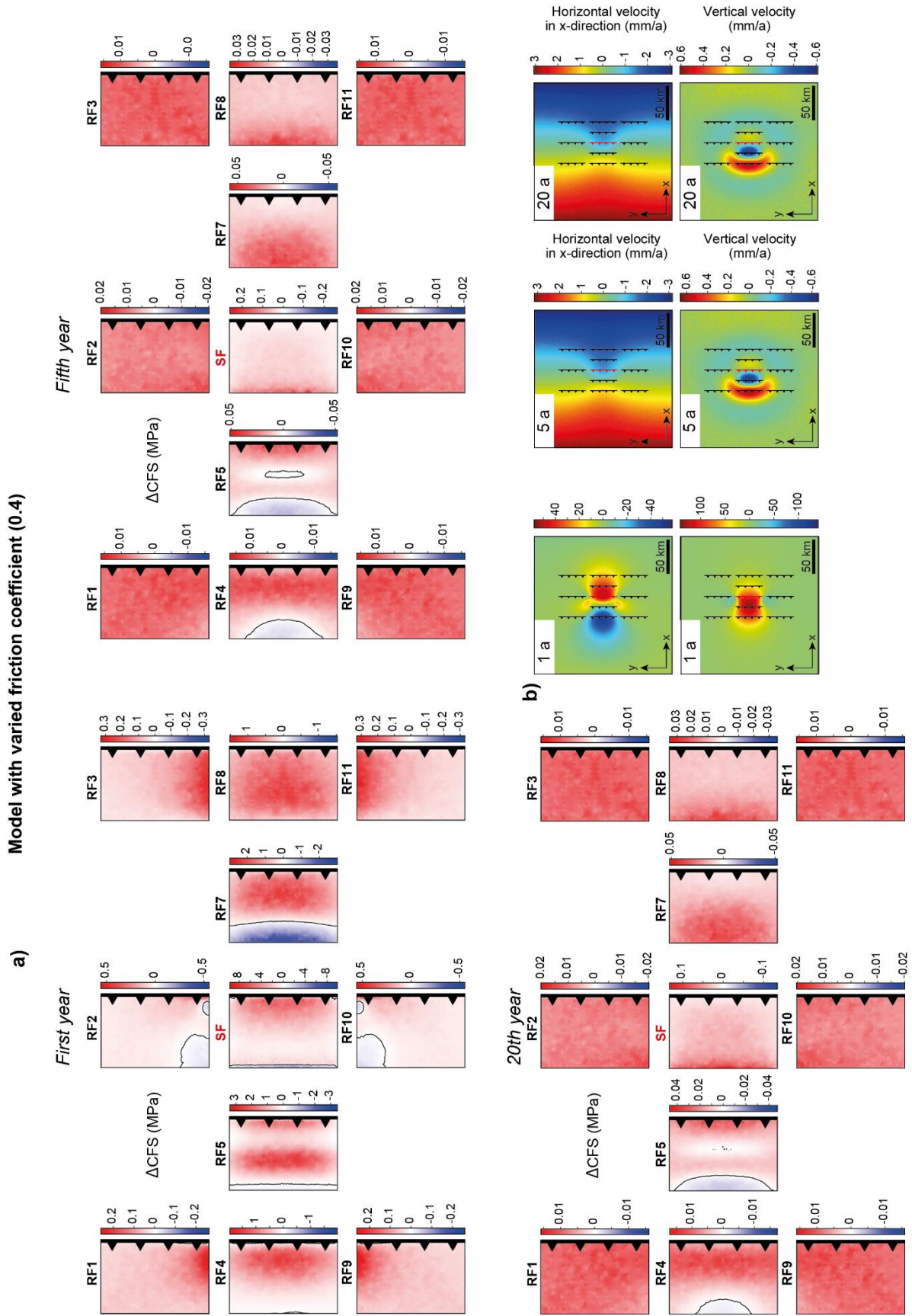
Figure 4.2: Thrust fault model with a friction coefficient of 0.4 at different time intervals. **a)** Postseismic Coulomb stress changes. Distances between faults in the fault array are not to scale. b) Postseismic horizontal velocity field in x-direction and vertical velocity field.

all faults except RF4 and RF5 show solely positive stress changes. In both normal and thrust fault models, the patterns in the first year completely resemble the first month and are also similar to the first year of the reference models $R1_{nf}$ and $R1_{tf}$, the magnitudes are slightly higher on most faults of the thrust fault model. In the following years up to the 50th year, the models evolve similarly to both reference models with slightly lower and higher magnitudes in each year in the normal and thrust fault models, respectively. The surface velocities of the normal fault (Figure 4.1b) and thrust fault (Figure 4.2b) models in the first month are similar to the reference models $R1_{nf}$, and $R1_{tf}$. The normal fault model shows shortening across the source fault and subsidence around the model center, extension across RF5 and uplift of the model center can be observed in the thrust fault model. In the second month, the velocities strongly decrease by one and two orders of magnitude in both models in horizontal and vertical direction, respectively. In the third month, the velocities decrease further, the horizontal velocity field changes direction to extension across the normal source fault and uplift of the normal source fault, while RF5 subsides. In the thrust fault model, it changes to shortening across the source fault and uplift of RF4 and subsidence of RF5 and the source fault. The first year in both models resembles the first month and evolves similarly to $R1_{nf}$ and $R1_{tf}$.

4.2 Models with variable coseismic slip

Figures 4.3a and 4.4a show the postseismic Coulomb stress changes for the models with a coseismic slip of 1 m. In the first month, the stress change pattern resembles the pattern of the reference model $R1_{nf}$, but the magnitudes of the stress changes on most faults are half those of the reference model, between 1.5 MPa on RF5 and 0.1 MPa on RF1 and RF9. In the second month, all faults, except RF5 experience solely positive stress changes and decrease by two orders of magnitudes to values between 0.08 MPa on RF5 and 0.02 on RF1 and RF9. Over the next month, the stress changes further decrease, in the sixth month, all faults are positive. In the thrust fault model, the source fault and all receiver faults next to the source fault experience both, positive and negative stress changes. On most faults, the stress changes are half of those of the reference model $R1_{tf}$. In the second month, the stress changes decrease by one order of magnitude and all receiver faults of the hanging wall and RF7 show a mixed pattern of positive and negative stress changes. In the third month, all faults experience solely positive stress changes, while in the sixth month, RF5 becomes partly negative at the lower part. The stress changes further decreased. The first year of the normal and thrust fault model resembles the first month of both models with lower stress changes compared to $R1_{nf}$ and $R1_{tf}$. From the fifth

123

year onwards, solely positive stress changes can be found on all normal faults with values up to 0.02 MPa and no changes over the following decades. In the thrust fault model, RF5 still shows positive and negative stress changes until the 20th year, the stress changes slowly decrease over the decades until they reach values of up to 0.025 MPa in the 50th year. The surface velocities of the first month in the normal (Figure 4.3b) and thrust fault (Figure 4.4b) models are lower than in $R1_{nf}$ and $R1_{tf}$, the patterns are similar. The velocities decrease by one order of magnitude in the second month in both models. In the normal fault model, the direction changes to extension across the source fault, uplift of the source fault and subsidence of RF5 in the third month. In the same month, the surface velocities of the thrust fault model switch to shortening across the fault, subsidence of the source fault and uplift of RF4. There are no significant changes between the third and the sixth month. The first year in the normal and thrust fault model resembles the first year of models $R1_{nf}$ and $R1_{tf}$ with velocities half of the reference models. The surface velocities evolve similarly to $R1_{nf}$ and $R1_{tf}$ until the 50th year.

The normal (Figure 4.5a) and thrust fault (Figure 4.6a) models with a coseismic slip of 3 m show higher stress change magnitudes, between 4 MPa on RF5 and RF7 and 0.3 MPa on RF1 and RF9 and a similar pattern compared to $R1_{nf}$ and $R1_{tf}$. In the second month, the stress changes decrease by one order of magnitude. In the normal fault model, a mix of positive and negative stress changes still can be found on RF5. In the third and sixth month, also RF4 experience positive and negative stress changes, the magnitudes on all faults decrease further. In the thrust fault model, positive and negative stress changes can be observed on all faults of the hanging wall, on RF7 and RF8 in the second month. In the third and sixth month, negative stress changes only remain on RF4 and RF5. The stress change distribution and magnitudes of the first year resemble the first month in both models. While in the second year of the normal fault model only RF5 shows a mixed pattern of positive and negative stress changes, a second negative zone of stress changes appears on RF4 in the fifth year. Both receiver faults remain positive and negative until the 50th year. From the first to the 50th year, the stress changes are higher than in model $R1_{nf}$. In the thrust fault model, the second year resembles the stress changes magnitudes and pattern of the second month with zones of negative stress changes only on RF4 and RF5. These zones remain until the 50th year, while the stress changes on all faults slowly decrease. The surface velocities (Figures 4.5b and 4.6b) in both models in the first month are higher compared to the reference models, while the patterns are similar. The velocity fields start to extend and shorten across the normal and thrust source faults, respectively, and show uplift of the normal source fault, subsidence of normal RF5 and a disturbed field of uplift and subsidence around the thrust source fault from the third month onwards. The evolution of the

surface velocities in the normal fault model over the years is similar to R1$_{nf}$, but the surface remains slightly more disturbed between RF5 and the source fault. The horizontal velocity field of the thrust fault model evolves similarly to R1$_{tf}$, while the vertical velocity field is more disturbed with a zone of uplift in the area of RF4 and R7 and subsidence between RF5 and the source fault.
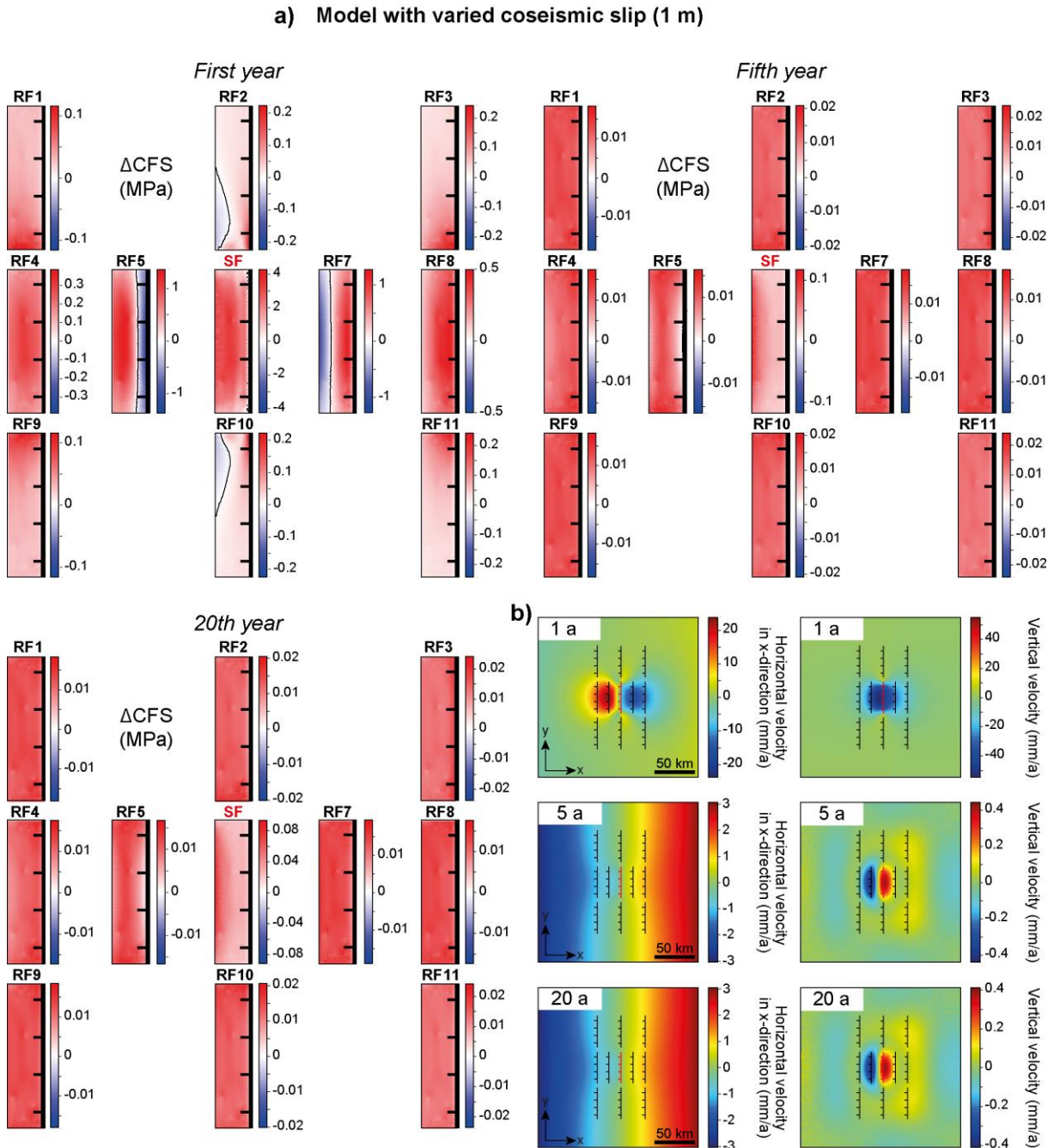
a) Model with varied coseismic slip (1 m)

Figure 4.3: Normal fault model with a coseismic slip of 1 m at different time intervals. **a)** Postseismic Coulomb stress changes. Distances between faults in the fault array are not to scale. b) Postseismic horizontal velocity field in x-direction and vertical velocity field.

125

Figure 4.4: Thrust fault model with a coseismic slip of 1 m at different time intervals. **a)** Postseismic Coulomb stress changes. Distances between faults in the fault array are not to scale. b) Postseismic horizontal velocity field in x-direction and vertical velocity field.

Figure 4.5: Normal fault model with a coseismic slip of 3 m at different time intervals. **a)** Postseismic Coulomb stress changes. Distances between faults in the fault array are not to scale. b) Postseismic horizontal velocity field in x-direction and vertical velocity field.
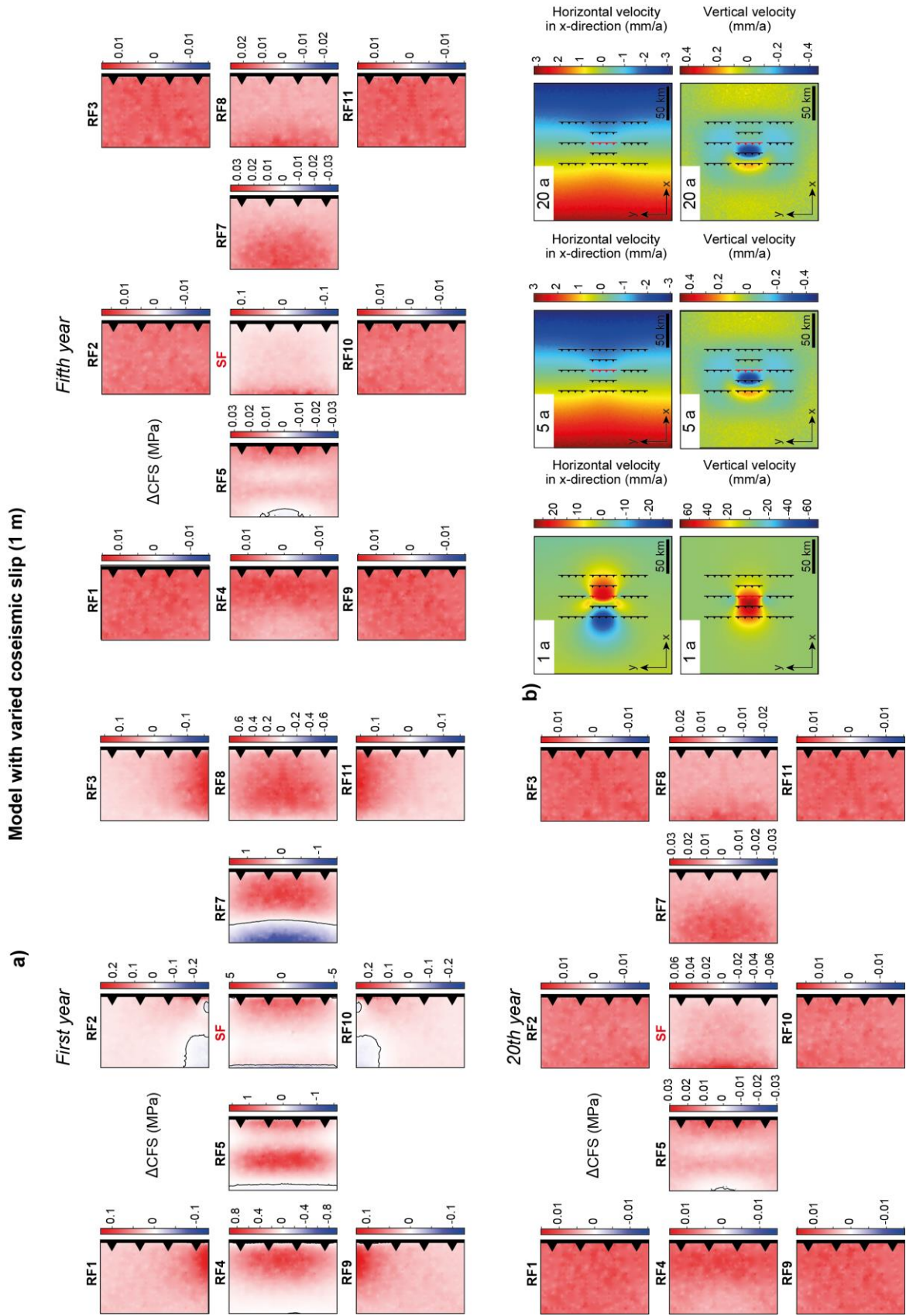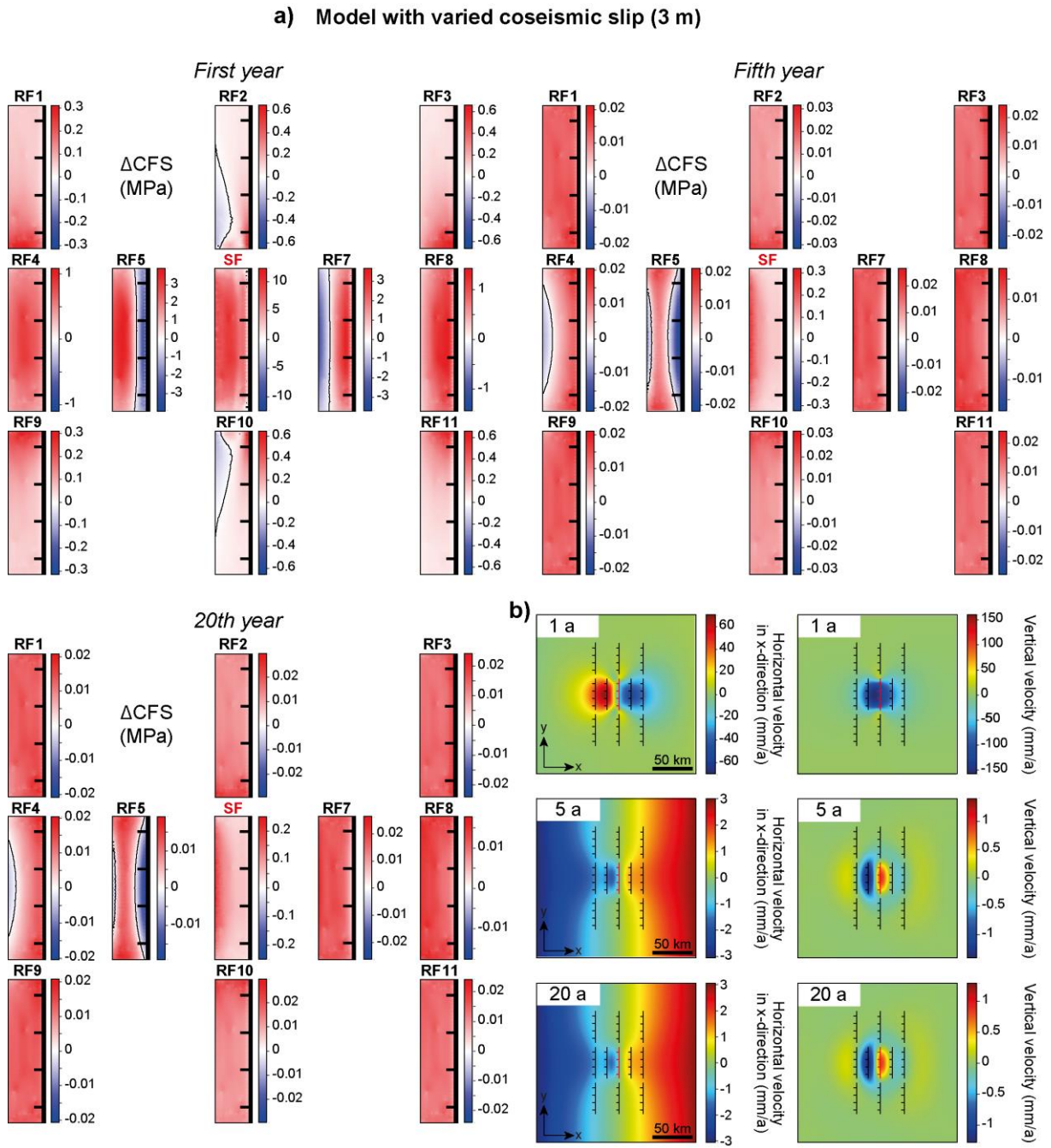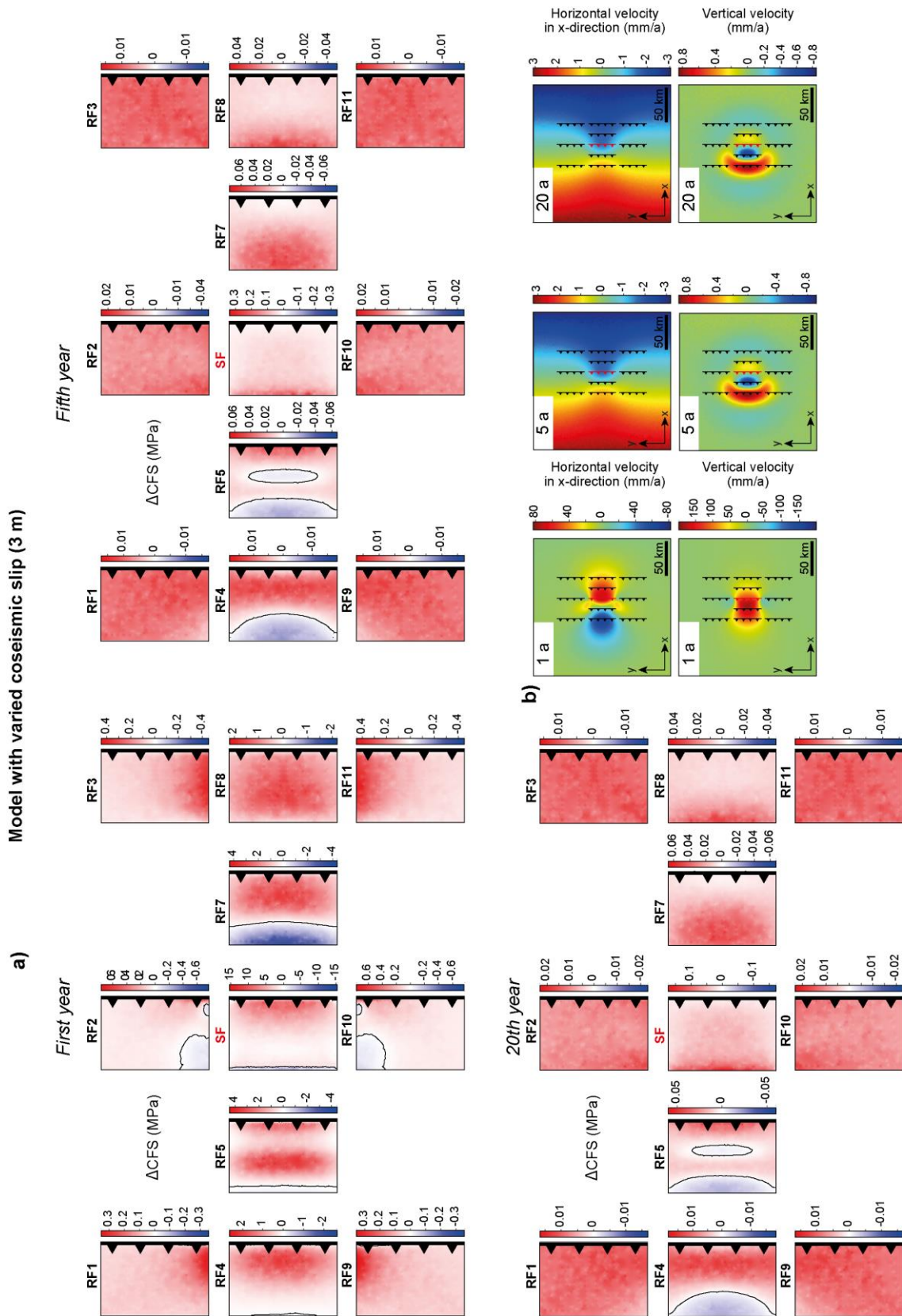
Figure 4.6: Thrust fault model with a coseismic slip of 3 m at different time intervals. **a)** Postseismic Coulomb stress changes. Distances between faults in the fault array are not to scale. b) Postseismic horizontal velocity field in x-direction and vertical velocity field.

128

4.3 Models with variable deformation rate

In the normal fault model with a lower extension rate of 4 mm/a in Figure 4.7a, higher Coulomb stress changes than in the reference model $R1_{nf}$ of up to 2.5 MPa (RF5) can be found on the receiver faults on the hanging wall and along-strike to the source fault in the first month. The Coulomb stress distribution is similar. In the second month, the stress changes reach magnitudes of up to one order lower than in model $R1_{nf}$, with a maximum of 0.15 MPa (RF5). All faults are positive, except RF5. In the third and sixth month, the magnitudes of the Coulomb stress changes further decrease and RF4 and RF5 experience a pattern of positive and negative stress changes. In the normal fault model, the stress change pattern and magnitudes of the first year resemble the reference model $R1_{nf}$. In the second year, the pattern is similar to model $R1_{nf}$ with the stress change magnitudes being slightly lower. From the fifth year onwards up to the 50th year, besides RF5, also RF4 shows positive and negative stress changes, the stress change magnitudes only slowly decrease with a maximum value of 0.02 MPa on RF2 and RF10, slightly lower than in $R1_{nf}$. The thrust fault model in Figure 4.8a shows a different evolution in the early postseismic phase, compared to the reference model $R1_{tf}$. In the first month, only RF2, RF5, RF7 and RF10 experience positive and negative stress changes, on most faults, the stress changes show slightly higher or lower magnitudes, with a maximum value of ~3 MPa on RF5 and RF7. In the second month, the stress changes decrease by one order of magnitude. In the third and sixth month, RF4 and RF5 still show positive and negative stress changes, which decreased to values up to 0.01 MPa. The pattern and magnitudes of the stress changes in the first and second year of the thrust fault model resemble the first month and the first and second year of the reference model $R1_{tf}$. In the fifth year, the pattern is similar, but the magnitudes are slightly lower than in $R1_{tf}$. Up to the 50th year, positive and negative stress changes can be found on RF4 and RF5 with magnitudes between 0.01 and 0.03 MPa. The surface displacements in both directions in the normal fault model (Figure 4.7b) show a similar pattern than the same month of the reference model $R1_{nf}$, but with slightly higher velocities. In the second month, the velocities strongly decrease by one order of magnitude. The pattern of the second month resembles the pattern of the sixth month of the reference model. The horizontal velocity field changes direction to extension across the source fault and the source fault starts to experience uplift in the third month. The surface displacements of the thrust fault model (Figure 4.8b) with a lower shortening rate are similar to the reference model $R1_{tf}$ in the first month but the velocities strongly decrease by one order of magnitude in the second month. The velocity field

a) Model with varied extension rate (4 mm/a)

Figure 4.7: Normal fault model with an extension rate of 4 mm/a at different time intervals. a) Postseismic Coulomb stress changes. Distances between faults in the fault array are not to scale. b) Postseismic horizontal velocity field in x-direction and vertical velocity field.

indicates a change to shortening across the fault and in the area between RF5 while the source fault starts to subside in the third month. From the first year until the 50th year, the evolution of the surface displacements in both models similar to $R1_{nf}$ and $R1_{tf}$.

Figure 4.8: Thrust fault model with a shortening rate of 4 mm/a at different time intervals. a) Postseismic Coulomb stress changes. Distances between faults in the fault array are not to scale. b) Postseismic horizontal velocity field in x-direction and vertical velocity field.
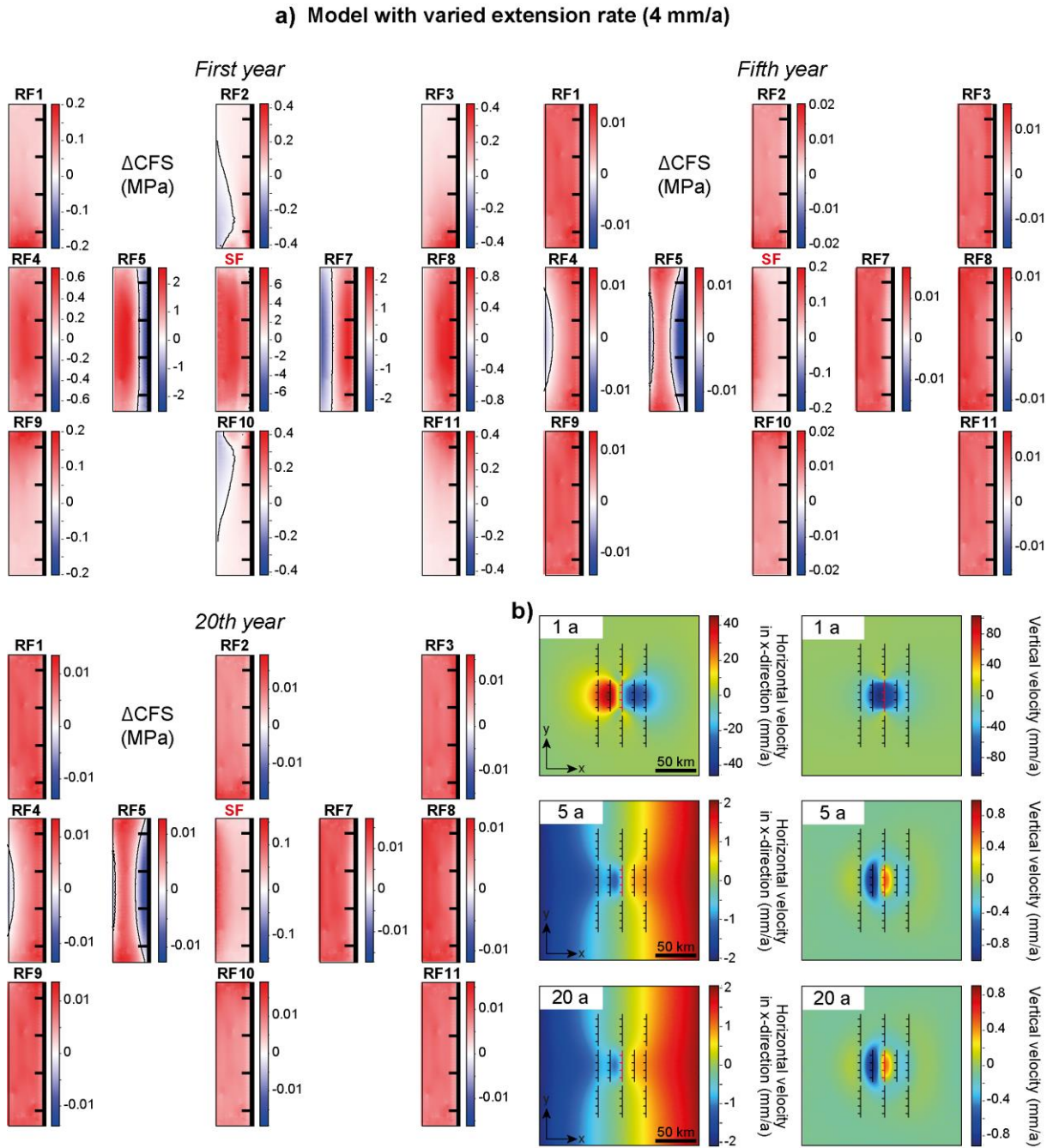
131
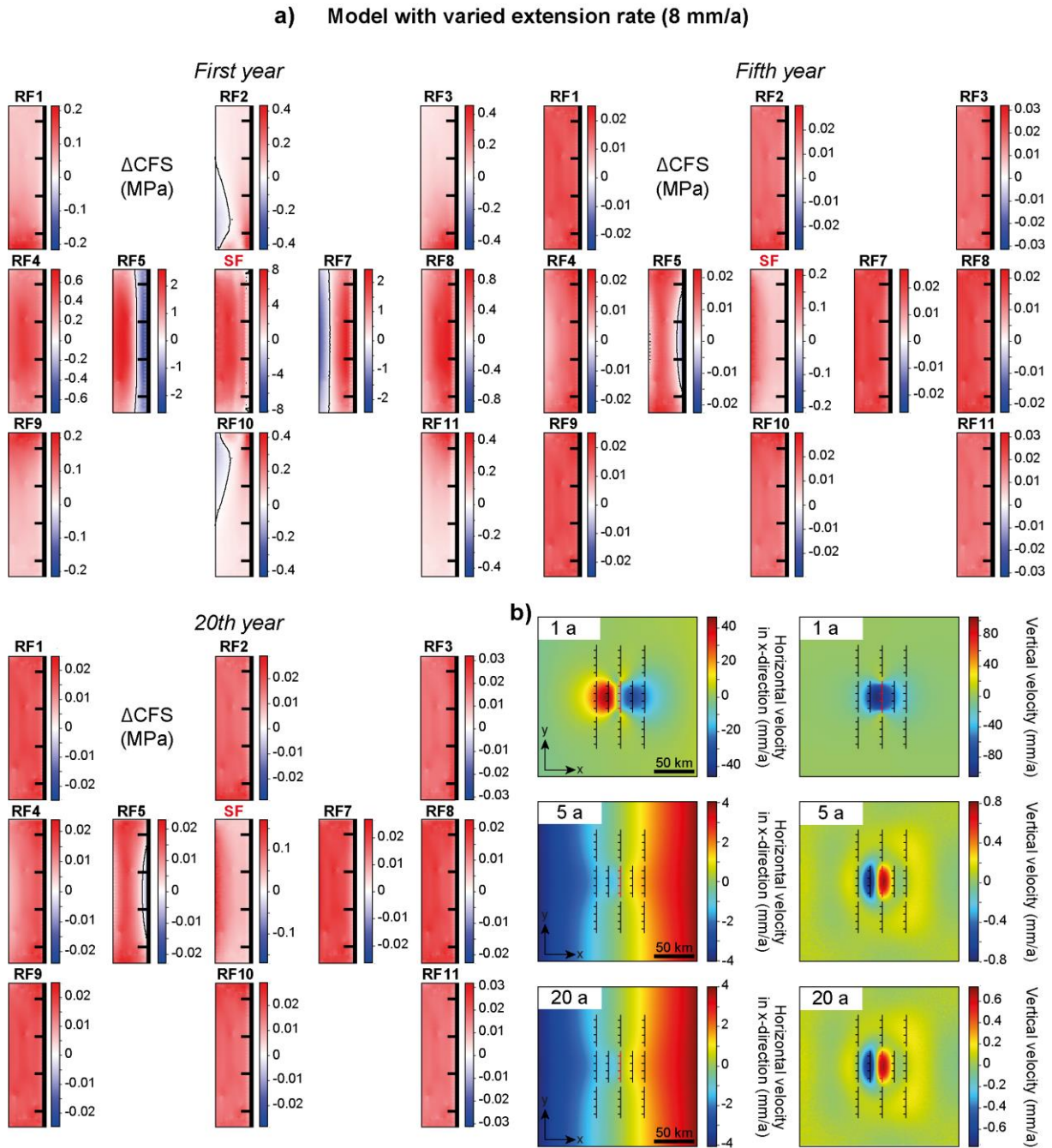
Figure 4.9: Normal fault model with an extension rate of 8 mm/a at different time intervals. a) Postseismic Coulomb stress changes. Distances between faults in the fault array are not to scale. b) Postseismic horizontal velocity field in x-direction and vertical velocity field.

Figure 4.9 shows the normal fault model with a higher extension rate of 8 mm/a. In the first month, the Coulomb stress changes on the hanging wall, on the source fault and along-strike to the source fault are slightly higher than in the reference model R1$_{nf}$ with a similar pattern (Figure 4.9a). In the second month, the Coulomb stress changes decrease by up to two orders of magnitudes, all faults, except RF5, experience positive stress changes, which further decrease
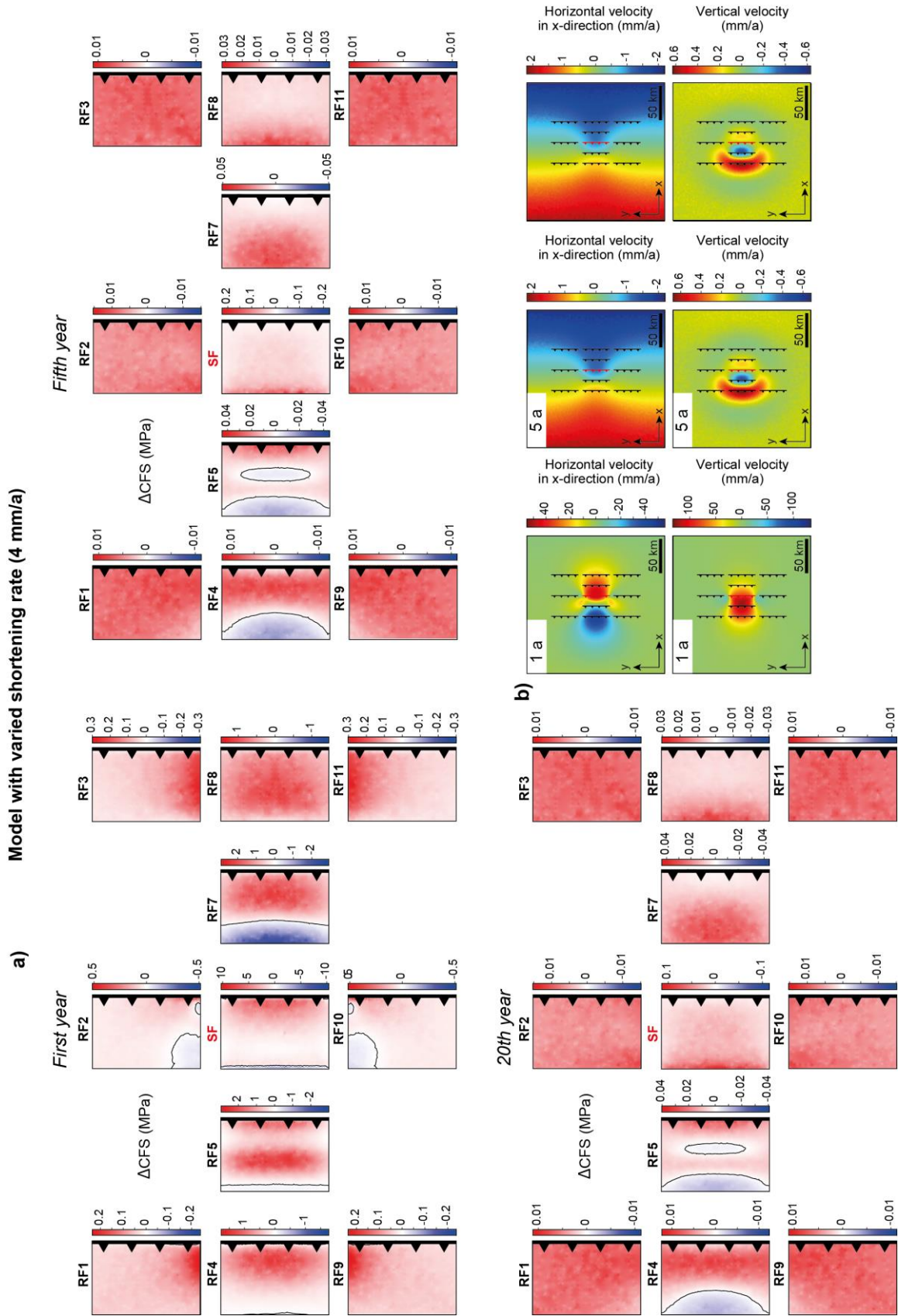
Figure 4.10: Thrust fault model with a shortening rate of 8 mm/a at different time intervals. a) Postseismic Coulomb stress changes. Distances between faults in the fault array are not to scale. b) Postseismic horizontal velocity field in x-direction and vertical velocity field.
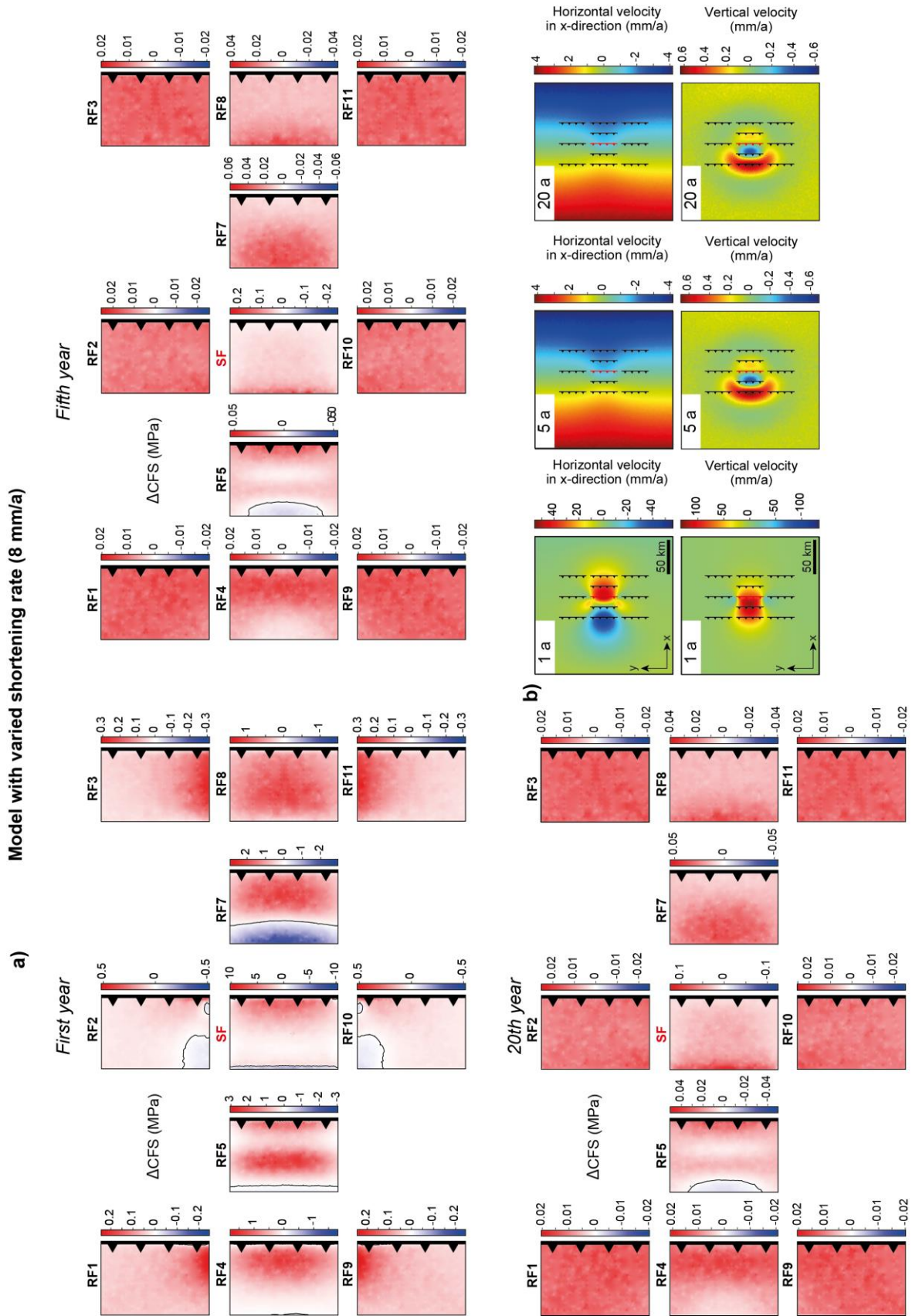
133

over the next months. The thrust fault model with a higher shortening rate of 8 mm/a (Figure 4.10) shows slightly higher or lower stress changes on most faults in the first month, compared to the reference model. Only RF2, RF5, RF7 and RF10 experience positive and negative stress changes. In the second month, the stress changes decrease by one order of magnitude, on the receiver faults of the hanging wall and RF7, a mixed pattern can be found. In the third month, all faults are positive, while in the sixth month, RF5 becomes partly negative again. The first year of both the normal and thrust fault models, resembles the first year of $R1_{nf}$ and $R1_{tf}$, respectively. The normal fault model evolves similarly to $R1_{nf}$, the thrust fault model only slightly differs from the evolution of $R1_{tf}$. The surface velocities of the normal fault model with a higher extension rate (Figure 4.9b) are a bit higher than in $R1_{nf}$ in the first month, but the pattern is similar. The velocities stronger decrease in the second month, the movements switch direction to extension across the source fault und uplift of the source fault in the third month. In the sixth month, the velocities are still one magnitude higher compared to $R1_{nf}$. The velocity fields of the first month of the thrust fault model with a higher shortening rate (Figure 4.10b) resemble $R1_{tf}$, in the second month, the velocities decrease by one order of magnitude in horizontal direction and two orders of magnitudes in vertical directions. In the third month, the horizontal velocity field changes direction to shortening across the fault. The area between RF5 and the source fault starts to subside, while the area around the source fault and RF4 still shows uplift. From the first to the 50th year, the evolution of the vertical and horizontal surface velocity fields in both models is similar to models $R1_{nf}$ and $R1_{tf}$, just with a higher regional extension rate.

5. Discussion

Based on 2D and 3D finite-element models with variable parameters, this thesis provides insights into the spatio-temporal evolution and the combined effect of pore fluid pressure changes and viscoelastic relaxation on the velocity and stress field during the earthquake cycle of normal and thrust faults. In a systematic parameter study, the influence of the different parameter on the model results have been evaluated in terms of postseismic pore pressure changes and vertical and horizontal velocities in a 2D model domain and in terms of co- and postseismic Coulomb stress changes as well as vertical and horizontal surface velocities in a 3D model domain. In the following, the main findings of the parameter study and the relative importance of the different parameters and processes are discussed. The modeled results of this thesis are compared with geodetic measurements, stress change analyses and the evolution of aftershocks for natural faults and earthquakes. Note, that the relative importance of poroelastic effects and viscoelastic relaxation, the influence of different permeabilities and viscosities on the velocity and stress field as well as the comparison with different analyses of GPS data and earthquake sequences are already discussed in some detail in Chapter 2.4 and 3.4. Finally, the limitations of both model domains and the applicability of the models for a specific earthquake, earthquake prediction and hazard assessments are discussed.

5.1 Relative importance of viscoelastic relaxation and poroelastic effects for the velocity and stress field

The sudden coseismic slip on the fault alters the pore pressure and leads to an over-pressurized and under-pressurized area on the hanging wall and footwall, respectively around the normal fault tip and *vice versa* around the thrust fault tip. The surface and crustal movements induced by the slip indicate in vertical direction hanging wall subsidence and footwall uplift in the normal fault model and hanging wall uplift and footwall subsidence in the thrust fault model. Horizontally, extension across the fault, but shortening within the hanging wall and footwall can be found in the normal fault model, whereas shortening across the fault and extension within the hanging wall and footwall occur in the thrust fault model. These are typical movements for normal and thrust fault earthquakes and are consistent with geological and geodetical observations from intra-continental dip-slip earthquakes (e.g., e.g. Cheloni et al., 2010; Chen et al. 2006; King and Vita-Finzi, 1981; Lin et al., 2009; Liu-Zeng et al., 2009; Serpelloni et al., 2012; Yu et al., 2001). The coseismic slip of 2 m causes a typical stress drop of 20-30 MPa on

the source fault in both models and mostly negative Coulomb stress changes on the other receiver faults. The largest coseismic increase of Coulomb stress can be found on the receiver faults along-strike of the source faults tips.

Already in the early postseismic phase, the coseismic displacement field is strongly altered by poroelastic effects, whereas the stress field is immediately influenced by both, poroelastic effects and viscoelastic relaxation, as shown by the reference models, which consider only one of the two processes, respectively (Figures 3.3-3.10). The highest stress changes and surface velocities occur on the receiver faults parallel to the source fault. The coseismically induced pore pressure changes normalize immediately after the earthquake by fluid diffusion with fluids flow from over-pressurized regions to under-pressurized regions (cf. Antonioli et al., 2005; Chiarabba et al., 2009). Poroelastic effects lead to strong velocity perturbations with surface and crustal movements of hanging wall and footwall subsidence as well as shortening across the fault in the normal fault model and uplift of both sides as well as extension across the fault in the thrust fault model. These vertical movements are also recognizable in literature (e.g., Mandler et al., 2021; Chen et al., 2006). Viscoelastic relaxation does not change the coseismic displacement pattern this way in the postseismic phase, which indicates that the strong postseismic movements observed in both normal and thrust fault models are only caused by poroelastic effects. The Coulomb stress distribution is immediately changed to mostly positive stress changes by both processes, but in models considering poroelastic effects Coulomb stress changes of up to two orders of magnitudes higher can be found compared to models with only viscoelastic relaxation. Hence, poroelastic effects lead to strong signals in the early postseismic phase on large spatial scales, which dominate the velocity and stress field. Signals from viscoelastic relaxation are already recognizable in the early postseismic phase as shown by the models considering only viscoelastic relaxation, but are overlapped by the stronger poroelastic effects.

The timescale in which poroelastic effects cause strong signals and dominate the velocity and stress field depends on the permeability in the upper crust, whereas a permeability of the lower crust has a negligible effect on the model results. High permeabilities between 10^{-10} m^2 and 10^{-14} m^2 lead to fast fluid flow dissipation times of a few months up to one year, within which the pore pressure is redistributed to hydrostatic conditions. This process influences the surface and crustal movements, in a way that the strong velocity perturbations strongly decrease and the pattern changes within the following few months up to the fifth year. Higher permeabilities also cause a strong decrease in the Coulomb stress magnitudes, but the stress changes on

receiver faults near the source fault are still high enough to potentially trigger another earthquake (>0.1 MPa) up to the 10th year (King et al., 1994). In contrast, models with low permeabilities (10^{-15} m^2 and 10^{-17} m^2) show slow pore pressure dissipation times of several decades, leading to weaker velocity perturbations, lower initial magnitudes and a slower decrease over time. Lower permeabilities affect the Coulomb stress distribution for decades, but the magnitudes are not high enough over the tenth year to trigger earthquakes.

The influence of viscoelastic relaxation on the velocity and stress field depends on the viscosity of the lower crust. Higher viscosities (>10^{20} Pa s) indicate weak velocity perturbations with low velocities, which barely change over the decades, and stress changes only slightly higher than the stress changes caused by the interseismic stress accumulation. Lower viscosities (<10^{20} Pa s) show a stronger effect on the velocity and stress field, causing strong velocity perturbations with higher velocities and high positive and negative Coulomb stress changes over long distances around the source fault, as shown in previous theoretical studies before (e.g., Bagge & Hampel 2017, Nostro et al., 2001). The velocities and Coulomb stress changes strongly decrease over the years, but are high enough until the 10th year to trigger another earthquake on the receiver faults near the source fault. In combination with a sufficiently low permeability in the upper crust, viscoelastic relaxation dominates the postseismic velocity and stress field in models with a low viscosity already in the early postseismic phase. In models with a combination of a low permeability and a high viscosity, poroelastic effects and viscoelastic relaxation are weak, but cause Coulomb stress changes, which overlap with interseismic stress accumulation for several decades. Depending on the permeability and viscosity structure in the crust, poroelastic effects may affect the velocity and stress field for longer than expected and viscoelastic relaxation may influence the velocity and stress field earlier than expected. Hence, both processes may interact and overlap over longer timescales than expected (e.g., Freed and Lin, 2001; Luo and Liu, 2010; Albano et al., 2017, 2019, 2021; Nespoli et al., 2018).

5.2 Relative importance of friction coefficient, coseismic slip and deformation rate for the velocity and stress field

The friction coefficients of 0.6 in the reference models and 0.4 in the parameter study are typical intermediate values used for Coulomb stress change calculations of intra-continental dip-slip faults (e.g., Bagge and Hampel, 2016, 2017; Freed, 2005; King et al., 1994; Lin et al., 2011; Nostro et al., 1997; Ryder et al., 2012) and are constant over the entire model run. The decrease

of the friction coefficient from 0.6 to 0.4 reduces the resistance to sliding and the time to reach a constant slip rate (Hampel and Hetzel, 2012). Hence, the length of the preseismic phase in the models is reduced in models with a lower friction coefficient. The reduction of the friction coefficient has only a minor effect on the stress distribution and only slightly changes the magnitude of the co- and postseismic Coulomb stress changes.

The models with varied extension/shortening rates show that the deformation rate only affects the magnitude of the Coulomb stress changes caused by the interseismic strain accumulation. An increase of the extension/shortening rate of a few mm/a leads to an increase of the Coulomb stress changes by a few MPa in the late postseismic phase and *vice versa*. The deformation rate affects how fast the model reaches a constant slip rate and either decreases or increases the length of the preseismic phase of the model run. The results indicate, that earthquakes with a coseismic slip of 2 m lead to similar Coulomb stress changes, regardless of whether the region is tectonically active with a fast deformation rate or a low-strain region. Strong earthquakes can therefore also occur in areas with a low extension/shortening rate if the required stress has accumulated over a sufficiently long period of time. While strong earthquakes, such as the $M_w = 7$ earthquake with a slip of 2 m in the models of this thesis, occur more frequently at plate boundaries with deformation rates of 10-100 mm/a, hundreds to thousands of years are required in continental interiors with low rates of a few mm/a, but the damage is the same or even significantly higher than at plate boundaries (England and Jackson, 2011).

The coseismic slip has the largest influence on the Coulomb stress magnitudes as well as the velocities, both are proportional to each other, respectively. A reduction of the coseismic slip to 1 m leads to a decrease of the co- and postseismic Coulomb stress magnitudes on all faults and a decrease of horizontal and vertical velocities by 50%. An increase of the coseismic slip by 50% to 3 m results in an increase of the stress change magnitudes and velocities by 50%. An increase or decrease of the coseismic slip also causes the Coulomb stress changes and velocities to decrease slower or faster, respectively, and the interseismic stress accumulation to dominate sooner or later.

5.3 Comparison with natural earthquakes

The Central Apennines and the northern Emilia-Romagna region in Italy are characterized by complex active faults that have experienced a series of moderate to strong dip-slip earthquakes (Figure 5.1a). The 1997 Umbria-Marche, the 2009 L'Aquila, the 2012 Emilia-Romagna and the 2016 Amatrice-Visso-Norcia seismic sequences with magnitudes between $M_w = 5$ and

$M_w = 6$ were investigated by a number of studies, which analyzed the role of different transient processes for the deformation and stress field and aftershock distribution (Albano et al., 2017, 2019; Antonioli et al., 2005; Chiarabba et al., 2009; Cocco et al., 2000; Mandler et al., 2021; Riva et al., 2007; Tung and Masterlark, 2018). These studies came to different results, though most of them came to the conclusion that solely static Coulomb stress changes cannot explain the observed deformation pattern and distribution of aftershocks, but that poroelastic effects and viscoelastic relaxation play significant roles. For example, only three of eight earthquakes of the 1997 Umbria-Marche normal fault seismic sequence are located in areas with positive static stress changes (Cocco et al., 2000) and some early aftershocks of the 2009 L'Aquila earthquake occurred in regions with negative static stress changes in the near-field and remain unexplained (Figure 5.1b, Serpelloni et al., 2012). Investigations of the aftershock distribution in the first 40 days after the Umbria-Marche earthquake with different model techniques showed, that the migration of aftershocks is consistent with the modeled fluid flow and pore pressure evolution (Antonioli et al., 2005; Chiarabba et al., 2009). Antonioli et al. (2005) derived a high permeability of 7.4×10^{12} m^2 for the study area. Both studies neglected viscoelastic relaxation. Based on the forward modeling by Riva et al. (2007), the observed postseismic deformation in the same region can be explained by postseismic viscoelastic relaxation. Their models containing poroelastic effects do not fit the observed deformation, the signal is much smaller than the observed GPS deformation. However, they used extreme values for the Poisson ratios, which influenced the results. They also used GPS measurements between the third and sixth year and not from the beginning of the postseismic phase and a low viscosity value of 10^{18} Pa s for the crust. Following the permeability and viscosity values used in these studies, the model with a high permeability and a low viscosity in this thesis (V1 or PV1, Chapter 3, Figures 3.18 or 3.23) agrees with the findings of Riva et al. (2007), that the signal of poroelastic effects in the velocity field disappeared between the second and fifth postseismic year and that viscoelastic relaxation has a strong effect on the velocities. However, the models show, that poroelastic effects still have an influence on the Coulomb stress field until the fifth year. Although Riva et al. (2007) did not investigate Coulomb stress changes, it should be considered that poroelastic effects are effective over longer time scales. Due to the high permeability, poroelastic effects dominate the stress and velocity field in the early postseismic phase, but for such low viscosities in the region, described in several studies (e.g. Aoudia et al., 2003; Mandler et al., 2021; Riva et al. 2007; Tung and Masterlark, 2018), viscoelastic relaxation also plays a role in the early postseismic phase and should not be neglected, as done by Antonioli et al. (2005) and Chiarabba et al. (2009).

GPS data of the horizontal velocity field after the $M_w = 6.3$ L'Aquila earthquake indicate a non-linear time-dependent velocity decrease until the third month, after which the observed velocities become linear again, but the velocities are still disturbed after two years. This non-linear transient phase in the velocity field may be connected to postseismic viscoelastic relaxation (Cenni et al., 2012). This observation for the velocity field is consistent with the modeled evolution of the velocity fields in this thesis, which experience a non-linear evolution especially in the first few months after the earthquake. But the models show, that this non-linear evolution is caused by poroelastic effects and the time during which the velocities become linear again depends on the permeability. The observations of the non-linear, exponential decrease of the velocities within the first months by Cenni et al. (2012) could be an indication of a high permeability (10^{-12} m^2 to 10^{-13} m^2) in this region, following the models in this thesis. This observation is also an example, as indicated in this thesis, that it is important to choose the right time interval for the analysis of postseismic geodetic data, because integrated over a specific period of time, for example, one year, the non-linear signals often overlap the linear signals and the velocity field could then be misinterpreted.

Other studies also explain their results with only one transient effect, although a part of them take both processes into account. By using finite-element models with different permeabilities, Albano et al. (2017, 1019) provided, that poroelastic effects drive the occurrence of aftershocks in the early postseismic phase of the Emilia-Romagna and Amatrice-Visso-Norcia seismic sequences, related to the pore pressure dissipation process and hence the permeability. Earthquake-induced pore pressure gradients fully dissipated after a few days to a few months, if the permeability is high enough, leading to strong poroelastic effects (Figure 5.1 c-d, Albano et al., 2017, 2019) with a strong effect on the stress field. The modelled deformation fits well with the observed postseismic deformation after the Emilia-Romagna earthquake, indicating uplift in the early postseismic phase and even after two years. This deformation pattern is consistent with the model in this thesis with the same permeability (10^{-14} m^2 to 10^{-15} m^2) used by Albano et al. (2017). For the 2016 Amatrice-Visso-Norcia, earthquakes, the 26 October 2016 $M_w = 5.9$ Visso earthquake occurred when the fluid overpressure induced by the 24 August $M_w = 6.0$ Amatrice earthquake had not yet fully dissipated (Albano et al., 2019). However, several aftershocks shown by Albano et al., (2017, 2019) are still located in areas with negative stress changes (Figure 5.1e) and they totally ignore the viscoelastic relaxation process, which should be considered, following the low viscosity structure, which has a strong impact on the velocity and stress field already from the second month onwards. Tung and Masterlark (2018), who investigated the spatio-temporal evolution of aftershocks after the Amatrice earthquake
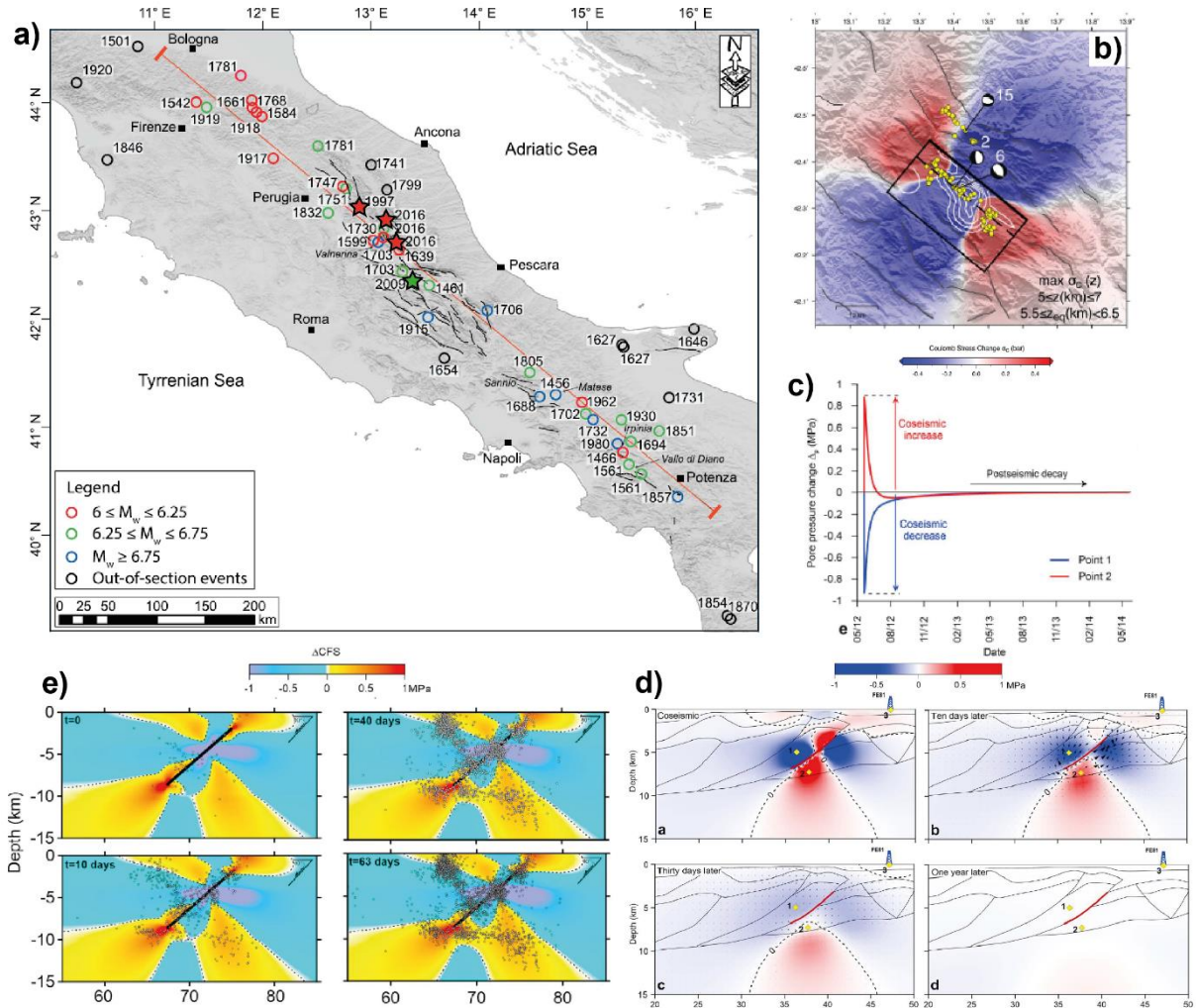
Figure 5.1: Overview of earthquake sequences in Central Italy. a) Map of $M_w>6$ historical earthquakes along the Apennines, stars show the 1997 Umbria-Marche sequence, the 2009 L'Aquila earthquake and the 2016 Amatrice-Visso sequence (modified from Verdecchia et al., 2018). b) Static Coulomb stress changes at a 5 to 7 km depth interval and aftershocks in the first week after the L'Aquila earthquake (modified from Serpelloni et al., 2012). c-d) Coseismic and postseismic pore pressure changes and decay modeled for one year after the Emilia-Romagna earthquake (modified from Albano et al., 2017). e) Modeled postseismic Coulomb stress changes and aftershocks up to the 63rd day after the Amatrice earthquake (modified from Albano et al., 2019).

with 3D finite-element models agreed with the results from Albano et al. (2019), the aftershock migration fit with the pore pressure migration, the best results are achieved with a relatively low permeability of 10^{-16} m^2. Tung and Masterlark (2018) also calculate Coulomb stress changes from viscoelastic relaxation, but argued that this component can be neglected, because the contribution for the stress field is too small. However, they only considered viscoelastic behavior in the mantle and not in the lower crust. That the viscosity of the lower crust plays an important role for the velocity and stress field, is shown in this thesis and already by previous studies (e.g., Bagge et al., 2017; Hampel and Hetzel, 2016). Model PV2 in this thesis (Chapter

3, Figure 3.24) is comparable with the permeability and viscosity structure and indicates, that especially in the case of a low permeability, used by Tung and Masterlark (2018), it is important to consider viscoelastic relaxation, because the viscoelastic relaxation already dominate the stress field in the first month, if the viscosity in the lower crust is low enough, as in the region of the Central Apennines, whereas poroelastic effects are weak, but recognizable for decades.

For the 2015 $M_w = 7.8$ Gorkha thrust earthquake on the Central Himalayan (Figure 5.2) thrust Coulomb stress changes as well as aftershock distribution and postseismic deformation in consideration of one or both of the two processes are investigated by different studies (Tung et al., 2018a; Wang and Fialko, 2018; Yadav et al., 2018; Yang et al., 2018; Zhao et al., 2017). A calculation of static Coulomb stress changes at different depths by Yang et al. (2018) showed, that most of the aftershocks occurred in areas of positive static Coulomb stress changes, 70% in an area 150 km east of the main shock. Some aftershocks can be found in zones of negative stress changes. There are also areas with high positive stress changes, but only little aftershock occurrence (Figure 5.2b). These uncertainties are explained by the simplification of the actual complex fault geometry plane and the used parameters and it is suggested that dynamic stress changes or pre-stress could play a role in the occurrence of aftershocks (Yang et al., 2018). That the Coulomb stress changes could be altered by transient processes is not taken into account. Tung et al. (2018a) and Yadav et al. (2018), who analyzed postseismic Coulomb stress changes within the first month after the Gorkha main shock by considering poroelastic effects, indicate that a high percentage of aftershocks occur within zones of positive pore pressure changes. One of the large aftershocks 17 days after the mainshock occurred in a region, which showed positive coseismic stress changes, which are even further increased due to poroelastic effects and fluid flow (Figure 5.2f). The results of this thesis confirm that poroelastic effects alter the coseismic stress field immediately after the earthquake and may turn negative stress changes into positive or further increase the stress changes and bring a fault even closer to failure, for example on the receiver faults along-strike to the source fault, which may correspond to the region of the aftershock. However, Tung et al. (2018a) tested different crustal permeabilities in the range of 10^{-9} to 10^{-21} m^2 and they concluded that a low permeability of 10^{-17} m^2 or 8.32×10^{-18} m^2 is the best fitting value for the region. The models in this thesis indicate, that a low permeability causes very weak poroelastic effects and hence very low magnitudes of Coulomb stress changes in the early postseismic phase. As mentioned in several studies, a low viscosity with values between 10^{18} Pa s and 10^{19} Pa s is assumed beneath the Main Himalaya Thrust system (Hong and Liu 2021; Wang and Fialko, 2018; Zhao et al., 2017). The thrust model PV2 with a low permeability and a low viscosity in this thesis (Chapter 3, Figure 3.28) shows a

142

strong influence of viscoelastic relaxation on the velocity and stress field already in the early postseismic phase. That viscoelastic relaxation may play a more important role in this case is
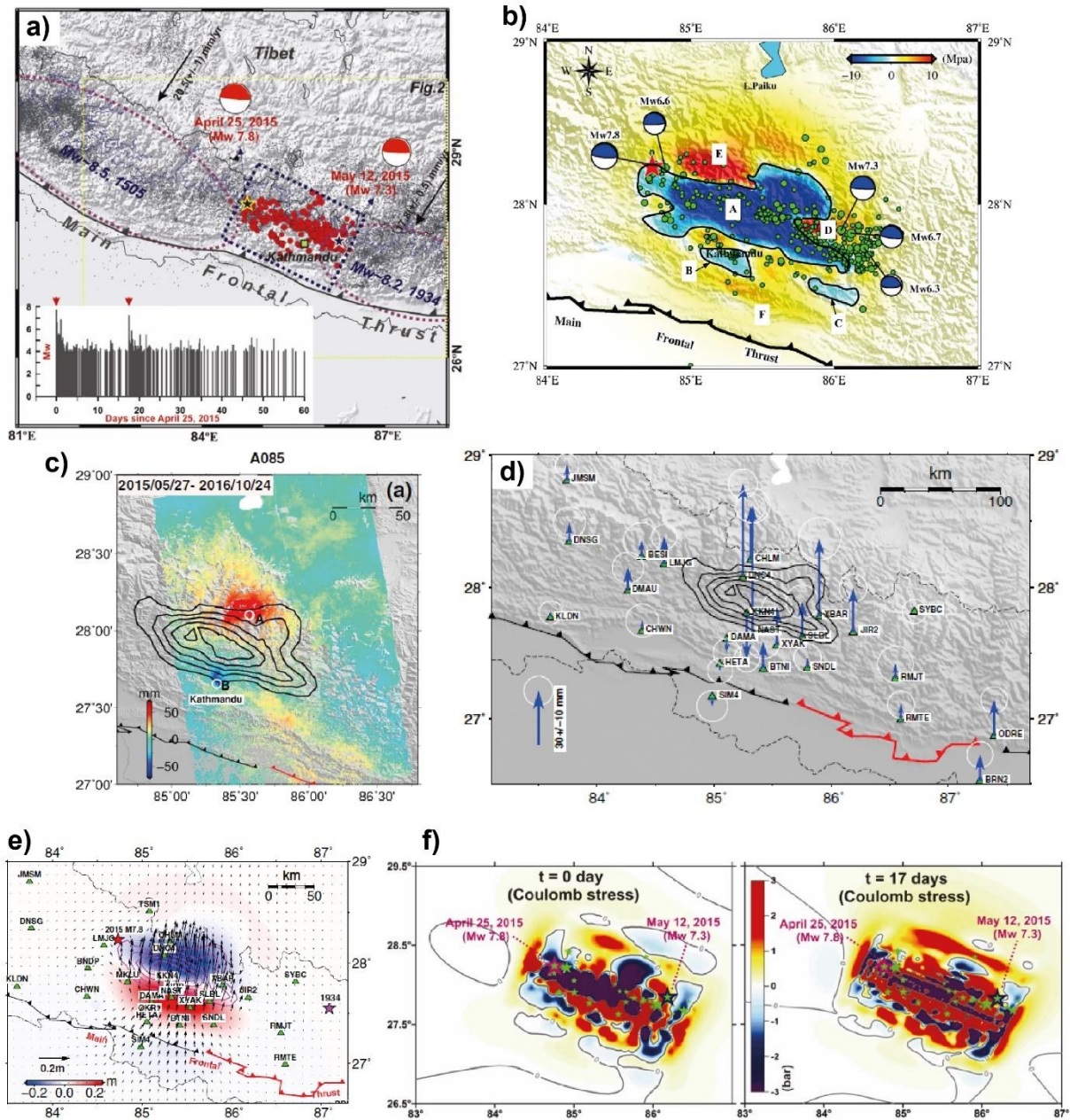

Figure 5.2: Overview of the 2015 Gorkha earthquake. a) Seismotectonics of the region, epicenters of the 25 April mainshock and the 12 May aftershock (stars) and aftershocks (red circles), (modified from Yadav et al., 2018). b) static Coulomb stress changes and aftershock distribution of the Gorkha earthquake (modified from Yang, et al., 2018). c-d) Observed postseismic vertical surface displacements from c) GPS measurements ~2 years after the mainshock and d) InSAR data ~1.5 years after the mainshock (modified from Wang and Fialko, 2018). e) predicted postseismic surface displacements due to viscoelastic relaxation 500 days after the mainshock (modified from Wang and Fialko, 2018). f) Postseismic Coulomb stresses at 15 km depth and aftershock distribution (modified from Yadav et al., 2018).

in assumption with analysis of postseismic deformation after the Gorkha earthquake, which considered poroelastic effects, viscoelastic relaxation and afterslip (Hung and Liu, 2021; Wang and Fialko 2018; Zhao et al., 2017). Zhao et al. (2017) modeled the different models separately. They found out that the observed postseismic uplift in the Tibet Plateau around the main fault cannot be explained by solely one process. A combination of viscoelastic relaxation and afterslip shows the best fit. Poroelastic effects can cause significant uplift on smaller spatial scales compared to viscoelastic relaxation, but a contribution of poroelastic effects worsens the misfit. Similar studies (Hung and Liu, 2021; Wang and Fialko, 2018) argue, that viscoelastic relaxation causes opposite movements compared to the observed postseismic southward and upward surface movements in the area of the main shock (Figure 5.2c-e) and that the contribution of poroelastic effects is too small. Hence, afterslip dominates the postseismic deformation in the first three years. In this thesis, most models show similar patterns of uplift around the source fault in the early postseismic phase mainly caused by poroelastic effects, the velocities decrease with decreasing permeability, but the models do not consider afterslip.

5.4 Model limitations

In contrast to the models of a homogeneous elastic half-space used in a number of previous studies (Okada, 1992), the finite-element models computed with ABAQUS provide the opportunity to implement viscoelastic layers and pore fluid pressure to calculate and analyze surface deformation, pore fluid flow, the strain and stress field and fault interaction. The models represent a simplification of the Earth's lithosphere without a specific geometry. The rheological parameters can vary between the different layers, but the individual layers are homogeneous and cannot reflect all heterogeneities of the lithosphere, for example the depth dependence of the permeability and viscosity. The viscosity is only implemented as linear temperature-independent Maxwell viscoelasticity, though the viscosity of the lithosphere behaves temperature-dependent and non-linear (e.g. Ellis et al., 2006; Freed and Bürgmann, 2004). The implementation of a temperature-controlled viscosity, which is possible with ABAQUS, led to too high computational effort or errors. Too high or too low values for the viscosity and permeability also led to very high computational effort or errors. The friction coefficient in the models is constant in the entire model run and does not contain temporal changes due to alteration of the strength of the rocks in the fault zone (Hampel and Hetzel, 2012). ABAQUS can capture different temporal scales. Every phase of the earthquake cycle can be adjusted. A high temporal resolution also means high computational effort and more

uncertainties in the results. A monthly and yearly time interval for the postseismic phase is recommended, whereas a daily interval only worked for the 2D models. Especially for the pore fluid pressure changes at high permeabilities, however, a resolution of one day would be desirable.

The systematic models in this thesis provide the theoretical evolution of the velocity and stress field after an earthquake caused by the coseismic slip, poroelastic effects, viscoelastic relaxation and interseismic stress accumulation, which can be used for the evaluation of the impact of these different processes. They do not consider afterslip, a specific fault geometry or a geological setting of a specific region. Faults in nature have complex fault geometries and conditions and the pre-stress state is unknown. Therefore, the models cannot be used for earthquake prediction and hazard assessments for a specific earthquake. But the models can help to understand how transient and non-transient processes influence the principal Coulomb stress change pattern over different time scales.

Conclusions and outlook

In this thesis, 2D and 3D finite-element models were applied, to investigate the interaction and relative importance of poroelastic effects and postseismic viscoelastic relaxation for the generation of Coulomb stress changes and the evolution of the velocity and stress field in combination with coseismic slip and interseismic stress accumulation during and after intra-continental earthquakes. The normal and thrust fault models with a generalized model setup including elastic and viscoelastic layers and pore fluid pressure provide insights into the general velocity and stress change pattern independent of a particular fault geometry, specific earthquake and tectonic setting. For the evaluation of the influence of different parameters on the model results, different experiments were conducted, in which the permeability, the viscosity, the friction coefficient, the coseismic slip and the deformation rate were varied successively in the models. This systematic parameter study shows, that the coseismic Coulomb stress changes are immediately altered in the first month after the earthquake. For sufficiently high permeabilities, poroelastic effects cause strong Coulomb stress changes and velocities in the early postseismic phase and dominate the stress and surface velocity field in the first two years after the earthquake. If the permeability is low enough, poroelastic effects overlap with signals from viscoelastic relaxation and interseismic stress accumulation for decades. Low viscosities lead to viscosity patterns and Coulomb stress change distributions showing a combined signal from poroelastic effects and viscoelastic relaxation already in the early postseismic phase. A variation of the friction coefficient, the coseismic slip and the deformation rate only have an effect on the magnitude of the Coulomb stress changes and velocities but not on the pattern. Poroelastic effects and viscoelastic relaxation have a strong influence on postseismic Coulomb stress changes and postseismic velocities and may overlap in the early postseismic phase up to decades, depending on the combination of upper-crustal permeability and lower-crustal viscosity. Therefore, for the analysis of Coulomb stress changes and geodetic data, both processes should be considered.

In future investigations, the rheology of the finite-element models, especially the viscoelastic and poroelastic behavior could be improved. The model setup can be adapted to a specific tectonic setting with a realistic fault geometry and local geological conditions, to calculate Coulomb stress changes and analyze geodetic data after a major natural earthquake, considering the combination of poroelastic effects, viscoelastic relaxation, coseismic slip, interseismic stress accumulation.

Acknowledgement

At this point, I would like to thank all the people who supported me during the processing and completion of this thesis.

At first, I would like to express my deepest gratitude to my supervisor Prof. Dr. Andrea Hampel for the opportunity to work on this interesting project. Thanks for all her excellent support, scientific discussions, effort, feedback, ideas, and interest and for sharing her experience and broad expertise with me. I have learned a lot.

I would like to thank Dr. Meike Bagge for her great support, for the nice conversations during her visits and for sharing her scientific and personal experience with me.

Furthermore, I would like to acknowledge Prof. Dr. Ulrich Heimhofer for making the effort to be my co-examiner and Prof. Dr. Stephan Peth for being a co-examiner and chairman of the examination committee.

Special thanks to my colleagues/roommates from the office in the attic for good conversations (although it often distracted me from work) and the nice time, inside and outside of the office. I had a lot of fun with you. I would also like to take the opportunity to thank my family and friends for everything.

References

ABAQUS Documentation, 2018. Dassault Systémes Simulia Corp.

Albano, M., Barba, S., Solaro, G., Pepe, A., Bignami, C., Moro, M., Saroli, M., Stramondo, S., 2017. Aftershocks, groundwater changes and postseismic ground displacements related to pore pressure gradients: Insights from the 2012 Emilia-Romagna earthquake. J. Geophys. Res. 122, 5622–5638. https://doi.org/10.1002/2017JB014009.

Albano, M., Barba, S., Saroli, M., Polcari, M., Bignami, C., Moro, M., Stramondo, S., Di Bucci, D., 2019. Aftershock rate and pore fluid diffusion: Insights from the Amatrice Visso-Norcia (Italy) 2016 seismic sequence. J. Geophys. Res. 124, 995–1015. https://doi.org/10.1029/2018JB015677.

Albano, M., Barba, S., Bignami, C., Carminati, E., Doglioni, C., Moro, M., Saroli, M., Samsonov, S., Stramondo, S., 2021. Numerical analysis of interseismic, coseismic and post-seismic phases for normal and reverse faulting earthquakes in Italy. Geophys. J. Int. 225, 627-645. https://doi.org/10.1093/gji/ggaa608.

Anderson, E.M., 1951. The Dynamics of Faulting. Oliver and Boyd, Edinburgh, 206 pp.

Antonioli, A., Piccinini, D., Chiaraluce, L., Cocco, M., 2005. Fluid flow and seismicity pattern: Evidence from the 1997 Umbria Marche (central Italy) seismic sequence. Geophys. Res. Lett. 32, L10311, https://doi.org/10.1029/2004GL022256.

Aoudia, A., Borghi, A., Riva, R., Barzaghi, R., Ambrosius, B.A.C., Sabadini, R., Vermeersen, L.L.A., Panza, G.F., 2003. Postseismic deformation following the 1997 Umbria-Marche (Italy) moderate normal faulting earthquakes. Geophys. Res. Lett. 30(7), 1390, https://doi.org/10.1029/2002GL016339.

Bagge, M., Hampel, A., 2016. Three-dimensional finite-element modelling of coseismic Coulomb stress changes on intra-continental dip-slip faults. Tectonophysics 684, 52-62. https://dx.doi.org/10.1016/j.tecto.2015.10.006.

Bagge, M., Hampel, A., 2017. Postseismic Coulomb stress changes on intra-continental dip-slip faults due to viscoelastic relaxation in the lower crust and lithospheric mantle: insights from 3D finite-element modelling. Int. J. Earth Sci. 106, 2895-2914. https://doi.org/10.1007/s00531-017-1467-8.

Bagge, M., Hampel, A., Gold, R.D., 2019. Modeling the Holocene slip history of the Wasatch fault (Utah): Coseismic and postseismic Coulomb stress changes and implications for paleoseismicity and seismic hazard. GSA Bulletin 2018, 131, 43–57. https://doi.org/10.1130/B31906.1.

Barbot, S., Fialko, Y., 2010. A unified continuum representation of post-seismic relaxation mechanisms: semi-analytic models of afterslip, poroelastic rebound and viscoelastic flow. Geophys. J. Int. 182, 1124-1140. https://doi.org/10.1111/j.1365-246X.2010.04678.x.

Beauducel, F., 2022. Okada: Surface deformation due to a finite rectangular source (https://www.mathworks.com/matlabcentral/fileexchange/25982-okada-surface-deformation-due-to-a-finite-rectangular-source), MATLAB Central File Exchange. Retrieved April 5, 2022.

Belardinelli, M.E., Cocco, M., Coutant, O., Cotton F., 1999. Redistribution of dynamic stress during coseismic ruptures: evidence for fault interaction and earthquake triggering. J. of Geophys. Res. 104, 14925–14945. https://doi.org/10.1029/1999JB900094.

Bennett, R.A., Wernicke, B.P., Niemi, N.A., Friedrich, A.M., Davis, J.L., 2003. Contemporary strain rates in the northern Basin and Range province from GPS data. Tectonics 22, 1008, https://doi.org/10.1029/2001TC001355.

Biot, M.A., 1941. General theory of three-dimensional consolidation. J. Appl. Phys. 12 (2), 155-164. https://doi.org/10.1063/1.1712886.

Burbank, D.W., Anderson, R.S., 2001. Tectonic Geomorphology. Blackwell Science Ltd., Australia, 160.

Burov, E.B., Watts, A.B., 2006. The long-term strength of continental lithosphere:"jelly sandwich" or "crème brûlée"? GSA Today 16 (1), 4-10. https://doi.org/10.1130/1052-5173(2006)016<4:tltSOc>2.0.cO;2.

Cheloni, D., D'Agostino, N., D'Anastasio, E., Avallone, A., Mantenuto, S., Giuliani, R., Mattone, M., Calcaterra, S., Gambino, P., Dominici, D., Radicioni, F., Fastellini, G., 2010. Coseismic and initial post-seismic slip of the 2009 M_w 6.3 L'Aquila earthquake, Italy, from GPS measurements. Geophys. J. Int. 181, 1539-1546. https://doi.org/10.1111/j.1365-246X.2010.04584.x.

Cenni, N., Mantovani, E., Baldi, P., Viti, M., 2012. Present kinematics of Central and Northern Italy from continuous GPS measurements. J. Geodyn. 58, 62-72. https://doi.org/10.1016/j.jog.2012.02.004.

Chen, H.-Y., Yu, S.-B., Kuo, L.-C., Liu, C.-C., 2006. Coseismic and postseismic surface displacements of the 10 December 2003 (Mw 6.5) Chengkung, eastern Taiwan, earthquake. Earth Planet Space, 58, 5‑21. https://doi.org/10.1186/BF03351908.

Chen, W.-P., Molnar P., 1983. Focal depths of intracontinental and intraplate earthquakes and their implications for the thermal and mechanical properties of the lithosphere. J. Geophys. Res. 88, 4183-4214. https://doi.org/10.1029/JB088iB05p04183.

Chéry, J., Carretier, S., Ritz, J.-F., 2001. Postseismic stress transfer explains time clustering of large earthquakes in Mongolia. Earth Planet. Sci. Lett. 194, 277-286. https://doi.org/10.1016/S0012-821X(01)00552-0.

Chiarabba, C., De Gori, P., Boschi, E., 2009. Pore-pressure migration along a normal-fault system resolved by time-repeated seismic tomography. Geology 37 (1), 67-70. https://doi.org/10.1130/G25220A.1.

Chiaraluce, L., 2012. Unravelling the complexity of Apenninic extensional fault systems: A review of the 2009 L'Aquila earthquake (Central Apennines, Italy). J. Struct. Geol. 42, 2-18. https://doi.org/10.1016/j.jsg.2012.06.007.

Chousianitis, K., Konca, A.O., 2021. Rupture Process of the 2020 M_w7.0 Samos Earthquake and its Effect on Surrounding Active Faults. Geophys. Res. Lett. 48. https://doi.org/10.1029/2021GL094162.

Cianetti, S., Giunchi, C., Cocco, M., 2005. Three-dimensional finite element modeling of stress interaction: An application to Landers and Hector Mine fault systems. J. Geophys. Res. 110. https://doi.org/10.1029/2004JB003384.

Cocco, M., Nostro, C., Ekström, G., 2000. Static stress changes and fault interaction during the 1997 Umbria-Marche earthquake sequence. J. Seismology 4, 501-516. https://doi.org/10.1023/A:1026507917308.

Cocco, M., Rice, J.R., 2002. Pore pressure and poroelasticity effects in Coulomb stress analysis of earthquake interactions. J. Geophys. Res. 107, 2030, https://doi.org/10.1029/2000JB000138.

Collettini, C., Niemeijer, A., Viti, C., Marone, C., 2009. Fault zone fabric and fault weakness. Nature 462, 907-910.

Crone, A.J., Machette, M.N., Bonilla, M.G., Lienkaemper, J.J., Pierce, K.L., Scott, W.E., Bucknam, R.C., 1987. Surface faulting accompanying the Borah Peak earthquake and segmentation of the Lost River fault, central Idaho. Bull. Seismol. Soc. Am. 77, 739–770. https://doi.org/10.1785/BSSA0770030739.

D'Agostino, Giuliani, N., R., Mattone, M., Bonci, L., 2001. Active crustal extension in the Central Apennines (Italy) inferred from GPS measurements in the interval 1994–1999. Geophys. Res. Lett. 28, 2121-2124. https://doi.org/10.1029/2000GL012462

D'Agostino, N., Avallone, A., Cheloni, D., D'Anastasio, E., Mantenuto, S., Selvaggi, G., 2008. Active tectonics of the Adriatic region from GPS and earthquake slip vectors. J. Geophys. Res. 113, B12413, https://doi.org/10.1029/2008JB005860.

Dempsey, D.E., Archer, R.A., Ellis, S.M., Rowland, J.V., 2013. Hydrological effects of dip-

slip fault rupture on a hydrothermal plume. J. Geophys. Res. 118, 195-211. https://doi.org/10.1029/2012JB009395.

Doan, M.L., Brodsky, E.E., Kano, Y., Ma, K.F., 2006. In situ measurement of the hydraulic diffusivity of the active Chelungpu Fault, Taiwan. Geophys. Res. Lett., 33, L16317. https://doi.org/10.1029/2006GL026889.

Ellis, S., Stöckhert, B., 2004. Elevated stresses and creep rates beneath the brittle-ductile transition caused by seismic faulting in the upper crust. J. Geophys. Res. 109, B05407. https://doi.org/10.1029/2003JB002744.

Eisbacher, G.H., 1991. Einführung in die Tektonik. Enke Verlag 310p.

England, P., Jackson, J., 2011. Uncharted seismic risk. Nature Geoscience 4, 348-349.

England, P.C., Walker, R.T., Fu, B., Floyd, M.A., 2013. A bound on the viscosity of the Tibetan crust from the horizontality of palaeolake shorelines. Earth Planet. Sci. Lett. 375, 44-56. https://doi.org/10.1016/j.epsl.2013.05.001.

Field, E.H., Dawson, T.E., Felzer, K.R., Frankel, A.D., Gupta, V., Jordan, T.H., Parsons, T., Petersen, M.D., Stein, R.S., Weldon II, R.J., Wills C.J., 2009. Uniform California Earthquake Rupture Forecast, Version 2 (UCERF2). Bull. Seismol. Soc. Am 99, 2053-2107. https://doi.org/10.1785/0120080049.

Foulger, G.R., Julian, B.R., 2015. Non-Double-Couple Earthquakes. Encyclopedia of Earthquake Engineering. https://doi.org/10.1007/978-3-642-36197-5_290-1.

Freed, A. M., 2005. Earthquake triggering by static, dynamic, and postseismic stress transfer. Annu. Rev. Earth Planet. Sci. 33, 335-367. https://doi.org/10.1146/annurev.earth.33.092203.122505.

Freed, A.M., Lin, J., 1998. Time-dependent changes in failure stress following thrust earthquakes. J. Geophys. Res, 103 (B10), 24393-24409. https://doi.org/10.1029/98JB01764.

Freed, A.M., Lin, J., 2001. Delayed triggering of the 1999 Hector Mine earthquake by viscoelastic stress transfer. Nature 411, 180-183. https://doi.org/10.1038/35075548.

Freed, A.M., Bürgmann, R., 2004. Evidence of power-law flow in the Mojave desert mantle. Nature 430, 548-551. https://doi.org/10.1038/nature02784.

Freed, A.M., Ali, S.T., Bürgmann, R., 2007. Evolution of stress in Southern California for the past 200 years from coseismic, postseismic and interseismic stress changes. Geophys. J. Int. 169, 1164–1179. https://doi.org/10.1111/j.1365-929 246X.2007.03391.x.

Friedrich, A.M., Wernicke, B.P., Niemi, N.A., Bennett, R.A., Davis, J.L., 2003. Comparison of geodetic and geologic data from the Wasatch region, Utah, and implications for the spectral

character of Earth deformation at periods of 10 to 10 million years. J. Geophys. Res. 108. https://doi.org/10.1029/2001JB000682.

Frohlich, C., 1994. Earthquakes with Non-Double-Couple Mechanisms. Science 264, 804-809. https://doi.org/10.1126/science.264.5160.804.

Ganas, A., Roumelioti, Z., Chousianitis, K., 2012. Static stress transfer from the May 20, 2012, M 6.1 Emilia-Romagna (northern Italy) earthquake using a co-seismic slip distribution model. Ann. Geophys. 55. https://doi.org/0.4401/ag-6176.

Gomberg, J., Reasenberg, P.A., Bodin, P., Harris, R.A., 2001. Earthquake triggering by seismic waves following the Landers and Hector Mine earthquakes. Nature 411, 462-466. https://doi.org/10.1038/35078053.

Gourmelen, N., Amelung, F., 2005. Postseismic mantle relaxation in the central Nevada seismic belt. Science 310, 1473–1476. https://doi.org/10.1126/science.1119798.

Hamiel, Y., Lyakhovsky, V., Agnon, A., 2005. Rock dilation, nonlinear deformation, and pore pressure change under shear. Earth Planet. Sci. Lett. 237, 577–589. https://doi.org/10.1016/j.epsl.2005.06.028.

Hampel, A., Karow, T., Maniatis, G., Hetzel, R. 2010. Slip rate variations on faults during glacial loading and postglacial unloading: Implications for the viscosity structure of the lithosphere. In: Pascal, C., Stewart, I.S., Vermeersen, B.L.A., eds. Neotectonics, Seismicity and Stress in Glaciated Regions, J. Geol. Soc. London 167, 385-399.

Hampel, A., Hetzel, R., 2012. Temporal variation in fault friction and its effects on the slip evolution of a thrust fault over several earthquake cycles. Terra Nova, 24, 357-362. https://doi.org/10.1111/j.1365-3121.2012.01073.x.

Hampel, A., Li, T., Maniatis, G., 2013. Contrasting strike-slip motions on thrust and normal faults: Implications for space-geodetic monitoring of surface deformation. Geology 41 (3), 299-302. https://doi.org/10.1130/G33927.1.

Hampel, A., Hetzel, R, 2015. Horizontal surface velocity and strain patterns near thrust and normal faults during the earthquake cycle: The importance of viscoelastic relaxation in the lower crust and implications for interpreting geodetic data. Tectonics 34. https://doi.org/10.1002/2014TC003605.

Hampel, A., Lüke, J., Krause, T., Hetzel, R., 2019. Finite-element modelling of glacial isostatic adjustment (GIA): Use of elastic foundations at material boundaries versus the geometrically non-linear formulation. Comput. Geosci. 122, 1-14. https://doi.org/10.1016/j.cageo.2018.08.002.

Hanks, T.C., 1977. Earthquake Stress Drops, Ambient Tectonic Stresses and Stresses That

Drive Plate Motions. Pure Appl. Geophys. 115, 441-458. https://doi.org/10.1007/BF01637120.

Hardebeck, J.L., Nazareth, J.J., Hauksson, E., 1998. The static stress change triggering model: Constraints from two southern California aftershock sequences. J. Geophys. Res. 103, 24427– 24437. https://doi.org/10.1029/98JB00573.

Hearn, J.L., Nazareth, J.J., Hauksson, E., 1998. The static stress change triggering model: Constraints from two southern California aftershock sequences. J. Geophys. Res. 103, 24427– 24437. https://doi.org/10.1029/98JB00573.

Henriquet, M., Avouac, J.-P., Bills, B.G., 2019. Crustal rheology of southern Tibet constrained from lake-induced viscoelastic deformation. Earth Planet. Sci. Lett. 506, 308-322. https://doi.org/10.1016/j.epsl.2018.11.014.

Hetzel, R., Tao, M., Niedermann, S., Strecker, M.R., Ivy-Ochs, S., Kubik, P.W., Gao, B., 2004. Implications of the fault scaling law for the growth of topography: mountain ranges in the broken foreland of north-east Tibet. Terra Nova 16, 157-162. https://doi.org/10.1111/j.1365-3121.2004.00549.x.

Hong, S., Liu, M., 2021. Postseismic Deformation and Afterslip Evolution of the 2015 Gorkha Earthquake Constrained by InSAR and GPS Observations. J. Geophys. Res. 126, e2020JB020230. https://doi.org/10.1029/2020JB020230.

Hsu, Y.-F., Huang, H.-H., Huang, M.-H., Tsai, V.C., Chuang, R.Y., Feng, K.-F., Lin, S.-H., 2020. Evidence for Fluid Migration During the 2016 Meinong, Taiwan, Aftershock Sequence. J. Geophys. Res. 125, e2020JB019994. https://doi.org/10.1029/2020JB019994.

Hsu, Y.-J., Segall, P., Yu, S.-B., Kuo, L.-C., Williams, C. A., 2007. Temporal and spatial variations of post-seismic deformation following the 1999 Chi-Chi, Taiwan earthquake. Geophys. J. Int. 169, 367-379. https://doi.org/10.1111/j.1365-246X.2006.03310.x.

Hsu, Y.-J., Simons, M., Williams, C., Casarotti, E., 2011. Three-dimensional FEM derived elastic Green's functions for the coseismic deformation of the 2005 Mw 8.7 Nias-Simeulue, Sumatra earthquake. Geochem. Geophys. Geosyst. 12, Q07013. https://doi.org/10.1029/2011GC003553.

Ingebritsen, S.E., Manning, C.E., 2010. Permeability of the continental crust: dynamic variations inferred from seismicity and metamorphism. Geofluids 10, 193-205. https://doi.org/10.1111/j.1468-8123.2010.00278.x.

Kanamori, H., Anderson, D.L., 1975. Theoretical basis of some empirical relations in seismology. Bull. Seismol. Soc. Am. 65, 1073-1095.

Kaufmann, G., Amelung, F., 2000. Reservoir-induced deformation and continental rheology in

vicinity of Lake Mead, Nevada. J. Geophys. Res. 105, 16341–16358. https://doi.org/10.1029/2000JB900079.

Kenner, S., Segall, P., 1999. Time-dependence of the stress shadowing effect and its relation to the structure of the lower crust. Geology 27 (2), 119-122. https://doi.org/10.1130/0091-7613(1999)027<0119:TDOTSS>2.3.CO;2.

King, G.C.P., Vita-Finzi, C., 1981. Active folding in the Algerian earthquake of 10 October 1980. Nature 292, 22-26. https://doi.org/10.1038/292022a0.

King, G.C.P., Muir-Wood, R., 1994. The impact of earthquakes on fluids in the crust. Ann. Geofis. 37 (6), 1453–1460. https://doi.org/10.4401/ag-4147.

King, G.C., Stein, R.S., Lin, J., 1994. Static Stress Changes and the Triggering of earthquakes. Bull. Seismol. Soc. Am. 84, 935-953.

Klemperer, S.L., 2006. Crustal flow in Tibet: geophysical evidence for the physical state of Tibetan lithosphere, and inferred patterns of active flow. Geol. Soc. London Spec. Publ. 268, 39–70. https://doi.org/10.1144/GSL.SP.2006.268.01.03.

Lai, W.-C., Koizumi, N., Matsumoto, N., Kitagawa, Y., Lin, C.-W., Shieh, C.-L., Lee, Y.-P., 2004. Effects of seismic ground motion and geological setting on the coseismic groundwater level changes caused by the 1999 Chi-Chi earthquake, Taiwan. Earth Planet Space, 56, 873-880. https://doi.org/10.1186/BF03352534.

Lin, A., Ren, Z., Jia, D., Wu, X., 2009. Co-seismic thrusting rupture and slip distribution produced by the 2008 M_w 7.9 Wenchuan earthquake, China. Tectonophysics 471, 203-215. https://doi.org/10.1016/j.tecto.2009.02.014.

Lin, J., Stein, R.S., 2004. Stress interaction in thrust and subduction earthquakes and stress interaction between the southern San Andreas and nearby thrust and strike-slip faults. J. Geophys. Res. 109, B02303. https://doi.org/10.1029/2003JB002607.

Lin, J., Stein, R.S., Meghraoui, M., Toda, S., Ayadi, A., Dorbath, C., Belabbes, S., 2011. Stress transfer among en echelon and opposing thrusts and tear faults: Triggering caused by the 2003 Mw=6.9 Zemmouri, Algeria, earthquake. J. Geophys. Res. 116, B03305, https://doi.org/10.1029/2010JB007654.

Liu-Zeng, J., Zhang, Z., Wen, L., Tapponnier, P., Sun, J., Xing, X., Hu, G., Xu, Q., Zeng, L., Ding, L., Ji, C., Hudnut, K.W., van der Woerd, J., 2009. Co-seismic ruptures of the 12 May 2008, M_s 8.0 Wenchuan earthquake, Sichuan: East–west crustal shortening on oblique, parallel thrusts along the eastern edge of Tibet. Earth Planet. Sci. Lett. 286, 355–370. https://doi.org/10.1016/j.epsl.2009.07.017.

Liu‐Zeng, J., Zhang, Z., Rollins, C., Gualandi, A., Avouac, J.-P., Shi, H., Wang, P., Chen, W.,

Zhang, R., Zhang, P., Wang, W., Li, Y., Wang, T., Li, Z., 2020. Postseismic deformation following the 2015 M_w7.8 Gorkha (Nepal) earthquake: New GPS data, kinematic and dynamic models, and the roles of afterslip and viscoelastic relaxation. J. Geophys. Res. 125, e2020JB019852. https://doi.org/10.1029/2020JB019852.

Luo, G., Liu, M., 2010. Stress evolution and fault interactions before and after the 2008 Great Wenchuan earthquake. Tectonophysics 491, 127-140. https://doi.org/10.1016/j.tecto.2009.12.019.

Malagnini, L., Lucente, F.P., De Gori, P., Akinci, A., Munafo, I., 2012. Control of pore fluid pressure diffusion on fault failure mode: Insights from the 2009 L'Aquila seismic sequence. J. Geophys. Res. 117, B05302. https://doi.org/10.1029/2011JB008911.

Mandler, E., Pintori, F., Gualandi, A., Anderlini, L., Serpelloni, E., Belardinelli, M.E., 2021. Post-seismic deformation related to the 2016 Central Italy seismic sequence from GPS displacement time-series. J. Geophys. Res. 126, e2021JB022200. https://doi.org/10.1029/2021JB022200.

Manning, C.E., Ingebritsen, S.E., 1999. Permeability of the continental crust: Implications of geothermal data and metamorphic systems. Rev. Geophys. 37 (1). https://doi.org/10.1029/1998RG900002.

Martinez-Garzon, P., Kwiatek, G., Bohnhoff, M., Dresen, G., 2017. Volumetric components in the earthquake source related to fluid injection and stress state. Geophys. Res. Lett. 44, 800–809. https://doi.org/10.1002/2016GL071963.

Masterlark, T., 2003. Finite element model predictions of static deformation from dislocation sources in a subduction zone: Sensitivities to homogeneous, isotropic, Poisson-solid, and half-space assumptions. J. Geophys. Res. 108, B11. https://doi.org/10.1029/2002JB002296.

Masterlark, T., Wang, H.F., 2002. Transient Stress-Coupling Between the 1992 Landers and 1999 Hector Mine, California, Earthquakes. Bull. Seismol. Soc. Am. 92 (4), 1470-1486. https://doi.org/10.1785/0120000905.

Meghraoui, M., Jaegy, R., Lammali, K., Albarède, F., 1988. Late Holocene earthquake sequences on the El Asnam (Algeria) thrust fault. Earth Planet. Sci. Lett. 90, 187-203. https://doi.org/10.1016/0012-821X(88)90100-8.

Meyer, B., Tapponnier, P., Bourjot, L., Métivier, F., Gaudemer, Y., Peltzer, G., Guo, S., Chen, Z., 1998. Crustal thickening in Gansu-Qinghai, lithospheric mantle subduction, and oblique, strike-slip controlled growth of the Tibetan Plateau. Geophys. J. Int. 135, 1-47. https://doi.org/10.1046/j.1365-246X.1998.00567.x.

Miao, M., Zhu, S., Chang, Y., Yuan, J., Wang, R., Han, P., 2021. Spatiotemporal evolution of pore pressure changes and Coulomb failure stress in a poroelastic medium for different faulting regimes. Earth and Space Science 8. https://doi.org/10.1029/2021EA001837.

Miller, A.D., Foulger, G.R., Julian, B.R., 1998. Non-Double-Couple Earthquakes: 2. Observations. Rev. Geophys. 36, 531-568. https://doi.org/10.1029/98RG00717.

Myers, W.B., Hamilton, W., 1964. Deformation accompanying the Hebgen Lake earthquake of August 17, 1959. U.S. Geol. Surv. Profess. Pap., 435-1, 55–98.

Nespoli, M., Belardinelli, M.E., Gualandi, A., Serpelloni, E., 2018. Poroelasticity and Fluid Flow Modeling for the 2012 Emilia-Romagna Earthquakes: Hints from GPS and InSAR Data. Geofluids 2018, 1–15. https://doi.org/10.1155/2018/4160570.

Nishimura, T., Thatcher, W., 2003. Rheology of the lithosphere inferred from postseismic uplift following the 1959 Hebgen Lake earthquake. J. Geophys. Res. 108 (B8). https://doi.org/10.1029/2002JB002191.

Nostro, C., Cocco, M., Belardinelli, M.E., 1997. Static Stress Changes in Extensional Regimes: An Application to Southern Apennines (Italy). Bull. Seismol. Soc. Am. 87, 234-248. https://doi.org/10.1785/BSSA0870010234.

Nostro, C., Piersanti, A., Cocco, M., 2001. Normal fault interaction caused by coseismic and postseismic stress changes. J. Geophys. Res. 106, 19391-19410. https://doi.org/10.1029/2001JB000426.

Nostro, C., Chiaraluce, L., Cocco, M., Baumont, D., Scotti, O., 2005. Coulomb stress changes caused by repeated normal faulting earthquakes during the 1997 Umbria-Marche (central Italy) seismic sequence. J. Geophys. Res. 110, B05S20. https://doi.org/10.1029/2004JB003386.

Nur, A., Booker, J.R., 1972. Aftershocks caused by pore fluid flow? Science 175, 885–887. https://doi.org/10.1126/science.175.4024.885.

Nur, A., Mavko, G., 1974. Post-seismic viscoelastic rebound. Science 183, 204-206. https://doi.org/10.1126/science.183.4121.20.

Oglesby, D.D., Day, S.M., O'Connell, D.R.H., 2003. Dynamic and static interaction of two thrust faults: A case study with general implications. J. Geophys. Res. 108. https://doi.org/10.1029/2002JB002228.

Okada, Y., 1985. Surface deformation due to shear and tensile faults in a half-space. Bull. Seismol. Soc. Am. 75, 1135–1154. https://doi.org/10.1785/BSSA0750041135.

Okada, Y., 1992. Internal deformation due to shear and tensile faults in a half-space. Bull. Seismol. Soc. Am. 82, 1018-1040. https://doi.org/10.1785/BSSA0820021018.

Panthi, A., Shanker, D., Singh, H. N., Kumar, A., Paudyal, H., 2011. ime-predictable model applicability for earthquake occurrence in northeast India and vicinity. Nat. Hazards Earth Syst. Sci., 11, 993–1002. https://doi.org/10.5194/nhess-11-993-2011.

Parsons, T., Stein, R.S., Simpson, R.W., Reasenberg, P.A., 1999. Stress sensitivity of fault seismicity: A comparison between limited-offset oblique and major strike-slip faults, J. Geophys. Res. 104 (B9), 20183–20202. https://doi.org/10.1029/1999JB900056.

Parsons, T., Ji, C., Kirby, E., 2008. Stress changes from the 2008 Wenchuan earthquake and increased hazard in the Sichuan basin. Nature 454, 509-510. https://doi.org/10.1038/nature07177.

Peikert, J., Hampel, A., Bagge, M., 2022. Relative importance of poroelastic effects and viscoelastic relaxation for postseismic velocity fields after normal and thrust earthquakes: Insights from 2D finite-element modelling. Tectonophysics 838, https://doi.org/10.1016/j.tecto.2022.229477.

Philip, H., Meghraoui, M., 1983. Structural analysis and interpretation of the surface deformation of the El Asnam earthquake of October 10, 1980. Tectonics 2, 17–49. https://doi.org/10.1029/TC002i001p00017.

Piombo, A., Martinelli, G., Dragoni, M., 2005. Post-seismic fluid flow and Coulomb stress changes in a poroelastic medium. Geophys. J. Int. 162, 507-515. https://doi.org/10.1111/j.1365-246X.2005.02673.x.

Pollitz, F.F., 1997. Gravitational viscoelastic postseismic relaxation on a layered spherical Earth. J. Geophys. Res. 102, 17921–17941. https://doi.org/10.1029/97JB01277.

Pollitz, F.F., Sacks, I.S., 2002. Stress triggering of the 1999 Hector Mine earthquake by transient deformation following the 1992 Landers earthquake. Bull. Seismol. Soc. Am. 92, 1487-1496. https://doi.org/10.1785/0120000918.

Pollitz, F.F., Stein, R.S., Sevilgen, V., Bürgmann, R., 2012. The 11 April 2012 east Indian Ocean earthquake triggered large aftershocks worldwide. Nature 490, 250-255. https://doi.org/10.1038/nature11504.

Reddy, C.D., Arora, S.K., Sunil, P.S., Prajapati, S.K., 2011. Earthquake related deformation cycle: perspectives from 2004 Sumatra and 2010 Chile mega-earthquakes. Disaster Advances, 4, pp. 13–21.

Reid, N. F., 1910. The Mechanism of the Earthquake. The California Earthquake of April 18, 1906. Rep. of the State Investigation Commiss. Vol. 2, pt. 1.

Rice, J.R., Cleary, M.P., 1976. Some basic stress diffusion solutions for fluid- saturated elastic porous media with compressible constituents. Rev. Geophys. 14, 227–241.

https://doi.org/10.1029/RG014i002p00227.

Riva, R.E.M., Borghi, A., Aoudia, A., Barzaghi, R., Sabadini, R., Panza, G.F., 2007. Viscoelastic relaxation and long-lasting after-slip following the 1997 Umbria-Marche (Central Italy) earthquakes. Geophys. J. Int. 169, 534-546. https://doi.org/10.1111/j.1365-246X.2007.03315.x.

Roberts, G.P., Michetti, A.M.; 2004. Spatial and temporal variations in growth rates along active normal fault systems: an example from the Lazio–Abruzzo Apennines, central Italy. J. Struct. Geol. 26, 339-376. https://doi.org/10.1016/S0191-1084 8141(03)00103-2.

Rousset, B., Barbot, S., Avouac, J.-P., Hsu, Y.-J., 2012. Postseismic deformation following the 1999 Chi-Chi earthquake, Taiwan: Implication for lower-crust rheology. J. Geophys. Res. 117, B12405. https://doi.org/10.1029/2012JB009571.

Rudnicki, J.W., 1986. Slip on an impermeable fault in a fluid-saturated rock mass. Geophys. Monogr. Ser. 37, 81–89. https://doi.org/10.1029/GM037p0081.

Ryder, I., Parsons, B., Wright, T.J., Funning, G.J., 2007. Post-seismic motion following the 1997 Manyi (Tibet) earthquake: InSAR observations and modelling. Geophys. J. Int. 169, 1009-1027. https://doi.org/10.1111/j.1365-246X.2006.03312.x.

Ryder, I., Bürgmann, R., Sun, J., 2010. Tandem afterslip on connected fault planes following the 2008 Nima-Gaize (Tibet) earthquake. J. Geophys. Res. 115, B03404. https://doi.org/10.1029/2009JB006423.

Ryder, I., Bürgmann, R., Fielding, E.; 2012. Static stress interactions in extensional earthquake sequences: An example from the South Lunggar Rift, Tibet. J. Geophys. Res. 117, B09405. https://doi.org/10.1029/2.012JB009365.

Ryder, I., Wang, H., Bie, L., Rietbrock, A., 2014. Geodetic imaging of late postseismic lower crustal flow in Tibet. Earth Planet. Sci. Lett. 404, 136-143. https://doi.org/10.1016/j.epsl.2014.07.026.

Scholz, C.H., 1987. Wear and gouge formation in brittle faulting. Geology 15 (6), 493-495. https://doi.org/10.1130/0091-7613(1987)15<493:WAGFIB>2.0.CO;2.

Scholz, C.H., 2002. The mechanics of earthquakes and faulting. New York; Cambridge University Press.

Scholz, C.H., 2010. Large Earthquake Triggering, Clustering, and the Synchronization of Faults. Bull. Seismol. Soc. Am. 100, 901-909, https://doi.org/10.1785/0120090309.

Scholz, C.H., 2019. The mechanics of earthquakes and faulting. Third Edition, Cambridge University Press, Cambridge, 493 p.

Scibek, J., 2020. Multidisciplinary database of permeability of fault zones and surrounding

protolith rocks at world-wide sites. Sci. Data 7, 95. https://doi.org/10.1038/s41597-020-0435-5.

Serpelloni, E., Anderlini, L., Belardinelli, M.E., 2012. Fault geometry, coseismic-slip distribution and Coulomb stress change associated with the 2009 April 6, Mw 6.3, L' Aquila earthquake from inversion of GPS displacements. Geophys. J. Int. 188, 473-489. https://doi.org/10.1111/j.1365-246X.2011.05279.x.

Shi, X., Kirby, E., Furlong, K.P., Meng, K., Robinson, R., Wang, E., 2015. Crustal strength in central Tibet determined from Holocene shoreline deflection around Siling Co. Earth Planet. Sci. Lett. 423, 145-154. https://doi.org/10.1016/j.epsl.2015.05.002.

Shimazaki, K., Nakata, T., 1980. Time-predictable recurrence model for large earthquakes. Geophys. Res. Lett. 7, 279-282. doi:10.1029/GL007i004p00279.

Sibson, R.H., 1994. Crustal stress, faulting and fluid flow. Geol. Soc. London Spec. Publ. 78 (1), 69–84. http://dx.doi.org/10.1144/GSL.SP.1994.078.01.07.

Slemmons, D.B., 1957. Geological effects of the Dixie Valley-Fairview Peak, Nevada, earthquake of December 16, 1954. Bull. Seismol. Soc. Am. 47, 353–375. https://doi.org/10.1785/BSSA0470040353.

Stein, R.S., 1999. The role of stress transfer in earthquake occurrence. Nature 402, 605-609. https://doi:10.1038/45144.

Stein, R.S., 2003. Earthquake Conversations. Scientific American 288, 72-79. https://doi.org/10.1038/scientificamerican0103-72.

Stein, R.S., Lisowski, M., 1983. The 1979 Homestead Valley Earthquake Sequence, California: Control of aftershocks and postseismic deformation. J. Geophys. Res. 88, 6477-6490. https://doi.org/10.1029/JB088iB08p06477.

Stein, R.S., King, G.C., Lin, J., 1992. Change in Failure Stress on the Southern San Andreas Fault System Caused by the 1992 Magnitude = 7.4 Landers Earthquake. Science 258. https://doi.org/ 10.1126/science.258.5086.1328.

Stein, R.S., Barka, A.A., Dieterich, J.H., 1997. Progressive failure on the North Anatolian fault since 1939 by earthquake stress triggering. Geophys. J. Int. 128, 594-604. https://doi.org/10.1111/j.1365-246X.1997.tb05321.x.

Stober, I., Bucher, K., 2015. Hydraulic and hydrochemical properties of deep sedimentary reservoirs of the Upper Rhine Graben, Europe. Geofluids 15, 464-482. https://doi.org/10.1111/gfl.12122.

Toda, S., Stein, R. S., Richards-Dinger, K., Bozkurt, S. B., 2005. Forecasting the evolution of seismicity in southern California: Animations built on earthquake stress transfer. J.

Geophys. Res. 110, https://doi.org/10.1029/2004JB003415.

Tung, S., Masterlark, T., 2018. Delayed Poroelastic Triggering of the 2016 October Visso Earthquake by the August Amatrice Earthquake, Italy. Geophys. Res. Lett. 45, 2221-2229. https://doi.org/10.1002/2017GL076453.

Tung, S., Masterlark, T., Dovovan, T., 2018a. Transient poroelastic stress coupling between the 2015 M7.8 Gorkha, Nepal earthquake and its M7.3 aftershock. Tectonophysics 733, 119-131. https://doi.org/10.1016/j.tecto.2018.02.003.

Tung, S., Masterlark, T., Lo, D.S.L., 2018b. Finite Element Models of Elastic Earthquake Deformation. In: Svalova, V. (ed.). Earthquakes. - Forecast, Prognosis and Earthquake Resistant Construction. IntechOpen. http://dx.doi.org/10.5772/intechopen.76612.

Turcotte, D. L., Schubert, G., 2002. Geodynamics (Second Edition). Cambridge University Press. http://dx.doi.org/10.1017/CBO9780511807442.

Vavrycuk, V., 2005. Focal mechanisms in anisotropic media. Geophys. J. I. 161, 334-346. https://doi.org/10.1111/j.1365-246X.2005.02585.x.

Verdecchia, A., Pace, B., Visini, F., Scotti, O., Peruzza, L., Benedetti, L., 2018. The role of viscoelastic stress transfer in long-term earthquake cascades: Insights after the Central Italy 2016–2017 seismic sequence. Tectonics 37, 3411–3428. https://doi.org/10.1029/2018TC005110.

Wallace, R.E., 1987. Grouping and migration of surface faulting and variation in slip rates on faults in the Great Basin province. Bull. Seismol. Soc. Am. 77, 868–876. https://doi.org/10.1785/BSSA0770030868.

Wan, Y., Shen, Z.K., 2010. Static Coulomb stress changes on faults caused by the 2008 Mw 7.9 Wenchuan, China earthquake. Tectonophysics 491, 105-118. https://doi.org/10.1016/j.tecto.2010.03.017.

Wang, H.F., 1997. Effects of deviatoric stress on undrained pore pressure response to fault slip. J. Geophys. Res. 102, 17943-17950. https://doi.org/10.1029/97JB01358.

Wang, C.-Y., Cheng, L.-H., Chin, C.-V., Yu, S.-B., 2001. Coseismic hydrologic response of an alluvial fan to the 1999 Chi-Chi earthquake, Taiwan. Geology 29 (9), 831-834. https://doi.org/10.1130/0091-7613(2001)029<0831:CHROAA>2.0.CO;2.

Wang, C.-Y. Wang, C.-H., Manga, M., 2004. Coseismic release of water from mountains: Evidence from the 1999 (M_w 7.5) Chi-Chi, Taiwan, earthquake. Geology 32 (9), 769-772. https://doi.org/10.1130/G20753.1.

Wang, K., Fialko, Y., 2018. Observations and Modeling of Coseismic and Postseismic Deformation Due To the 2015 M_w 7.8 Gorkha (Nepal) Earthquake. J. Geophys. Res. 123,

761-779. https://doi.org/10.1002/2017JB014620.

Wang, R., Lorenzo-Martin, F., Roth, F., 2006. PSGRN/PSCMP – A new code for calculating co- and post-seismic deformation, geoid and gravity changes based on the viscoelastic-gravitational dislocation theory. Comp. Geosci. 32, 527–541. https://doi.org/10.1016/j.cageo.2005.08.006.

Wang, W.-H., Chen, C.-H., 2001. Static Stress Transferred by the 1999 Chi-Chi, Taiwan, Earthquake: Effects on the Stability of the Surrounding Fault Systems and Aftershock Triggering with a 3D Fault-Slip Model. Bull. Seismol. Soc. Am. 91, 1041-1052. https://doi.org/10.1785/0120000727.

Wang, Y., Wang, F., Wang, M., Shen, Z.K., Wan, Y., 2014. Coulomb Stress Change and Evolution Induced by the 2008 Wenchuan Earthquake and its Delayed Triggering of the 2013 Mw 6.6 Lushan Earthquake. Seismol. Res. Lett. 85, 52-59. https://doi.org/10.1785/0220130111.

Wells, D.L., Coppersmith, K.J., 1994. New Empirical Relationships among Magnitude, Rupture Length, Rupture Width, Rupture Area, and Surface Displacement. Bull. Seismol. Soc. Am. 84 (4), 974-1002.

Wesnousky, S.G., Barron, S.D., Briggs, R.W., Caskey, S.J., Kumar, S., Owen, L., 2005. Paleoseismic transect across the northern Great Basin: J. Geophys. Res. 110. https://doi.org/10.1029/2004JB003283.

Yadav, R.K., Kundu, B., Gahalaut, K., Gahalaur, V.K., 2018. The 12 May 2015 Kodari earthquake (M_w 7.3) in Central Nepal: delayed triggering by the 25 April 2015 Gorkha earthquake (M_w 7.8). Current Science 114, https://doi.org/10.18520/cs/v114/i07/1534-1539.

Yang, Y., Chen, Q., Xu, Q., Liu, G., Hu, J.-C., 2018. Source model and Coulomb stress change of the 2015 M_w 7.8 Gorkha earthquake determined from improved inversion of geodetic surface deformation observations. J. Geodesy 93, 333-351. https://doi.org/10.1007/s00190-018-1164-9.

Yeats, R., 2012. Active Faults of the World, Cambridge Univ. Press, 621p.

Yu, G., Xu, X., Klinger, Y., Diao, G., Chen, G., Feng, X., Li, C., Zhu, A., Yuan, R., Guo, T., Sun, X., Tan, X., An, Y., 2010. Fault-scarp features and cascading-rupture model for the Mw 7.9 Wenchuan earthquake, eastern Tibetan Plateau, China. Bull. Seismol. Soc. Am. 100, 2590–2614. https://doi.org/10.1785/0120090255.

Yu, S.-B., Kuo, L.-C., Hsu, Y.-J., Su, H.-H., Liu, C.-C., Hou, C.-S., Lee, J.-F., Lai, T.-C., Liu, C.-C., Liu, C.-L., Tseng, T.-F., Tsai, C.-S., Shin, T.-C., 2001. Preseismic deformation and

coseismic displacements associated with the 1999 Chi-Chi, Taiwan, earthquake. Bull. Seismol. Soc. Am. 91, 995–1012. https://doi.org/10.1785/0120000722.

Yu, S.-B., Hsu, Y.-J., Kuo, L.-C., Chen, H.-Y., Liu C.-C., 2003. GPS measurement of postseismic deformation following the 1999 Chi-Chi, Taiwan, earthquake. J. Geophys. Res. 108 (B11), 2520. https://doi.org/10.1029/2003JB002396.

Zhang, P., Shen, Z., Wang, M., Gan, W., Bürgmann, R., Molnar, P., Wang, Q., Niu, Z., Sun, J., Wu, J., Sun, H., You, X., 2004. Continuous deformation of the Tibetan Plateau from Global Positioning System data. Geology 32, 809-812. https://doi.org/10.1130/G20554.1.

Zhao, B., Bürgmann, R., Wang, D., Tan, K., Du, R., Zhang, R., 2017. Dominant Controls of Downdip Afterslip and Viscous Relaxation on the Postseismic Displacements Following the M_w7.9 Gorkha, Nepal, Earthquake. J. Geophys. Res. 122, 8376-8401. https://doi.org/10.1002/2017JB014366.

Zhou, X., Burbey, T.J., 2014. Pore-Pressure Response to Sudden Fault Slip for Three Typical Faulting Regimes. Bull. Seismol. Soc. Am. 104, 793–808. https://doi.org/10.1785/0120130139.

Zhu, S., Cai, Y., 2009. Dynamic mechanisms of the post-seismic deformation following large events: Case study of the 1999 Chi-Chi earthquake in Taiwan of China. Sci. China Ser. D-Earth Sci. 52 (11), 1813-1824. https://doi.org/10.1007/s11430-009-0144-6.

Zhu, S., Miao, M., 2015. How Did the 2013 Lushan Earthquake (Ms = 7.0) Trigger its Aftershocks? Insights from Static Coulomb Stress Change Calculations: Pure Appl. Geophys. 172, 2481–2494. https://doi.org/10.1007/s00024-015-1064-3.

Curriculum Vitae

Name: Jill Peikert

Date of birth: 07.09.1990

Place of birth: Manly, Australien

Citizenship: German

06/2012   Abitur

10/2012 – 06/2016   Bachelor of Science: Geowissenschaften

Christian – Albrechts – Universität zu Kiel

04/2016 – 09/2019   Master of Science: Geophysik

Christian – Albrechts – Universität zu Kiel

10/2019 – 04/2020   Geologin

GEO-data Gesellschaft für Logging Service mbH

08/2020 – 08/2023   Wissenschaftliche Mitarbeiterin/Doktorandin

Institut für Geologie der Leibniz – Universität Hannover

List of publications

Peer-reviewed papers

Peikert, J., Hampel, A., and Bagge, M., (*accepted*). 3D Finite-Element Modeling of Coulomb stress Changes on Normal and Thrust Faults Caused by Pore Fluid Pressure Changes and Postseismic Viscoelastic Relaxation. Geosphere.

Peikert, J., Hampel, A., and Bagge, M., 2022. Relative importance of poroelastic effects and viscoelastic relaxation for postseismic velocity fields after normal and thrust earthquakes: Insights from 2D finite-element modelling. Tectonophysics 838, https://doi.org/10.1016/j.tecto.2022.229477.

Becker, D., Cristiano, L., **Peikert, J.**, Kruse, T., Dethof, F., Hadziioannou, C., Meier, T., 2020. Temporal Modulation of the Local Microseism in the North Sea. J. Geophys. Res. 125, https://doi.org/10.1029/2020JB019770.

Conference contributions

Peikert, J., Hampel, A., and Bagge, M., 2023. Relative Importance of Poroelastic Effects and Viscoelastic Relaxation for Co- and Postseismic Coulomb Stress Changes on Normal and Thrust faults: Insights from 3D Finite-Element Modeling. EGU General Assembly (poster).

Peikert, J., Hampel, A., and Bagge, M., 2022. Relative Importance of Poroelastic Effects and Viscoelastic Relaxation for Postseismic Velocity Fields and Coulomb Stress Changes on Normal and Thrust faults: Insights from Finite-Element Modeling. AGU Fall Meeting, Chicago (poster).

Peikert, J., Hampel, A., and Bagge, M., 2022. Relative importance of poroelastic effects and viscoelastic relaxation for postseismic velocity fields after normal and thrust earthquakes: insights from 2D finite-element modelling. GeoMinKlöln 2022, Köln (talk).

Peikert, J., Hampel, A., and Bagge, M., 2021. 2D finite-element modelling of the interaction between poroelastic effects and viscoelastic relaxation during the seismic cycle. GeoKarlsruhe 2021, online (talk).

Peikert, J., Hampel, A., and Bagge, M., 2021. 2D finite-element modelling of the interaction between poroelastic effects and viscoelastic relaxation during the seismic cycle. EGU General Assembly, online (talk).